Pulling Back the Veil: The Characterization and Habitability of Enshrouded Worlds

Giada Nicole Arney

A dissertation submitted in partial fulfillment of the
requirements for the degree of

Doctor of Philosophy

University of Washington

2016

Reading Committee:

Victoria Meadows, Chair

David Crisp

Shawn Domagal-Goldman

Program Authorized to Offer Degree:
Astronomy

University of Washington

Abstract

Pulling Back the Veil: The Characterization and Habitability of Enshrouded Worlds

Giada Nicole Arney

Chair of the Supervisory Committee:
Professor Victoria Meadows
Astronomy

This dissertation explores global atmospheric haze and cloud layers and shows that they are not impenetrable barriers to information about the lower atmosphere and surface environment of planets. Uncovering techniques to probe beneath these aerosol decks can reveal a wealth of knowledge about planetary environments that would otherwise be inaccessible. Hazes themselves may reveal much more than they conceal because photochemical haze layers can constrain important planetary processes and characteristics such as atmospheric redox state, surface gas source fluxes, planetary habitability, and possibly even signs of life. The spectral consequences of global aerosol decks can be significant. Unfortunately, based on historical efforts to understand cloud- and haze-covered solar system worlds, we know there is a high potential for spectral misinterpretation of globally-enshrouded worlds (e.g. Kuiper, 1944). Therefore, understanding how to properly interpret the remote observables of enshrouded exoplanets will be important to future exoplanet characterization efforts that will lack the advantage of ground-truthing within our lifetimes.

In the first section of this dissertation, I discuss sub-cloud observations of the closest globally-enshrouded planet: Venus. Venus has near-infrared spectral windows observable on the planet's nightside that allow remote sensing of thermal radiation emanating from below the cloud and haze deck. We observed Venus with the Apache Point Observatory 3.5m telescope TripleSpec spectrograph (R = 3500, λ=0.96-2.47 μm) on 1-3 March 2009 and on 25, 27, 30 November and 2-4 December 2010. With these observations and synthetic spectra generated with the Spectral Mapping and Atmospheric Radiative Transfer (SMART) model, I produced the first simultaneous maps of cloud opacity, acid concentra-

tion, water vapor (H_2O), hydrogen chloride (HCl), carbon dioxide (CO), carbonyl sulfide (OCS), and sulfur dioxide (SO_2) abundances in the Venusian sub-cloud atmosphere. Water measured at wavelengths near 1.18 μm (near-surface) averages 29±2 ppm (2009) and 27±2 ppm (2010), and measured near 1.74 μm (15-30 km) averages 33±2 ppm (2009) and 32±2 ppm (2010). Water in both of these altitude ranges is spatially homogeneous. Water measured near 2.4 μm (30-45 km) averages 34±2 ppm (2009) and 33±3 ppm (2010) and is spatially inhomogeneous and variable. Estimates retrieved from measurements of HCl near 1.74 μm indicate mixing ratios near 0.41±0.04 ppm (2009) and 0.42±0.05 ppm (2010). CO and OCS, (2.3-2.5 μm; 30-45 km in altitude), are spatially inhomogeneous and appear to be anticorrelated. CO (35 km) averages 25±3 ppm (2009) and 22±2 ppm (2010). OCS (36 km) averages 0.44±0.10 ppm (2009) and 0.57±0.12 ppm (2010). SO_2 measurements indicate average mixing ratios near 140±37 ppm (2009) and 126±32 ppm (2010). Many species display a hemispherical dichotomy in their distributions, and there is considerable spatial variability suggesting active processes with conservation between species. The most variable regions are just below the Venus cloud deck, and these may be related to changes in atmospheric circulation or virga events.

While Venus may be the closest current example of a world covered by haze and cloud, Earth itself may have hosted a global organic haze early in its history. This is significant because recognizing whether a planet can support life is a primary goal of future exoplanet spectral characterization missions. However, past research on habitability assessment has largely ignored the vastly different conditions that have existed in our planet's long habitable history. My study of hazy early Earth presents simulations of a habitable, yet dramatically different phase of Earth's history, when the atmosphere contained a Titan-like, organic-rich haze. Prior work has claimed that a haze-rich Archean Earth (3.8-2.5 billion years ago) would be frozen due to the haze's cooling effects (e.g. Haqq-Misra et al., 2008). However, no previous studies have self-consistently taken into account climate, photochemistry, and fractal hazes. Using coupled climate-photochemical-microphysical simulations, I demonstrate that hazes can cool the planet's surface by about 20 K, but habitable conditions with liquid surface water could be maintained with a relatively thick haze layer (τ~5 at 200 nm) even with the fainter young sun. I find that optically thicker hazes are self-limiting due to their self-shielding properties, preventing catastrophic cooling of the planet. Hazes may even enhance planetary habitability through UV shielding via their broad UV absorption signature, which can reduce surface UV flux by about 97% compared to a haze-free planet, and potentially allow for survival of land-based organisms at 2.6-2.7 billion years ago.

Hazy Archean Earth is the most alien world for which we have geochemical constraints on environmental conditions, providing a useful analog for similar habitable, anoxic exoplanets. To examine how organic haze may impact exoplanet habitability, I compared the production of fractal organic haze on Archean Earth-analog planets around several spectral types of stars: the sun at 2.7 billion years ago and at present day; the highly flaring M3.5V dwarf AD Leo; the M4V dwarf GJ 876; a modeled quiescent M dwarf; the K2V star ϵ Eridani; and the F2V star σ Boötis. In my simulations, planets orbiting stars with the highest or lowest UV fluxes did not form haze. Low UV-stars are unable to drive the photochemistry needed for haze formation. High UV stars generate photochemical oxygen radicals that halt the buildup of this haze. Hazes can impact planetary habitability via UV shielding and surface cooling, but this cooling seems unimportant for hazy M dwarf planets because the bulk of the M dwarf spectral energy arrives at longer infrared wavelengths where organic hazes are relatively transparent. I simulated hazy planet spectra for these exoplanet-analogs in reflected light, thermal emission, and transit transmission and found that the spectral features of organic hazes should be detectable with future telescopes. For 10 transits of a hypothetical Archean-analog planet orbiting GJ 876 observed by the James Webb Space Telescope (JWST) over 0.8 - 14 μm, haze, methane and carbon dioxide are detectable assuming photon-limited noise levels. For direct imaging of a planet at 10 pc using a coronagraphic 10-meter class ultraviolet-visible-near infrared telescope, a shortwave haze absorption feature would be strongly detectable at $>12\ \sigma$ in 200 hours. The apparent prevalence of hazy worlds in the known exoplanet population and in our solar system suggests that the impact of haze on planetary habitability and spectra are crucial to consider for future characterization of terrestrial exoplanets.

The impact of haze on habitability may have been far-reaching, and haze in the Archean could even have impacted the evolution of photosynthetic pigments because the spectrum of light reaching the planet's surface would have been reddened. I explore the consequences of this and show the spectrum of photons at the Earth's surface beneath a haze. In addition to haze, other types of UV shields would have been present in the Archean. I present spectra at several depths under water with and without dissolved Fe(II), a UV shielding compound that may have been in the Archean oceans. UV-tolerant phototrophs like *Chloroflexus aurantiacus* could have received a survivable level of UV irradiance under a haze and 10 cm of water containing 5 ppm dissolved Fe(II). With haze and other types of biochemical, chemical and physical UV shields, such organisms may have been protected even directly at the planet's surface.

Besides UV shielding and possible impacts on photosynthesis, there are other ways that an Archean haze the evolving biosphere were connected. Any haze in Archean Earth's atmosphere would have been strongly dependent on biologically-produced methane, and hydrocarbon haze may be a novel type of spectral biosignature on planets with substantial levels of CO_2. On planets with high levels of biogenic organic sulfur gases, photochemistry involving these gases can drive haze formation at lower CH_4/CO_2 ratios than methane photochemistry alone, providing another means to argue for biological activity on a haze-rich planet.

TABLE OF CONTENTS

LIST OF FIGURES

Figure Number Page

LIST OF TABLES

Table Number Page

ACKNOWLEDGMENTS

Working in the VPL, I've learned that it takes a village to model a planet. Given the number of people I want to thank, it clearly also takes a village to create a PhD scientist.

First, to my amazing advisors, I have been immensely lucky to be able to work with you. Vikki, I am incredibly grateful for all of the opportunities, mentorship, encouragement, and guidance you have provided me for the past six years. I look forward to collaborating with you in the future, and I thank you for helping me grow into the scientist I am today. Shawn, I am so grateful that you've been my co-advisor. Your patience, kindness, and infectious enthusiasm have made working with you so productive and enjoyable.

To the rest of my committee members, Dave Crisp, Roger Buick, Mark Claire, Eric Agol, and Mike Brown (see, it does take a village!): Thank you so much for your help and teachings over the years. Thanks to Dave to untangling the intricacies of radiative transfer and helping me understand how to use SMART. Thanks to Roger for introducing me to the concept of hazy Archean Earth. Thanks to Mark for teaching me a thing or two about how to be an astronomer doing geochemistry. Thanks to Eric for your teachings in class and beyond. Lastly, thanks to my GSR, Mike Brown, for helping the poor student who showed up in your office during her first week of grad school needing to learn about plate tectonics for her astrobiology class.

To my family, I love you and I am so grateful for all you have done for me over the years. Immeasurable thanks to Mom for loving me and believing in me always (Even when I was tearing through the house like a tiny hyper tornado! Even when I used up all the sugar to grow candy crystals – multiple times!). Mom, I couldn't have done this without you. To my sister Bianca, thanks for all the fun and mischievousness over the years. Adria and Erin, I can't believe you're both grown up now! I'm sure you will both go far! And, of course, thanks to Gigi, Rudi, and Brian!

Thank you to all my friends and to all of the grads in the astronomy department and

astrobiology program. Special shout out to my astrobiology partner in crime Julia!

To the whole VPL, thank you for being a source of wisdom and inspiration.

To Lupita, thanks for teaching me how to be a mentor and for being an wonderfully enthusiastic student to work with.

To the 2010 UW graduate admissions committee, thanks for believing in me! Looking to the future, I am so grateful to the anonymous reviewers who awarded me the NPP to work at Goddard next year!

Last but definitely not least: Jon, you mean so much to me. Your love and support have helped me in immeasurable ways throughout grad school. Thanks for dealing patiently with me all the times I've been under-rested and over-worked. Thanks for all the good times and adventures! My life is so much better because you're in it, and I look forward to our future.

DEDICATION

Per Nonna, con amore.

Chapter 1

INTRODUCTION

Besides the Autumn poets sing,
A few prosaic days
A little this side of the snow
And that side of the haze
- Emily Dickinson

We stand at the brink of a scientific revolution in comparative planetology: we have discovered far more exoplanets, and of different types, than the worlds in our solar system. As of this writing, we know of 2300 confirmed planets and 4700 Kepler candidates. Observations of potentially habitable terrestrial planets should be possible within the next decades. Kepler sample statistics suggest that there is at least one non-transiting and transiting Earth-sized planet (1-1.5 $R_\oplus$) in the habitable zones of M dwarf stars within 2.6 and 10.6 parsecs (pc), respectively (Dressing & Charbonneau, 2015). Another estimate puts the fraction of potentially habitable Earth-sized plants orbiting M dwarfs as high as 0.8 per star (Morton & Swift, 2014). The Transiting Exoplanet Survey Satellite (TESS) will search for these nearby worlds, and a handful of them may be observable with upcoming spaceflight missions such as the James Webb Space Telescope (JWST) and the Wide-Field Infrared Survey Telescope (WFIRST) (Beichman et al., 2014; Spergel et al., 2015). In the coming decades, dedicated large space telescopes such as the Habitable Exoplanet Imaging Mission (HabEx) and Large UV-Optical-IR surveyor (LUVOIR) concepts currently under consideration would allow us to directly image a larger sample of these highly interesting potentially habitable worlds, and search for biosignatures in their reflected light spectra (Bolcar et al., 2015; Dalcanton et al., 2015; Postman et al., 2010; Stapelfeldt et al., 2015; Seager et al., 2015).

One of the most important planetary characteristics to consider when observing and understanding exoplanet environments is the presence of aerosols - that is clouds, photochemical hazes and other small lofted particles. Aerosols are critically important to understand for four main reasons: (1) they are ubiquitous in planetary atmospheres in our own Solar System and appear common on exoplanets, (2) they are major contributors to overall planetary climate and energy balance; (3) and they can often frustrate attempts to remotely understand a planet's deep atmosphere because (4) they strongly impact planetary color and spectral appearance.

Aerosols may be common on planets elsewhere in the galaxy, and it is important to understand the conditions under which they are most likely to occur, what they can tell us about planetary environments, and which stars they are most likely to form around. In our solar system, globally cloud- and haze-enshrouded worlds occur frequently: all of the giant planets exhibit global clouds and haze in their atmospheres, Venus has a thick deck of H_2SO_4 cloud and haze, Titan is completely obscured by orange organic hazes, and even Pluto has thin yet multi-layered organic hazes (Rannou & Durry, 2009). Earth, of course, also has clouds and hazes in its atmosphere. We have also observed evidence for hazes or clouds in the transit transmission spectra of several exoplanets (Bean et al., 2010; Kreidberg et al., 2014; Knutson et al., 2014a,b; Sing et al., 2011). In fact, the only sub-Neptune-sized planet with an obviously clear atmosphere, thus far, is HAT-P-11b (Fraine et al., 2014). Based on our observations of these diverse worlds, it appears that clear sky planets are the exception rather than the rule.

The climate of a planet is strongly influenced by the presence of aerosols, so they are highly relevant to considerations of planetary habitability. Therefore, models of exoplanet climates that do not take aerosols into account are likely to produce inaccurate estimates of surface temperature, and they may under- or over-predict a planet's chances of being habitable. To take a familiar example, consider clouds on modern Earth. Clouds impact Earth's energy budget by scattering radiation at solar wavelengths and by absorbing at infrared (IR) wavelengths. However, their climatic impacts are complex because different types of clouds produce different net cooling or warming effects. High altitude cirrus clouds are largely transparent to incoming sunlight, and because they are cold, they radiate little IR energy to space and effectively absorb upwelling radiation from the warmer surface. The

IR radiated towards the ground adds to the direct sunlight already reaching the surface, causing net warming. By contrast, low clouds such as stratocumulus reflect most of the incoming solar radiation back to space and add little surface warming because they emit at temperatures similar to the surface temperature, so their net effect causes cooling. Climates of other worlds in our solar system are also strongly influenced by clouds and haze. The clouds and haze of Venus reflect over 70% of the total incident solar radiation back to space, and the residual insolation passing through the cloud deck is strongly absorbed. Our model shows that only about 3% of the incident radiation at the top of the cloud deck ever reaches the Venusian surface. The clouds themselves are effective absorbers of reradiated longwave radiation for wavelengths longer than 2.7 μm, contributing to the Venus greenhouse (Crisp, 1986). And, the relative transparency of the clouds to wavelengths shorter than 2.7 μm (see Section 2.6) provides an escape hatch for this hot planet's thermal emission. In Titan's atmosphere, a thick organic haze produces an antigreenhouse effect by scattering incident sunlight to space and remaining transparent to outgoing longwave radiation. Without a haze, the surface of Titan would be more than 20 K warmer (McKay et al., 1991). These examples show us that whenever atmospheric aerosols are present – particularly global aerosol layers – they have a pronounced impact on the planetary climate.

Despite their strong impact on planetary climates, aerosols can make it difficult to assess the surface temperature of worlds. In reflected light, optically thick cloud and haze decks can act as a new effective surface in a planet's spectrum, radiating upward with a blackbody temperature different from the solid surface of the world below. For example, the surface environments of Venus and Titan were poorly understood before development of technology and techniques to probe below their cloud and haze decks. On Venus, the effective emitting temperature at the top of its bright cloud and haze deck is 220 K, and this is an incredible 520 K colder than the actual surface temperature of about 740 K. By contrast, on Titan, the temperature of the surface is actually colder than it would be without haze's antigreenhouse cooling as mentioned previously. Early estimates of Titan's surface temperature measured at 8.4 μm were as high as 146 K (Hunten, 1974), but Titan's actual surface temperature is only around 94 K. The confusion here was caused by the warm stratosphere in Titan's atmosphere due to the haze's absorption of short wavelengths, similar to the stratosphere produced by the ozone layer on Earth. These two examples provide a stark illustration of the challenges of estimating surface temperatures on globally enshrouded worlds. But, as we have discussed, it will be particularly important to accurately characterize the surface environments of exoplanets to gauge their potential habitability.

Aerosols can produce other major spectral changes besides emitting at different temperatures than the surface. We have seen that exoplanet spectra are strongly affected by atmospheric aerosols: due to the long path lengths traveled by light in transit observations, hazes that are optically thin all the way down to the surface in reflected light can become optically thick at elevated altitudes in transit transmission observations. The spectrum produced from the light that is able to pass through the rarefied upper layers above the aerosol deck may lack absorption features, producing the featureless, “flat” transit transmission spectra plaguing exoplanet observers in recent years. This can also make it difficult to sense gases that condense out as clouds deeper in the atmosphere or gases soluble in clouds droplets. Other ways that global aerosol layers can frustrate remote characterization attempts can be again be found closer to home in the solar system. When Gerard Kuiper took spectra of Titan (Kuiper, 1944) and discovered the presence of an atmosphere, he speculated that its orange color was “due to the action of the atmosphere on the surface itself, analogous to the oxidation supposed to be responsible for the orange color of Mars.” Kuiper’s work was pioneering, but we now know that his interpretation was incorrect. It was not until 1973 that the presence of Titan’s orange haze deck was deduced through polarimetric measurements (Veverka, 1973).

This last example illustrates the kinds of challenges aerosols pose for observers, and it also illustrates the dangers of using first-order planetary properties such as color to characterize worlds without considering them in the proper planetary context. Had Kuiper known that Titan’s atmosphere is extremely reducing, it is unlikely that he would have proposed oxidation as the explanation for the orange color. Kuiper’s misinterpretation serves as a warning against under-designing the capabilities of spectroscopic instruments on future exoplanet observatories. We will need as much contextual information as possible to accurately characterize the nature of exoplanets that will never have the advantage of ground-truth measurements within our lifetimes.

As we have seen, aerosol decks can be spectral hindrances that hide planetary features and processes, but in this thesis, I will argue that in some cases, they can reveal more than they conceal.

I will show how the seemingly unreachable Venus sub-cloud atmosphere can be studied using remote observations at wavelengths where the cloud deck is transparent. Observations of the Venusian lower atmosphere can provide vital information about Venus' surface and near-surface temperature structure, abundances of sub-cloud trace gases, and the presence of global chemical cycles.

Planet-wide aerosol layers are relevant to habitable planets, too: our own planet may have hosted a Titan-like haze billions of years ago in the Archean geological period (about 4-2.5 billion years ago). I will show what such a haze-covered early Earth could have looked like to remote observers, and I will discuss how this haze may have impacted Archean climate and habitability. Organic haze, which was likely controlled by biogenic methane production on early Earth, may even be a signpost of life in the atmospheres of Archean-like exoplanets.

Despite their importance, studies of exoplanets frequently neglect aerosols. At the 2015 Division of Planetary Science meeting in National Harbor, MD, I participated in a press conference about my work on hazy early Earth. A well-meaning reporter asked me, "Would the haze have been present in addition to an atmosphere, or instead of?" While this question may seem amusing, sometimes, even scientists forget or ignore the fact that hazes and clouds are just as important to consider as gases. As I have argued above, neglecting the presence of aerosols in planetary atmospheres is fraught with the potential for complete mischaracterization of a planet's surface environment.

Studies of Earth as an exoplanet frequently examine idealized, clear-sky conditions (Segura et al., 2005; Kaltenegger et al., 2007), but we know this is not a realistic expectation simply by considering that water clouds cover about half of our planet. Decades from now, when (yes, when!) light from the first directly-imaged Earthlike exoplanet hits our telescopes, once the champagne-popping is over, we will face the serious and difficult task of properly interpreting its spectrum to deduce its atmospheric composition and surface conditions. To do this correctly, our considerations will have to include the possibility of aerosols, including globally-distributed ones.

Below, I briefly introduce the two types of aerosols to be considered in this thesis.

1.1 Sulfuric Acid

Venus' atmosphere contains a thick deck of sulfuric acid (H_2SO_4) clouds and haze extending between roughly 45 and 100 km in altitude, as described in more detail in Chapter 4. Sulfuric acid hazes are also relevant to Earth's atmosphere (although, of course, at much lower abundance than in Venus' atmosphere) because Earth's volcanic outgassing produces sulfur gases that can react to form H_2SO_4 (e.g. Hu et al., 2013). Misra et al. (2015) showed that H_2SO_4 aerosols in Earthlike atmospheres can be remotely detected in transit transmission observations, and such detections are particularly interesting because transient H_2SO_4 droplets in the stratosphere may be indicative of the type of explosive volcanism driven by plate tectonics. Similarly, in the atmosphere of Venus, the H_2SO_4 deck implies an ongoing volcanic source of SO_2, pointing to a geologically active planet (Fegley & Prinn, 1989; Bullock & Grinspoon, 2001).

1.2 Hydrocarbon Haze

Hydrocarbon haze (also called "organic haze") is present on Titan and may have been occasionally present in Archean Earth's atmosphere (see Chapter 5). Its formation is initiated by methane photolysis. The haze on Titan is a sink of methane, necessitating a methane source to form a persistent haze deck, but this source remains is uncertain (Tobie et al., 2006). For Archean Earth, some quantity of methane would have been produced by abiotic processes, but the bulk of the methane probably came from biological processes such as methanogenesis (Kharecha et al., 2005). Methanogenesis was one of the earliest metabolisms, and it produces H_2O and CH_4 through reactions involving H_2 and CO_2 (Kharecha et al., 2005; Ueno et al., 2006).

1.3 Planets considered in this Thesis

I consider two planets in this thesis: Venus and Archean Earth (3.8-2.5 billion years ago). Venus provides a nearby example of a world totally enshrouded by a thick cloud and haze deck composed of sulfuric acid droplets. However, even Venus' seemingly impenetrable aerosol layer is porous to information about the fascinating planet below. Meanwhile, if Archean Earth supported a global organic haze, this challenges our preconceptions of what an “Earthlike” planet is like: “pale blue” is not a prerequisite description for Earthlike dots. And, the hazy “pale orange dots” we simulate here for Archean Earth teach us that haze decks and habitability are inextricably linked, and interactions between haze and biospheres are complex. Below, I introduce both of these worlds in more detail.

1.3.1 Venus

The haze and cloud-enshrouded planet next door (Figure 1.1) provides an ideal case study for how to glean information from below a thick aerosol layer. Venus is a complex and intriguing planet, but its surface conditions were veiled in mystery for many decades, prompting wild speculations of swampy oases beneath the dense butter-colored clouds. A hint of the hot surface temperature came from millimeter wave observations in the late 1950s (Mayer et al., 1958), but confirmation of the true hellish nature of Earth’s twisted sister had to wait for spacecraft visits in the 1960s (Dickel, 1966; Avduevsky et al., 1968). However, had we understood the properties of the Venus cloud and haze particles earlier, she would have shared the secrets of her lower atmosphere with ground-based observers before this.

What we did not realize until the groundbreaking study by Allen & Crawford (1984) is that the Venus clouds are transparent in the near-infrared (NIR), allowing thermal radiation from below the cloud deck to escape to space. Allen and Crawford detected an unexpected excess of radiation near 1.74 μm and 2.3 μm on the planet’s night side. It was subsequently shown that these spectral regions measure thermal emission from below the cloud deck (Allen, 1987) thereby allowing remote exploration of the Venusian lower atmosphere. After their seminal discovery, subsequent Venus spectral windows sensitive to the surface and lowest scale height ($\sim$16 km) were discovered at 1.0, 1.10, 1.18, 1.27, and 1.31 μm (Carlson et al., 1991; Crisp et al., 1991a). These windows all exist between strong CO_2 and H_2O absorption bands, where the atmosphere is relatively transparent. The thermal emission seen in the Venusian NIR windows must be observed on the night side of the planet because sunlight reflecting off the bright clouds overwhelms it on the dayside.

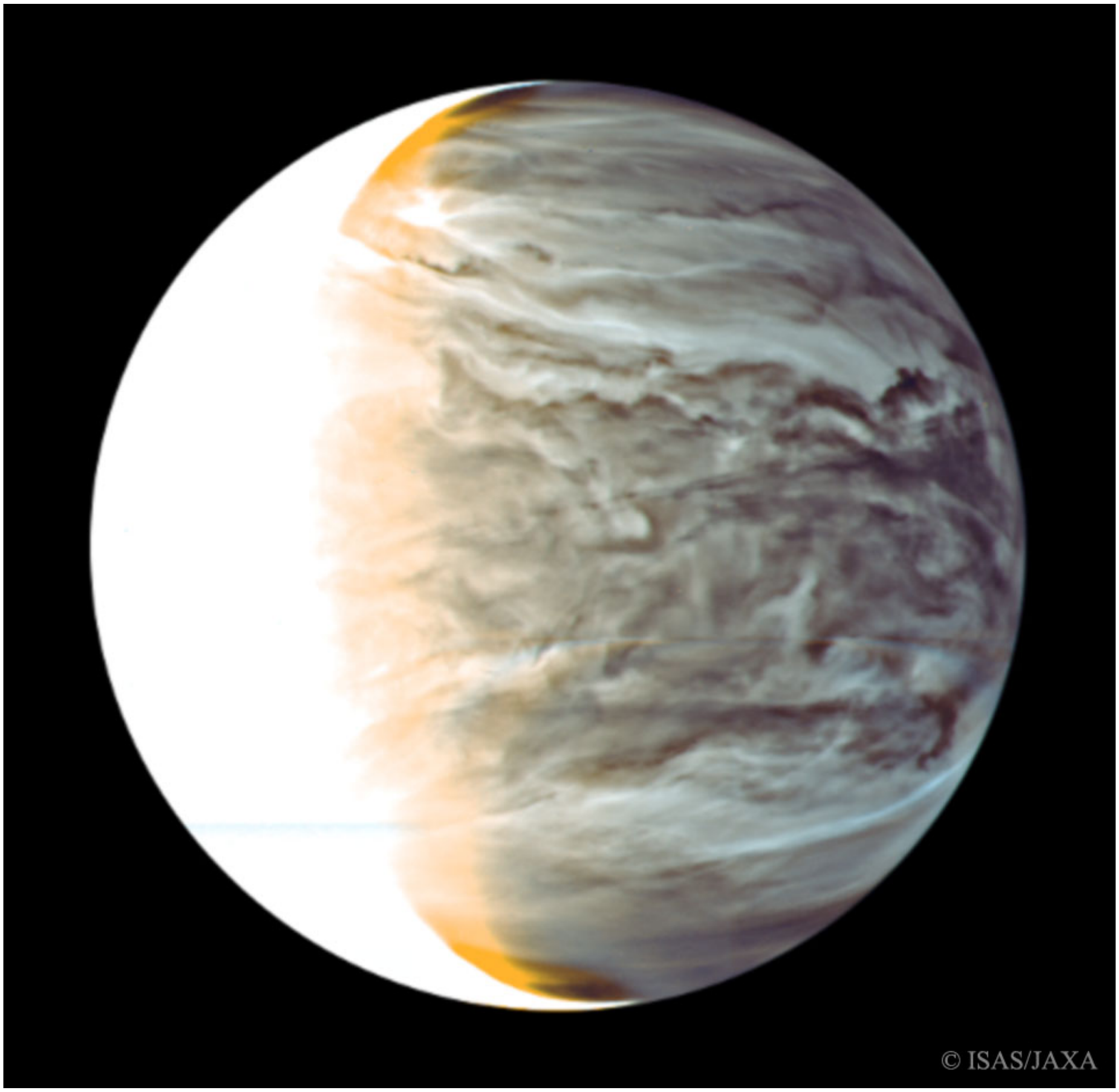

Figure 1.1: Clouds on the nightside of Venus are visible in this beautiful image taken in the near-infrared by the JAXA Akatsuki spacecraft.

Although the scattering optical depth of the Venus clouds is high even in the NIR window region, absorption from the sulfuric acid aerosols is not efficient here, (see Section 2.6 for further discussion) allowing the escape of sub-cloud thermal radiation after being multiply scattered. It is the combination of relative transparency of the H_2SO_4 aerosols and the lack of CO_2 and H_2O absorption in the NIR window regions that make the windows' existence possible. Thicker clouds lead to decreased radiance measured in the NIR windows, and cloud opacity is observed in the Venus windows to be highly variable both spatially and temporally (Chapter 4).

The shorter wavelength windows (<1.3 μm) in particular probe deeply into the Venus atmosphere, and the window at 1 μm is highly sensitive to thermal variations of the surface: 96% of the radiation in this window is direct surface thermal emission (Meadows & Crisp, 1996). The depths probed most sensitively by all the Venusian NIR windows are summarized in Table 1.1. Because the windows sense different heights in the atmosphere, vertically resolved information can be measured across the entire 1.0-2.5 μm range, allowing observers to paint a complex picture of the Venus-sub cloud environment and search for correlations between chemical species at different altitudes and different spatial locations.

Table 1.1: The Venus Near-Infrared Windows. Altitudes shown are the altitudes of greatest sensitivity to the Venus NIR spectral windows. Information in this table is derived from Taylor et al. (1997), Tsang et al. (2008a), and Chamberlain et al. (2013).

Window (μm)	Wavelength Range	Depth
1.0	0.98 - 1.035 μm	surface
1.10	1.08 - 1.11 μm	0-15 km
1.18	1.15 - 1.20 μm	0-15 km
1.28	1.25 - 1.35 μm	0-30 km
1.31	1.30 - 1.31 μm	10-50 km
1.74	1.71 - 1.755 μm	10-30 km
2.3	2.20 - 2.50 μm	20-45 km

1.3.1.a The Venus Sulfuric Acid Cloud Deck

Sulfuric acid is generated photochemically from SO_2, the net result of which is $CO + SO_2 + O_2 + H_2O \longrightarrow CO_2 + H_2SO_4$ (Yung & DeMore, 1982). SO_2 is thought to be produced by volcanic emissions (Esposito et al., 1997), so H_2SO_4 clouds and hazes may be a strong indicator of volcanism on Venus and also on distant exoplanets (Hu et al., 2013).

The Venusian H_2SO_4 is produced photochemically in the upper cloud (Yung et al., 1984) at altitudes around 60 km (160 mbar) (Hashimoto & Imamura, 2001), producing a fine haze. By diffusion, the H_2SO_4 can condense into the main cloud deck. The bottom of the cloud deck is determined by the altitude where the H_2SO_4 vapor pressure exceeds its saturation vapor pressure: this occurs at roughly 47 km ($\sim$2 bars). Below this altitude, the sulfuric acid is in the gas phase down to about 38 km ($\sim$4 bars), where the H_2SO_4 gas is thermally decomposed at temperatures of about 430 K (Bullock & Grinspoon, 2001) through:

$$\mathrm{H_2SO_4} \longrightarrow \mathrm{SO_3} + \mathrm{H_2O}$$

Outgassed SO_2 can be lost to reactions with Venus surface minerals. The amount of SO_2 in the Venus atmosphere has been estimated to be in excess of equilibrated conditions by a factor of 100, implying a source within the past 20 million years (Bullock & Grinspoon, 2001). Another estimate evaluating the rate of SO_2 reactions with surface calcium minerals suggests a even shorter cloud deck lifetime of only two million years (Fegley & Prinn, 1989).

Cloud-top variations of SO_2 have been observed across several decades of Pioneer Venus and Venus Express observations (Marcq et al., 2012), implying a long-term cycling mechanism bringing SO_2 from the lower atmosphere to above the upper cloud and haze deck. This may be related to atmospheric dynamics and transport of H_2SO_4 particles and vapor from the deep atmosphere, or possibly to injections via volcanism. However, initial searches for active volcanism were not fruitful. An analysis of Venus Express (VEx) data taken with the Venus Monitoring Camera (VMC) between October 31, 2007 through June 15, 2009 in the 1 μm nightside spectral window was unable to discover any hot spots that might be indicative of volcanic activity (Shalygin & Basilevsky, 2012). More recently, however, nine emissivity anomalies due to compositional differences were identified by the VEx Visible and Infrared Thermal Imaging Spectrometer (VIRTIS) as sites of potentially recent volcanism (Smrekar et al., 2010). There are purported lava flows associated with these anomalies estimated to be 2.5 million years old at most, and more likely to be as young as 250,000 years old or less (Smrekar et al., 2010) based on expected weathering rates of freshly emplaced basalts. The emissivity anomalies sit atop regions of thin, elastic lithosphere according to Magellan gravity data, strengthening the volcanism interpretation. In 2015, even better evidence for active volcanism on Venus was uncovered with a new analysis of VMC data. Four temporally variable surface hotspots were discovered at the Ganiki Chasma rift zone near volcanoes Ozza Mons and Maat Mons (Shalygin et al., 2015), suggestive of present volcanic activity. However, interpreting these types of observations correctly is a challenge. The scattering footprint of radiation from the Venus surface escaping through the cloud deck is about 100 km^2, so smaller areas of increased thermal emission are smeared out. In addition, variations in the lower cloud deck opacity can imprint their own brightness variations on the Venusian surface that might be mistaken for hotspot activity (see Section 4.3.2.a for further discussion of this phenomenon, which we call "cloud ghosting"). Future evidence of Venusian volcanism could be bolstered by simultaneous observation of a hotspot and increased abundance of volcanically-produced atmospheric species in its vicinity. We discuss our own search for such events in Chapter 4. This search did not find evidence of any volcanic activity.

As mentioned previously, sulfur-containing aerosols exist on other solar system planets. Volcanism on Earth releases H_2S and SO_2 that can react to produce H_2SO_4 or S_8 particles. More oxidizing conditions favor H_2SO_4 production, and more reducing conditions such as those that existed early in Earth's history favor S_8 (Hu et al., 2013; Zahnle et al., 2006). Organic sulfur gases can affect H_2SO_4 production on inhabited worlds with organic sulfur-emitting biospheres: chemistry involving dimethyl sulfide (DMS), which is produced by life, also produces H_2SO_4 (Toon et al., 1987). On early Mars, if SO_2 emissions were sufficiently high, sulfur-containing hazes may also have been produced (Tian et al., 2010).

1.3.2 Hazy Archean Earth

Global aerosol decks are not just features of alien planets. During the Archean period (3.8-2.5 billion years ago, Figure 1.2), an intermittently present organic haze similar to Titan's may have existed in our planet's atmosphere (Pavlov et al., 2001b; Trainer et al., 2004, 2006; DeWitt et al., 2009; Hasenkopf et al., 2010; Zerkle et al., 2012; Kurzweil et al., 2013; Claire et al., 2014; Izon et al., 2015). Thus, Archean Earth can serve as an archetype of organic-rich, hazy, habitable exoplanets (Figure 1.3). Organic haze, whose formation is initiated by methane photolysis, would have scattered and absorbed incoming solar radiation, heating the stratosphere while cooling the planet's surface (McKay et al., 1991). The haze's strong interactions with incoming and outgoing radiation can produce strong remotely detectable spectral features that can inform us of the presence of this type haze on exoplanets.

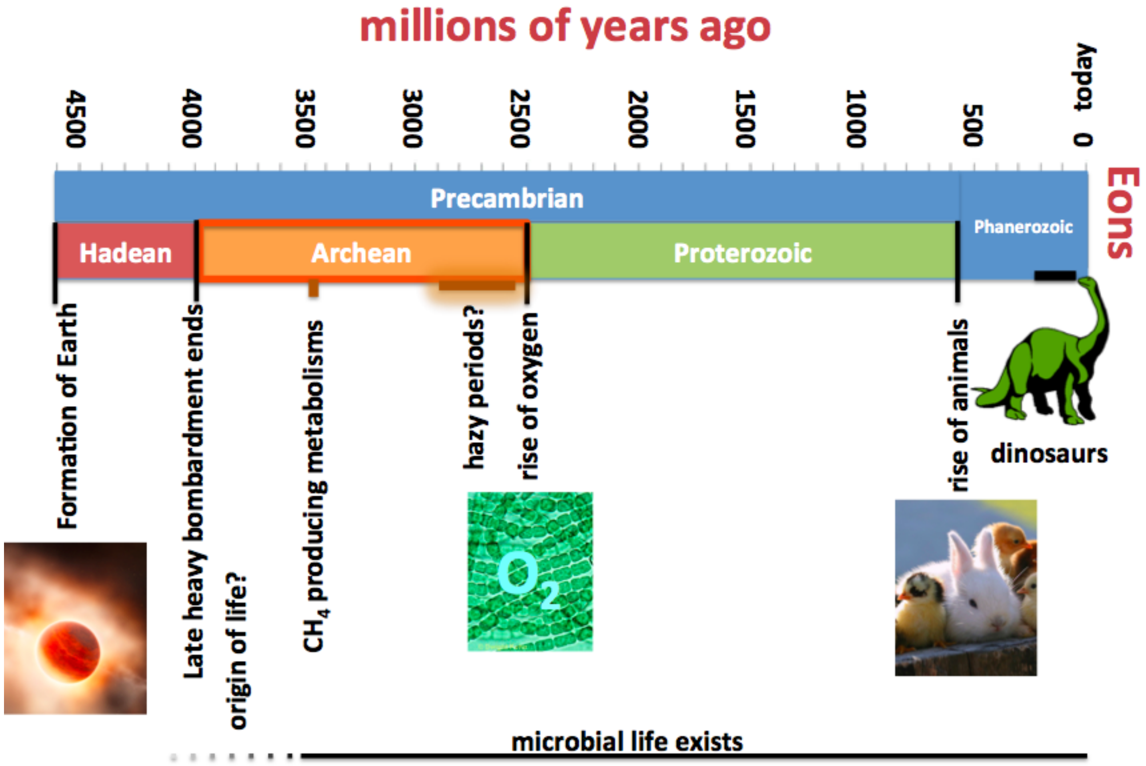

Figure 1.2: A simplified timeline of major events in Earth's history. A period with possibly hazy intervals is indicated. Bunny image from www.wallpapervortex.com.

Geochemical evidence for an Archean haze centers around correlations observed between sulfur and organic carbon isotopes that can constrain surface UV flux and the atmospheric redox state. A short review of this evidence can be found in Chapter 5 and references therein. In Archean Earth's atmosphere, organic haze could have formed when the ratio of methane

(CH_4) to carbon dioxide (CO_2) in the atmosphere was above 0.1, and its formation under Archean-analog atmospheric conditions has been observed in the laboratory (Trainer et al., 2006; DeWitt et al., 2009; Hasenkopf et al., 2010, 2011). Hazy Archean Earth is important to consider as a distinctly different phase of our planet's evolution: it is a habitable (and inhabited) world whose spectrum bears little resemblance to our planet today. Because CH_4 can be produced by several abiotic processes (Kasting, 2005; Kelley et al., 2005; Etiope & Sherwood Lollar, 2013; Guzmán-Marmolejo et al., 2013), and CH_4-producing metabolisms (i.e., methanogenesis) are simple and evolved early on Earth (Ueno et al., 2006; Kharecha et al., 2005; Woese & Fox, 1977), methane-rich terrestrial exoplanets with organic haze may occur frequently.

The interactions of haze with incoming sunlight would have had important consequences for the climate of our young planet, and this may be relevant to hazy exoplanets (Pavlov et al., 2001a; Haqq-Misra et al., 2008; Domagal-Goldman et al., 2008; Wolf & Toon, 2010; Hasenkopf et al., 2011). The cooling effects associated with geologically-constrained CO_2 abundances and an Archean haze under a fainter young sun (Sagan & Chyba, 1997) might suggest surface conditions would have been too cold to support life. However, the work I have done on the hazy Archean does not support this. Using paleosol constraints on CO_2 measured by Driese et al. (2011), which estimates the partial pressure of CO_2 (pCO_2) in the Archean atmosphere at 2.7 billion years ago (Ga) as 0.0036-0.018 bars, I found that habitable conditions are possible at 2.7 Ga for 0.5 and 1 bar atmospheres, even with the fainter young Sun (Arney et al. 2016 and Chapter 5). Habitable conditions are possible under a haze for three reasons: first, we used fractal-shaped (see Chapter 2) rather than spherical particles, which result in less cooling (Wolf & Toon, 2010); second, haze formation was found to be self-limiting due to UV self-shielding, which shuts off haze formation; third, the lower temperature limit we considered "habitable" was revised based on the results of 3D climate modeling studies showing that planets like Archean Earth can maintain stable open ocean belts at global average temperatures as low as 250 K (Charnay et al., 2013).

Particularly relevant to the search for life beyond our solar system, CH_4 has been considered as a type of spectral biosignature (albeit one that must be treated carefully as it also has geological sources – see Etiope & Sherwood Lollar (2013) for a review). At wavelengths

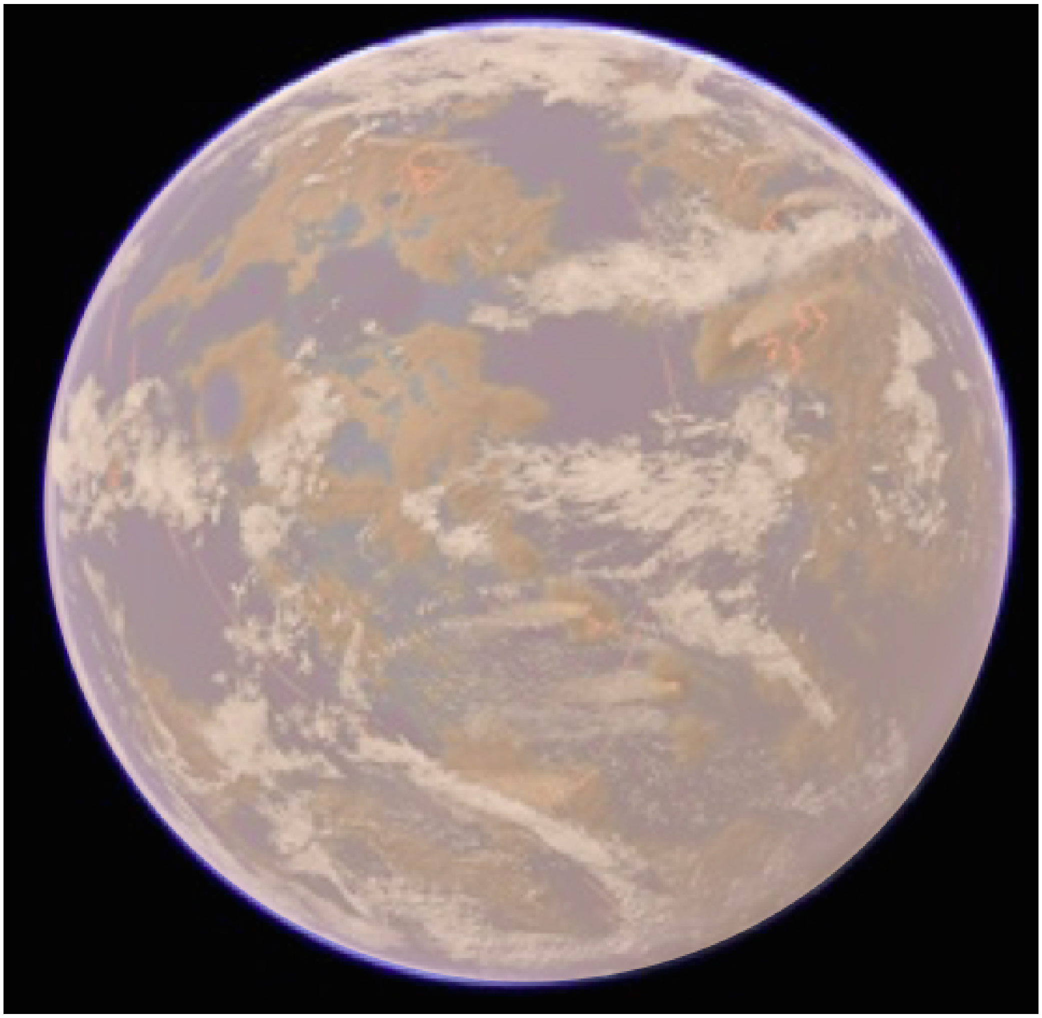

Figure 1.3: A hypothetical image of hazy Archean Earth. Image credit: yooniqimages.com

<0.5 μm, a broad and deep absorption feature produced by a thick haze (the reason why Titan is orange) can be more dectable than the absorption features from CH_4 itself. This makes haze a useful indirect signal of the presence of CH_4, similar to how O_3 can be an indirect signal of O_2 (e.g. Des Marais et al., 2002). Of course, there are other UV absorbers that may mimic the haze feature, and these "haze false positives" are discussed in Chapter 6. Significantly, production of an organic haze in a relatively CO_2-rich atmosphere like Archean Earth's (as opposed to Titan, which is extremely reducing) may require surface fluxes of methane higher than those predicted to be plausible from geological processes alone as discussed in Chapters 5-7.

1.3.3 Sources of methane for hydrocarbon haze

Similar to the H_2SO_4 deck on Venus, the presence of a long-lived organic haze implies an active source of methane. On Titan, the source of the methane that – through complex photochemistry – ends up as organic haze is uncertain. The haze is an irreversible sink for methane (Atreya et al., 2006), and the atmospheric haze on Titan would last only 10-100 million years without a replenishing methane source (Niemann et al., 2005). Once methane is converted to haze, haze particles are deposited on the surface and are not converted back into methane (Atreya et al., 2006). This could mean that we are observing Titan at an unusual time in its history, but it seems more likely to suppose that Titan is somehow outgassing (or accreting) methane. On Earth, biologically-produced methane has a higher ratio of ^{12}C to ^{13}C than non-biological methane because organisms preferentially uptake the lighter isotope. However, the $^{13}C/^{12}C$ ratio measured for Titan's methane does not support a biological interpretation (Niemann et al., 2005). It has been suggested that Titan's methane is released from the subsurface through degassing of clathrate hydrates (Tobie et al., 2006). These clathrates may have captured methane from the primordial nebula Titan formed from.

On Archean Earth, there are numerous potential sources of methane, although biological processes likely dominated, as they do today (Kharecha et al., 2005). Methanogenesis, an anaerobic metabolism deeply rooted in the tree of life that likely evolved early in Earth's history (Woese & Fox, 1977; Ueno et al., 2006), can uptake CO_2 and H_2 to form CH_4 and H_2O:

$$\mathrm{CO_2 + 4\,H_2 \longrightarrow CH_4 + 2\,H_2O}$$

Methanogenesis has only been observed in types of Archaea, and it occurs in a number of anoxic environments on modern Earth including animal guts and hydrothermal vents (Ver Eecke et al., 2012). In the latter environment, the methanogens react H_2 contained in reduced fluids emanating from the vents with CO_2 dissolved in the seawater. On Earth today, the flux of methane produced by biology is roughly 10^{11} molecules/cm^2/s (Pavlov et al., 2001a), and the Archean biotic flux has been estimated to range somewhere between 1/3 - 2.5 times this modern value (Kharecha et al., 2005).

The abiotic production rate of methane is less certain. Serpentinization, the hydration of olivine and pyroxene, is the dominant abiotic source of methane on Earth today (Kelley et al., 2005; Guzmán-Marmolejo et al., 2013; Etiope & Sherwood Lollar, 2013). Serpentinization produces H_2, which can subsequently react with gases such as CO_2 or CO to form CH_4. Kasting & Catling (2003) estimated the abiotic flux of methane as 1/300th the biotic rate. However, more recent measurements by Kelley et al. (2005) at the Lost City hydrothermal system indicate that abiotic methane production rates may actually be as high as 1/30th the biotic flux.

Etiope & Sherwood Lollar (2013) presented a comprehensive review of abiotic methane production on Earth. They discuss that abiotic production has been roughly estimated at 1/26th of the biotic flux by Emmanuel & Ague (2007), consistent with the Kelley et al. (2005) Lost City estimates.

A different line of argument to estimate the abiotic methane production from serpentinization on Earth comes from Guzmán-Marmolejo et al. (2013). These authors calculate how much methane can be produced given current crustal spreading rates as a function of available FeO in the crust and by considering that CO_2 is the limiting reactant for methane production in serpentinziation. They estimate that the maximum amount of abiotic methane that can be produced from serpentinization is 6.8×10^8 molecules/cm^2/s for 1 Earth mass planet, which is only 1/160th the biotic flux (Guzmán-Marmolejo et al. (2013) also estimate the rate as 1.3×10^9 molecules/cm^2/s for a five Earth mass planet). However, note that these results are contingent on the assumption of the modern-day Earth crustal spreading rate.

Considering all of the above estimates, abiotic methane production rates between approximately 1/30 - 1/150th the present biotic flux seem reasonable to assume for modern Earth.

In the Archean, abiotic methane production rates are even less certain than they are today. If the early planet had faster seafloor spreading rates or a higher fraction of seafloor ultramafic rocks, enhanced abiotic methane compared to the modern planet would have been possible (Kasting, 2005; Shaw, 2008). Faster seafloor spreading rates may be reasonable to assume given that the young planet was hotter, so convection may have proceeded more efficiently. How tectonics operated in the Archean remains uncertain, but geological evidence and numerical modeling support the existence of plate tectonics during this period (Kerrich & Polat, 2006).

Considering all of the above, finding an organic haze in the atmosphere of a planet with Archean-like CO_2 levels would be indicative of highly interesting processes that imply ongoing geological activity and/or biological methane production with high methane source fluxes (Kharecha et al., 2005). Such a planet should be flagged for closer follow-up studies to investigate ways of discriminating between geological and biological CH_4 sources and to search for other signs of habitability and life.

1.4 Relevance to Astrobiology

The aerosols considered here, H_2SO_4 and organic haze, are closely tied to processes related to planetary habitability, biological activity, and remote sensing of planetary characteristics.

As we discussed, clouds and haze can impact a planet's habitability by scattering sunlight back to space, cooling the surface temperature. In estimating exoplanet temperatures, models must account for any aerosols that may be present or their temperature estimates may be wildly inaccurate. Additionally, the cooling properties of aerosol decks have implications for the boundaries of the habitable zone, the region around a star where surface liquid water can be stable (Kasting et al., 1993; Kopparapu et al., 2013). Estimates of the inner edge of the habitable zone that neglect cloud feedback processes suggest that the inner edge of the habitable zone in our solar system is at 0.99 astronomical units (AU) (Kopparapu et al., 2013). However, when cloud feedbacks are accounted for, this edge is pushed inwards of 0.93 AU (Wolf & Toon, 2014). Global haze layers could produce even more cooling, and there may be a "hazy habitable zone" (HHZ) closer to the star than the traditional boundaries. We discuss the implications of the HHZ further in Section 6.4.3.

Because the existence of these aerosols in an atmosphere implies production of the gases that form them (i.e. SO_2 and CH_4), their detection in a planetary atmosphere could suggest active geological processes relevant to habitability. Plate tectonics, in particular, may be a prerequisite for long-term habitability through regulation of the surface temperature via the inorganic carbon cycle (Walker et al., 1981). Plate tectonics is extremely difficult to sense remotely, but aerosols may provide hints of its existence. As mentioned before, the presence of H_2SO_4 aerosols in the stratosphere of an Earthlike exoplanet could suggest the type of explosive volcanism that occurs at continental plate boundaries (Misra et al., 2015). For organic hazes, as we have seen, methane can be sourced from biological or non-biological processes. However, even abiotic methane would be highly interesting on an Earthlike exoplanet. As we have discussed, serpentinization produces most of our planet's abiotic methane inventory. To occur, serpentinization requires two things that are highly relevant to habitability. First, serpentinization requires water to react with olivines and pyroxenes, so detection of methane (or organic haze, whose spectral signatures may be stronger) in an Earthlike atmosphere could suggest the presence of liquid water. Second, serpentinization requires fresh mafic seafloor minerals to react with. Although authors have suggested that water could percolate through cracks in seafloor layers to find fresh material to react with in the case of Jupiter's moon Europa (Vance et al., 2007), it seems likely that creation of new seafloor crust is needed for the maintenance of robust serpentinziation on long timescales. This again hints that plate tectonics might be operating on an exoplanet. More intriguingly, existing measurements and models suggest that the presence of an organic haze on an Earthlike exoplanet requires a higher methane production rate than is thought to be plausible from abiotic processes alone, so organic haze in an Earthlike atmosphere could be a sign of life. This is different from a Titan-like world with an extremely reducing atmosphere and cold temperature, which does not require high methane fluxes to produce the haze.

Both H_2SO_4 and organic haze strongly alter their planets' spectra, both in reflected light and in transit transmission, allowing them to be remotely observed. We discuss the spectral features of H_2SO_4 and organic haze in great detail in the following chapters. The spectral signatures of these aerosols can be extremely strong, making them potentially more detectable than the gases that formed them. Their spectral behavior may even be beneficial to surface biospheres: organic haze and SO_2, a precursor to H_2SO_4, produce broad ultraviolet (UV) absorption features, so such aerosols may provide UV shields for surface life. It is particularly interesting to consider the existence of such a hazy UV shield in the Archean because the Archean atmosphere was anoxic and therefore lacked the ozone layer present in the modern atmosphere. Archean Earth with no UV shield would have received enough UV to sterilize the surface, forcing organisms to take refuge under water and other types of chemical and physical UV shields. We will show in Chapter 5 that organic haze in the Archean atmosphere could have reduced the flux of short wavelength UV radiation reaching the surface by two orders of magnitude, and UV radiation reaching organisms could have been diminished even further by dissolved Fe(II) in a water column as discussed in Chapter 7. The Archean UV flux under a haze would still have been too high to allow the survival of most modern organisms, but it may have been low enough to be tolerated by certain UV-resistant microbes such as *Chloroflexus aurantiacus* that have been studied as analogs for Archean phototrophs (Pierson et al., 1992).

Considering all of the above, it is clear that atmospheric aerosols are highly relevant to astrobiology. Analyses of exoplanet spectra will need to consider aerosols to understand the habitability of a planet's surface environment (i.e. temperature, UV shielding). Furthermore, aerosols such as organic haze and H_2SO_4 can imply geological activity important to habitability, and their spectral features are strongly detectable. Finally, they may also provide evidence of life if the sources of CH_4 and other organics can be determined.

1.5 Structure of this Thesis

In the following chapters, I will explain what enshrouded worlds like Venus and Archean Earth can teach us about understand planetary properties such as gas abundances, habitability and photochemistry. Chapter 2, "A Primer on Particles", presents information on particle scattering and absorption physics that provides a basis for understanding how aerosols behave in the studies presented later on. Chapter 3 describes the models used here. In Chapter 4, I present a study of the Venus lower atmosphere, sensed below its cloud and haze layers, and I show the first simultaneous and spatially-resolved ground-based measurements of H_2SO_4 droplet concentration, cloud opacity, H_2O, HCl, CO, OCS, and SO_2. In Chapters 5-7, I tell the story of "The Pale Orange Dot", a dramatically different phase of our planet's evolution when Archean Earth was enshrouded by an organic haze. Chapter 5 examines how this haze would have impacted the climate, habitability, and spectrum of Archean Earth. Chapter 6 extends our study of Archean Earth to Archean-analog exoplanets to examine the formation and detectability of organic haze on Earthlike worlds orbiting several spectral types of stars. In Chapter 7, I consider how haze could be a biosignature in the presence of organic sulfur gases and how it could have impacted Archean photosynthetic life. Finally, in Chapter 8, I summarize my findings and conclusions.

Chapter 2

A PRIMER ON PARTICLES

“What exactly is haze?” is the most frequent question I get asked when speaking about my research. The words haze, clouds, and aerosols are often used interchangeably, so this section aims to define them clearly and remove any clouds of confusion. Following these definitions, it is important to understand the basic vocabulary and physics of particle absorption and scattering, so I present a broad overview of important concepts related to how particles interact with photons. After this, I present a discussion of fractal particles, which are important for organic hazes. Finally, I discuss atmospheric windows in the context of Venus and Titan, which are important consequences of the basic particle properties discussed here. Much of the information in this chapter is derived from the introductory atmospheric radiation textbook by G. Petty (Petty, 2006), the aerosol dynamics book by K. Sheldon (Sheldon, 2000), and the excellent course notes by R. Grainger[1].

2.1 A note on terminology

In this context, “haze” refers to photochemically-produced particulates suspended in a planet’s atmosphere. In Titan’s atmosphere (and possibly Archean Earth’s), photochemical reactions involving methane produce organic haze particles through a complex and poorly-understood series of polymerization reactions (McDonald et al., 1994; Khare et al., 1984a; Trainer et al., 2006). In Titan’s atmosphere, these reactions are known to include ion chemistry (Waite et al., 2007). In Venus’ atmosphere, photochemical reactions involving SO_2 and H_2O produce a high-altitude H_2SO_4 haze (Yung & DeMore, 1982):

$$\mathrm{SO} + h\nu \longrightarrow \mathrm{S} + \mathrm{O}$$

$$\mathrm{S} + \mathrm{O_2} \longrightarrow \mathrm{SO} + \mathrm{O}$$

$$\mathrm{SO_2} + \mathrm{O} + \mathrm{M} \longrightarrow \mathrm{SO_3} + \mathrm{M}$$

---

[1] http://eodg.atm.ox.ac.uk/user/grainger/research/aerosols.pdf

$$SO_3 + H_2O + M \longrightarrow H_2SO_4 + M$$

A “cloud” is produced from condensation and coagulation when a parcel of air reaches saturation vapor pressure. Saturation vapor pressure, which depends only on temperature, defines when the vapor pressure of the gas is in equilibrium with liquid phase. Below Venus’ high altitude photochemical H_2SO_4 haze, it also has H_2SO_4 clouds, which form from condensation and coagulation of H_2SO_4 in the gaseous phase. Below 38 km, where $T \sim 430$ K, the H_2SO_4 breaks down through thermal decomposition (Bullock & Grinspoon, 2001) into the gases that formed it through upper atmosphere photochemistry:

$$H_2SO_4 \longrightarrow SO_3 + H_2O$$

Earth, of course, has water clouds, and Titan contains clouds of condensed methane (Brown et al., 2002).

An “aerosol” is the generic term for particulates in an atmosphere and can refer to phenomena such as haze, clouds, and other small suspended debris blown from the surface (e.g. dust, sand, and even microbes). “Particles” is also used as a generic term to describe the individual constituents of aerosols.

2.2 Refractive Indices

Scattering physics has its own rich vocabulary that can lead to confusion if not clearly defined. Here, I define refractive indices and optical efficiencies so that they may be understood in the context of later chapters. The purpose here is not to rigorously derive all relevant quantities but rather provide an overview of key nomenclature, show important equations to give physical insight, and, where applicable, describe why certain particle-photon interactions arise.

2.2.1 Refractive indices

“Refractive indices”, “indices of refraction”, and “optical constants” are synonymous and describe the ways materials of particular compositions interact with light. Refractive indices, R, are complex numbers, containing both a real and an imaginary component:

$$R = n + ik \tag{2.1}$$

The real refractive index, usually denoted with n, is a dimensionless quantity that is defined as

$$n = \frac{c}{c'} \tag{2.2}$$

Here, c is the speed of light in a vacuum and c' is the phase velocity of light in a nonabsorbing medium. The real refractive index measures how much light is bent in a medium. At the boundary between two substances, the phase velocity is altered, which causes light to change direction. We can write this phase velocity, c', as

$$c' = \frac{1}{\sqrt{\epsilon\mu}} \tag{2.3}$$

Here, ϵ refers to electric permittivity and μ to the magnetic permeability of a medium. We can also write, for the speed of light in a vacuum,

$$c = \frac{1}{\sqrt{\epsilon_0\mu_0}} \tag{2.4}$$

Here, ϵ_0 and μ_0 are constants representing the electric permittivity and magnetic permeability of free space. So, for the real refractive index, we can write that

$$n = \frac{c}{c'} = \frac{\sqrt{\epsilon\mu}}{\sqrt{\epsilon_0\mu_0}} \tag{2.5}$$

Let us consider the variables in this equation in more detail. The electric permittivity (a measure of the resistance of forming an electric field in a medium) of a material can be written as

$$\epsilon = \epsilon_0(1 + \chi) + i\frac{\sigma}{\omega} \tag{2.6}$$

ϵ_0 is the previously mentioned real valued constant and $\omega = 2\pi\mu$ is the angular frequency (radians per second) of a varying electric field, but, importantly, the other terms here depend on the material in question. χ defines the electric susceptibility of a medium, and σ is the conductivity. Similarly, we can consider μ, a measure of the ability of a medium to support a magnetic field, as

$$\mu = \frac{\mathbf{B}}{\mathbf{H}} \tag{2.7}$$

$\mathbf{H}$, the auxiliary magnetic field, represents how a magnetic field $\mathbf{B}$ can organize magnetic dipoles in a given medium. **The point of explaining where n comes from is to illustrate how it is a fundamental property of what a substance is made of and is independent of the material's size or shape.** This is also true for the imaginary refractive index, k, which is discussed below.

Previously, we considered light traveling through a nonabsorbing medium, but light traveling through real material will be attenuated. We can quantify this attenuation by considering the imaginary component of the refractive index, k. In an absorbing (i.e. physical) medium we must actually consider the previous equation 2.2 as

$$R = \frac{c}{c'} \tag{2.8}$$

Again, R is the complex index of refraction ($R = n + ik$). In a nonabsorbing medium, c' represented the phase speed of light in the medium as discussed above. For an absorbing medium, this is not precisely true but remains a reasonable approximation. The imaginary index of refraction, k, quantifies how much radiation a medium absorbs when light passes through. We use the "absorption coefficient" $\beta_a(k)$ to measure this attenuation. For a propagating plane wave with initial intensity I_0 traveling through a medium over distance z, we can write:

$$I = I_0 e^{-\beta_a(k) z} \tag{2.9}$$

So, the quantity $1/\beta_a(k)$ gives the distance for the flux to be absorbed by a factor of e^{-1}. We can relate β_a to k with

$$\beta_a = \frac{\omega k}{c} = \frac{4\pi k}{\lambda} \tag{2.10}$$

where λ is the wavelength under consideration. Note that β_a has units of inverse length. We can rewrite equation (2.9) as

$$t = \frac{I}{I_0} = e^{-\beta_a(k)z} \tag{2.11}$$

This form is called Beer's law, and t is the transmittance of light through a medium (in this case, only considering attenuation by absorption). Beer's law shows us that the rate light is attenuated in a medium is governed by β_a (and, ultimately, by k). We may also define β_s to describe how much light is scattered in a medium, and we can describe the total extinction in a medium with β_e where $\beta_e = \beta_a + \beta_s$.

The optical depth τ of a slab of material of length z can be written as

$$\tau = \beta_e z \tag{2.12}$$

So we can rewrite Beer's law for the total attenuation from scattering and absorption in terms of the optical depth as

$$t = \frac{I}{I_0} = e^{-\beta_e(k)z} = e^{-\tau} \tag{2.13}$$

Note that the complex refractive index R depends not only on the composition of the material but also on temperature and pressure of the material under consideration, so it is important that measurements of n and k in the laboratory be done under conditions applicable to relevant planetary environments. Also note that n and k are not independent of one another but in fact are closely coupled together through a set of formulae called the Kramer-Kroning relations. In principle, it is possible to use these relations to calculate n from k and vice versa. Both refractive indices also depend on strongly on wavelength: for instance, a person who wears glasses and has seen herself on an infrared camera knows that while glass is transparent (has a low imaginary refractive index) at visible wavelengths, it is quite opaque (has a high imaginary refractive index) at infrared wavelengths (Figure 2.1).

At a macroscopic level, we can understand n as a measure of the degree light gets bent in a medium and k as the degree a medium absorbs light, but at a microscopic level, the situation is more complex. On the very small scale, these indices of refraction arise from

Figure 2.1: The author looking into the NASA Jet Propulsion Laboratory museum infrared camera. The left image is taken at infrared wavelengths and shows the author's glasses clearly; the right image is at visible wavelengths.

constructive and destructive interference of light being scattered off the constituent atoms and molecules of a substance. More fundamentally, as an electromagnetic field propagates through a substance, its oscillatory electric and magnetic fields will cause charges in the medium to oscillate and emit their own waves at the same frequency, but typically with a phase delay. When we speak of light propagating in a medium, we really are referring to all of the traveling electromagnetic fields, both the original field and the ones emitted by the oscillating charges. Some of the energy of the oscillating charges will be radiated in other directions, and this is the phenomenon we refer to as scattering. If the electrons emit a wave that is 180° out of phase with the original wave, this causes total destructive interference and results in the absorption we quantify with the imaginary refractive index. In reality, the phase of the wave emitted is typically between 90° and 180°, so there is some degree of both scattering and absorption.

We are all familiar with the optical phenomena that result from refractive indices in our everyday lives. Here are a few examples. The twinkling of a star is caused by subtle variability of atmospheric pressure, which in turn causes small variations in n, bending the starlight in slightly different directions. Rainbows are caused by dispersive refraction, whereby light of different colors gets bent at different angles in a medium. The color of a ruby results from a higher value of k (more absorption) at shorter, bluer wavelengths and a lower value of k (less absorption) at longer, redder wavelengths, which is ultimately caused by impurities of chromium in the molecular structure of the gem.

2.3 Optical Efficiencies, Rayleigh Theory, and Mie Theory

Accurate measurements of refractive indices are necessary for accurate determination of the optical cross sections, which are used to calculate the optical efficiencies of particles (and, ultimately, an accurate synthetic spectrum containing those particles). **While the refractive indices are independent of particle morphology, optical efficiencies depend on a particle's shape and size.**

When we consider how radiation interacts with particles, size is critical. We will define a "size parameter", relating the radius of the particle, r, to the wavelength of interacting light as

$$x \equiv \frac{2\pi r}{\lambda} \tag{2.14}$$

Mie theory is used to describe how spherical particles interact with light and refers to solutions to Maxwell's equations for photons intercepting spheres. Rayleigh theory is one of the limiting behaviors of Mie theory. The purpose of this section is not to deeply delve into or derive Rayleigh or Mie theory. However, we can discuss some of the results of Mie and Rayleigh theory here to gain understanding of how particles of a given size interact with light.

Let us consider scattering of light by a spherical particle. The scattering cross section is defined by equating the total energy scattered by a particle in every direction to the energy of an incident beam of radiation falling in area σ_g. This is the scattering cross section, σ_s, which is generally not equivalent to the particle's geometric radius, σ_g. The dimensionless scattering efficiency Q_{scat} is defined as

$$Q_{scat} = \frac{\sigma_s}{\sigma_g} \tag{2.15}$$

In other words, Q_{scat} is the ratio of the total scattered radiation to the total energy of the beam incident on particle's geometric cross section. We can similarly define an absorption efficiency, Q_{abs}, as the total absorbed radiation relative to the total energy incident on a particle's geometric cross section. The extinction efficiency, Q_{ext}, which quantifies the total amount of energy removed from an incident beam, is defined as the sum of Q_{scat} and Q_{abs}. That is, $Q_{ext} = Q_{scat} + Q_{abs}$. It is also useful to define a quantity called the "single scattering albedo", ω, which is defined by the ratio of Q_{scat}/Q_{ext} and describes how much of the extinction comes from scattering alone. A perfectly nonabsorbing particle would have $\omega = 1$.

If a particle is much smaller than the wavelength of light hitting it ($x \ll 1$), all parts of the particle will experience approximately the same oscillating electromagnetic field, and the particle will become an oscillating dipole, which produces its own electromagnetic field and radiates energy in all directions. We call this behavior Rayleigh scattering. For this type of scattering, the intensity of scattered radiation is inversely proportional to the fourth power of the wavelength, and this is why blue light of shorter wavelengths is preferentially scattered in all directions over the sky compared to longer wavelengths.

The Q efficiencies depend on the aforementioned optical constants $R = n + ik$ of a material. For the Rayleigh scattering limit, the scattering efficiency is given by

$$Q_{scat} = \frac{8}{3}x^4 Re\left\{\frac{R^2-1}{R^2+2}\right\}^2 \tag{2.16}$$

and here, Re shows that we consider the real part of this equation. Note the dependence on the size parameter x^4, which scales as $1/\lambda^4$ for Rayleigh scattering as discussed above. We can write the absorption efficiency of Rayleigh scattering as

$$Q_{abs} = -4xIm\left\{\frac{R^2-1}{R^2+2}\right\} \tag{2.17}$$

Here, the Im indicates that we take the imaginary part of this equation.

For particles that are much larger than the wavelength of light intercepting them (i.e. $x \ll 1$), the scattering efficiency approaches 2. That is, $Q_{scat} \to 2$ for large particles or very short wavelengths of light. This limit is considered the geometric scattering limit.

For particles of intermediate size ($x \sim 1$) compared to the wavelength of light, Rayleigh theory is inapplicable because the field surrounding the particle is no longer uniform, so full Mie theory must come to bear on the problem. The full solution to the Mie problem is expressed in polar coordinates (r, ϕ, θ) as an infinite series of orthogonal basis functions depending on ϕ, spherical Bessel functions depending on θ, and Legendre polynomials depending on r. In Mie theory, Q_{ext} and Q_{scat} can be written as:

$$Q_{ext} = \frac{2}{x^2} \sum_{m=1}^{\infty} (2m+1) Re(a_m + b_m) \tag{2.18}$$

$$Q_{scat} = \frac{2}{x^2} \sum_{m=1}^{\infty} (2m+1)(|a_m|^2 + |b_m|^2) \tag{2.19}$$

where a_m and b_m are Mie scattering coefficients and are themselves functions of x and R. In practice, the number of terms needed from these infinite series depends on the particle size: larger particles require more terms, which is why the run time and output files for codes that calculate these properties become larger as particle size increases.

Figure 2.2 shows the extinction efficiency Q_{ext} as a function of x for nonabsorbing particles (that is, $Q_{ext} = Q_{scat}$). The n value used here corresponds to water at visible wavelengths. The top panel has a linear x- and y-axis, and the bottom panel has a logarithmic x- and y-axis so that the Rayleigh scattering regime can be clearly seen. We can see from the peak in Q_{ext} in this figure that photons will tend to have the strongest interaction with particles of about the same size as their wavelength (vertical dashed line). Thus, larger particles will preferentially interact with redder light and smaller particles will preferentially interact with bluer light. At small values of x ($\lambda \gg r$), Rayleigh scattering dominates and Q_{ext} follows the expected x^4 dependence. At large values of x ($\lambda \ll r$) we can see the geometric scattering limiting behavior as $Q_{ext} \to 2$.

For particles that absorb (nonzero k), the optical efficiencies are simpler than those shown in Figure 2.2: the series of smaller maxima and minima resulting from constructive

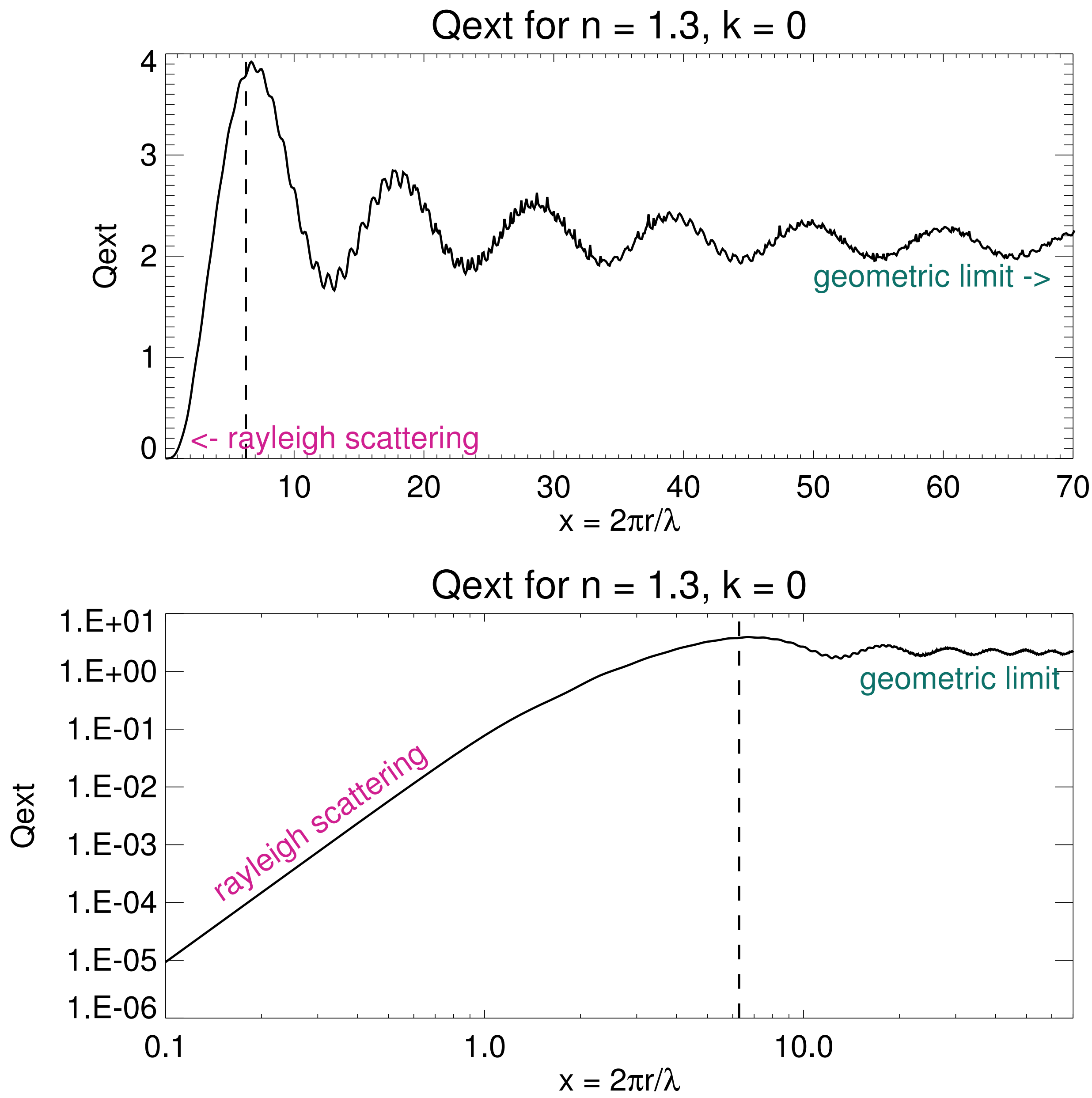

Figure 2.2: The extinction efficiency for particles as a function of x. These particles do not absorb ($k = 0$) and have $n = 1.3$, which represents water at visible wavelengths. The geometric scattering limit and Rayleigh scattering regime are indicated. The vertical dashed line indicates where $\lambda = r$.

and destructive interference of transmitted and scattered light are diminished. This can be seen in Figure 2.3, which adds a nonzero k value to the refractive index generating the curve previously shown in Figure 2.2.

Figures 2.2 and 2.3 do not represent the true wavelength-dependent behavior of particles. In actuality, n and k are wavelength-dependent. Therefore, we show the Q_{ext} curves for spherical organic haze particles of several sizes as a function of wavelength in Figure 2.4 alongside the indices of refraction used to generate them.

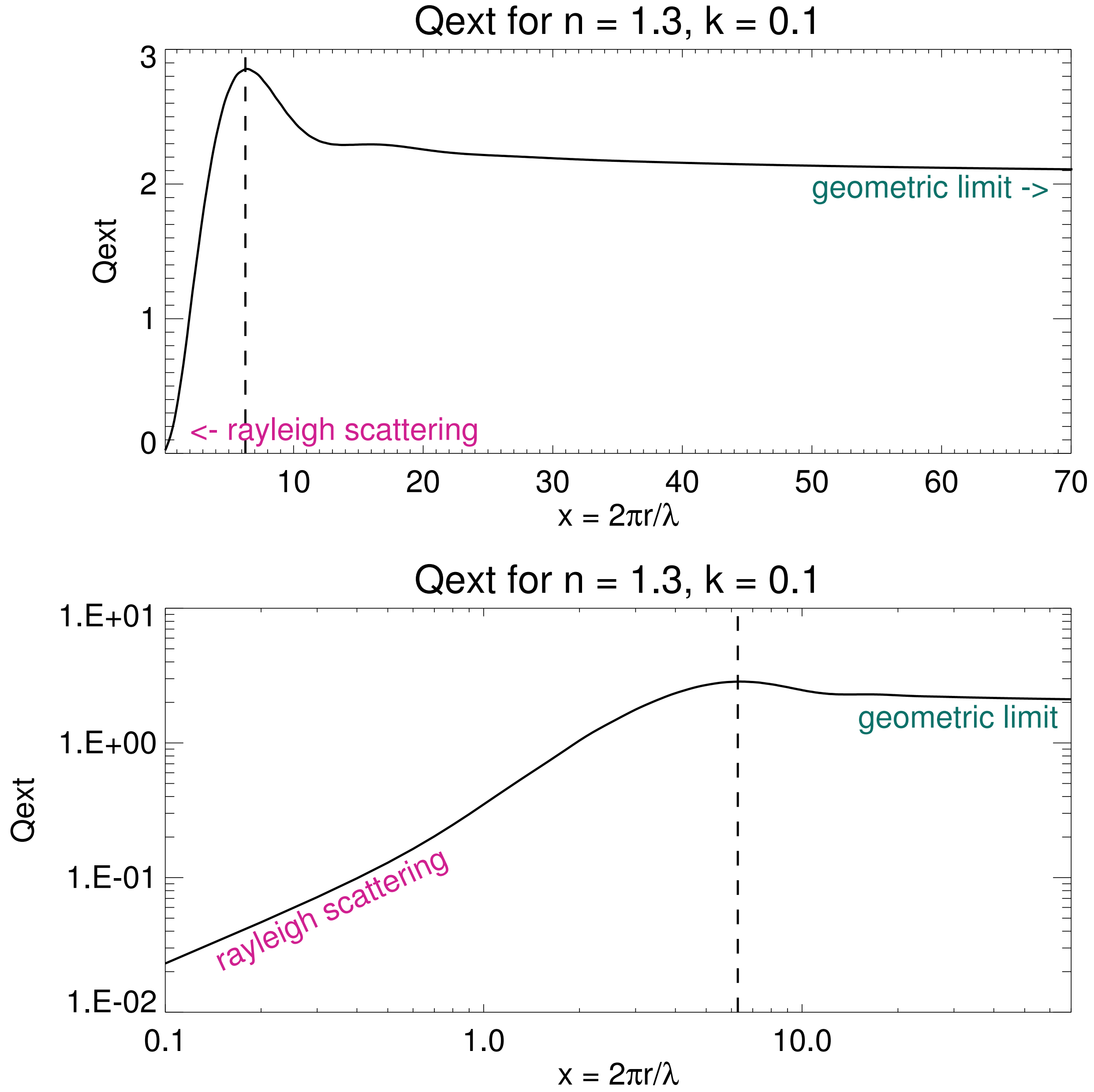

Figure 2.3: The extinction efficiency for particles as a function of x. These particles absorb ($k = 0.1$) and still have $n = 1.3$. The geometric scattering limit and Rayleigh scattering regime are indicated as in Figure 2.2. The vertical dashed line indicates where $\lambda = r$.

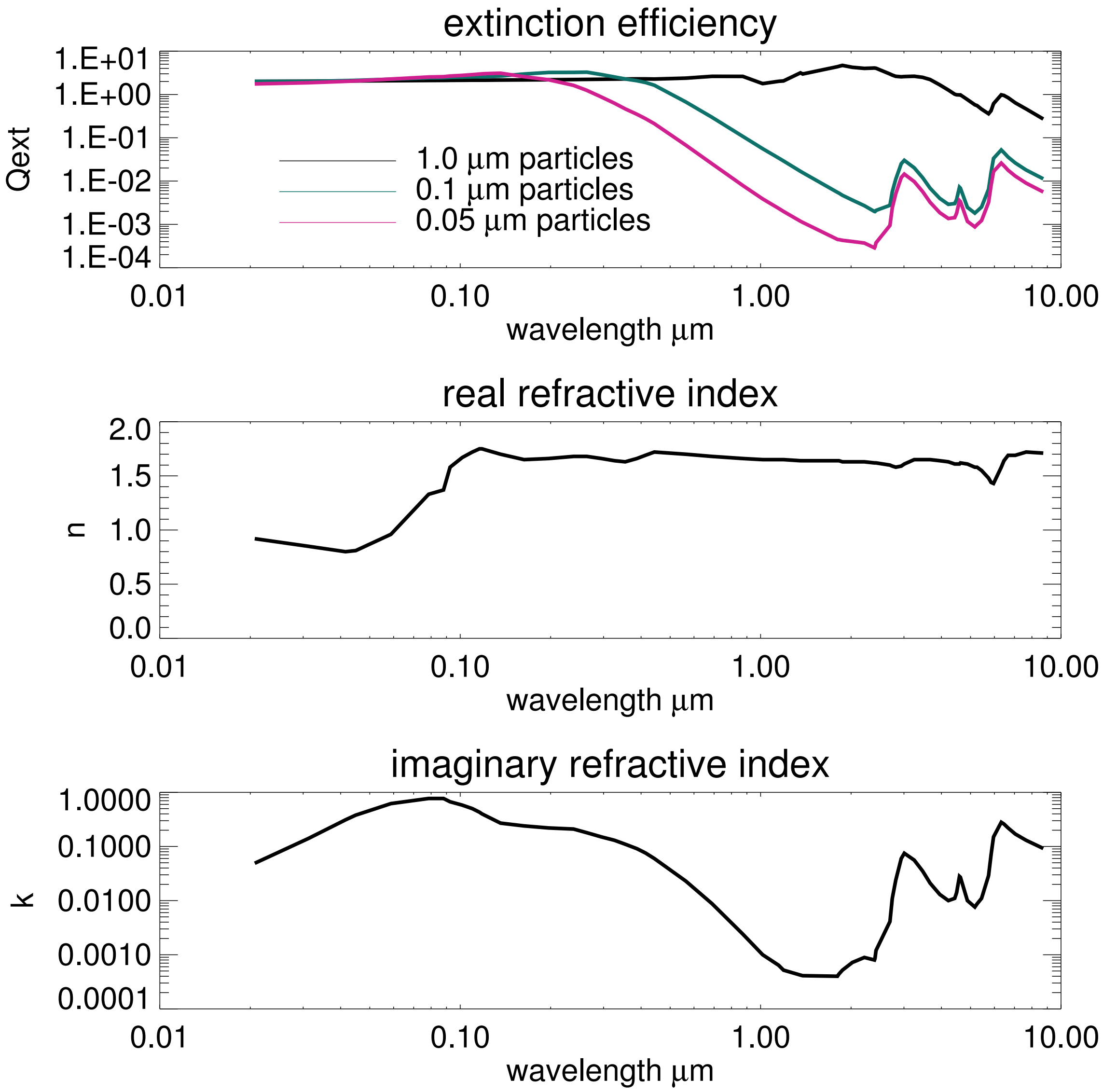

Figure 2.4: The extinction efficiency for organic haze particles of three sizes as a function of wavelength. These particles assume refractive indices for organic haze from Khare et al. (1984a), shown in the middle and bottom panels. Peaks and troughs in the refractive indices in the middle and bottom panels are echoed in the Q_{ext} curves in the top panel. The geometric scattering limit is apparent as the curves approach $Q_{ext} \sim 2$ at small wavelengths where the particle size becomes much larger than the wavelength.

2.4 Particle Distributions and Phase Functions

In a real atmosphere, particles follow a size distribution rather than being monomodal (i.e. all the same size). A log-normal size distribution is frequently used for particles and can be written as

$$N(r) = \frac{N_0}{\sqrt{2\pi}} \frac{1}{r} \frac{1}{ln(s)} e^{-\left[\frac{(ln(r)-ln(r_m))^2}{2ln^2(s)}\right]} \tag{2.20}$$

where N represents the number density of particles at each radius r, N_0 is the total particle number density, r_m is the mean radius, and s is related to the standard deviation σ of $ln(r)$ by $\sigma = ln(s)$. A typical aerosol population has $s = 1.5$ (Tolfo, 1977).

For a distribution of particles, we can rewrite our formula for optical depth as:

$$\tau = z \int_{r_{min}}^{r_{max}} \pi r^2 Q_{ext}(\lambda, r) N(r) dr = z\beta_{ext} \tag{2.21}$$

As we have discussed, the size of a particle relative to the wavelength of a photon determines how strongly it interacts with that photon, but it also affects the direction light is scattered. We quantify this directional behavior with the “phase function,” which describes how particles redistribute scattered radiation over a series of angles Φ where Φ is the angle between the original direction of a photon and its scattered direction. The integral of the phase function over 4π steradians equals 1. We can think of the phase function as a probability density that tells the likelihood of a photon to be scattered in the direction of a solid angle of area $d\Omega$:

$$1 = \frac{1}{4\pi} \int_{4\pi} P d\Omega \tag{2.22}$$

We can also define a parameter called the “asymmetry parameter”, denoted with g. This parameter represents the first moment of the scattering phase function (i.e. the integral of the product of the phase function and the cosine of the scattering angle integrated over a sphere).

$$g = \frac{1}{4\pi} \int_{4\pi} P(cos\Theta) cos\Theta d\Omega \tag{2.23}$$

The asymmetry parameter equals 1 if a particle distribution is perfectly forward scattering, 0 for perfect isotropic scattering, and -1 for perfect backscattering. Large particles ($x \gg 1$) will tend to have $g \sim 1$, and Rayleigh scattering with small particles ($x \ll 1$) has $g \sim 0$.

Typically, full scattering phase functions are complicated. An approximation often used is the Henyey-Greenstein phase function (Henyey & Greenstein, 1941), which depends on g and can be written as

$$P_{HG}(cos\Theta) = \frac{1 - g^2}{1 + g^2 - 2gcos\Theta^{3/2}} \tag{2.24}$$

The Henyey-Greenstein phase function produces isotropic scattering for values of $g = 0$ and increasingly scatters photons in the forward direction as $g \to 1$. This is useful because it approximates the overall behavior of a true phase function. However, the Henyey-Greenstein phase function is smooth and does not show higher order details such as rainbows and the sharp forward diffraction peak captured by the full Mie phase function (As a side note, rainbows are caused by a single internal reflection of light within a raindrop, and the secondary rainbow results from two internal reflections, and this behavior can be seen in a full phase function). Nevertheless, the Henyey-Greenstein phase function is useful for applications when a full phase function is impractical or difficult to compute or when the scattered radiation field is described by a simple analytic model such as a 2-stream approximation.

2.5 Fractal Particles

Particles are often approximated as spheres so that Mie scattering (for which there are numerous existing codes) can be employed, but true aerosols are often nonspherical. In particular, organic hazes such as those on Titan are best approximated as fractal particles (Rannou et al., 1997; Brasil et al., 1999).

Fractal aggregates can be modeled as a collection of n_{mon} spherical "monomers" of radius r_{mon} that produce an effective geometric aggregate radius r_f. Figure 2.5 shows a graphic illustration of a fractal particle compared to spherical monomers. A useful analogy

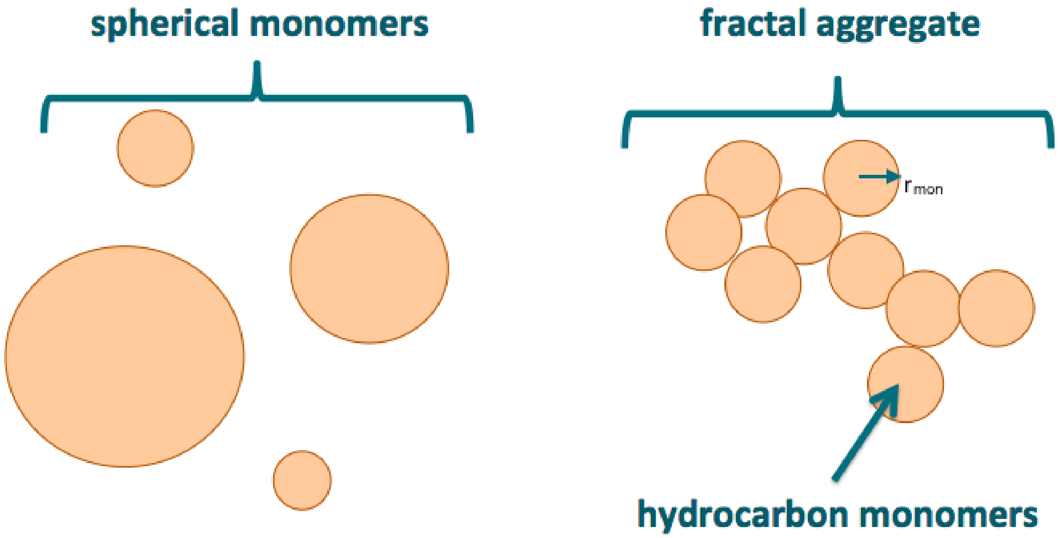

Figure 2.5: A graphical representation of spherical versus fractal particle morphology (in this case, for hydrocarbon particles)

for considering fractal particles is a bunch of grapes: the individual grapes represent the monomers, while the whole bunch represents the total aggregate. For fractal particles, these quantities are related by the equation

$$n_{mon} = \alpha \left(\frac{r_f}{r_{mon}} \right)^{D_f} \tag{2.25}$$

Here, α represents a dimensionless constant of order unity and D_f is the "fractal dimension." $D_f = 3$ represents a spherical (non-fractal) particle, and $D_f = 1$ represents a string of linearly chained monomers. Typical fractals are usually modeled with $D_f = 2 - 2.4$ (Wolf & Toon, 2010).

A useful approximation for scattering by fractal particles is the "mean-field approximation" (Botet et al., 1997). This approximation makes the assumption that the scattering coefficients a_m and b_m (see equations 2.18 and 2.19) for each monomer in an aggregate do not vary between monomers but instead can be approximated by the same value given by the mean electromagnetic field within the aggregate.

The mean-field approximation considers the total energy scattered by a fractal aggregate as the sum of the Mie fields scattered by each monomer in the fractal. Thus, fractal particles behave more like smaller particles (the monomers) than an equivalent mass spherical particle: this explains why fractal particles produce more extinction of short wavelengths than equivalent-mass spherical particles. As discussed previously in the context of Mie scattering, small particles ($r < \lambda$) will tend to most strongly interact with shorter wavelengths. So, fractal particles made up of many small monomers each acting as a Mie scatterer will produce more extinction in the UV than in the visible even if the total aggregate size is comparable to visible-wavelength light. In fact, larger fractal aggregates composed of larger numbers of smaller scattering monomers will produce even more extinction in the UV compared to smaller fractal aggregates composed of fewer monomers. In general, compared to spherical particles of equal mass, fractal particles produce more extinction in the UV but less in the visible and NIR, so their UV shielding abilities are enhanced while their anti-greenhouse properties are diminished. This property is not strongly dependent on the choice of refractive indices of the particle material (Wolf & Toon, 2010) and thus can be considered a general property of fractal aerosols.

In actuality, the optical efficiencies of fractal aggregates are more complex than a simple summation of many Mie fields scattered by the small monomers because the bulk aggregate also interacts with radiation. We have discussed how radiation preferentially interacts with particles of size comparable to its wavelength: so, shorter wavelength radiation will preferentially interact with the monomers, but longer wavelengths will preferentially interact with the bulk aggregate.

Figure 2.6 shows the extinction, scattering, and absorption efficiencies for a 0.5 μm spherical particle (rose solid line), a 0.5 μm fractal particle composed of 0.05 μm monomers (violet solid line), and a 0.05 μm monomer scaled up by a factor of 10 in each panel to fit onto the same y-axis. (turquoise dashed line). As expected, the fractal particle produces more extinction at short wavelengths than the comparable spherical particle. However, its extinction and scattering efficiencies do not decrease as quickly with increasing wavelength as the behavior of the 0.05 μm monomer. The flatter Q_{scat} slope (a consequence of the flatter Q_{ext} slope) for the fractal particle is due to longer wavelengths scattering off the bulk aggregate. However, note the similarity of the absorption efficiency of the fractal and the 0.05 μm monomer. Although we see that scattering can be caused by interactions with the monomers or the bulk fractal aggregate, the absorption efficiencies of the fractal aggregate and the monomers are the same except for a shift in amplitude. All of the absorption in a fractal aggregate is due to interactions with the monomers. The asymmetry parameter is also interesting, as it shows that fractal particles produce more forward scattering at longer wavelengths than equivalent mass spheres. The combination of less extinction at longer wavelengths and increased forward scattering means that a haze of fractal particles produces less cooling than a haze of spherical particles because less visible radiation is attenuated on its path to a planet's surface (e.g. Wolf & Toon, 2010).

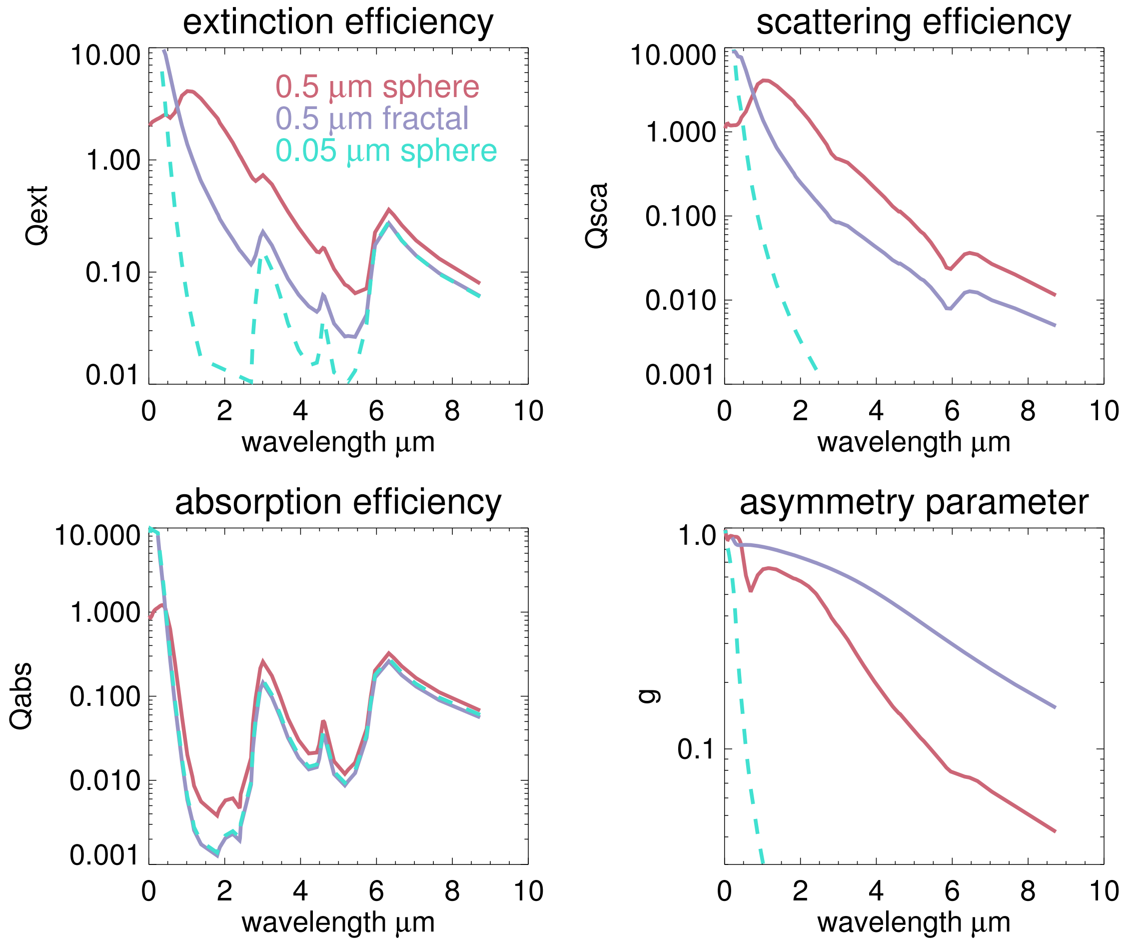

Figure 2.6: The optical efficiencies and asymmetry parameter of 0.5 μm particles (spherical and fractal), and 0.05 μm spherical monomers (this is the size of the monomers comprising the fractal particle). The monomer Q values and g values are multiplied by a factor of 10 in each panel.

2.6 Spectral windows in aerosol-rich atmospheres: a consequence of particle properties

The atmospheres of Venus and Titan are generally regarded as opaque and impenetrable due to their thick decks of H_2SO_4 cloud and haze (in the case of Venus) and organic haze (in the case of Titan). These richly complex aerosol layers hindered our ability to understand the nature of these worlds for many years as discussed in Chapter 1.

Although Venus and Titan have globally-distributed aerosol decks, it is possible to see to the surfaces of both of these worlds from Earth using “spectral windows”. These windows are regions in wavelength-space where the atmosphere is transparent. An example of a spectral window in Earth’s atmosphere is the visible wavelength range between violet and red light, which allows these wavelengths to arrive relatively unimpeded to the ground. This spectral window conveniently overlaps with the peak emission of the solar spectrum, and biology has evolved to utilize this light: for example, these are the wavelengths our eyes are sensitive to, and the close correspondence of the reaction centers of chlorophyll in green plants with the peak of the photon distribution at the ground has been remarked on in the literature (Kiang et al., 2007b,a, and see Chapter 7)

On Venus, atmospheric windows between 1 and 2.5 μm allow thermal radiation from below the cloud deck to escape to space. These windows must be observed on the planet’s night side because on the day side, the thermal radiation emanating in them is overwhelmed by sunlight reflected by the Venusian cloud deck. The windows exist between CO_2 and H_2O absorption bands and where the cloud deck is non-absorbing. Figure 2.7 shows Q_{abs} and Q_{scat} of four lognormal size distributions of Venus cloud particles. Although Q_{scat} is large-valued for $\lambda < 2.7\mu m$, Q_{abs} is small-valued here because the imaginary index of refraction, k, for H_2SO_4 is also small-valued at these wavelengths (bottom panel of Figure 2.7). This allows photons to escape through the cloud deck without being absorbed (although they are scattered multiple times on the way out resulting in an approximately 100 km^2 horizontal scattering footprint).

In Titan’s atmosphere, atmospheric windows in the near-infrared can be sensed on the day side: incident sunlight can penetrate through its atmosphere and be reflected by the surface back to space at wavelengths where CH_4 is not absorbing. Figures 2.4 and 2.6 show the optical efficiencies of organic haze particles decreasing with increasing wavelength, particularly for fractal particles, allowing organic haze to become more transparent at these longer wavelengths.

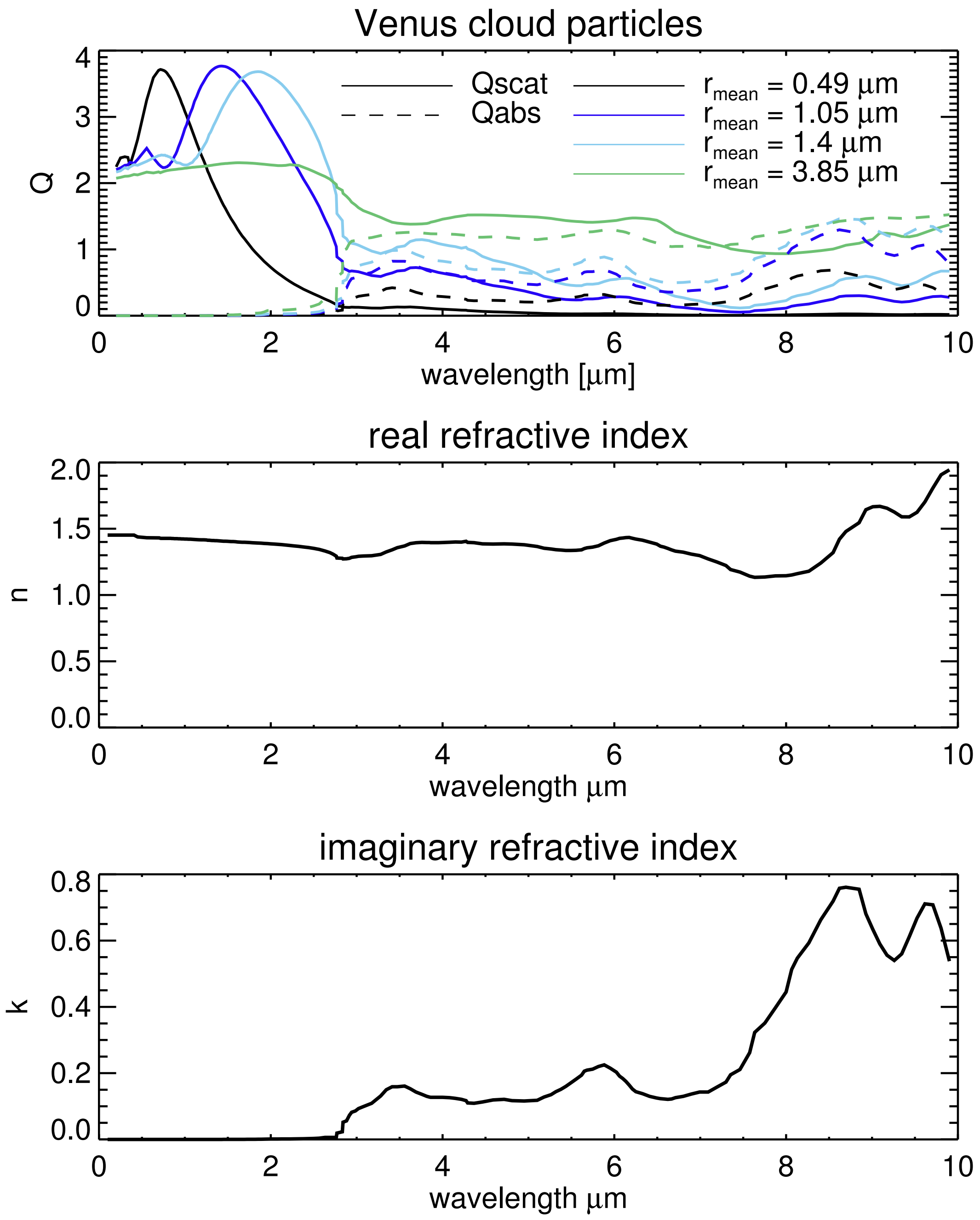

Figure 2.7: Q_{abs} and Q_{scat} for four different Venus particle sizes corresponding to the four major particle populations in the planet's atmosphere. Note that, as expected, the peaks of the Q_{scat} curves shift to longer wavelengths as particle size increases because particles "prefer" to interact with wavelengths of about the same size. Venus' cloud particles are largely non-absorbing at wavelengths shorter than about 2.7 μm. We can see this absorption behavior in the imaginary refractive index for H_2SO_4 in the bottom panel. Also shown is the real refractive index (middle panel), which is relatively flat across this wavelength range. Refractive indices are from Palmer & Williams (1975).

2.7 Relevance to later chapters

The particle properties discussed in this chapter are relevant to the results presented in Chapters 4-6. In Chapter 4, I will show measurements through the Venus near-infrared spectral windows that are made possible by the behavior of the H_2SO_4 refractive and scattering indices shown here. Chapters 5-7 discuss the climate, UV shielding, and spectral appearance of Archean Earth and Archean-analog words rich in organic haze. The climate and UV shielding abilities of an organic haze are closely tied to the particle shape: because fractal particles produce less cooling and more UV-absorption, the climate and UV-shielding of these hazes are strongly influenced by their nonspherical nature. And, the spectra of planets with organic haze show absorption features that are due to the behavior of the imaginary index of refraction for organic haze particles.

Chapter 3

MODELS

In this chapter, I describe the models used to retrieve the properties of the Venus lower atmosphere and to simulate the environment and spectrum of Archean Earth, with an emphasis on parts of these models relevant to hazes and clouds.

Briefly, for our Venus study, we generated synthetic Venus spectra using the Spectral Mapping Atmospheric Radiative Transfer code (`SMART`), a 1-D line-by-line fully multiple scattering radiative transfer model originally developed by David Crisp (Meadows & Crisp, 1996; Crisp, 1997). The `SMART` model is capable of producing highly accurate synthetic representations of planetary spectra and has been validated against solar system planets (Meadows & Crisp, 1996; Robinson et al., 2011; Arney et al., 2014).

To simulate the hazy Archean environment with boundary conditions consistent with recent geochemical constraints, we used a coupled 1D photochemical-climate model we call `Atmos`. Unlike previous studies of the Archean climate under a haze, we use realistic fractal (rather than spherical) particles, which have different spectral properties and climatic effects (see Chapter 2). Our study also represents the first time where temperature feedbacks have been investigated in relation to haze production in Archean Earth's atmosphere. Previous studies (Pavlov et al., 2001a; Haqq-Misra et al., 2008; Domagal-Goldman et al., 2008) involving climate modeling have included the haze's impact on temperature, but not corresponding temperature feedbacks on haze formation. We find that haze formation is dependent on the atmospheric temperature (Section 5.3.1.b), so this climate coupling is critical for accurate results.

Here, I first describe the coupled photochemical-climate model used to simulate organic hazes on Archean-like planets. Second, I describe the radiative transfer model `SMART` used to simulate spectra of Venus and Archean Earth, and I describe codes associated with `SMART`. Third, I describe the fractal mean field scattering code I use to generate inputs to `SMART` and the photochemical-climate model for fractal particles. Finally, I discuss the James Webb Space Telescope (JWST) and coronagraphic noise simulator used to simulate observations of exoplanets with realistic noise sources for their respective telescope systems.

3.1 Atmos: A Coupled Photochemical-Climate Model

Our coupled photochemical-climate model, `Atmos` , is used to simulate Archean Earth's photochemistry and climate. To use `Atmos`, the photochemical model (which includes particle microphysics) is run first to generate an initial atmospheric state based on user-specified boundary conditions (gas mixing ratios; fluxes or deposition efficiencies; the solar constant; the stellar spectral type; total atmospheric pressure; and the initial temperature-pressure profile). The initial temperature profile specified in `Atmos` for Archean Earth has a surface temperature of 275 K and an isothermal atmosphere of 178 K above 12 km for a 1 bar atmosphere. After the photochemical model has run, its outputs for altitude, pressure, gas mixing ratios, haze particle sizes and haze number densities are passed into the climate model. The climate model uses the photochemical model's solution (and the same stellar spectrum) as its initial conditions and runs until it reaches a converged state. It then feeds updated temperature and water vapor profiles back into the photochemical model. The models iterate back and forth in this manner until the atmosphere stops changing. An example of `Atmos` finding convergence can be seen in Figure 3.1.

3.1.1 Photochemical Model

The photochemical portion of the code is based on the 1-D photochemical code developed originally by Kasting et al. (1979), but version that we use here was significantly modernized and updated in Zahnle et al. (2006) and uses the haze formation scheme described in Pavlov et al. (2001a). It was modified by E. Wolf to include fractal hydrocarbon hazes following the methods presented in Wolf & Toon (2010), and was first used to study fractal hazes on Archean Earth in Zerkle et al. (2012). Note that the version of the model used here can simulate atmospheres ranging from extremely anoxic ($pO_2 = 10^{-14}$) to modern-day O_2 levels (Zahnle et al., 2006), and even super-oxygenated conditions with greater O_2 concentrations than modern Earth (Schwieterman et al., 2016). Subsequent studies using

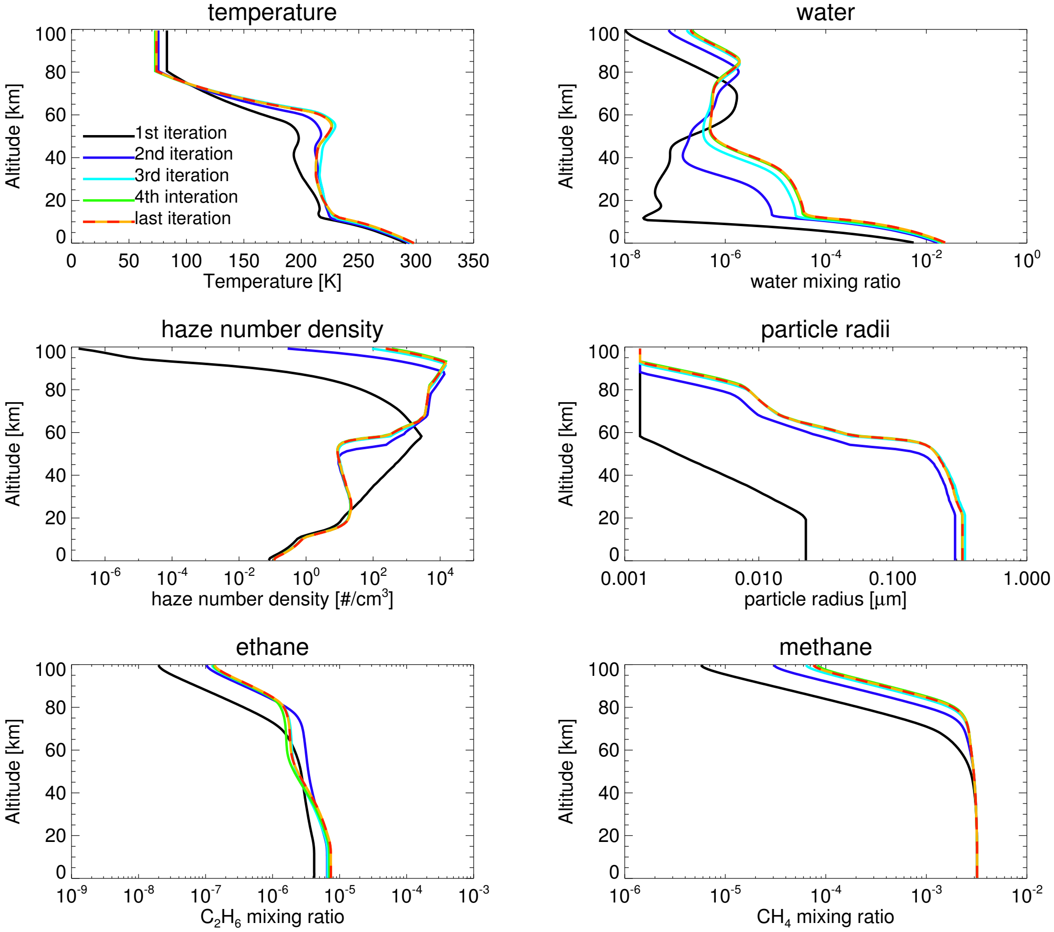

Figure 3.1: The colored lines represent each coupling iteration of the `Atmos` model for the temperature, gaze, and several gases. The dashed red and yellow line shows the last iteration.

this model or other versions of it to study fractal haze formation include Harman et al. (2013); Kurzweil et al. (2013); Claire et al. (2014). There are numerous other studies involving various versions of this photochemical model to study atmospheres without hazes (Kasting & Donahue, 1980; Selsis, 2000; Pavlov & Kasting, 2002; Ono et al., 2003; Segura et al., 2003, 2005; Zahnle et al., 2006; Grenfell et al., 2007; Segura et al., 2007; Catling et al., 2010; Segura et al., 2010; Domagal-Goldman et al., 2011; Rugheimer et al., 2013; Domagal-Goldman et al., 2014; Rugheimer et al., 2015; Harman et al., 2015; Schwieterman et al., 2016).

Our model atmosphere is divided into 200 plane-parallel layers from the surface to 100 km, with a layer spacing of 0.5 km. Appendix Table 1 shows our list of chemical reactions used when simulating Archean Earth. Our Archean scheme includes 76 chemical species, 11 of which are short-lived (Appendix Table 2). Short-lived species are computed in photochemical equilibrium (i.e. no transport considered) and are not part of the Jacobian solved self-consistently at each timestep. The mixing ratio of each species is found by solving flux and mass continuity equations in each layer simultaneously using a reverse-Euler method, providing exact solutions at steady-state. Vertical transport by molecular and eddy diffusion are included, and boundary conditions that drive the model can be set for each species at the surface and the top of the atmosphere. A δ 2-stream method is used for radiative transfer (Toon et al., 1989). Fixed isoprofiles are assumed for CO_2 and N_2.

As in Zerkle et al. (2012), we set a fixed mixing ratio of CH_4 at the surface; the model then calculates the surface flux necessary to maintain this mixing ratio. Since haze formation scales with the CH_4/CO_2 ratio, we find this is the most straightforward way to explore haze thicknesses in our atmospheres. Note that when we discuss CH_4/CO_2 values in later chapters, these refer to the ratio at the planetary surface because CH_4 does not follow an isoprofile – it decreases with increasing altitude – although CO_2 is considered well-mixed.

Aerosol formation follows the method used in Kasting et al. (1989) as described and updated in Pavlov et al. (2001a). Immediate precursors to haze particles are formed through the reactions $C_2H + C_2H_2 \longrightarrow C_4H_2 + H$ and $C_2H + CH_2CCH_2 \longrightarrow C_5H_4 + H$. Since the full chemical scheme that leads to aerosol formation is not well understood from laboratory or theoretical studies (Hicks et al., 2015; Hallquist et al., 2009), it is assumed that C_4H_2 and C_5H_4 condense directly to haze particles (called HCAER and HCAER2, respectively, in Appendix Table 1). In a real atmosphere, larger molecules would form before aerosol condensation occurs, and back-reactions should occur, so this model may overestimate the rate of aerosol formation. In Pavlov et al. (2001a), the authors suggest that if the real aerosol formation rate is slower, the atmosphere would compensate by increasing the CH_4/CO_2 ratio, which increases the polymerization rate. Further discussion of haze formation pathways and caveats of the approach we use here can be found in Chapter 5. The model's particles form initially with a radius of 0.001 μm. Each layer of the atmosphere has a monomodal size distribution with the particle size calculated by comparing the coagulation lifetime to the particle removal lifetime via diffusion into another layer or by sedimentation at the surface. The aerosols can grow when the coagulation lifetime is longer than the lifetime for removal in a layer.

The maximum radius of a spherical haze particle (i.e. a haze "monomer") is set to 0.05 μm, the same nominal value used by Wolf & Toon (2010) and similar to the size of the monomers of Titan's fractal haze aggregates (Rannou et al., 1997; Tomasko et al., 2008). Particles smaller than this size are treated with Mie scattering. Particles larger than this size are treated as fractal agglomerates of n_{mon} spherical monomers of radius R_{mon} that clump into a larger aggregate with an effective geometric radius R_f given by the relation presented in Chapter 2 for fractal particles:

$$n_{mon} = \alpha\Big(\frac{r_f}{r_{mon}}\Big)^{D_f} \tag{3.1}$$

Recall from Chapter 2 that α represents a dimensionless constant of order unity, and D_f is the "fractal dimension," which can take on values between 1 and 3. $D_f = 3$ represents a spherical (non-fractal or classical Mie) particle, while $D_f = 1$ represents a string of chained monomers. Titan's fractal aggregates are thought to have a fractal dimension of about 2 on average for the aerosol population (Rannou et al., 1997; Larson et al., 2015). Note that the "effective geometric radius" we refer to above is only to characterize the size of the fractal particle and does not indicate we use Mie scattering for our fractal particles; with the exception of our smaller spherical particles ($R < 0.05\mu m$), the fractal scattering physics we use in all parts of our study is the fractal mean field approximation (Botet et al., 1997). The model's fractal production methods are discussed in Zerkle et al. (2012) (including its supplementary online information) where they were first implemented. Additional information about fractal particles and their geometry can be found in, e.g., Köylü et al. (1995) and Brasil et al. (1999). The mean field approximation used for fractal scattering has been validated against scattering by silica fractal aggregates (Botet et al., 1997) and Titan's hazes (Rannou et al., 1997).

As in Wolf & Toon (2010), the fractal dimension of our particles varies from 1.5 to 2.4 for aggregate particles, and larger aggregates have a larger fractal dimension to account for folding as the particles coagulate. Recall from Chapter 2 that, compared to spherical particles, fractal particles produce more extinction in the ultraviolet (UV) but less in the visible and near infrared (NIR). This diminishes their cooling abilities and enhances their UV shielding capabilities. In addition, fractals tend to be more forward scattering in the visible and NIR and more isotropically scattering in the UV compared to equal mass spherical particles. We use optical constants measured by Khare et al. (1984a) for our organic haze particles. A discussion of our choice of optical constants can be found in Chapter 5.

In the version of the photochemical model used here, we corrected an error relating to the calculation of the number of C_5H_4 molecules composing HCAER2 haze particles. Previously, the model calculated the number of molecules per HCAER2 particle inappropriately using the mass of C_4H_2 instead of C_5H_4. We added additional particle sizes to the model's scattering grid, increasing the number from 34 particle sizes to 51, and we added options to use different monomer sizes and optical constants than the ones used in our nominal study. Gas mixing ratios at the surface can be more finely tuned than in previous versions of the model with the addition of a significant figure to the species input file.

The photochemical model is considered converged when redox is conserved and a re-run of the model using the last run's output as initial conditions occurs quickly (i.e. < 50 timesteps).

3.1.2 Climate Model

Our climate model was originally developed by Kasting & Ackerman (1986). The model has evolved considerably since its first incarnation and versions of it have been applied in subsequent studies on varied topics such as the habitable zones for several stellar spectral types (Kopparapu et al., 2013), the climate of early Mars (Ramirez et al., 2013), the atmospheres of Earth-like planets around various stellar types (Segura et al., 2003, 2005, 2010; Rugheimer et al., 2015), clouds in exoplanet atmospheres (Kitzmann et al., 2010, 2011a), and the climate of early Earth (Haqq-Misra et al., 2008). The version we used is based directly on that used by Kopparapu et al. (2013). It uses a correlated-k method to compute absorption by spectrally active gases (O_3, CO_2, H_2O, O_2, CH_4, and C_2H_6). This model has CO_2 and H_2O correlated k coefficients updated as described in Kopparapu et al. (2013). Our older CH_4 coefficients may overestimate the surface temperature by ≤ 5 K at the CH_4 mixing ratios used here (Byrne & Goldblatt, 2015). However, as we discuss in Chapter 5, our model under-predicts the Archean temperature by about 2-5 K compared to 3D climate models with more complete physics describing the planetary system, so these two effects may cancel each other out. The aforementioned gas profiles are passed to the climate model from the photochemical model when running in coupled mode. The net absorbed solar radiation in each layer of the atmosphere is computed using a δ2-stream multiple scattering algorithm (Toon et al., 1989) spanning from $\lambda = 0.2$ to 4.5 μm in 38 spectral intervals. For net outgoing IR radiation, we use a separate set of correlated-k coefficients for each gas in 55 spectral intervals spanning wavenumbers of 0 - 15,000 cm^{-1}.

We have made several modifications to the climate model used here. The model previously incorporated the spectral effects of spherical hydrocarbon particles, and it has been updated in our study to include fractal hydrocarbon scattering efficiencies using the mean field approximation of Botet et al. (1997). We have also updated the model so that haze profiles can be passed to it from an input file or by the photochemical code; in previous versions of the climate model, haze distributions were hardcoded and had to be edited manually. Other coupling subroutines have been improved to be able to accept input about atmospheric pressure, stellar parameters, and haze parameters from the photochemical model. We corrected a discrepancy in the spacing between atmospheric layers in the routine that outputs coupling files for the photochemical model: our photochemical model layer spacing is 0.5 km, but a layer spacing of 1 km had been hardcoded. We also added options to turn ethane opacity and 1D ice-albedo feedbacks (described in Chapter 5) on or off from an input file.

We have been unable to run the climate model to convergence using the same top-of-atmosphere pressure used for the photochemical model: the photochemical model extends to 100 km, but we have only been able to successfully run the climate model up to about 80 km for our 1 bar atmospheres. Thus, when temperature and water profiles are passed from the climate model to the photochemical model, they are fixed at their values at the top of the climate grid. At these altitudes, the atmosphere is thin, and the particles are very small; both of these effects lead to this portion of the atmosphere having little impact on radiative transfer and climate. We performed a sensitivity test to determine how the temperature at these altitudes affects the resultant haze distribution in the photochemical model, to determine the sizes of the largest haze particles produced. We find that a 80 K isotherm above 80 km yield results that differ from a 50 K isotherm by less than 5%. In the climate model, shifting the particles in Figure 3.1 above 80 km down to lower altitudes alters the surface temperature by < 0.5 K.

The climate model is considered converged when the change in surface temperature between timesteps and change in flux out the top of the atmosphere are sufficiently small (both typically on the order of 1×10^{-5} times these values).

3.2 The SMART Model

To generate synthetic spectra, we use the `SMART` code, a 1-D line-by-line fully multiple scattering radiative transfer model (Meadows & Crisp, 1996; Crisp, 1997). To generate transit transmission spectra, we use the $\texttt{SMART}-\texttt{T}$ model (Misra et al., 2014b). This version of `SMART` uses the same inputs as the standard code but simulates the longer path lengths and refraction effects involved in transit transmission.

The Line-by-Line Absorption Coefficients (`LBLABC`) code, a companion to `SMART`, creates line-by-line absorption files for input gas mixing ratios and temperature-pressure profiles. To generate absorption coefficient files, we use the HITRAN 2012 database (Rothman et al., 2013) for Archean Earth. For Venus, HITRAN linelists are completely inadequate for modeling H_2O and CO_2 bands, so other linelists were used for these gases. For H_2O, line parameters were obtained from the high temperature HITEMP 2010 database (Rothman et al., 2010). The BT2 database (Barber et al., 2006) was identified by Bailey (2009) as the best linelist at the time for modeling water in the Venus atmosphere, but the subsequent HITEMP 2010 database was constructed based on BT2 and with updated line positions (Rothman et al., 2010). HITEMP 2010 has been used to successfully model Venus' spectrum (Barstow et al., 2012; Arney et al., 2014) and has been used to model runaway and moist greenhouse climates (Goldblatt et al., 2013; Kopparapu et al., 2013). For CO_2, we use the linelist constructed largely by R. Wattson described in Pollack et al. (1993). The HITEMP 2010 linelist was initially used for CO_2, but it significantly under-predicts the absorption between the 1.1 μm and 1.18 μm Venus spectral windows. This spectral region is critical to model accurately because the short wavelength side of the 1.18 μm window is used to measure water in the lowest atmospheric scale height. The older CO_2 HITEMP used in Pollack et al. (1993) (frequently called the "High-T" linelist in the literature) was therefore used in preference. See Bézard et al. (2011) for additional discussion of CO_2 linelists used for modeling the Venus spectrum.

`SMART` can incorporate aerosols: as input, it requires "cloud files" with altitude-dependent opacities, plus the wavelength-dependent optical property file for each distinct particle mode, describing the particle asymmetry parameter and the extinction, scattering, and absorption efficiencies (Q_{ext}, Q_{scat}, and Q_{abs}), and the angle-dependent phase function. For Venus' cloud particles, which are composed of a concentrated solution of H_2SO_4 and H_2O, we use refractive indices from Palmer & Williams (1975). Organic hazes employ the indices of refraction measured by Khare et al. (1984a). For spherical particles (such as small sub-fractal "monomer" organic haze particles or the clouds in the Venus atmosphere), we use the code "Miescat," to calculate these efficiencies (Wiscombe, 1980; Crisp, 1986; Crisp et al., 1989; Meadows & Crisp, 1996). For fractal organic haze particles, we use scattering inputs from the Wolf & Toon (2010) photochemical study generated with the fractal mean field approximation (Botet et al., 1997) (see Chapter 2). In `SMART`, spherical particles use a full Mie phase function, while fractal particles employ a Henyey-Greenstein phase function (Henyey & Greenstein, 1941).

3.2.1 Aerosols in SMART from Atmos

To create `SMART` cloud files from `Atmos` haze outputs, we wrote a script that bins the haze particles generated by the photochemical model into specified size bins (also called particle "modes") while preserving the total mass of haze particles in each atmospheric layer. The particle mode sizes we use span from 0.001 μm - 2 μm; larger particles do not exist in our Archean `Atmos`-generated atmospheres due to rainout (our Venus atmosphere model includes larger particle sizes). Spherical modes are R = 0.001 μm, 0.005 μm, 0.01 μm, and 0.05 μm. Fractal modes are R = 0.06 - 2 μm with 4 modes between 0.06 and 0.1, 10 equally spaced modes between 0.1 μm and 1 μm, and 2 μm. In total, this represents 19 particle modes.

In each layer of the `SMART` cloud files, we include a mixture of two particle modes; the mass density contributed by the two modes is selected based on the distance in log space of the `Atmos` particle radius to each neighboring `SMART` size bin. For example, if `Atmos` produces a particle of radius 0.33 μm in a layer, the corresponding layer in `SMART` will include 0.3 μm and 0.4 μm particles each comprising 50% of the layer's mass. This binning is necessary because the photochemical model generates many dozens of finely differentiated haze particle radii, but `SMART` model runtime with this many particle sizes is infeasible.

Once we have binned the `Atmos` particle radii to our `SMART` size grid, we must compute the total optical depth from each particle mode at a reference wavelength in each atmospheric layer. We arbitrarily select 1 μm as our reference wavelength. As discussed in Chapter 2, optical depth in a layer, τ, from particles of a given radius, r, depends the number density of particles per particle size, $n(r)$, the thickness of the atmospheric layer, z, and the wavelength-dependent extinction efficiency, Q_{ext}:

$$\tau = z \int_{r_{min}}^{r_{max}} \pi r^2 Q_{ext}(\lambda, r) N(r) dr \tag{3.2}$$

For fractal particles ($r > 0.05\mu m$), the cross sectional area and the corresponding extinction efficiencies are computed relative to the radius of an equal mass spherical particle, following the conventions of mean-field approximation (Botet et al., 1997). Spherical particles in `SMART` follow log-normal size distributions using the radii mentioned previously with a mode standard deviation of 1.5, which is realistic for an aerosol distribution (Tolfo, 1977). For fractal particles, we use a monodisperse distribution, the same size distribution used to compute our inputs from the previous Wolf & Toon (2010) fractal haze study and the same distribution used in the `Atmos` model.

3.3 Fractal Code

Fractal physics files containing Q_{ext}, Q_{abs}, Q_{scat}, and g for our nominal hazy Archean Earth study were kindly provided by E. Wolf. These same files were used in Wolf & Toon (2010) in the first study of fractal organic hazes on early Earth. By reformatting these files, we were able to easily use them in `SMART`.

While useful, these files had some limitations. All of them used the same nominal Wolf and Toon monomer size ($r_{mon} = 0.05$ μm,) and optical constants from Khare et al. (1984a), which did not give us the ability to test how variations in these parameters could affect haze properties. These files also had a short wavelength cutoff of 0.25 μm, which was concerning because accurate UV optical efficiencies are critically important to photochemistry and for investigating the UV shielding abilities of haze. Initially, the files were extrapolated out to Lyman-Alpha ($\lambda = 0.1216$ μm), but this seemed unsatisfactory given the importance of accurate UV measurements.

Rather than ask Eric Wolf to run more fractal files for me, it seemed beneficial to learn how to generate them on my own. The original Wolf and Toon optical constants were generated with the fractal mean field approximation (see Chapter 2), and the fractal mean field approximation code from the original group that devised it (Botet et al., 1997; Rannou et al., 1997) is listed at Scattport.org, a repository of publicly available particle scattering codes[1]. From this database, I was able to obtain the codes. Deciphering the input file and determining how to run the code required trial and error.[2] A difficulty of the fractal code was that it accepted optical constants and output scattering efficiencies at only one wavelength at a time from an input file, which had to be edited each time the code was run for a new wavelength. Generating input files for `Atmos` and `SMART` at many wavelengths in this manner would be highly impractical, so it was necessary to modify the code to read in columns of wavelength-dependent optical constants and automatically output correctly-formatted files

---

[1] http://www.scattport.org/index.php/light-scattering-software/multiple-particle-scattering/303-fractal-ol (note, however, that the links to the code are broken; I was able to obtain it by emailing the owner of scattport.org)

[2] And liberal use of Google Translate. Most of the comments and variables names are in French and German.

for `SMART`, the photochemical model, and the climate model. Once working, it was simple to feed in a new optical constant file or change the size of the monomers and generate a whole new set of optical efficiency inputs for all three models at once. As a consistency test, I compared the new optical efficiencies I generated using the Khare refractive indices for $r_{mon} = 0.05\mu m$, and I found they agreed with the files provided by E. Wolf to within 1%.

3.4 JWST and Coronagraph Noise Simulators

Some of the spectra presented in Chapter 6 for hazy Earthlike planets orbiting different stars were run through the James Webb Space Telescope (JWST) simulator from Deming et al. (2009) and through the coronagraph noise simulator from Robinson et al. (2016).

The JWST model we use can simulate the Mid-Infrared Instrument (MIRI) (Wright et al., 2004), the Near-Infrared Spectrograph (NIRSpec) (Ferruit et al., 2012) and the Near Infrared Imager and Slitless Spectrograph (NIRISS) (Doyon et al., 2012). The simulator includes noise from thermal emission from the telescope, sunshade, and instrument, and it includes zodiacal light. D. Deming has argued that photon-limited noise may be possible for JWST as demonstrated for Hubble Space Telescope observations of bright stars (Kreidberg et al., 2014), and this assumption is used in our simulations. This may be too optimistic, requiring much longer integration times than we use for our simulated observations in Chapter 6. The JWST spectra presented in Chapter 6 illustrate the noise level that must be achieved to enable observations of Earthlike exoplanets.

The coronagraph noise model (Robinson et al., 2016) simulates local and exo-zodiacal light, telescope thermal emission, dark current, read noise, and light leakage. It is highly customizable, allowing users to alter the distance to the planet-star system, the planet-star distance, the planet radius, the telescope diameter, the stellar spectrum, the telescope and instrument throughput, the inner and outer working angles, and the exposure time.

Chapter 4

SPATIALLY-RESOLVED MEASUREMENTS OF H_2O, HCL, CO, OCS, SO_2, CLOUD OPACITY, AND ACID CONCENTRATION IN THE VENUS NEAR-INFRARED SPECTRAL WINDOWS

Portions of this chapter were originally published in collaboration with V. S. Meadows, D. Crisp, et al. in the August 2014 edition of the Journal of Geophysical Research: Planets (Arney et al., 2014, *JGR:Planets*, 119, 1860-1891; ©2014 John Wiley and Sons), and are reproduced below with the permission of John Wiley and Sons.

4.1 Introduction and Background

Venus is our nearest planetary neighbor and represents a class of worlds which may be common throughout the galaxy (Kane et al., 2014). If Venus is characteristic of the end-state of the evolution of habitable planets, this cloud- and haze-enshrouded world may exemplify a type of planet frequently found interior to the habitable zone boundaries of other stars. We can use Venus as a general example for how to derive the characteristics of planets below thick H_2SO_4 cloud decks. However, to use the technique from this chapter on our sister planet, thermal radiation emanating from the planet's night side must be observed. Such observations will be challenging on exoplanets that are spatially unresolved: the day and nightside spectral information will occupy a single pixel, and bright reflected dayside radiation will overwhelm the nightside thermal emission. Therefore, this is not a technique that can be used with the first generation of exoplanet observing missions. However, on planets with substantially thinner H_2SO_4 hazes and clouds, we may be able to sense reflected solar radiation deeper into the planet's atmosphere, possibly down to the surface at the near-infrared wavelengths examined in this chapter where H_2SO_4 is relatively transparent. In the more distant future, telescope concepts such as the "Exo-Earth Mapper" would use interferometry involving multiple space telescopes to construct spatially-resolved maps of exoplanets, and these methods used to remotely characterize the Venus deep atmosphere could be employed.

Early studies suggested that Venus was more Earth-like in its past, with a substantial amount of water, as inferred from its high D/H ratio (McElroy et al., 1982; Donahue & Hodges, 1992); although, the interpretation of an early watery Venus has been disputed (Grinspoon et al., 1993; Hamano et al., 2013). Nevertheless, the general desiccation of planets with stable liquid surface water through the runaway or moist greenhouse processes (Ingersoll, 1969; Kasting et al., 1983, 1984; Kasting, 1988; Goldblatt & Watson, 2012; Goldblatt et al., 2013) is expected to operate interior to the inner edge of the habitable zones of extrasolar systems (Kopparapu et al., 2013). Solar evolution may drive Earth into a Venus-like state in the future as the sun's luminosity increases and the inner edge of the solar habitable zone sweeps past 1 AU. Future identification of exo-Venus planets is important because they can inform measurements of an empirical inner edge to the habitable zone and will tell us the frequency of runaway greenhouse planets. Understanding the evolutionary path to exo-Venus analogs can be informed by studying the runaway greenhouse planet in our own solar system.

Independent of exoplanets, Venus is a fascinating planet in its own right. Despite its similar size and bulk composition to Earth, Venus and Earth have strikingly different atmospheres. Venus is a world whose surface temperature is hot enough to melt lead, whose surface pressure is equivalent to swimming at 1 km underwater, and whose 96% CO_2 atmosphere contains choking sulfuric acid clouds. Its complex atmosphere exhibits several features still not well understood such as superrotation (e.g. Yamamoto & Takahashi, 2004) and an unknown UV-absorber (e.g. Esposito, 1980). Both the upper and lower atmospheric regions are complex and changeable, exhibiting variations of minor gaseous species on observable timescales. We will examine some of these variations in the lower atmosphere (below 45 km) in this chapter. This region contains nearly the entire mass of the atmosphere but is hidden by thick photochemically-generated clouds.

Historically, one of the most challenging aspects of studying Venus was characterizing the planet below the planet-wide cloud and haze layers that obscure the lower atmosphere at visible wavelengths. However, as we have discussed in Chapters 1 and 2, spectral windows discovered by Allen & Crawford (1984) are observable between 1 and 2.5 μm on the planet's night side and allow access to the sub-cloud atmosphere and surface.

Absorption features from H_2O, HDO, CO, HCl, hydrogen fluoride (HF), SO_2, and OCS can be measured in the NIR windows, providing a means to quantify their abundances in the Venusian lower atmosphere. Table 4.1 summarizes the results of previous studies in these NIR windows. In general, these analyses suggest that water in the lower atmosphere has little variability except possibly near the base of the cloud deck, where it may be correlated (Bell et al., 1991) or anticorrelated with cloud opacity (Tsang et al., 2010; Barstow et al., 2012). Previous studies show that CO and OCS may be spatially anticorrelated: CO is enhanced at higher latitudes compared to the equatorial region, and OCS tends to display the opposite behavior. The causes of these patterns are discussed in Sections 4.4 and 4.5. Figure 4.1 illustrates these spectral windows and shows the approximate spectral locations where minor gases absorb. A thorough review of the Venus NIR windows is given in Taylor et al. (1997), and we have discussed these windows in the context of particle scattering properties in Chapter 2.

Table 4.1: Measurements of gases

Window (μm)	Species	Measurement (ppm)	Reference
1.18	H_2O		
		30±15	de Bergh et al. (1995)
		45±10	Meadows & Crisp (1996)
		44±9	Bézard et al. (2009)
		27±6	Bailey (2009)
		32.5	Haus & Arnold (2010)
		30+10/-5	Bézard et al. (2011)
		31+9/-6	Chamberlain et al. (2013)
1.74	H_2O		
		50 (20-28 km)	Carlson et al. (1991)

		30±7.5	Pollack et al. (1993)
		30±10	de Bergh et al. (1995)
		25±5	Iwagami et al. (2008)
1.74	HCl		
		∼0.5	Bézard et al. (1990)
		0.48±0.12	Pollack et al. (1993))
		0.40±0.05	Iwagami et al. (2008)
2.3	CO		
		30 (<22 km)	Bézard et al. (1990)
		45 (42 km)	
		7-30 (30 km)	Carlson et al. (1991)
		23±5 (36 km)	Pollack et al. (1993)
		da/dz = 1.20±0.45 ppm/km	
		(47-44)±2.7	Collard et al. (1993)
		25-30	Marcq et al. (2005)
		22.5±3.5 (30 km),	Marcq et al. (2006)
		24±2 (36 km); more at high latitudes	
		24±3 to 31±2 (36 km)	Marcq et al. (2008)
		23±2 (at equator at 35 km)	Tsang et al. (2008a)
		32±2 (60° S at 35 km)	
		27±3 to 35±3 (35 km)	Tsang et al. (2009)
		∼25 to 35	Barstow et al. (2012)
		24.9 ± 2.4/2.9 at 10.5°N/S	Cotton et al. (2012)
2.3	H_2O		
		∼40	Bézard et al. (1990)
		40 (dry profile)	Bell et al. (1991)
		200 (wet profile)	
		25 (30-35 km)	Carlson et al. (1991)
		30±6 at 33 km	Pollack et al. (1993)

		30+15/-10	de Bergh et al. (1995)
		26±4	Marcq et al. (2006)
		31±2 (30-40 km)	Marcq et al. (2008)
		(22-35)±4;	Tsang et al. (2010)
		∼30-45 ppmv (35 km)	Barstow et al. (2012)
		∼50 ppmv (50 km)	
2.3	OCS		
		0.25 (below 50 km)	Bézard et al. (1990)
		0.2-1.0	Carlson et al. (1991)
		4.4±1 (33 km)	Pollack et al. (1993)
		da/dz = -1.58±0.30 ppm/km	
		∼1-6, (35 km)	Marcq et al. (2005)
		5-20 (30 km)	Marcq et al. (2006))
		2.4±1 -ñ 4±2 (33 km)	Marcq et al. (2008)
2.3	SO_2		
		130±40	Bézard et al. (1993)
		180±70 (70 km; uniform)	Pollack et al. (1993)
		130±50 (uniform)	Marcq et al. (2008)

Unlike previous studies, our analysis involves simultaneous spectroscopically (R=3500) and spatially resolved observations of the Venusian night side taken throughout the 1-2.5 μm region. Our pixel scale is ∼120 km/pixel, but the seeing at our observing site (∼1”) produces an effective resolution of ∼300 km. Using these data, we can look for correlations between the species measured in this entire spectral range. We present the first spatially-resolved maps of H_2O, HCl, CO, OCS, SO_2, cloud opacity, and acid concentration measured simultaneously, and the spread of our observations in time allows us to examine

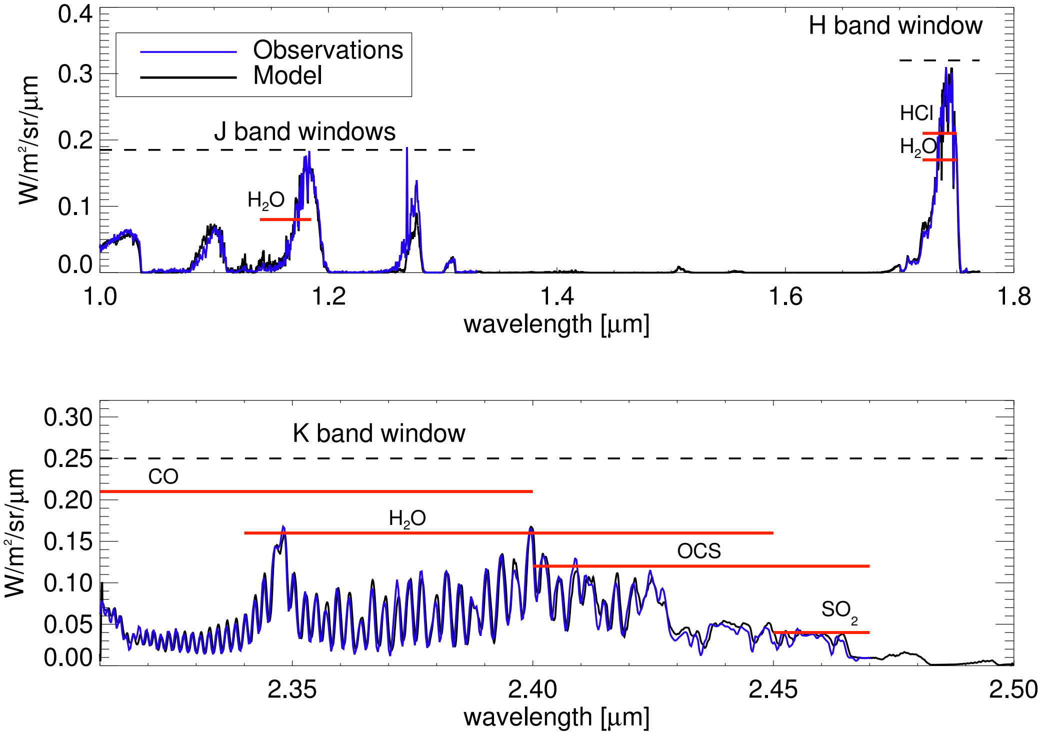

Figure 4.1: The Venus spectral window regions used to measure minor atmospheric species. Approximate spectral regions where gases absorb are marked. The poor agreement between the observed and synthetic spectra near 1.27 μm is due to O_2 airglow in the Venus mesosphere not included in our model.

temporal variability. Venus Express can produce high spatial resolution (50-100 km, limited by the atmospheric scattering footprint (Drossart et al., 2007)) maps of gases in the Venus atmosphere using VIRTIS-M, but its spectral resolution is low (R$\sim$100-600 from 1.05-5.99 μm) (Drossart et al., 2007), and it can only view a small portion of the planet at a time. The higher resolution spectrograph aboard Venus Express, VIRTIS-H (R$\sim$1840-5000 from 1.84-4.99 μm) (Drossart et al., 2007) can measure gases with greater sensitivity than VIRTIS-M, but it lacks imaging capability. Our ground-based observations allow us to fill the gaps between Venus Express' capabilities, producing low-resolution maps of the entire night side of the planet seen from Earth but with high spectral resolution.

Table 4.2: Summary of our Venus observational parameters

Date	Observing Time	Visible Venus Terminator	Venus-sun Elongation	Angular Diameter	Illuminated Fraction	Observing Airmass	Observing Cloud Coverage
3/1/09	Post-dusk	Evening	34.7°	45.1”	19.10%	2.5-5.0	Thin clouds
3/2/09			34.0°	45.8”	18.20%	2.2-5.4	Partly cloudy
3/3/09			33.2°	46.5”	17.20%	2.2-4.0	Mostly cloudy
11/25/10	Pre-dawn	Dawn	34.2°	46.7”	18.10%	2.0-3.2	Partly cloudy
11/27/10			35.7°	45.2”	20.00%	1.9-3.9	Mostly clear
11/30/10			37.7°	43.0”	22.70%	1.9-3.2	Clear
12/2/10			38.8°	41.7”	24.40%	1.8-3.4	Clear
12/3/10			39.4°	41.0”	25.30%	1.8-3.2	Clear
12/4/10			39.9°	40.4”	26.10%	1.8-3.8	Mostly clear

4.2 Observations and Data Reduction

Viewing opportunities of the Venus night side spectral windows occur approximately every 18 months for a few weeks before or after inferior conjunction. For this study, Venus was successfully observed at two separate intervals: prior to inferior conjunction on 1-3 March 2009, and after inferior conjunction in 2010 on 25, 27, 30 November, and 2-4 December. The corresponding inferior conjunctions occurred on 29 March 2009 and 31 October 2010, respectively. We obtained Nyquist-sampled spectra with the Astrophysical Research Consortium 3.5-m telescope at Apache Point Observatory (Sunspot, NM) using TripleSpec (λ=0.96-2.47 μm, R=3500 for the 1.1” slit) (Wilson et al., 2004). TripleSpec’s wavelength coverage is dispersed over 5 spectral orders. A summary of our observations is provided in Table 4.2.

To create data cubes, we observed using a drift-scan technique similar to that of Meadows & Crisp (1996). The spectrograph slit was aligned along the north-south direction of the planet just off the night side limb and then the telescope scanned toward the day lit crescent until the edges of the crescent became visible. Then, the telescope was scanned back toward the night side limb. This technique generated three to seven useable scans across the planet over each approximately 2-hour observing period. Exposure times were matched to the scan rate to build up data cubes with two spatial (along the slit length and in the scan directions) and one spectral dimension. The “slit” direction runs north-south on Venus disk, which subtends 110 pixels long (0.39”). The “scan” direction runs east-west and averages 130 pixels long (the scan length depends on how much off-limb sky was collected on a given scan).

Initial data reduction steps on the 2D spectra were accomplished with Spextool, an IDL package designed for use with TripleSpec (Vacca et al., 2003, 2004; Cushing et al., 2004). The Spextool suite performs flat fielding, wavelength calibrations, telluric correction, flux calibration, and order merging; our final calibrated spectra stitch all cross-dispersed orders together. Venus was observed at high airmass (spanning from roughly 2-5), and it was not possible to obtain adequate A0 stars for telluric correction on each night. Instead, we used sunlight scattered off the limb of the Venus crescent to simulate a G2V “standard star” with the identical airmass as Venus. This method of using scattered sunlight as a standard star is described in more detail in Meadows & Crisp (1996) and Chamberlain et al. (2013).

It is necessary to remove contamination from sky brightness from the data cubes. The darkening or brightening post-dusk or pre-dawn sky during our observations in 2009 and 2010, respectively, introduced sky brightness changes across each scan. Sky brightness variations in the slit direction are removed by taking a column of sky pixels beyond the night side limb and subtracting it from each column towards the crescent; then, the sky brightness in the scan direction is removed using a row of pixels beyond the northern or southern limb of the planet and subtracting it from each row. For some data cubes, a full sky row could not be obtained for the entire scan direction because the planet filled up to the edges of the spectrographic slit. In these cases, a low-order polynomial was fit to the available sky pixels and extended to fit the unavailable sky pixels. The sky brightness produced by the polynomial was visually inspected prior to use to ensure reasonable behavior.

Scattered dayside crescent light also contaminates the planet’s night side and must be removed. We removed crescent light from each pixel by obtaining a sample of unsaturated crescent light scattered just off the planet. The crescent spectrum was used to remove contamination from scattered crescent light in the planetary spectra by scaling it to match the radiance in a spectral region where flux from the Venus night side should be zero (e.g. 1.220-1.245 μm) for each spatial pixel on the planet and then subtracting the scaled crescent spectrum from the entire 0.96-2.47 μm wavelength range. Removing the crescent contamination is challenging because the crescent is extremely bright compared to the night side, and, as discussed in the following sections, some features in our maps of the spatial distribution of atmospheric species near the day-night terminator may be caused by residual scattered crescent light.

Once the contamination due to sky and crescent light has been removed, the three to seven data cubes from each night were coadded to create a master data cube for each night of observations. The planet was shifted slightly in position on each scan, so it was necessary to align the scans before they could be coadded. This was done by fitting a circle with the same angular diameter as the planet to the curved night side limb, then identifying the pixel closest to the circle's center. The scans were shifted to align the central pixels and then coadded.

4.3 Modeling Venus Synthetic Spectra

We generated synthetic Venus spectra using the Spectral Mapping and Atmospheric Radiative Transfer code (`SMART`), which is described in detail in Chapter 3.

4.3.1 Basic Model Inputs

Gases included in our Venus model atmosphere are carbon dioxide (CO_2), water (H_2O), HDO, hydrogen chloride (HCl), hydrogen fluoride (HF), sulfur dioxide (SO_2), carbon monoxide (CO), and carbonyl sulfide (OCS). Figure 4.2 shows the atmospheric profiles of the gases in the lower atmosphere used in our nominal model. For species whose abundance is not constant with altitude (CO, OCS), we quote the measured abundances at a specified altitude. The HDO/H_2O ratio is set at 130 times the terrestrial value. As discussed in Chapter 3, linelists for HDO, HCl, HF, SO_2, CO, and OCS were taken from the HITRAN 2012 database (Rothman et al., 2013). Also, as described in Chapter 3, high temperature line lists (HITEMP and the "High-T" list) were used for H_2O and CO_2 because HITRAN does not adequately reproduce their absorption features in the Venus atmosphere.

The lineshape functions used for CO_2 and H_2O are those described in Meadows & Crisp (1996): the far wings of H_2O lines are modeled as a super-Lorentzian profile, while the CO_2

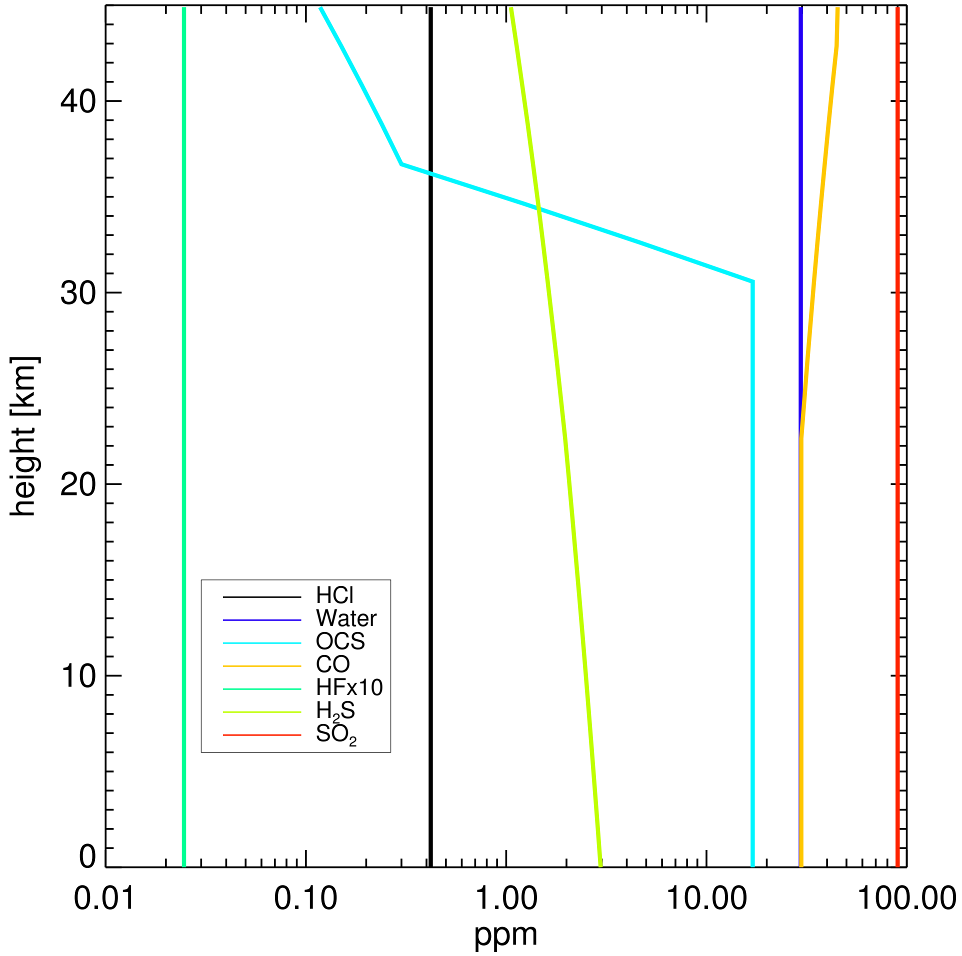

Figure 4.2: Profiles of gases in the lower atmosphere in our nominal atmosphere model.

far wings are sub-Lorentzian. In order to fit the shapes of the 1.74 μm and 2.3 μm windows, we must assume a CO_2 continuum absorption α (cm^{-1} amagat^{-2}) providing extra opacity. This opacity affects the behavior of the far wings of strong molecular bands, in this case CO_2 bands. There are disagreements in laboratory measurements of α at room temperature for the 2.3 μm window: α has been measured to be $\alpha = 2.0 \times 10^{-8}$ cm^{-1} amagat^{-2} (Moore, 1971; Moskalenko, 1979), $\alpha = 4.0 \times 10^{-8}$ cm^{-1} amagat^{-2} (the mean value measured by Tonkov et al. (1996)), and a high value of $\alpha = 1.6 \times 10^{-7}$ cm^{-1} amagat^{-2} (Brodbeck et al., 1991). For the 2.3 μm window, we choose the value of α that minimizes the root mean square discrepancy in the region between 2.20 and 2.29 μm where CO_2 is the only significant absorber. $\alpha = (2.5 \pm 0.5) \times 10^{-8}$ cm^{-1} amagat^{-2} is found to be the best fit continuum opacity for the 2.3 μm window, in agreement with Pollack et al. (1993) and slightly lower than that of Marcq et al. (2006) ($\alpha = 3.5 \times 10^{-8}$ cm^{-1} amagat^{-2}). Although no laboratory measurements have been made of α in the 1.74 μm window, our model cannot produce an acceptable fit to this window if α is set to zero. We selected the 1.74 μm window continuum opacity which best fit the ratio of the width to the height of the 1.74 μm window. $\alpha = (6.0 \pm 0.9) \times 10^{-9}$ cm^{-1} amagat^{-2} is our best fit value for this window, close to the values of de Bergh et al. (1995) ($\alpha = 5.0 \times 10^{-9}$ cm^{-1} amagat^{-2}) and Pollack et al. (1993) ($\alpha = 7 \times 10^{-9}$ cm^{-1} amagat^{-2}). We treat the CO_2 continuum opacity as constant across the 2.3 and 1.74 μm windows, but this may be an approximation given that others (Tonkov et al., 1996) have observed strong wavelength dependency of α. The J-band (1-1.31 μm) complex of windows is well fit by our model without assuming CO_2 continuum absorption, so we set α equal to zero for these windows, although recent work by Snels et al. (2014) indicates a small but nonzero value of α in the J-band (5.47×10^{-10} cm^{-1} amagat^{-2}), and Bézard et al. (2009) and Bézard et al. (2011) need a continuum opacity to reproduce variations of J-band spectral intensity with surface variations.

The surface is assumed to be Lambertian and its albedo is set at 0.15, consistent with a basaltic surface. Previous studies have reported surface emissivity variations (Hashimoto & Sugita, 2003; Haus & Arnold, 2010); however, we do not attempt to account for these here as surface processes are outside the scope of this study.

4.3.2 Modeling Cloud Opacity

Because the optical properties (Palmer & Williams, 1975) of the Venus clouds vary with wavelength (Figure 2.7), modeling the cloud deck is important for removing the wavelength-dependent spectral effects caused by variable cloud coverage. The main cloud deck and hazes extend between altitudes of 45 and 70 km. These clouds are thought to be composed of a solution of photochemically-generated H_2SO_4 and water vapor (Sill & Carm, 1972; Young,

Table 4.3: A summary of the aerosol parameters included in the model

Mode	Effective Radius (μm)	Variance
1	0.49	0.22
2	1.05	0.19
2'	1.40	0.207
3	3.85	0.262

1975; Pollack et al., 1978). The cloud deck is bounded above and below by thinner haze layers. The main deck can be divided into three major layers with different sized particles (Crisp, 1986), summarized here. The upper haze (>70 km) is composed of mode 1 particles approximately 0.4 μm in radius. The upper cloud (57-70 km) contains mode 2 particles, which have a modal radius near 1.4 μm, and mode 1 particles. The middle and lower clouds (50-57 km and 48-50 km, respectively) consist of mode 2 particles and mode 3 particles with a mean radius of 3.85 μm, as well as the sub-micron haze. Mode 3 particles are responsible for most of the mass and opacity of the cloud deck (Crisp, 1986), and these particles may have a crystalline component (Knollenberg & Hunten, 1980). (Toon et al., 1984) proposed that these mode 3 particles are the large-particle tail of the mode 2 size distribution. Venus cloud models have been produced by several authors (Tomasko et al., 1985; Crisp, 1986; Grinspoon et al., 1993; Pollack et al., 1993) and there have been recent attempts to better constrain the global cloud structure (Satoh et al., 2009; Barstow et al., 2012).

We adopt the cloud model from Crisp (1986) as our nominal model. Our nominal cloud model assumes cloud droplets which are 75% H_2SO_4 by weight. The cloud particles are modeled with log-normal size distributions and are assumed to be spherical droplets. Model effective radii and variances for each mode are shown in Table 4.3

The single scattering albedo (the ratio of scattering efficiency to total extinction efficiency, see Chapter 2) of the cloud particles is near 1 for the J-band complex of windows (1-1.31 μm), so the effect from the clouds on this region is mostly to reduce the radiance uniformly with wavelength. In the H- (1.74 μm) and K-band (2.3 μm) windows, however, the single scattering albedo is less than unity, so the clouds impose a wavelength-dependent spectral attenuation as opacity changes (i.e. as the density or size of cloud particles changes). For high opacity cloud regions, radiation from below the cloud deck is greatly attenuated, and the clouds' own emission can become a significant fraction of the total detected radiance. This is particularly evident in the 2.3 μm window, which changes shape in high opacity cloud regions (Figure 4.3). The increase in radiance at longer wavelengths is due to the clouds' thermal emission dominating the 2.3 μm window signal. In extreme cases of unrealistically thick clouds, our modeled spectra of the 2.3 μm window approach pure cloud emission spectra.

4.3.2.a Cloud "Ghosting"

Because altering the opacity of the clouds changes both the intensity and spectral shape of the 1.74 μm and 2.3 μm windows, variations in cloud opacity can affect the estimated abundances of atmospheric species and must be accounted for. In Figure 4.3, all of the spectra shown have the same column abundances of atmospheric gases, but the shape of the window becomes clearly distorted as cloud opacity increases. If we do not correct for variations in cloud opacity in our spectral model, an illusionary "ghostly" imprint correlated to the cloud opacity pattern on maps of gas abundances can emerge. We call this phenomenon "cloud ghosting." For instance, in regions of very thick clouds, the high contribution of cloud thermal emission has a similar impact on the spectral shape as decreasing the abundance of atmospheric species. Marcq et al. (2006) commented on the possibility of a spurious correlation between cloud opacity and water vapor abundance being inferred if cloud opacity variations are not correctly included.

Cloud ghosting has the greatest potential to be problematic in the 2.29 - 2.46 μm spectral range where the cloud particles have the highest extinction coefficient. As we describe in Section 4.5.2, we find some evidence of correlations between various gases and the cloud optical depth that persist after our removal of cloud ghosting through the procedure described below. It can be difficult to determine whether these correlations are real or whether they result from insufficient correction of the cloud in certain regions. Species such as wa-

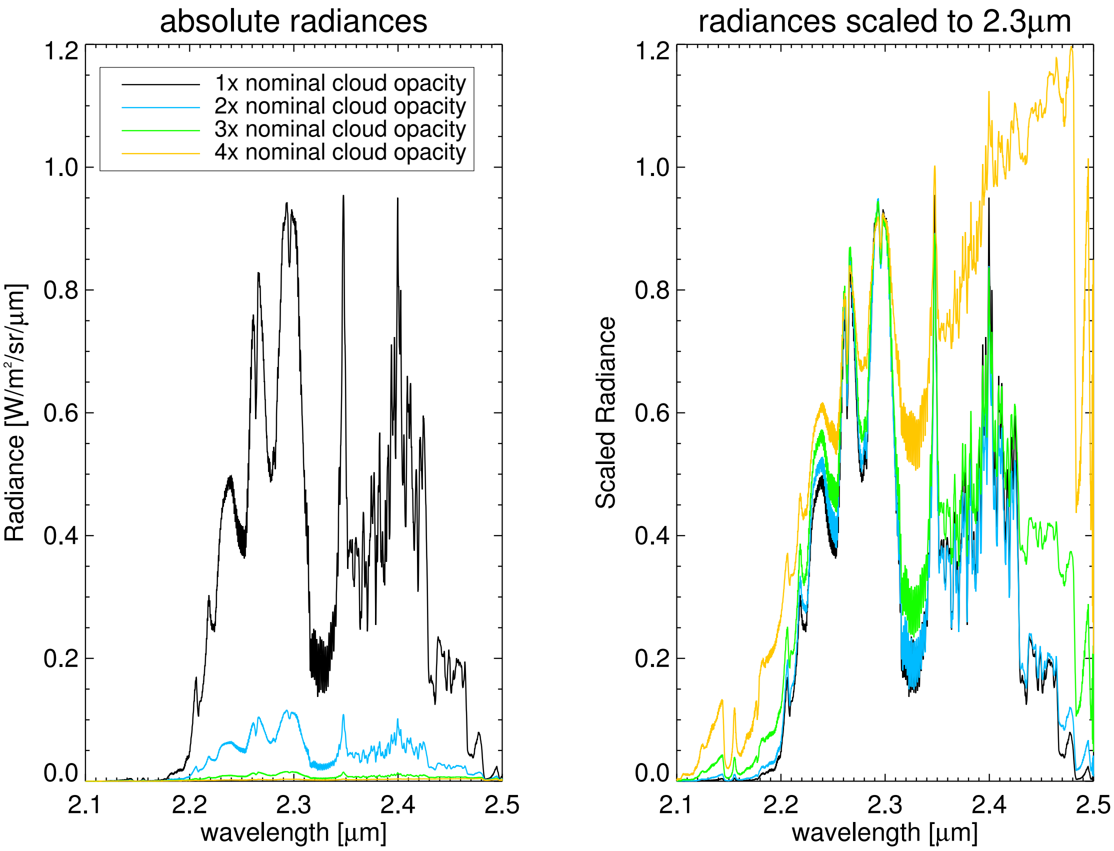

Figure 4.3: The effect of changing the cloud opacity on the radiance and shape of the 2.3 μm window. Each spectrum shown here has the same gaseous mixing ratios, but the spectral shape changes dramatically as cloud opacity changes. The plot on the left shows absolute radiances; the plot on the right shows each spectrum with radiances scaled to be identical at 2.3 μm to make changes to the spectral shape clear.

ter vapor and CO have been reported in previous studies to be anticorrelated with cloud opacity (Tsang et al., 2010; Barstow et al., 2012) but we urge caution of the interpretation of similar features reported here. Just as residual scattered light can contaminate the dark side of Venus due to the challenges of accurately removing dayside radiation on every pixel, residual cloud ghosting features may remain due to the difficulties of completely correcting the spectral effects of variable cloud properties, especially at the longest wavelength end of our spectra where cloud ghosting is strongest, and towards the planet's poles where the cloud structure is not well constrained. Features that appear to be correlated with the cloud pattern are discussed in Section 4.5.

4.3.2.b Removing Cloud Effects

To first order, the most obvious consequence of wavelength-dependent cloud opacity on the spectral windows are changes to the relative amplitudes of the peak radiances in the windows. We varied the opacity of each layer in our cloud model and found that changes in the lower cloud deck opacity have an order of magnitude greater impact on the spectral radiance compared to changes elsewhere in the cloud deck. Thus, the most important source of variations in brightness across the spectral windows is variations in the lower cloud deck optical depth where the bulk of the mode 3 particles can be found.

The cloud particles are composed of a concentrated solution of H_2SO_4 and H_2O. Our nominal model assumes 75% H_2SO_4 droplets; however, studies have suggested that a higher acid percentage may be more realistic, especially in the middle and lower clouds (Krasnopolsky, 2007; Barstow et al., 2012). The complex index of refraction of the cloud droplets depends on the acid percentage: Palmer & Williams (1975) lists the real and imaginary indices of refraction for 75%, 84.5% and 95.6% sulfuric acid/water solutions. These data have been widely used to model the Venus cloud particles. The intensities of the 1.74 μm and 2.3 μm spectral windows are sensitive to the imaginary index of refraction, k (the extinction coefficient, see Chapter 2), of the cloud particles. The imaginary index is orders of magnitude higher for these windows than the J-band windows (1-1.31 μm), so the longer wavelength windows are the most strongly affected by cloud opacity variations and changes in acid concentration. See Figure 4.4 for a plot of k at 75%, 84.5% and 95.6% acid from 1-2.5 μm. The imaginary index of refraction is wavelength-dependent and does not systematically increase or decrease linearly going from 75% to 95% acid. At a particular wavelength, if k increases, the observed radiance will decrease. However, if the cloud thickness increases, the radiance will also decrease. In general, the magnitude of changes in the observed radiance is more strongly driven by changes in the cloud opacity than changes in the acid percentage. For example, changing the acid percentage from 75% to 95% increases the integrated 2.3 μm window spectral intensity by only 10%, whereas increasing the lower cloud deck opacity by 20% decreases the spectral intensity by 30%. We find low and high opacity regions typically differ by a factor of 1.5-2.5 times our nominal opacity, a difference that results in almost an order of magnitude change to the integrated 2.3 μm intensity. Still, acid concentration variations can create cloud-ghosting effects, so our model allows variations in both cloud opacity and the acid percentage. The lower cloud deck opacity was allowed to vary from 0 to 5 times the optical depth of our nominal model in increments of 0.05, while acid percentage could be set discretely at 75%, 84.5%, or 95.6% using values measured by Palmer and Williams (1975). Barstow et al. (2012) assume it is possible to linearly interpolate intermediate values between 84.5% and 95.6% acid, but the authors note that including 75% makes it impossible to assume linearity. We choose to include 75%, and we do not use the Barstow et al. (2012) interpolation method. Even if it were possible to measure acid percentages intermediate to 75%, 85%, and 95%, applying a wavelength-dependent spectral correction using intermediate percentages is extremely challenging because, as shown in Figure 4.4, the behavior of the indices of refraction at these three concentrations is complicated: linear interpolation using the 75% and 95% refractive indices does not actually predict the measured refractive indices for 85% across our wavelength range. Therefore, we do not assume the information we have can predict other refractive indices that have not been measured. We could not find sources listing intermediate indices of refraction at Venus-like temperatures.

To remove spectral effects from acid concentration variations across the planet, we created synthetic spectra in which acid percentages were set at 75%, 84.5%, and 95.6%. Then, for each pixel, we identified the most closely matched synthetic spectrum to the intensity of radiation near 1.74 μm and 2.22 μm using the "branch plot" method employed by Barstow et al. (2012) (note Barstow et al. used 1.74 μm and 2.20 μm, but we do not have sufficient signal-to-noise in our data to use 2.20 μm). Once the acid concentration that produces the closest match in each pixel is determined, we apply a wavelength-dependent correction to scale the spectral brightness and spectral shape to our nominal acid concentration (75%) so that the acid concentration becomes effectively constant across the planet and the remainder of variations can be assumed to be associated with cloud opacity.

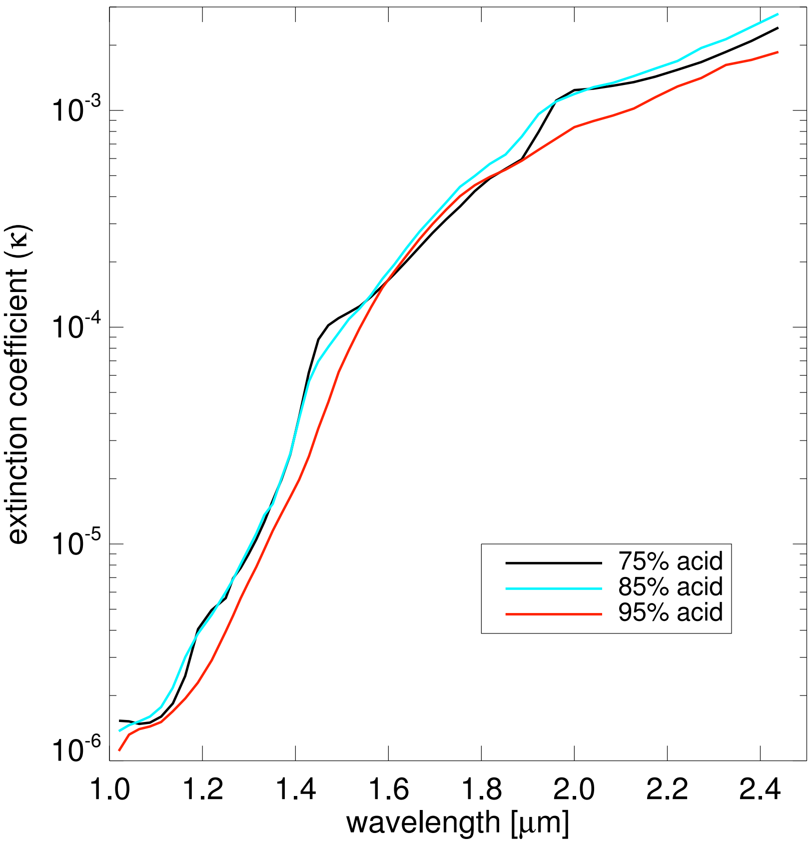

Figure 4.4: The extinction coefficient (k) values at different wavelengths (from Palmer & Williams (1975)).

Next, to determine the cloud opacity in a given pixel, we use the acid-corrected spectra and find the cloud opacity best matched to the spectral shape and absolute radiance in the spectral regions between 1.750 and 1.754 μm ($I_{1.75}$) and between 2.26 and 2.28 μm ($I_{2.27}$). These areas have CO_2 as the only significant absorber, they are not sensitive to surface elevation variations (as most of the windows between 1-1.31 μm are), and they are less affected by scattered crescent light compared to other regions tested (e.g. the 1.31 μm window). For each pixel, we found the cloud opacity that minimizes the discrepancy between the observed and synthetic spectrum in $I_{1.75}$ and $I_{2.27}$. Then, a correction was applied to each pixel to scale its spectrum to the spectral shape and brightness of our nominal cloud model (considered 1 times the lower cloud opacity of the Crisp (1986) model). Figure 4.5 shows an example image from 3 December 2010 of the planet's flux integrated between 2.27-2.28 μm, where CO_2 is the only significant absorber before and after applying the acid and cloud opacity corrections. The before image displays striking dark and light cloud contrast features, while the after image is largely homogeneous with typical maximum pixel-to-pixel variations on the order of 10%. Residual brightness variations in the after image may be due to acid concentrations intermediate to the quantized percentages we use or other changes in the composition or structure of the cloud deck. Figure 4.6 illustrates how cloud opacity and acid changes alter the spectrum. Barstow et al. measure the ratio of mode 3 to mode 2 particles using the ratio of the radiances at 2.29 μm and 1.74 μm. Our synthetic spectra systematically under-predict the radiance at 2.29 μm, so we cannot use this wavelength for measurements as Barstow et al. did. We tested the sensitivity of our cloud-corrected spectra to the mode 3:mode 2 ratio. First we found the mode 3:mode 2 ratio that most closely reproduces the spectral shape and intensity in our $I_{1.75}$ and $I_{2.27}$ measurement regions for a given lower cloud deck opacity. For example, a spectrum with 2 times the nominal lower cloud deck opacity has a similar spectral shape and intensity as a spectrum with 2.25 times the nominal mode 3:mode 2 ratio. Dividing a synthetic spectrum with 2 times the lower cloud deck opacity by a synthetic spectrum with 2.25 times the mode 3:mode 2 ratio produces a line that is almost flat across the 1.74 and 2.3 μm windows, so disentangling the spectral effects of the total lower cloud deck opacity from the mode 3:mode 2 ratio is difficult at our level of spectral sensitivity since they have a similar effect on the spectral shape.

4.3.3 Temperature-Pressure Profile

The temperature-pressure (T-P) profile in Venus' lower atmosphere is believed to change latitudinally (Seiff et al., 1985). Changes in the T-P profile have been shown to alter the spectral shape of the 2.3 μm window (Tsang et al., 2008a), and this could affect our estimated abundances of atmospheric species at different latitudes, particularly towards

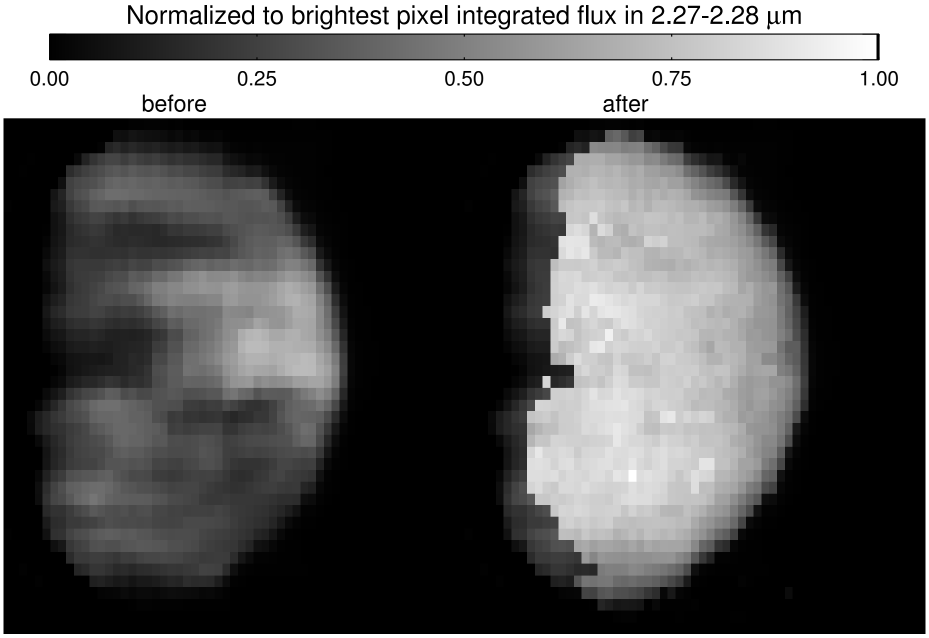

Figure 4.5: The image on the left shows pronounced opacity variations on Dec. 3 2010 due to variable cloud cover. A wavelength-dependent cloud correction mask is multiplied into the left image to produce the image on the right. On the right image, cloud-contrast features have largely been removed.

the poles where the spectral shape is impacted most strongly from changes to the T-P profile. We adopt the temperature-pressure profiles given by Seiff et al. (1985), changing our T-P profile for each range of latitudes given by those authors to minimize the impact of latitudinal T-P changes on our atmospheric gas estimations.

4.3.4 Gas Abundance Retrieval

The abundance of each gas is estimated by performing a least squares fit to the spectral region(s) where each gas absorbs using sets of synthetic spectra with different mixing ratios of the gas under consideration. Table 4.4 shows the spectral regions used to measure the gases investigated by this study (H_2O, HCl, CO, OCS, and SO_2).

Although the wavelength ranges selected to measure the species in Table 4.4 have little overlap (these regions were selected where a species most dominates with the least con-

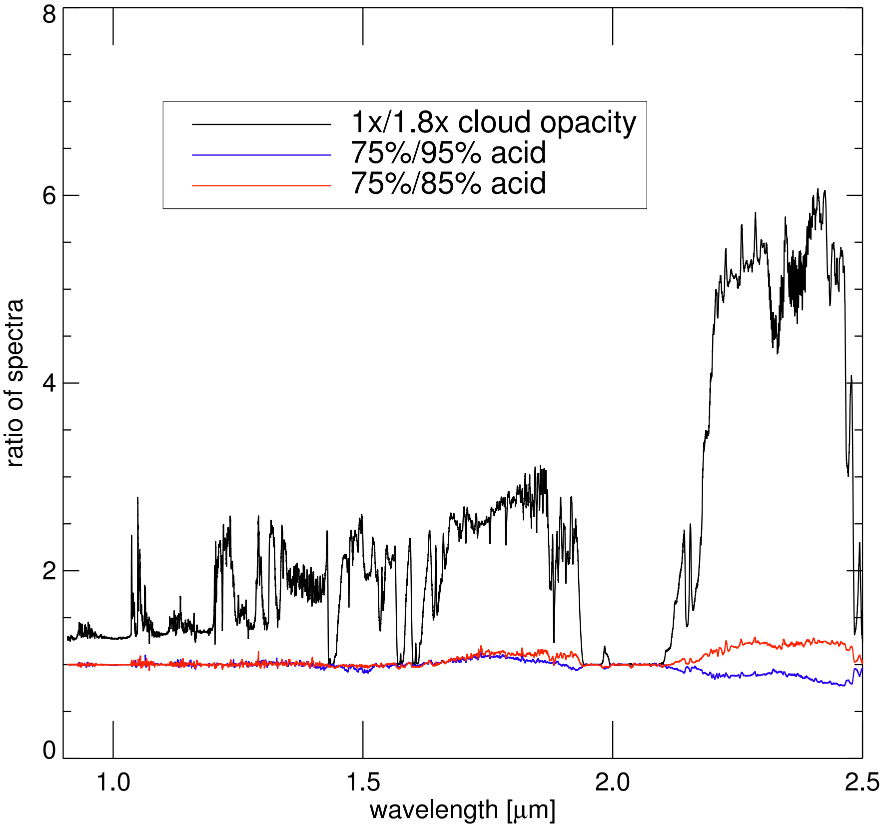

Figure 4.6: A comparison of ratios of spectra with different cloud opacity and acid concentrations. A discrepancy in the acid percentage cannot be responsible for the higher cloud opacities we determine compared to our nominal model.

tamination from other species), the spectrally active regions of many species do overlap (Figure 4.1). In the 2.3 μm window, the part of the spectrum sensitive to CO extends into the spectral region where we retrieve H_2O. H_2O is active in the region where we retrieve OCS, and both H_2O and OCS are active in the region where SO_2 is retrieved. Because the spectral influence of H_2O is minimal shortward of 2.34 μm, CO can be retrieved with little interference from other gases at wavelengths between 2.3 and 2.34 μm. Once CO is

Table 4.4: Spectral ranges for measurement of each gas

Species	Wavelength ranges(s) (μm)
Water	1.16-1.19, 1.72-1.75, 2.35-2.40
CO	2.3-2.34
HCl	1.72-1.75
OCS	2.415-2.450
SO_2	2.450-2.470

retrieved, its abundance in each pixel on the Venus disk is set in the model, and H_2O can be determined between 2.34-2.4 μm. After this, the H_2O abundance in each pixel is set. OCS can then be retrieved from 2.41-2.45 μm. Lastly, OCS is fixed in each pixel, and SO_2 can be retrieved longward of 2.45 μm. In this way, the abundance of each gas depends iteratively on the retrieved abundances of the previous gases.

The 1.74 μm window presents a greater challenge than the 2.3 μm window because the spectrally active regions of H_2O and HCl overlap across the entire window and cannot be distinguished at our resolution. The two gases can be disentangled, however, using the method outlined in Iwagami et al. (2008), which we adopt here. This method performs a least squares fit to linear combinations of various amounts of H_2O and HCl in order to best fit the 1.74 μm window. See Iwagami et al. (2008), for full details.

4.4 Measurements and Discussion

Our estimates of cloud opacity, acid concentration, and gas mixing ratios are presented in Figures 4.7 through 4.24. For each set of observations, we present maps of retrieved properties together with binned latitude and longitude plots. Between three and seven scans taken over approximately two hours were averaged together each night to produce the final products. In addition, we averaged all of the nightly scans together to produce maps with the overall averages of the full 2009 and 2010 observing runs. North points up on the maps. On the latitude and longitude plots, the colored dotted lines are the nightly averages corresponding to each individual map, and thick black line corresponds to the coadded mean of all observations and its associated error. To aid in intercomparison between measurements, all maps are shown together in Figures 4.25 and 4.26.

To minimize the impact of contamination by scattered light, the data cube pixels selected for these maps were screened to select only those with no significant radiance in spectral regions between the windows, which should have little or no flux. Pixels on the extreme right side of our maps from the 2009 dataset and pixels on the extreme left of our 2010 maps may still be contaminated by scattered crescent light, since these pixels are near the day-night terminator, although the pixels closest to the crescent have been excluded in this analysis. Anomalous features near the crescent are assumed to result from imperfect removal of scattered sunlight.

We do not estimate the error on our measurements from the variations in our retrievals because some degree of spatial variation across Venus is expected to be real for many species. Thus, a simple estimate of error from the standard deviation of our measurements can be an over-estimate that incorporates actual physical variations. Instead, we estimate error with the following approach. An error spectrum from Poisson noise and other instrumental uncertainties is propagated by Spextool and saved for each datacube. We add this error to the observed spectrum to produce two $\pm 1\sigma$ uncertainty spectra from which cloud opacity, acid concentration and gas abundances are retrieved to estimate the random error on each measurement of these atmospheric properties in every pixel. Some species must be measured sequentially (Section 4.3.4), so measurement of these species (S) will depend on previously measured quantities (P_0, P_1, P_2, ..., P_n). For example, OCS can only be retrieved in the 2.3 μm window after measurement of acid concentration, cloud opacity, CO abundance, and H_2O abundance. To estimate the error for a species S dependent on previous measurements, we vary each P_0 - P_n over its 1σ range of uncertainty before estimating the error on S. It is more difficult to estimate the uncertainty produced by a non-exact match between our observations and model fits, $\chi^2_{red} > 1$, which may be due to imperfections in our radiative transfer model and input linelists. We approximate a "goodness-of-fit" error by comparing the residuals between the observed spectra and best-fit synthetic spectra (BFS) to the residuals between the BFS and other synthetic spectra with known gas abundances. For

Table 4.5: Average Lower Cloud Optical Depths

2009		2010	
Date	Average Optical Depth	Date	Average Optical Depth
3/1/09	22	11/25/10	17
3/2/09	17	11/27/10	24
3/3/09	21	11/30/10	19
		12/2/10	23
		12/3/10	20
		12/4/10	19

example, consider a case where the BFS for an arbitrary pixel has 30 ppm of water vapor with a total residual of X between it and the observed spectrum in a particular wavelength range. We then fit a series of synthetic spectra to the 30 ppm BFS model spectrum, and the one with the closest residual to X, where X is the residual found between the observed spectrum and the BFS, is our best estimate of goodness-of-fit error. If the spectrum with the residual closest to X was generated with 32 ppm, then 2 ppm is considered our goodness-of-fit error. This error is added in quadrature to our previously described random error estimate. In all cases, our goodness-of-fit error estimate comprises at least half of the total error estimate.

4.4.1 Cloud Opacity

Estimates of the opacity of the lower cloud deck across the planet are shown in Figures 4.7 and 4.8. In general, the estimated cloud opacity values are higher than those in our nominal model. The average measured lower cloud optical depth is 21±2 for the 2009 dataset and 20±2 for the 2010 dataset. These values correspond to 1.8±0.20 and 1.7±0.20 times the nominal lower cloud deck opacities, respectively. Although the overall averages from both years of observations are similar, cloud opacity varies from night-to-night. Table 4.5 lists the average optical depths from each night of observations.

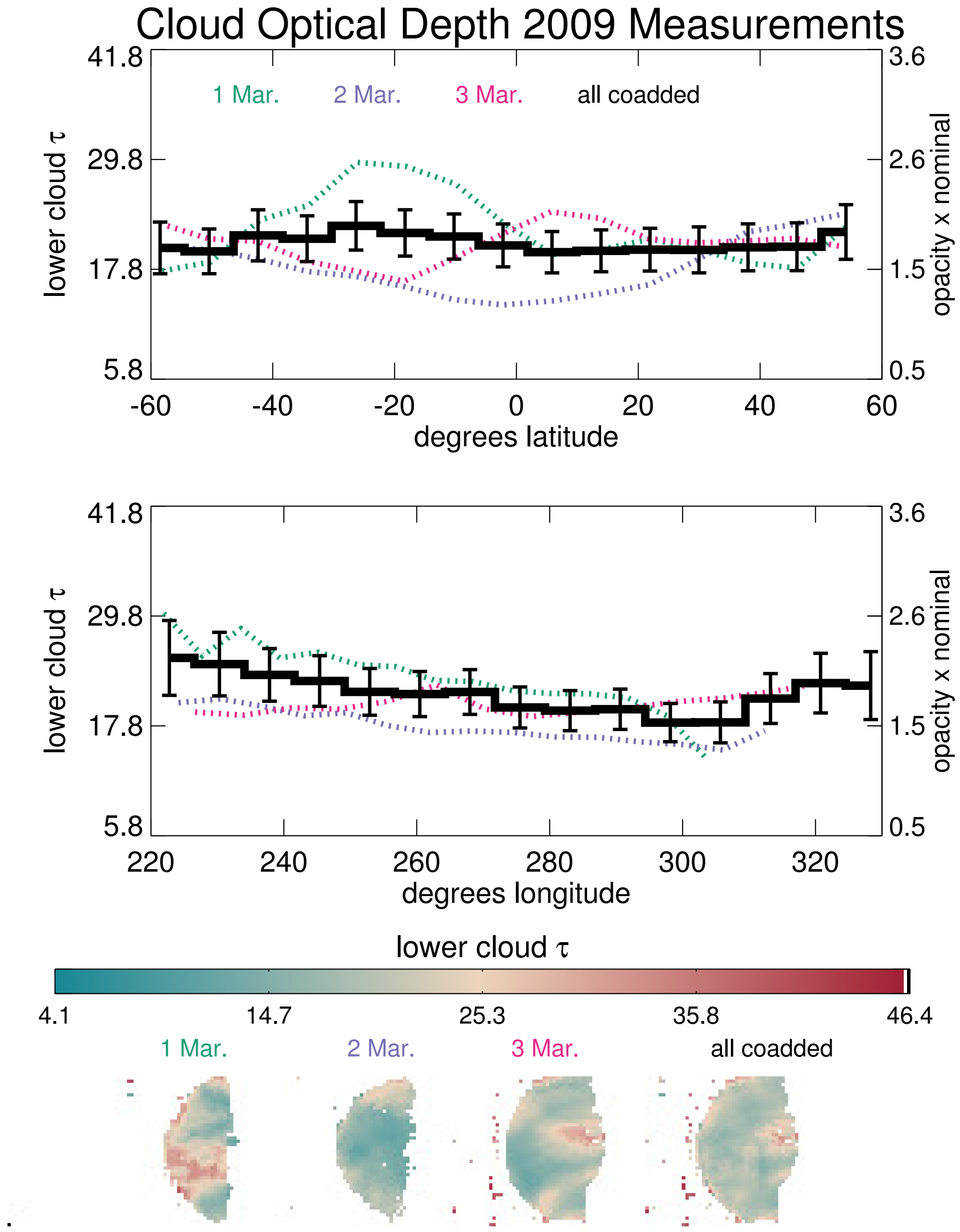

Figure 4.7: Cloud opacity maps from 2009. Opacity quoted here refers to the scaling factor required to multiply our nominal cloud optical depths by to achieve a good spectral fit.

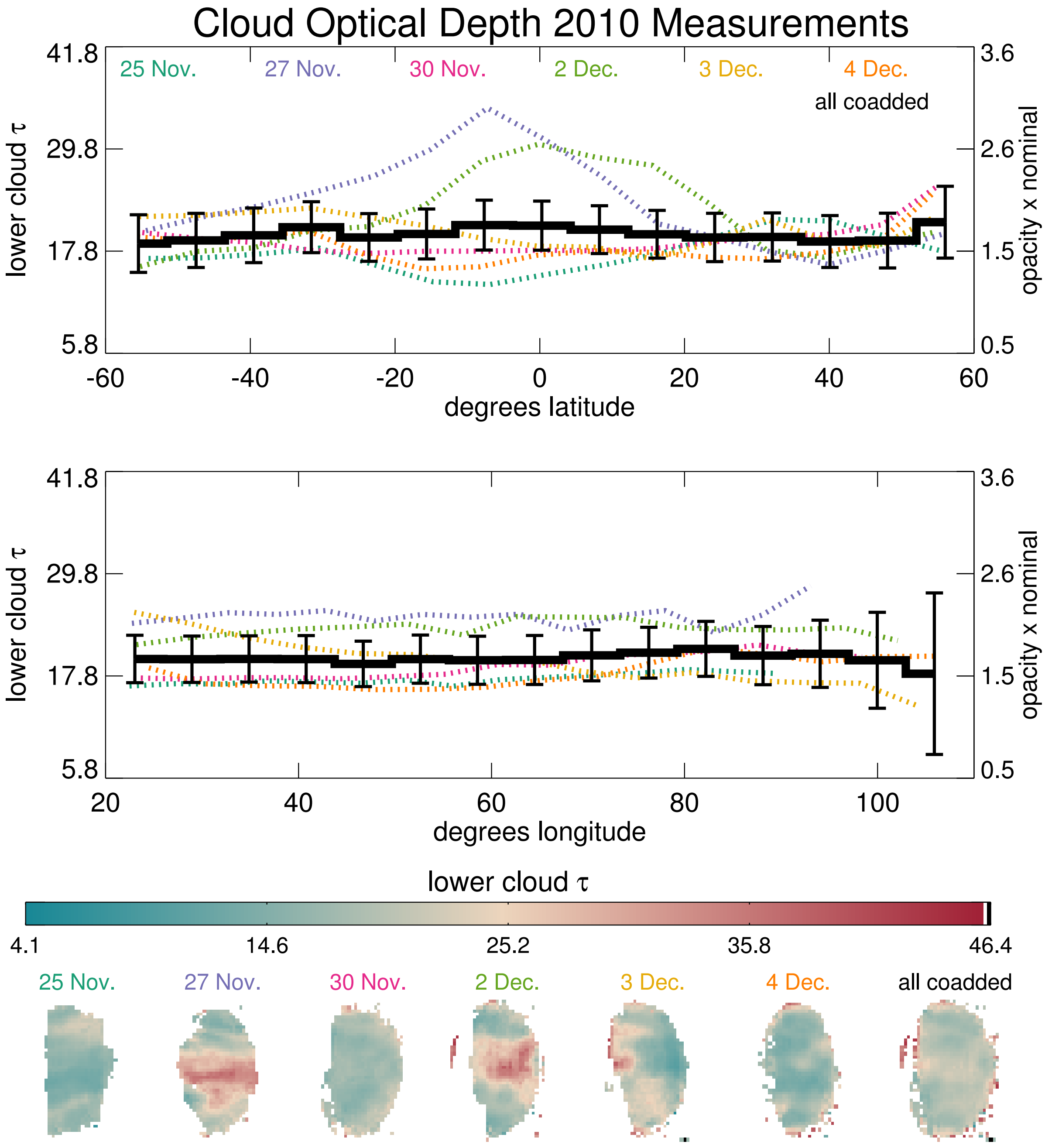

Cloud Optical Depth 2010 Measurements

Figure 4.8: Cloud opacity maps from 2010. Opacity quoted here refers to the scaling factor required to multiply our nominal cloud optical depths by to achieve a good spectral fit.

The features with the most opaque clouds tend to be near the equator, although nightly cloud coverage is highly variable. Highly opaque clouds (greater than or equal to 2.5 times the nominal model opacity, or an optical depth of approximately 30) are common, being seen on slightly less than half of all the nights, and when these features are present, they tend to be within 20° of the equator except for the southern feature on 1 March which extends to 30-40°S. Our high average opacities compared to our nominal model cannot be caused by discrepancies in our measurement of the acid concentration. Figure 4.6 shows the ratio of spectral intensities from synthetic spectra with 1.0 and 1.8 times the nominal cloud opacity and ratios of our acid concentrations. It is clear that uncertainties in acid concentrations, alone, cannot be responsible for the observed changes in brightness.

Each night of our observations shows distinct cloud opacity patterns. The regions with the most opaque clouds in 2009 are in the southern hemisphere on 1 March and the "finger" of cloud at low latitude extending from the crescent terminator on 3 March. On 3 March 2009, a large region of low opacity clouds occupied the southwestern portion of the planet, and on 2 March, the least opaque clouds were seen except near the poles. In 2010, the region with the lowest cloud opacity is the feature in the northeast region of the planet on 3 December. Other regions with low cloud opacity are the diagonal band on 25 November and the "fingers" of low opacity on 4 December. The most opaque cloud features are the equatorial band on the night of 27 November and the equatorial feature on 2 December.

4.4.2 Acid Concentration

Although we only used modeled spectra with discrete 75%, 84.5% and 95.6% sulfuric acid/water solutions, our results (Figures 4.9 and 4.10) include intermediate values because each final nightly measurement map represents the average of 3-7 scans across the planet on that night. Thus, for example, a pixel in which the acid percentage was measured at 75% in two scans and 84.5% in a third scan will result in a final averaged value of 78%. To make more accurate measurements of the Venus aerosol acid concentrations, more measurements of the indices of refraction at varied acid concentrations at Venusian temperatures are needed.

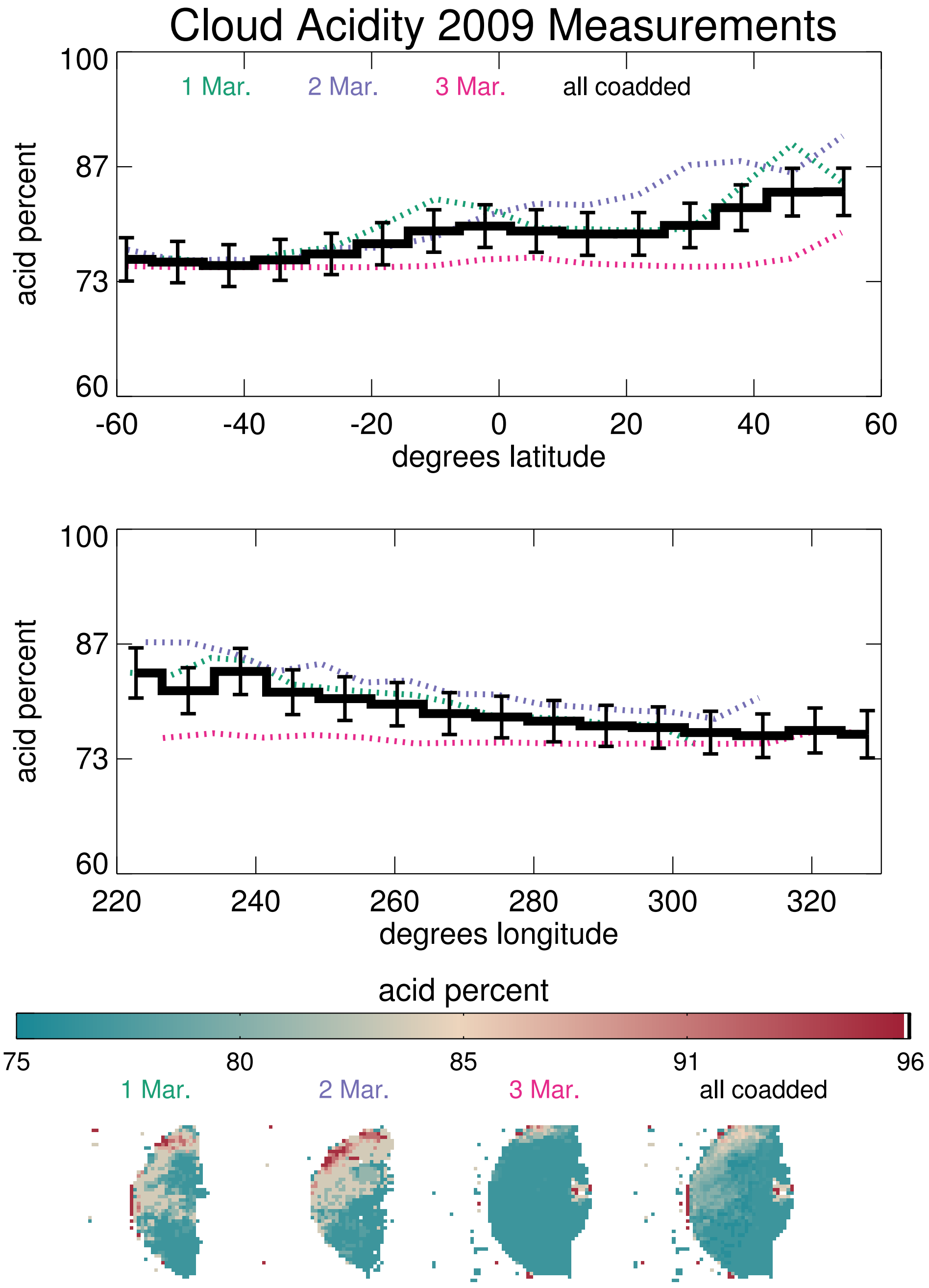

Figure 4.9: Acid concentration maps from 2009. Note the hemispherical dichotomy of higher H_2SO_4 concentration in the north.

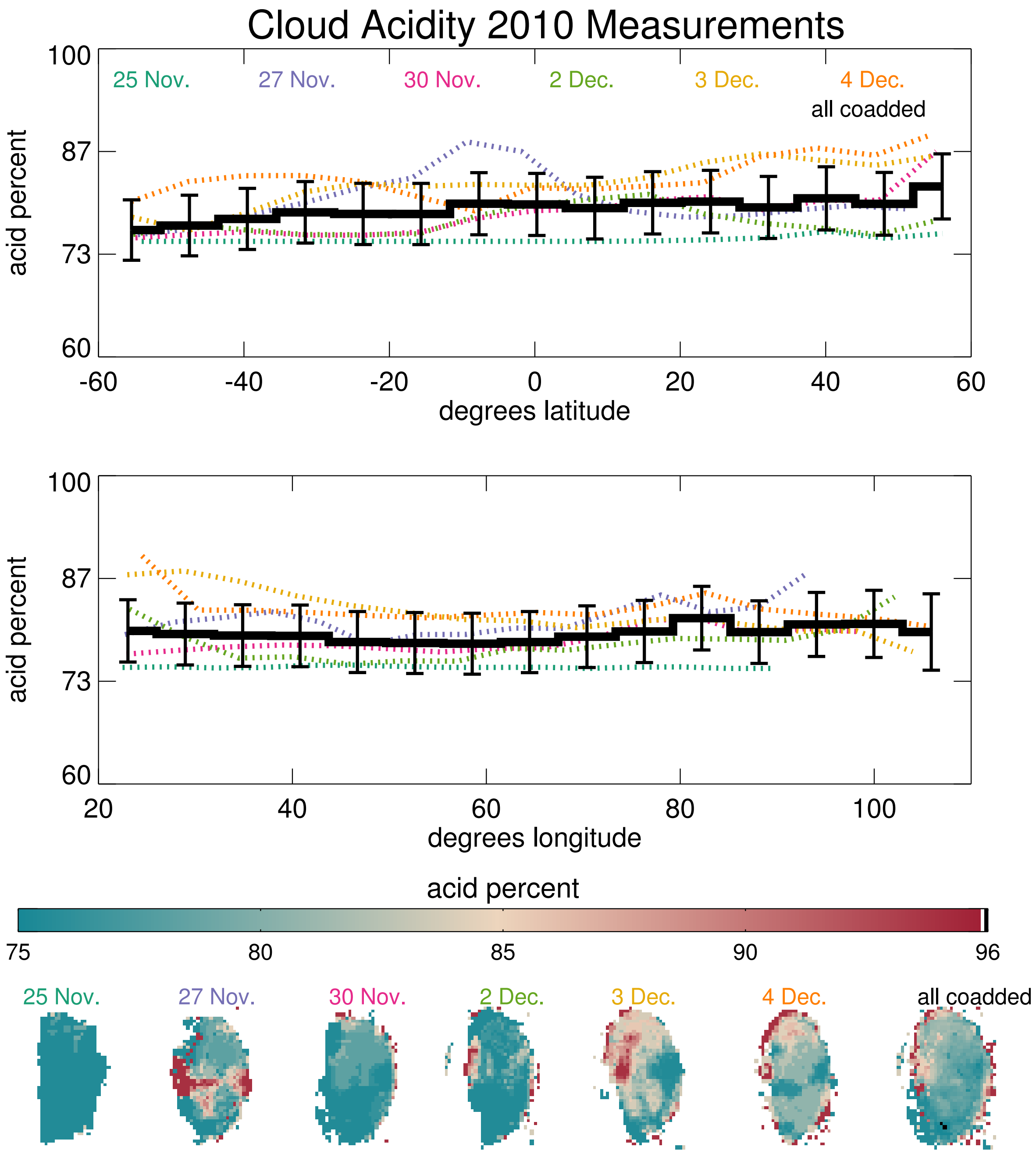

Figure 4.10: Acid concentration maps from 2010. There may be a hemispherical dichotomy with more H_2SO_4 concentration in the north.

Our nominal cloud model assumes cloud particles that are 75% sulfuric acid, although the average value we find for our quantized acid measurements is somewhat higher. The average value measured for both the 2009 and 2010 observations is 79±3% (2009) or ± 4% (2010). Our average values are consistent with Young (1975), which predicted that H_2SO_4 concentration should be between 75% and 85%. There are striking features in the acid concentration maps (Figures 4.9 and 4.10). In both the 2009 and 2010 observations, acid concentrations in the northern hemisphere are higher than those of the southern hemisphere, and although we only have observations for three nights in 2009 and six nights in 2010, within each observation set, there appears to be a dichotomy. In the 2009 observations, the average acid measurement in the southern hemisphere is 76±3%, and for the north, the average is 83±4%. In 2010, the average is 77±4% in the south and 81±4% in the north. Barstow et al. (2012) found more sulfuric acid at the south pole than the equator but did not measure the northern hemisphere. The Barstow study used data between July 2006 and November 2008, earlier than the observations described here, so differences may be due in part to temporal changes in the Venus atmosphere. We find hemispherical dichotomies amongst a number of gases discussed in the following sections, suggesting that there may be real hemispherical trends in the Venus atmosphere that vary on unknown timescales.

Our acid maps for 3 March 2009 and 25 November 2010 are largely flat and featureless with measured values almost uniform at 75%. These two nights are unusual, however, as most of our nights do not display spatially uniform acid concentrations. Further discussion of the acid maps is presented in Section 4.5 together with variations in gas abundances and cloud opacity that may be related.

4.4.3 Gas Mixing Ratios

We measured water vapor, CO, HCl, OCS, and SO_2 below the Venusian cloud deck. The results of these measurements are presented here.

Table 4.6: J-band water vapor measurements

Name	Wavelength (μm)	Comparison Reference	This paper measurement 2009 (ppm)	This paper measurement 2010 (ppm)	Reference measurement (ppm)
f1	1.1734-1.1748	Chamberlain et al. (2013)	28±2	29 ± 2	34 ± 4.50
f2	1.1766-1.1782		31±2	29 ± 2	37 ± 6.88
f3	1.1803-1.1833		29±4	28 ± 3	31 ± 4.22
peak	1.1750-1.1850		27±2	28 ± 1	31 ± 2.15
M&C	1.1698-1.1769	Meadows and Crisp (1996)	29±2	28 ± 2	45 ± 10
		Bailey (2009)			27 ± 6
Short wavelength side	1.6-1.9	n/a	29±2	27 ± 2	n/a

4.4.3.a Water in the 1.18 μm window

Water vapor absorbs on the short-wavelength side of the 1.18 μm window. This region is primarily sensitive to water vapor below 16 km, in the lowest atmospheric scale height. To aid comparison to previous studies, we measured the water vapor abundance in the spectral regions studied by Chamberlain et al. (2013), the region studied by Meadows & Crisp (1996) and Bailey (2009), and in the entire short-wavelength side of the window. CO_2 is the only significant absorber on the long-wavelength side of the 1.18 μm window, so this spectral region cannot be used for minor species retrieval. For some regions, we adopt the names used in Chamberlain et al. (2013) to aid comparison. Table 4.6 summarizes these measurements.

The somewhat high value of Meadows & Crisp (1996) given in Table 4.6 is likely a byproduct of the incomplete high temperature line lists available at the time it was published, as discussed by Bailey (2009). The re-analysis of Meadows & Crisp (1996) by Bailey (2009) using the BT2 linelist resulted in the smaller measurement of 27±6 ppm, consistent with our results. We believe this illustrates the importance of complete, accurate linelists in making measurements such as these. In Figures 4.11 and 4.12, we display maps from the "short-wavelength side" of the 1.18 μm window since it is representative of the whole sensing region.

Our maps are consistent with no significant spatial variation in the water abundance in the lowest atmospheric scale height, and spatial variations we do see can be attributed to path length truncation or artifacts. The anomalous feature with decreased water abundance in the northern hemisphere in the 2009 dataset on each of the three nights is located over Beta Regio, a 5 km high shield volcano centered at 35 degrees N, 283 degrees E. The smaller amount of water vapor over this feature is likely a path length effect since Beta Regio, being higher than its surroundings, truncates the path length of our line-of-sight through the atmosphere. The linear feature of higher water abundance running north-south on our observations from 25 November 2010 is almost certainly an artifact. Identically placed linear features can be seen on several of our other gas abundance maps for 25 November, suggesting that this column of pixels is contaminated. We interpret the linear features on 3 December 2010 as artifacts and the spotty features on 4 December as cloud ghosting. Chamberlain et al. (2013) found no spatial variations for 1.18 μm water except a potential minor decrease of water vapor from the equator to the south pole. We see no significant spatial variations of this sort.

4.4.3.b Water in the 1.74 μm window

Water vapor and HCl absorb at the peak and on the short-wavelength side of the 1.74 μm window. This window is most sensitive to these gases at altitudes from 16 to 35 km. On the long-wavelength flank of the window, CO_2 is the only strong absorber, so this region is not useful for measuring minor species.

We estimate an average of 33±2 ppm of water in our 2009 observations and 32±2 ppm in our 2010 observations, indicating that this species has no significant planet-wide temporal

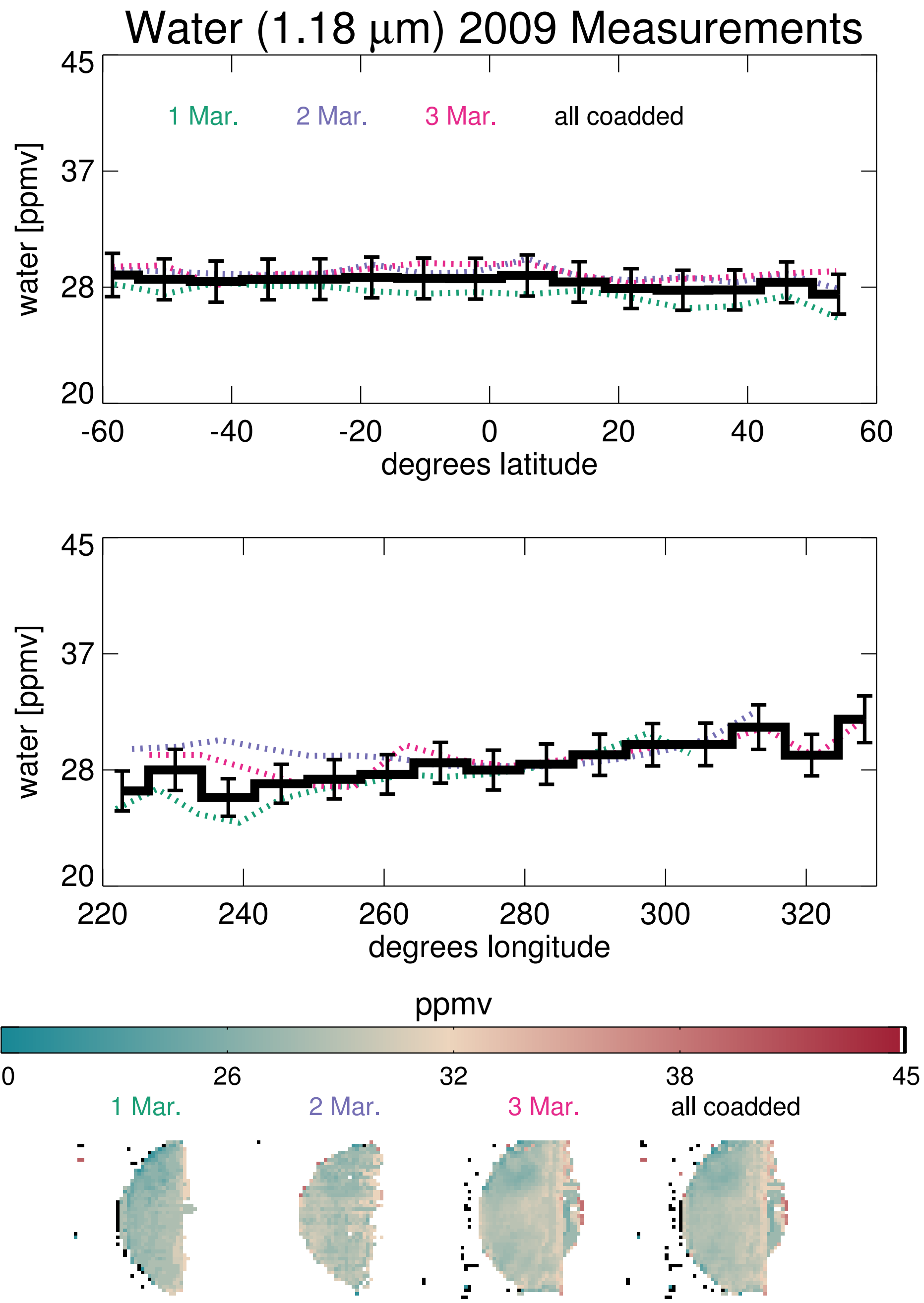

Figure 4.11: 1.18 μm water measurements in 2009. The dark feature in the northern hemisphere on all three nights is located over the 5 km high shield volcano Beta Regio. The decreased water vapor over Beta Regio is probably a path length effect.

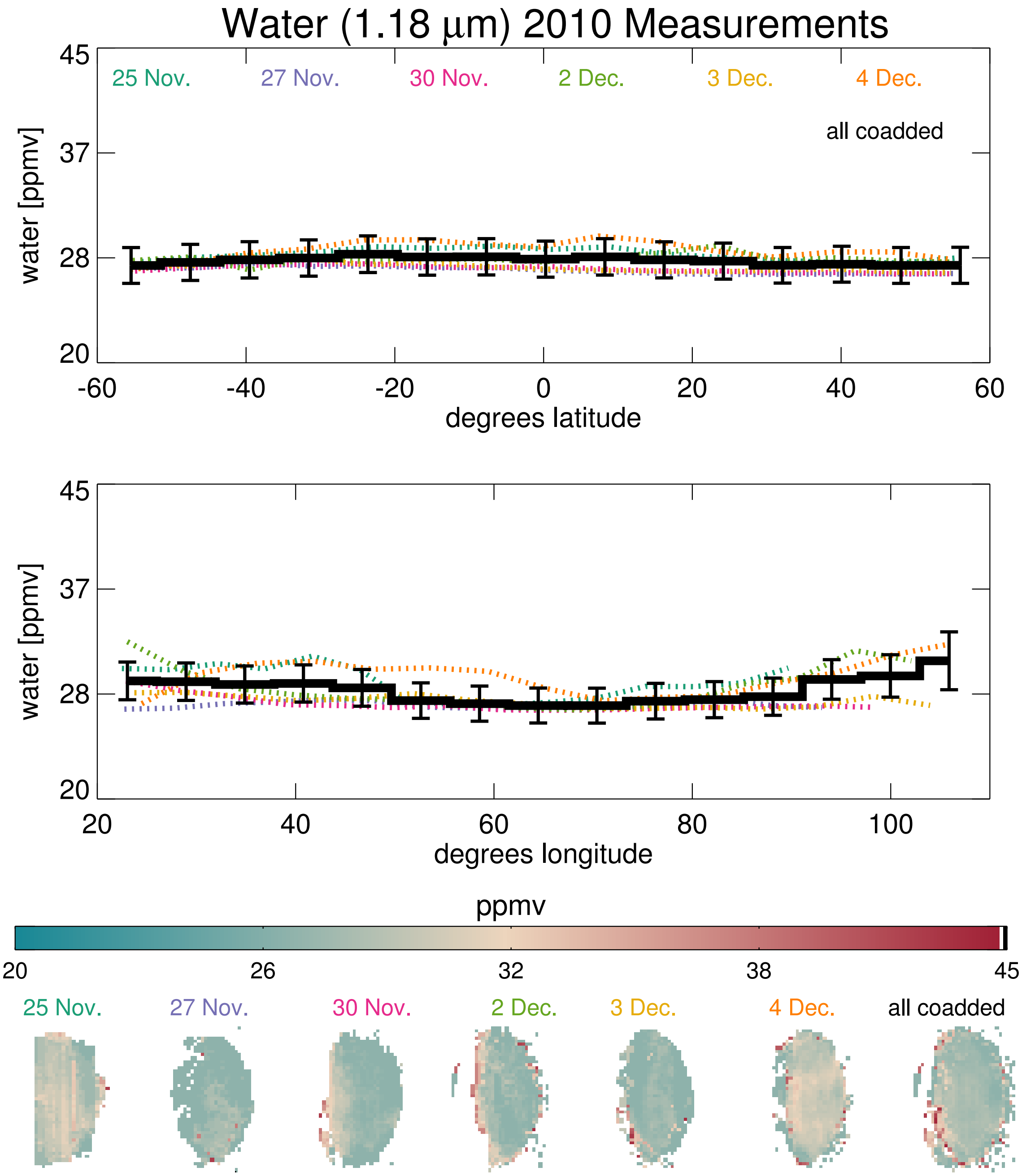

Figure 4.12: 1.18 μm water measurements in 2010

variations at these altitudes between these two dates. Maps of H-band (near 1.74 μm) water vapor are presented in Figures 4.13 and 4.14. Water vapor in the H-band in the 2009 observations shows no significant spatial variation, consistent with our results showing no spatial variations in the 1.18 μm window. On 27 November 2010, there is slightly less water vapor at low latitudes near the crescent terminator. This is near the equatorial region of thick clouds on the same night, possibly indicative of a negative correlation between water vapor and cloud opacity (as suggested by Tsang et al. (2010) and Barstow et al. (2012) for the 2.3 μm window), although it is also possible that this region simply suffers from crescent contamination. The 2 December data show a very small depletion of water vapor in the northern hemisphere.

4.4.3.c Water in the 2.3 μm window

The 2.3 μm window is sensitive to water vapor from roughly 30 to 45 km altitude, which is near the bottom of the lower cloud deck. We estimate an overall average of 34±2 ppm in our 2009 observations and 33±3 ppm in our 2010 observations. While we find statistically identical averages from both years of measurement, the spatial distribution of water vapor varies significantly as seen in Figures 4.15 and 4.16. Several nights in 2010 (25 November; 2-4 December) have more water vapor in the north than the south, although 27 November and 30 November do not show this trend. The enhancement of north vs south is about 15% for 25 November, 30% for 2 December, 20% on 3 December, and 18% on 4 December. Additionally, a banding pattern is present in our maps in 2009 but absent in 2010. The bands are discussed further in Section 4.5, as are possible weak anticorrelations with the cloud opacity patterns observed in 2010.

The spatial variations present in the K-band (2.4 μm) water maps are absent in the J- and H-band maps (1.18 and 1.74 μm, respectively). The only feature that may be correlated to the K-band is the northern 2 December feature mentioned in Section 4.4.3.b. This feature shows water depletion in the H-band, but there is higher water abundance in the K-band. This feature aside, any active processes that influence water in the K-band evidently do not persist lower into the atmosphere. There is a large vertical shear in the zonal wind between the altitude ranges sensed by the J (0-16 km) and K (30-45 km) windows that would quickly wipe out vertically coherent features.

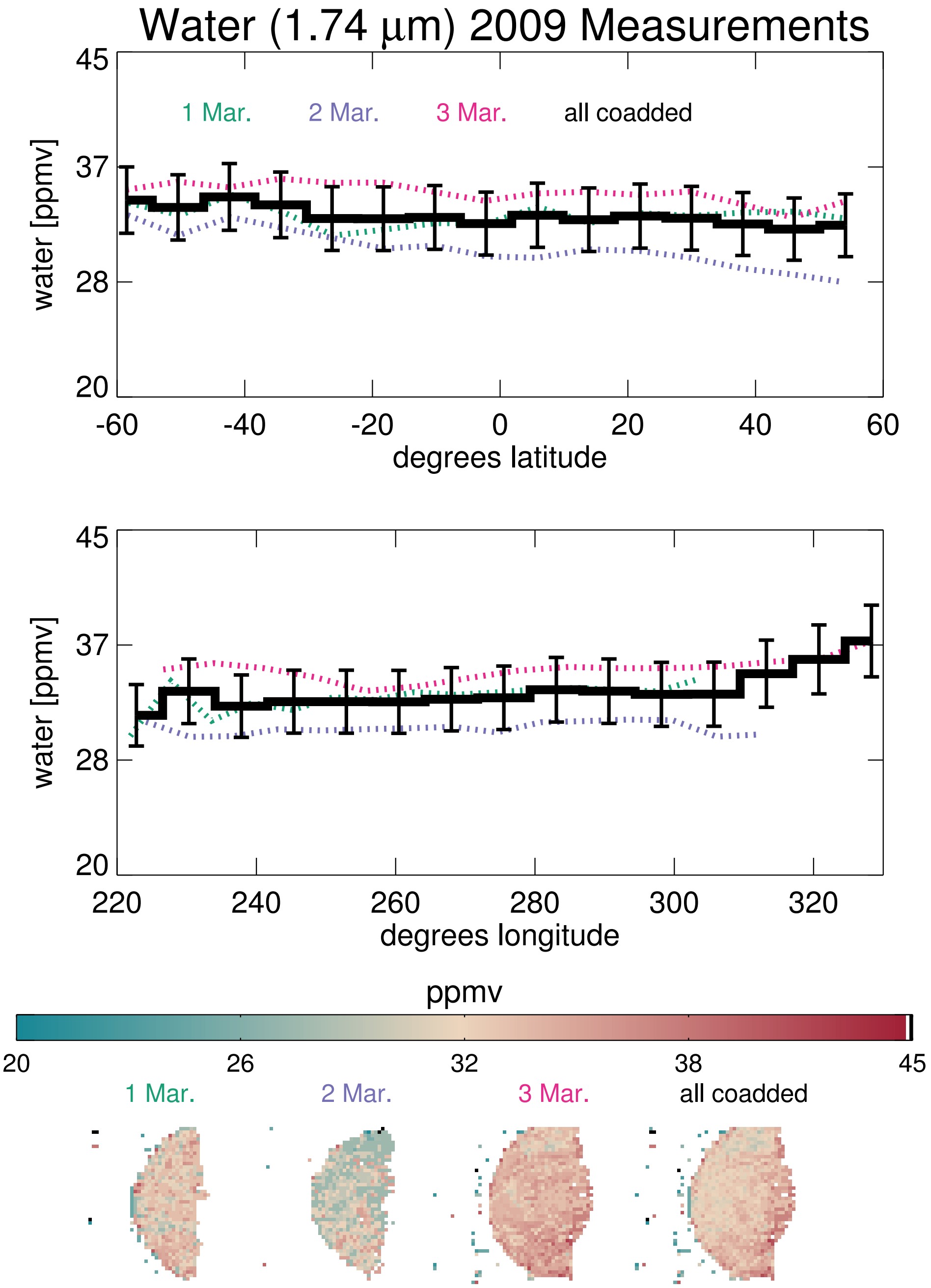

Figure 4.13: 1.74 μm water measurements in 2009

4.4.3.d HCl in the 1.75μm window

The largest reservoir of Cl compounds in the Venus atmosphere is HCl (Yung & DeMore, 1982; Krasnopolsky, 2007, 2012; Zhang et al., 2012). Like water vapor near 1.18 μm and 1.74

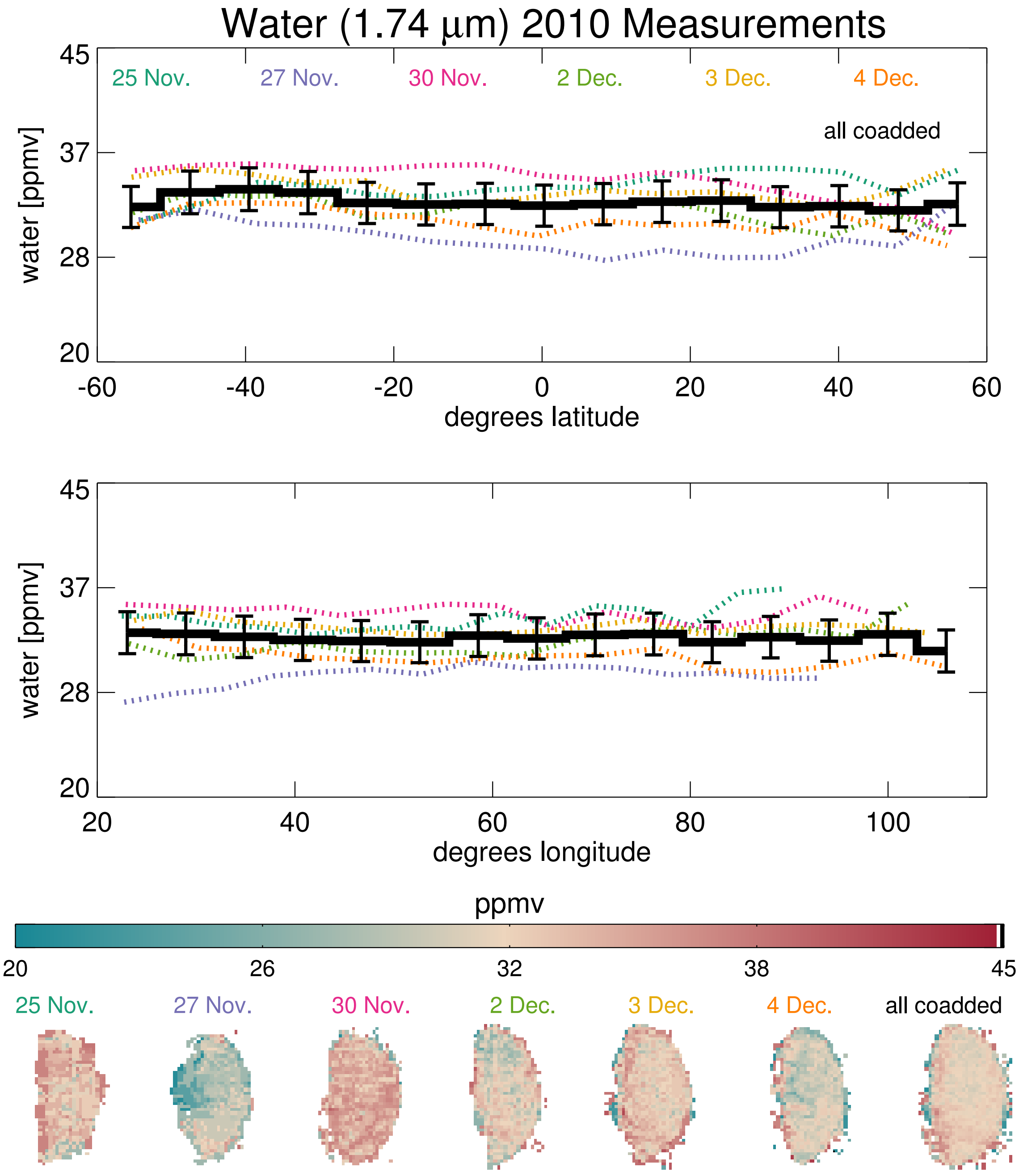

Figure 4.14: 1.74 μm water measurements in 2010

μm, HCl appears to have no major spatial variations (Figures 4.17 and 4.18). We retrieved a uniform distribution of this gas across the planet with a mean value of 0.41±0.04 in our 2009

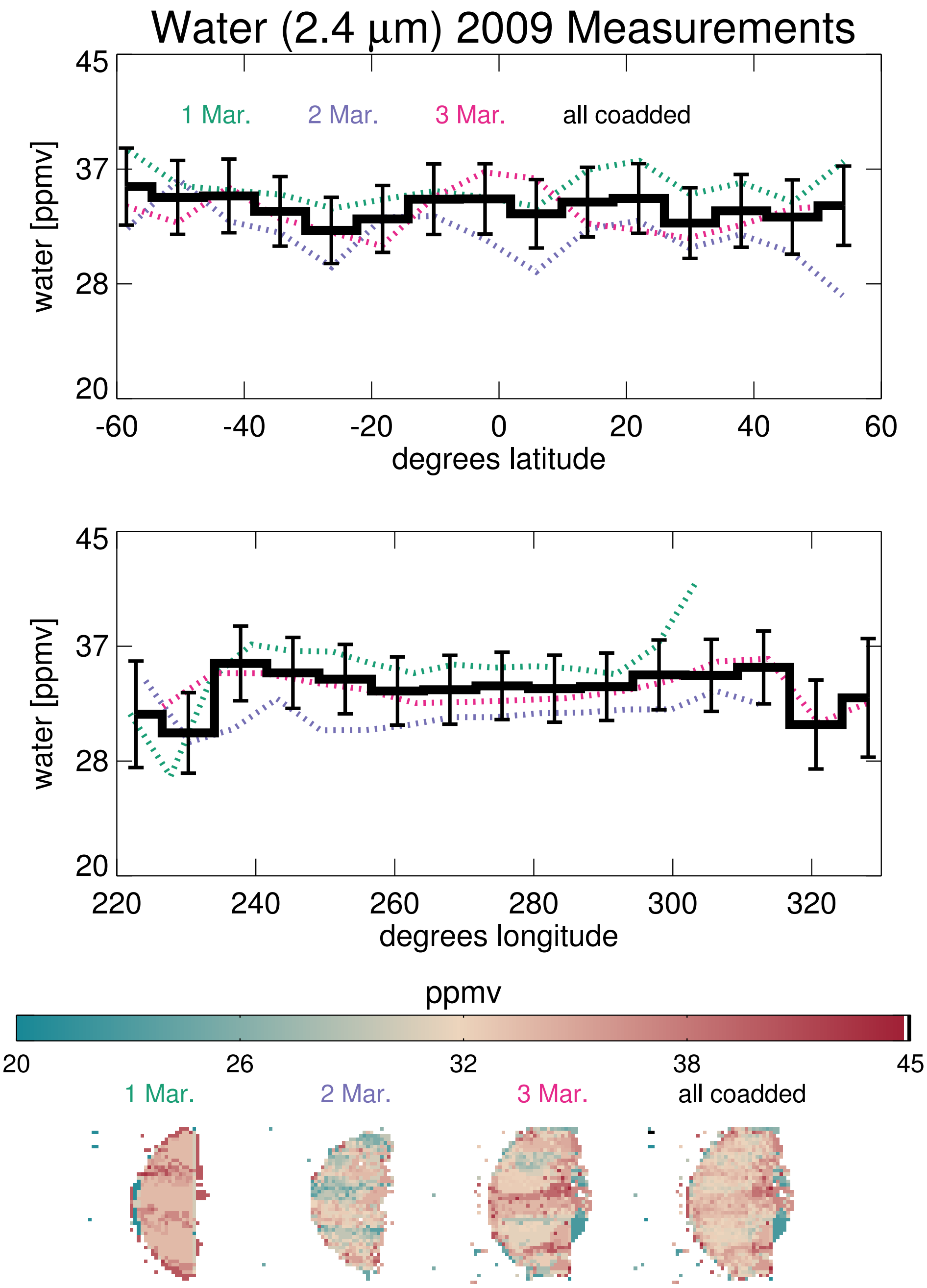

Figure 4.15: 2.4 μm water measurements in 2009. Note the unusual banding pattern.

observations and 0.42±0.05 ppm in our 2010 observations. These values are comparable to the results of Iwagami et al. (2008) (0.40±0.05 ppm), Pollack et al. (1993) (0.48±0.12 ppm)

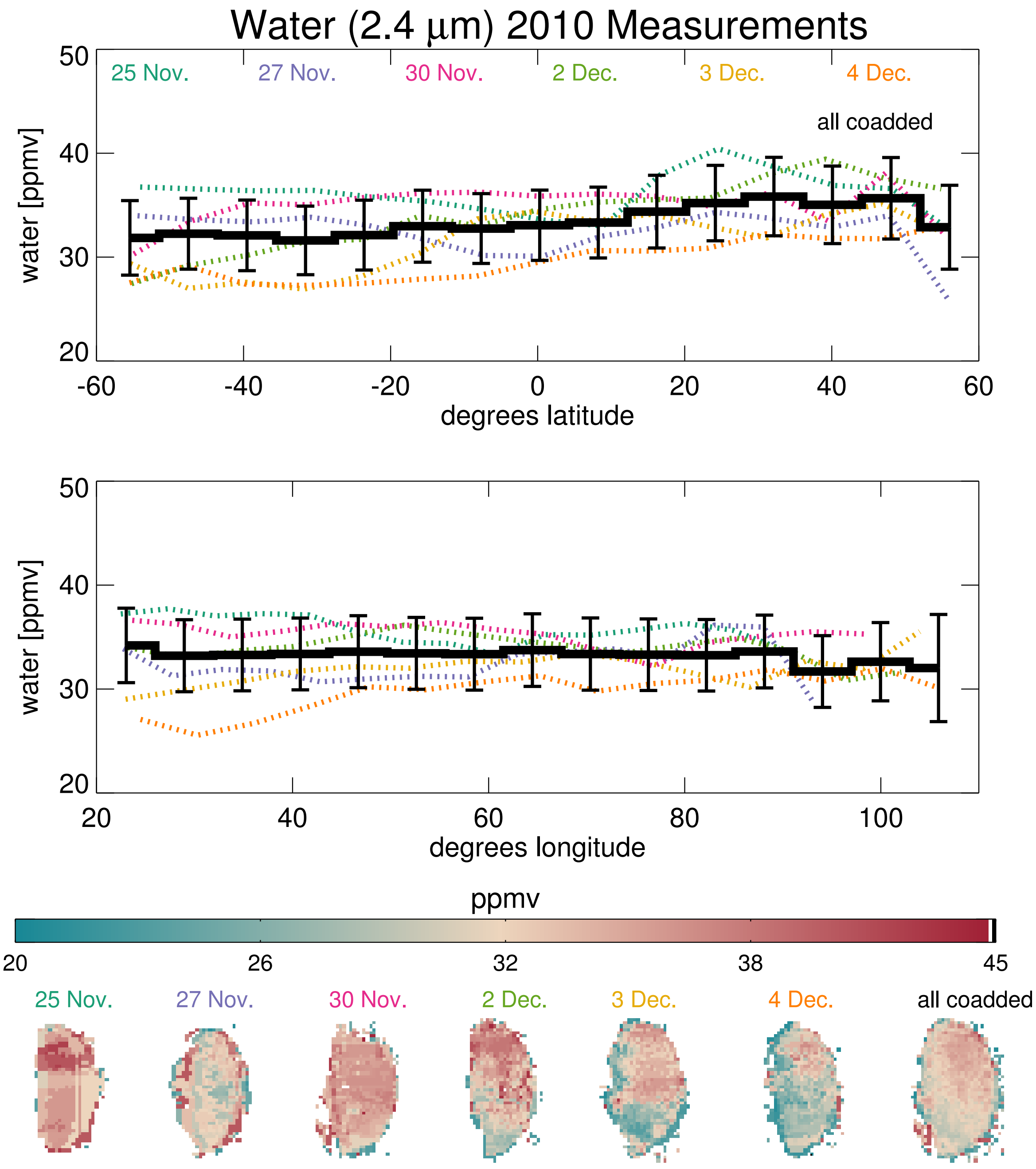

Figure 4.16: 2.4 μm water measurements in 2010. There may be a hemispherical dichotomy of more H_2O in the north.

and Bézard et al. (1990) (0.5 ppm).

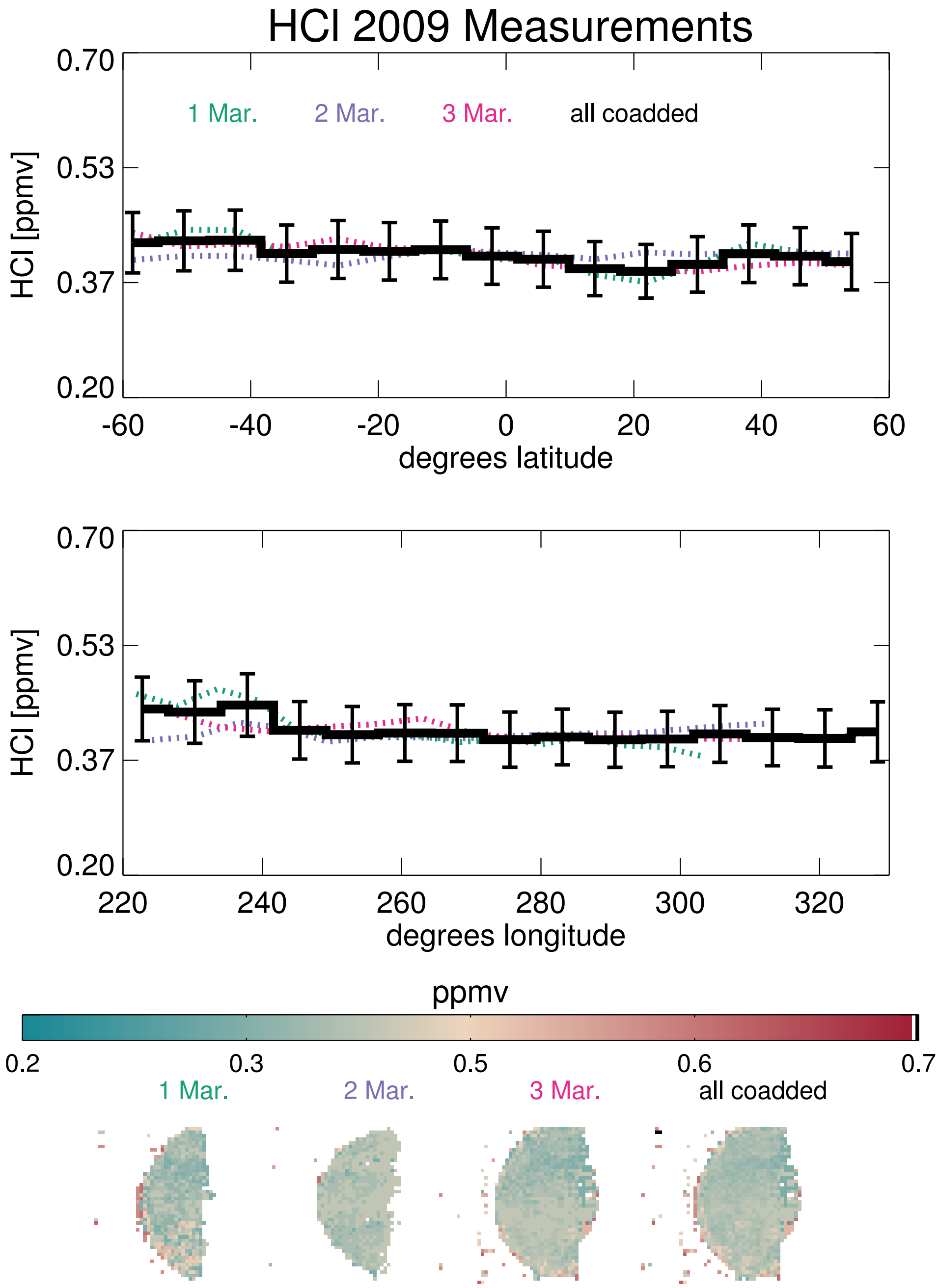

Figure 4.17: HCl measurements in 2009.

Above the cloud deck on the Venus day side, Iwagami et al. (2008) measured 0.74±0.06

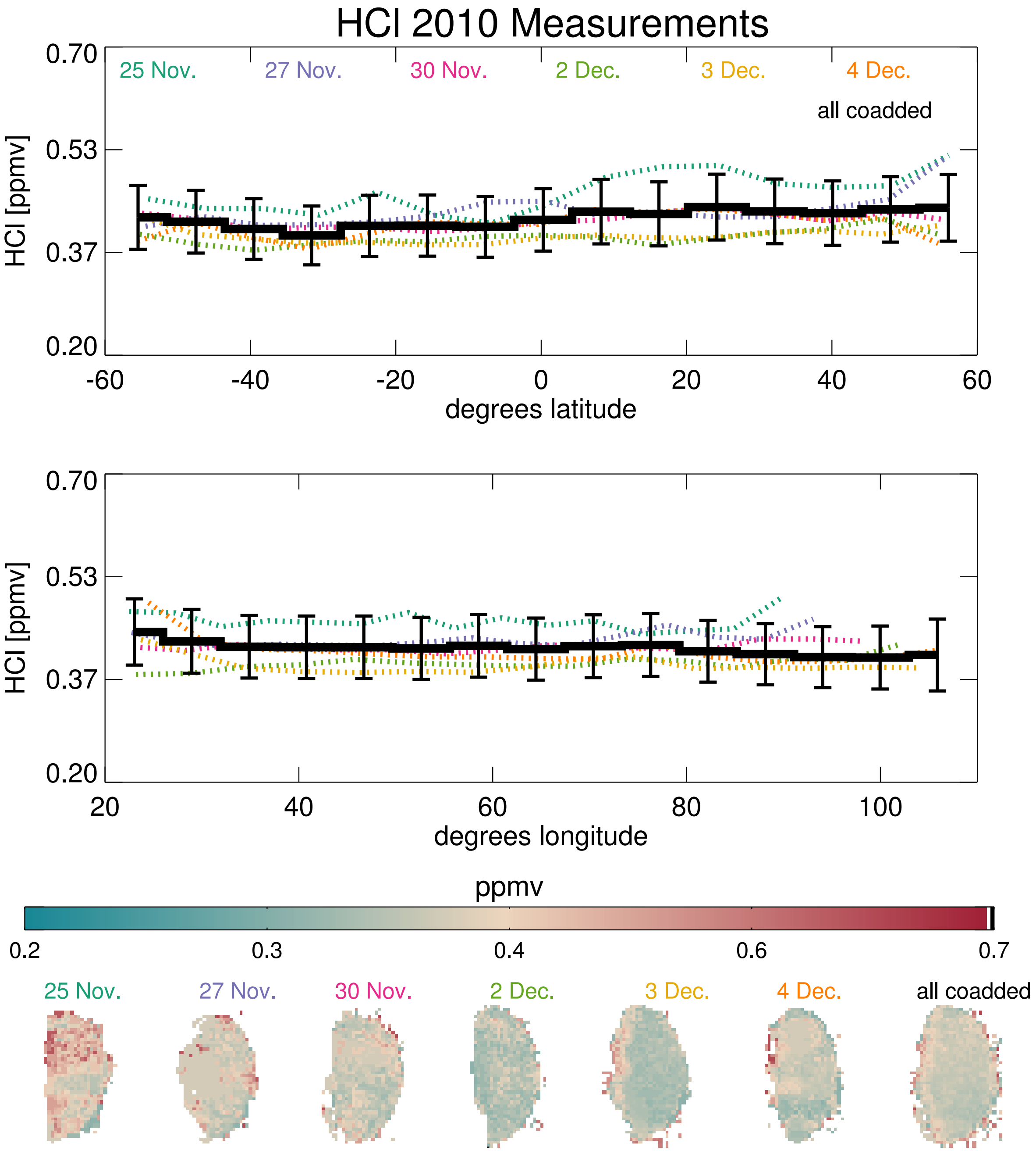

Figure 4.18: HCl measurements in 2010

ppm HCl, suggesting a strong source of HCl in or above the clouds. However, more recent work measured HCl at 0.40±0.03 ppm above the clouds (Krasnopolsky, 2010a), which is consistent with a uniformly mixed profile. The constancy of HCl measurements over the past 20 years suggests that the HCl abundances at these altitudes are equilibrium values not controlled by outgassing or atmospheric cycling.

4.4.3.e CO in the 2.8 μm window

Existing studies indicate that the CO mixing ratio is not constant with height in the lower atmosphere (Pollack et al., 1993; Tsang et al., 2008b, 2009; Barstow et al., 2012): between roughly 30 and 40 km, the amount of CO increases with height. OCS has been found to decrease with height at these same altitudes, and chemical models indicate that these vertical gradients can be understood as a conversion between these species (Krasnopolsky, 2007; Yung et al., 2009). Because the CO mixing ratio is not constant in the lower atmosphere, we must report our measured abundance at a specific altitude. Here, we report our CO abundance measurements at 35 km and adopt the nominal CO atmospheric profile of Cotton et al. (2012).

For our observations in 2009 and 2010, we measure mean values of 25±3 and 22±2 ppm, respectively, across the planet. Within 20° of the equator, we measure an average of 22±2 ppm (2009) and 19±2 ppm (2010). Above 50°N, we measure on average 37±4 ppm (2009) and 25±3 ppm (2010); below 50°S, the average is 29±3 ppm (2009) and 31±3 ppm (2010). Figures 4.19 and 4.20 show our CO maps.

CO is produced above 60 km in the atmospheric column via the photodissociation of CO_2 and possibly through the reaction $CO_2 + SO_2 + h\nu \longrightarrow CO + SO_3$ (Krasnopolsky, 1986). Subsidence at approximately 60° N and S associated with equator-to-pole circulation is thought to carry the freshly produced CO to the lower atmosphere (Collard et al., 1993). As CO circulates towards lower latitudes in the lower atmosphere, it is converted back to CO_2 and into sulfur species such as OCS (Marcq et al., 2005; Krasnopolsky, 2007). Consistent with previous studies (Marcq et al., 2006, 2008; Tsang et al., 2008b, 2009; Cotton et al., 2012), we find that CO abundance is enhanced near the cold collar at 60° N and S and less abundant towards the equator.

There are three interesting things to note from our 2009 CO measurements. First,

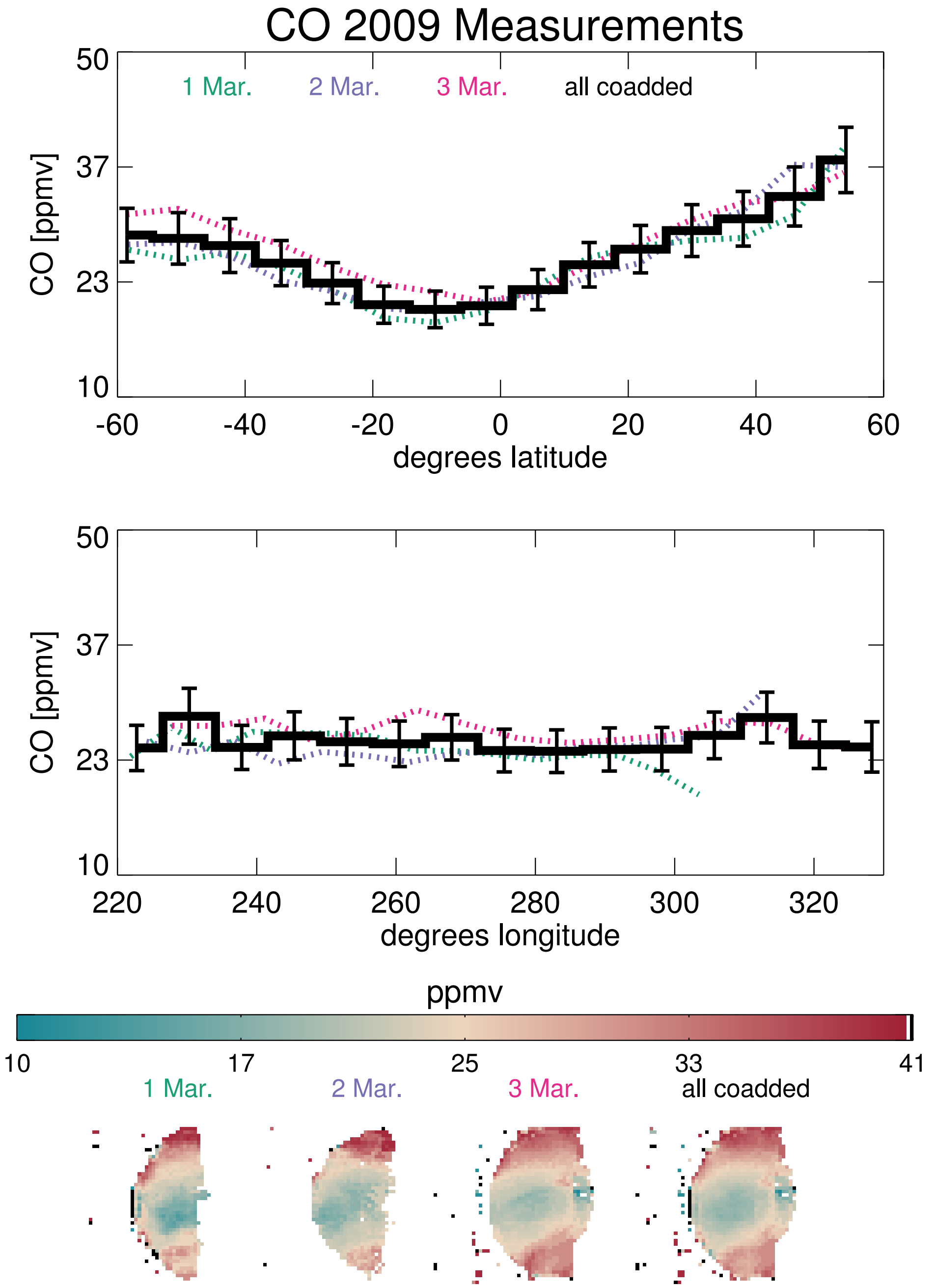

Figure 4.19: CO measurements in 2009. We see evidence of more CO in the northern hemisphere than the southern hemisphere.

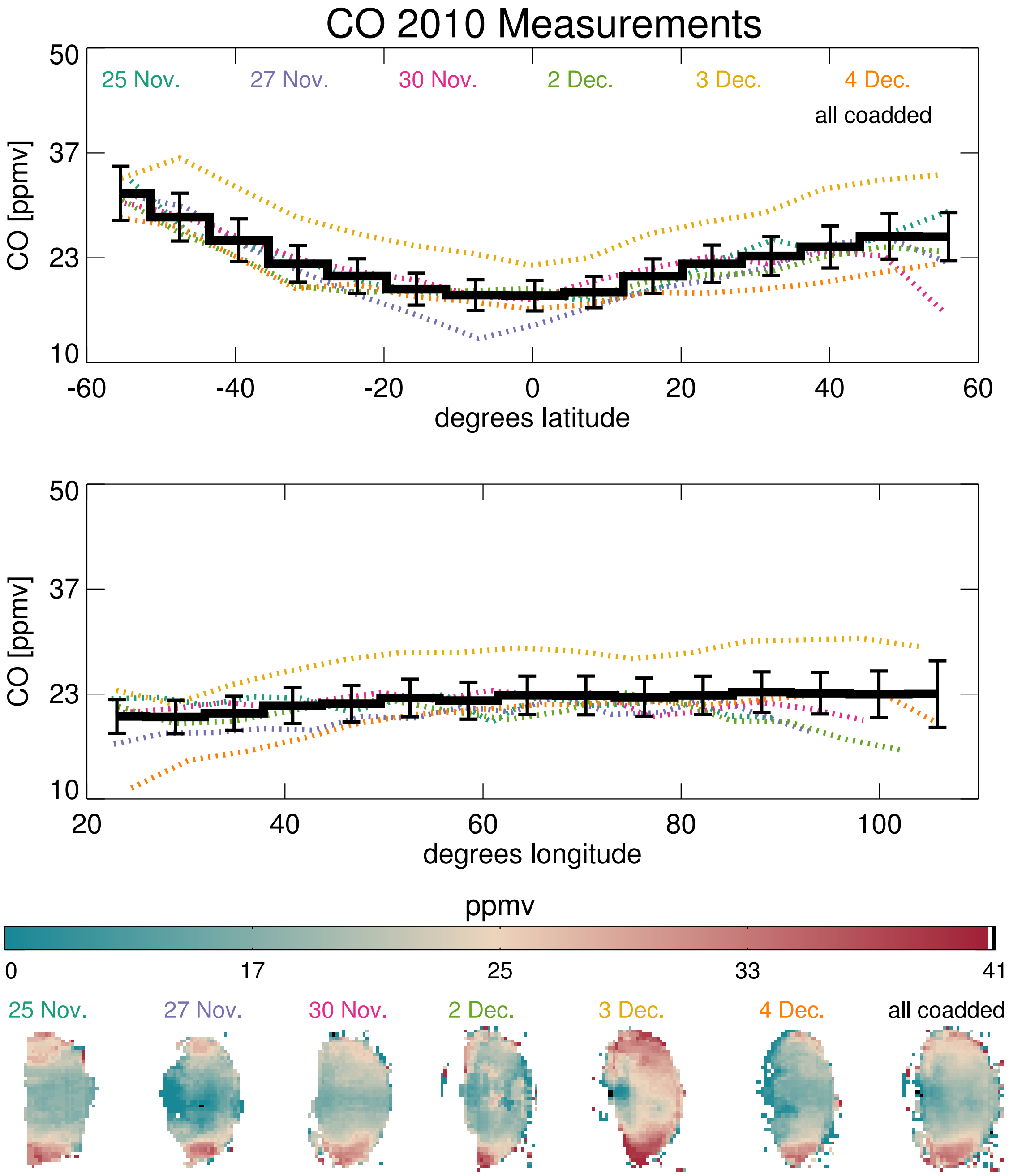

Figure 4.20: CO measurements in 2010. There is more CO in the southern hemisphere, a reversal of the 2009 hemispherical dichotomy.

the lower latitude minimum in 2009 is shifted south of the equator but appears to drift northwards over each night (this is similar to the drift seen in the water vapor bands at the same latitudes, discussed in Section 4.5). The minimum on 1 March is centered near 10-20°S, and by 3 March, it is centered just south of the equator. 20°S is similar to the latitude of the CO minimum observed by Marcq et al. (2008). Second, a hemispherical dichotomy may be present. The 2009 dataset has approximately 25% more CO in the north than the south. Collard et al. (1993) similarly measured 35% more CO in the north than the south, although Tsang et al. (2009) pointed out that the Collard et al. (1993) measurement technique may be susceptible to contamination from cloud opacity. Cotton et al. (2012) also found evidence of a higher amount of CO in the north than the south. Third, our time series of data suggests that the mixing ratio of CO near the downwelling branch of the southern Hadley cell may increase between 1 March and 3 March by roughly 14%. In addition, we find that between 1 March and 3 March, the amount of CO near the low latitude minimum increases by roughly 17%. Meanwhile, near 60°N, the CO amount declines by about 10% from the first night to the third. These changes in the distribution of CO may be related to fluctuations in atmospheric circulation patterns.

The 2010 dataset indicates that there is about 20% more CO in the south than the north, a reversal of the hemispherical dichotomy seen in the 2009 data. The enhancement of CO in the south compared to the north is consistent with the findings of Tsang et al. (2009) and Marcq et al. (2006), both of which observed evidence of more CO in the south than the north. In Cotton et al. (2012), although more CO was observed in the north than the south over the whole dataset, annual time variable trends may be present. Maps produced in July 2004 appear to have more CO in the north than the south, but maps from December 2005 seem to have roughly equal amounts in each hemisphere (11 December is an exception which may have more CO in the south). In 2007, the north once again appears to have more CO than the south. Figures 9 and 10 in Cotton et al. (2012) display these measurements. Taken together with previous studies, our measurements between 2009 and 2010 may be consistent with an oscillatory hemispherical dichotomy, but more work must be done to understand the cause of the dichotomy and the timescales and mechanisms involved in its apparent reversals.

In addition to the hemispherical dichotomy, we observe variations from night-to-night in the amount of CO in 2010. Consistent with our findings, Tsang et al. (2009) similarly observed marked daily variations. For example, our observations from 3 December show about 20% more CO than the other nights in 2010. The preceding night in our dataset, 2 December, also has patches of elevated CO in the equatorial region compared to the poles. It is unclear whether these are real features or whether an unknown source of contamination (e.g. cloud ghosting) is artificially enhancing the amount of CO in these maps. Cotton et al. (2012) also measured one night with anomalously high CO compared to preceding nights in their dataset (4 December 2005) and attributed the enhanced CO mixing ratio to possible contamination from crescent light.

Cotton et al. (2012) argued that the bulk of the variations in CO abundance may not occur near 35 km, where the measurements are most sensitive to these variations. Instead, these authors suggest that the data are better explained by variations higher in the atmosphere, near 45 km. To calculate the abundance of CO assuming variations near 45 km, we follow the approach used by Cotton et al. allowing CO variations above 40 km and holding the abundance profile fixed below 40 km using the same nominal profile as those authors. If CO variations above 40 km rather than near 35 km is responsible for the spatial variations of this gas, more CO is needed to produce spatial variations in the observed spectrum, since the sensitivity of the spectrum to CO at 40 km is less than that at 35 km. Assuming the “Cotton profile”, we estimate a mean value of 74±12 ppm in 2009, and 65±8 in 2010 with nearly identical spatial distribution patterns. We mention these measurements for comparison with the discussion in Cotton et al. (2012). For the rest of this paper, we assume the measurements given by our nominal profile as stated in the beginning of this section.

4.4.3.f OCS in the 2.3 μm window

Like CO, OCS is a spatially variable species. Spatially resolved estimates of OCS are shown in Figures 4.21 and 4.22. We report our measurements at 36 km to facilitate comparisons with Marcq et al. (2006). We measure overall averages of 0.44±0.10 ppm (2009) and 0.57±0.12 ppm (2010) across the observable night side. The mean values within 20 degrees of the equator are 0.54±0.13 ppm (2009) and 0.61±0.12 ppm (2010). The mean values in the northern hemisphere are 0.51±0.11 ppm (2009) and 0.60±0.12 ppm (2010); in the southern hemisphere, we measure 0.48±0.10 ppm (2009) and 0.48±0.08 ppm (2010). The 2010 hemispherical dichotomy is strongest in our observations from 30 November and 2 December. Krasnopolsky (2010b) measured OCS abundance in the southern hemisphere to be 25% lower than in the northern hemisphere, although these measurements were made at the cloud tops. Marcq et al. (2006) found depletion of OCS below 40°S in the lower atmosphere possibly correlated with a CO increase. CO-OCS anticorrelation is discussed in Section 4.5.

Previous studies such as Pollack et al. (1993) suggest that the atmospheric mixing ratio of OCS has a steep negative abundance gradient as altitude increases. The steep gradient in OCS between roughly 30 and 40 km has been attributed to reactions of OCS with sulfur species to produce CO (Krasnopolsky, 2007). Marcq et al. (2006) show that the shape of the spectrum in the OCS absorbing region is more strongly dependent on the OCS gradient than the OCS abundance, suggesting that it is easier to constrain the OCS gradient than the OCS abundance if the gradient and abundance are varied simultaneously (the opposite is found for CO: the spectrum is more sensitive to CO's abundance than gradient). Here, we are more interested in mapping the distribution of OCS than its gradient. However, we do estimate the gradient in order to create OCS profiles for quantifying the abundance.

To estimate the OCS gradient, we create a 2D grid of several hundred synthetic spectra in which OCS abundance and gradient between 30 and 40 km are treated as free parameters and both varied. Then, the best-fit synthetic spectra are determined for each pixel in our data cubes, and the gradient is estimated as the mean of our array of best-fit gradient values. Overall, we measure an average gradient of -0.51±0.22 ppm/km in 2009 and -0.42±0.10 ppm/km in 2010 for the OCS slope at 33 km. For comparison, Marcq et al. (2006) measured an average slope of -0.28±0.1 ppm/km at 36 km, and Pollack et al. (1993) measured -1.58±0.30 ppm/km. We assume that the gradient is constant across the planet for each set of observations in the measurements presented here. A discussion of measurements in which the gradient and abundances are simultaneously treated as free parameters is found in Section 4.5.

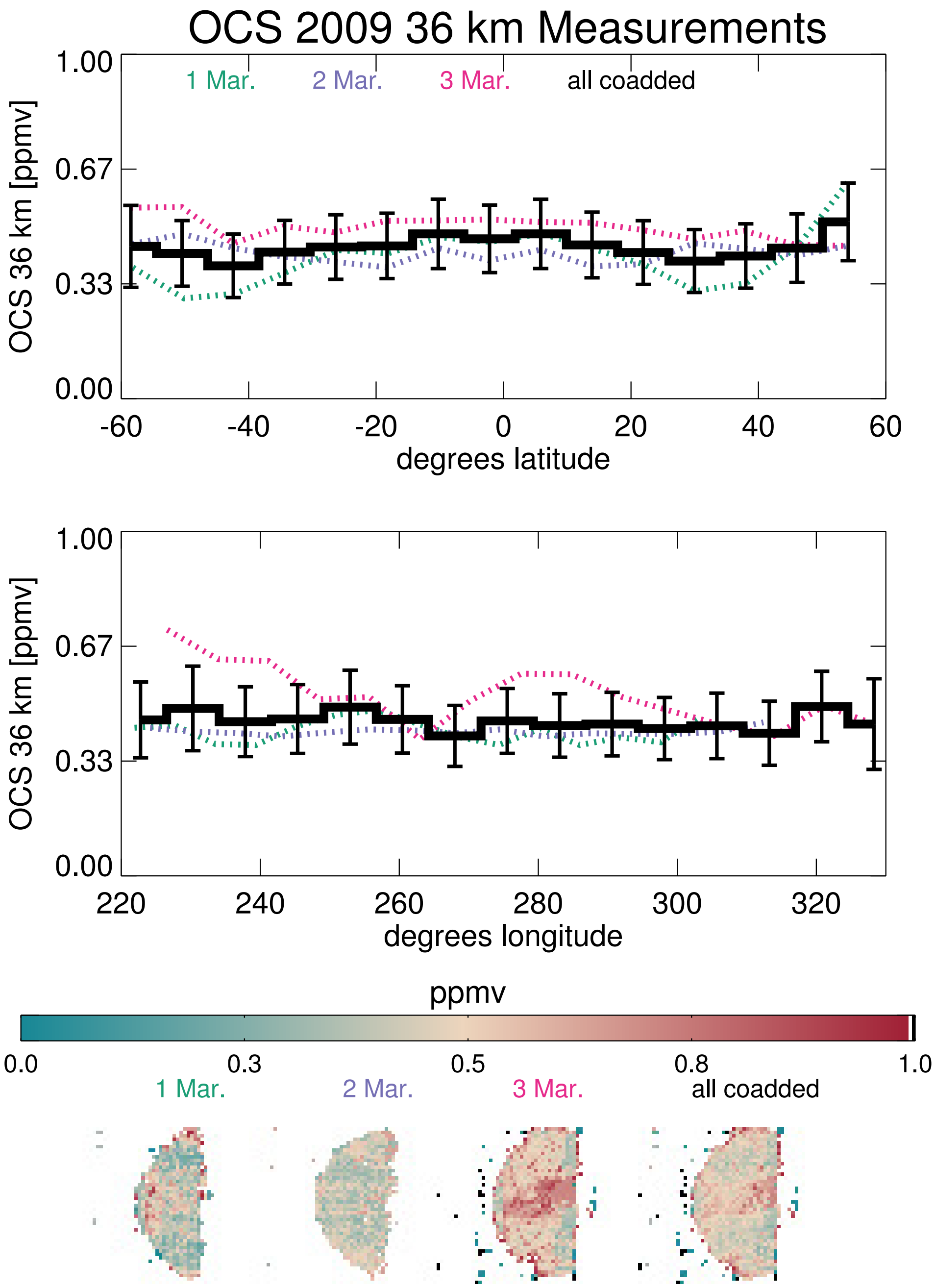

Figure 4.21: OCS measurements in 2009. On 3 March, the equatorial enhancement of OCS anticorrelates with the equatorial depletion in CO.

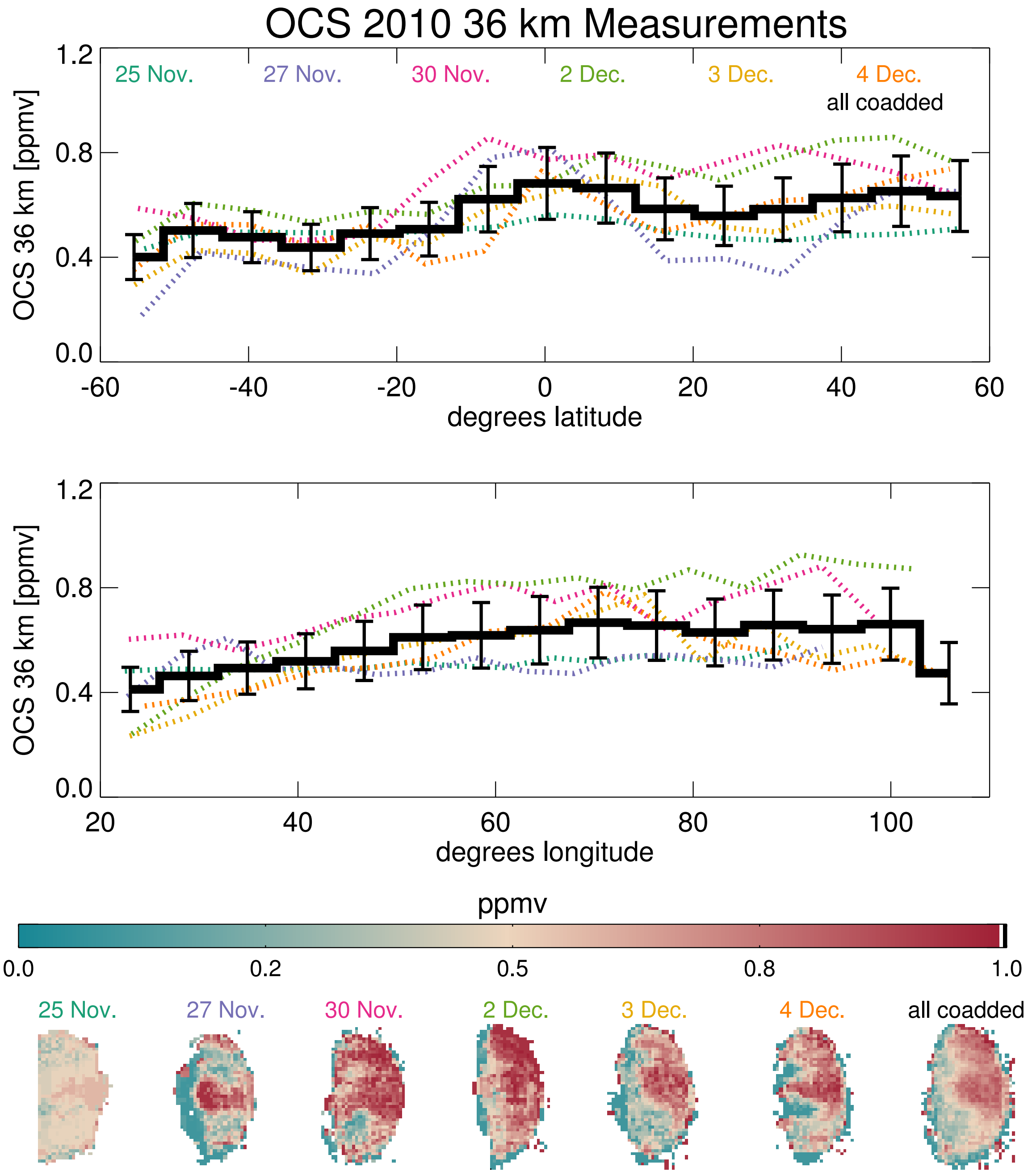

Figure 4.22: OCS measurements in 2010. We see higher amounts of OCS near the equator and north of the equator.

Tsang et al. (2008a) show that the spectral region where OCS is measured can be affected by changes in the temperature structure. We attempted to correct for latitudinal temperature profile variations using the temperature structure versus latitude information given in Seiff et al. (1985), but a symmetric treatment of the temperature structure on either side of the equator does not remove the hemispherical dichotomy we see here.

4.4.3.g *SO_2 in the 2.3 μm window*

Sulfur dioxide (SO_2) is the dominant sulfur species in the Venusian atmosphere. The mixing ratio of SO_2 varies on decadal timescales above the cloud tops (Marcq et al., 2012). This is most likely attributable to long term variations in atmospheric dynamics, although volcanic injections of SO_2 cannot be ruled out. SO_2 may therefore be an important tracer of cyclical variations in the atmosphere of Venus.

Maps of SO_2 are given in Figures 4.23 and 4.24. SO_2 is difficult to measure since it is active in a narrow spectral range near the long wavelength cutoff of our spectrograph's sensing region. In our 2009 observations, we estimate an average value of 140±37 ppm across the planet. Within 20 degrees of the equator, we estimate 130±35 ppm. In the northern hemisphere, the average value is 156±42 ppm, and in the southern hemisphere, it is 135±36 ppm. This potential hemispherical dichotomy may actually result from cloud ghosting or other biases as discussed in Section 4.5. In 2010, we measure 126±32 ppm on average, 130±33 ppm near the equator, 142±36 ppm north of the equator, and 108±27 ppm south of the equator. The equatorial, northern, and southern values for SO_2 agree within the quoted error bars, but these error estimates have a large contribution from systematic effects (approximately two-thirds of the SO_2 error bars), so the relative error between these latitude regions is smaller.

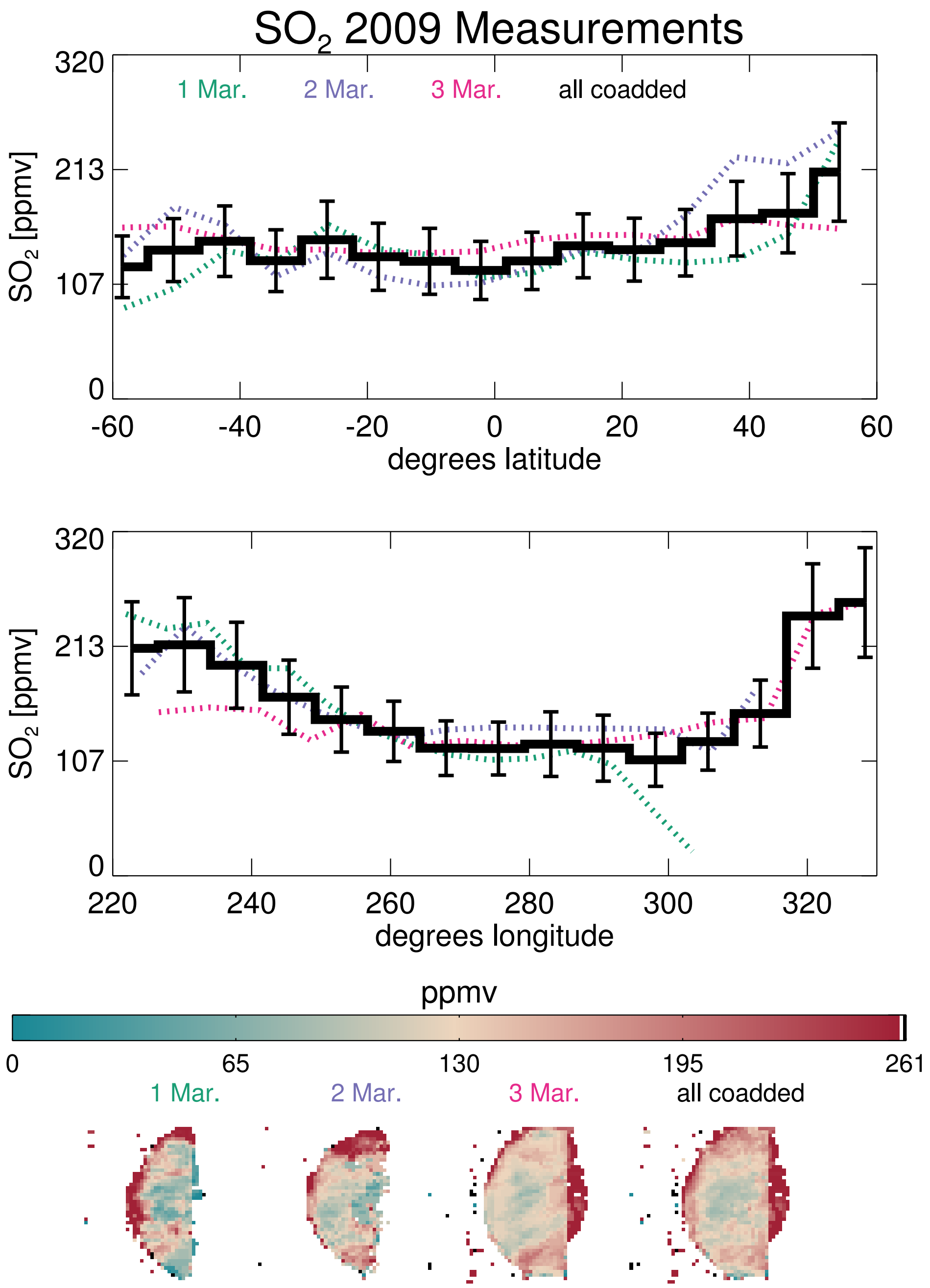

Figure 4.23: SO$_2$ measurements in 2009.

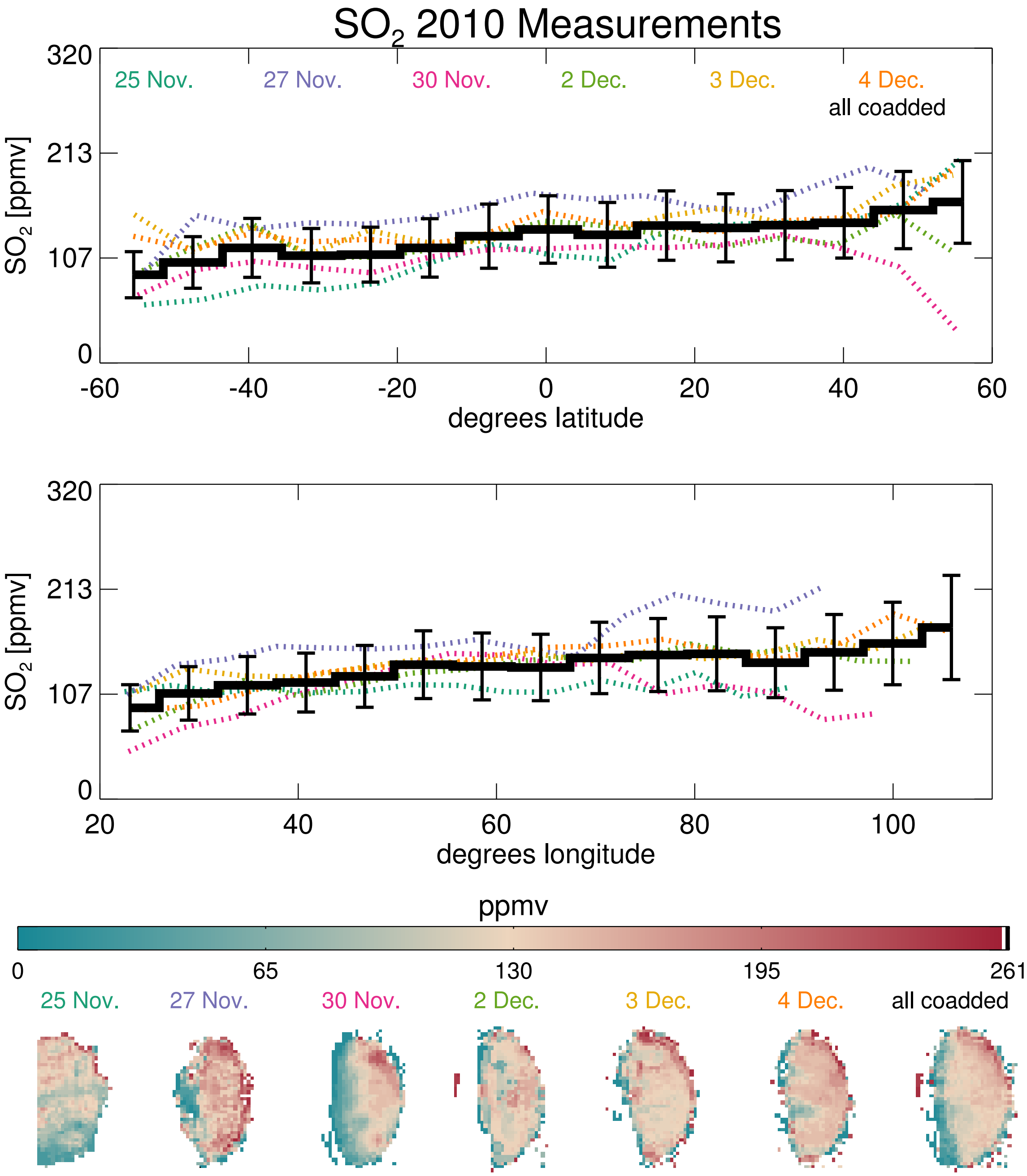

Figure 4.24: SO$_2$ measurements in 2010. There may be a hemispherical dichotomy of more SO$_2$ in the north.

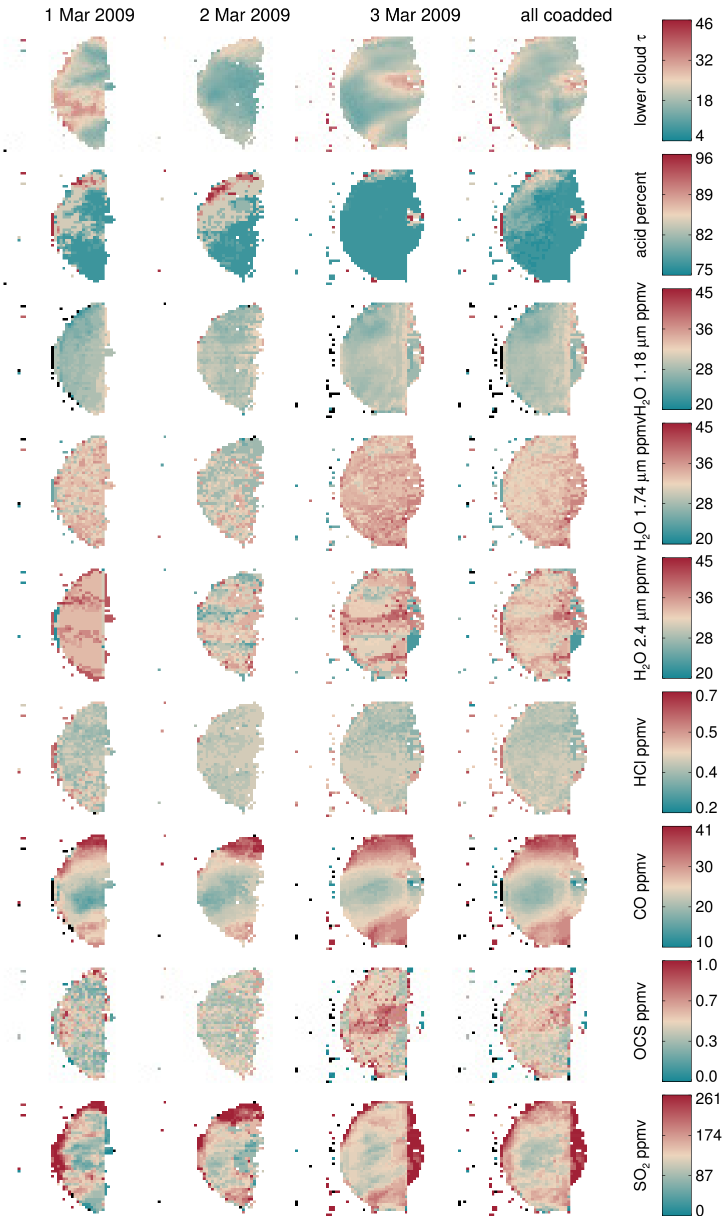

Figure 4.25: All 2009 maps.

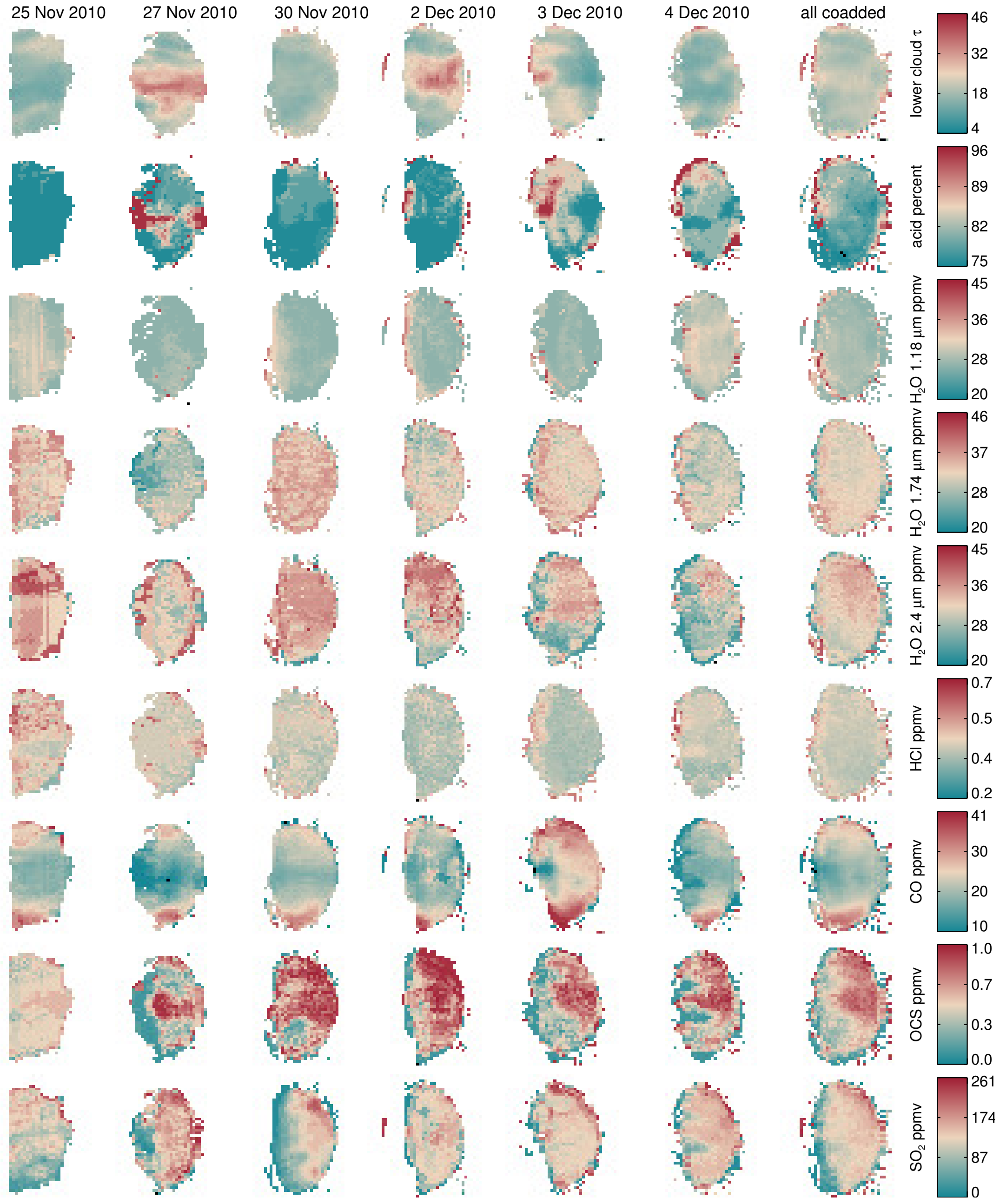

Figure 4.26: All 2010 maps.

4.5 Species Interrelationships

This study is the first to observe J-H-K-band range simultaneously to produce maps of cloud opacity, acid concentration, water vapor, HCl, CO, OCS, and SO_2. We therefore have the unique opportunity to search for correlations and temporal variations between these species, which can trace the chemistry and dynamics of the lower atmosphere.

4.5.1 Average Measurements

A summary of our average measurements are presented in Table 4.7. In general, the year-to-year variations are no greater than those seen on any one night. The greatest change is seen in OCS. Despite the constancy of the average measurements, we see significant spatial variations for species in the 2.3 μm window suggesting a dynamic sub-cloud region.

4.5.2 Cloud-Acid-Gas Correlations

Barstow et al. (2012) found a strong correlation between sulfuric acid content and cloud opacity such that acid percentage decreases as cloud opacity decreases (using 1.74 μm radiance as a proxy for cloud opacity). We find that there are several places in our acid maps where this trend occurs (acid maps are given in Figures 4.9 and 4.10; cloud opacity maps are given in Figures 4.7 and 4.8). On the 27 November 2010 map there is a band of thick clouds across the equator; co-located is a region with high acid concentration. The high cloud opacity feature near the equator on 2 December is partially mirrored by the patches of higher acid concentration, although the correlation here is much weaker than on 27 November. On 3 December a patch of low-opacity clouds near the northwestern limb of the planet is roughly spatial coincident with a patch of low acid concentration, although the region of low acid concentration is more centered on the equator than the region of thin clouds. Also on 3 December, a region of higher acid concentration near the crescent in the northern hemisphere overlaps with a region of modestly elevated cloud opacity. Similarly, the equatorial "finger" of thin clouds on 4 December corresponds to a "finger" of low acid concentration. The correlation coefficients between the cloud and acid maps across the whole surface are: no correlation on 25 November, $r = 0.46$ (27 November), 0.22 (30 November),

Table 4.7: A summary of our average measurements in the Venus near-infrared spectral windows

Species	2009 Average (ppm)	2010 Average (ppm)
Lower cloud optical depth	21±2	20±2
H_2SO_4 concentration	79%±3%	79%± 4%
H_2O (1.18 μm)	29±2	27±2
H_2O (1.74 μm)	33±2	32±2
H_2O (2.4 μm)	34±2	33±3
HCl	0.41±0.04	0.42±0.05
CO (35 km)	25±3	22±2
OCS (36 km)	0.44±0.10	0.57±0.12
SO_2	140±37	126±32

0.24 (2 December), 0.29 (3 December), 0.21 (4 December).

Although some regions on the Venus disk have cloud-acid correlations in 2010, we find that this correlation is not universal in our dataset. This is particularly evident in the 2009 maps in which there are no obvious spatial mappings between acid and cloud maps except possibly the "fingers" of thin cloud in the northern hemisphere on our 1 March maps that may correspond to a region of low acid and thus follow the expected trend. These ground-based observations, at higher spectral resolution (R = 3500) than the Venus Express data used by Barstow et al. (2012) (R∼100-600) do not corroborate the strong correlation seen between cloud opacity and acid content. However, Barstow et al.'s Venus Express data were at higher spatial resolution (50-100 km compared to our effective resolution of 300 km) and it is possible that the cloud-acid correlation is more apparent on smaller spatial scales than we can resolve.

Previous studies (Tsang et al., 2010; Barstow et al., 2012) have also reported an anti-correlation between cloud opacity and the water vapor mixing ratio, and one earlier study found a very high amount of K-band (2.3 μm) water vapor in a region of thin clouds (Bell et al., 1991). Anticorrelation between cloud optical thickness and water vapor may be due to the to break down of cloud particles into water vapor below the cloud deck via $H_2SO_4 \longrightarrow SO_3 + H_2O$ (Krasnopolsky, 2007). In this case, optically thin clouds indicate cloud dissolution and therefore enhanced water. Tsang et al. (2010) Section 6 provides a discussion of several possible mechanisms for cloud-water anticorrelation. The Tsang et al. results, however, may be contaminated by cloud ghosting, as the authors point out that the retrieved abundance of water is sensitive to the imaginary coefficient of the cloud particle refractive index, but 75% sulfuric acid is assumed for all acid cloud particles. As we noted previously, improved measurements of the indices of refraction at varied H_2SO_4/H_2O concentrations would be greatly beneficial to studies such as these. Barstow et al. (2012) also found that regions with very thick clouds have less water vapor in the 2.3 μm window, although the Barstow study did not show a correlation between water vapor and thinner clouds in our measurement region as noted by Tsang et al. (2010). We also note that optically thick clouds can mask higher water vapor mixing ratios below the clouds, and cloud emission can partially fill H_2O lines, further reducing the retrieved H_2O abundance.

We also searched for cloud opacity-water abundance anticorrelations, and some features on our maps suggest this, but the anticorrelation is less pronounced than the results of Tsang et al. (2010). On 27 November, there is a patch of depleted water vapor near the equator spatially coincident with the thickest clouds. Conversely, the feature of thick clouds on 2 December does not correlate with a region of depleted water as might be expected if this species was strongly anticorrelated to the cloud optical depth. The night of 3 December has approximately 30% less water south of 20°S compared to the rest of the planet, and the shape of the enhanced water vapor region in the northern hemisphere is similar to the thin cloud feature on this night.

Although the regional cloud opacity-water vapor anticorrelation was somewhat weak, we observed a marked hemispherical dichotomy in sulfuric acid, water vapor and sulfur dioxide that may be related to cloud dissolution processes. Our maps indicate higher aerosol sulfuric acid concentration in the northern hemisphere, and in 2010, a higher water vapor and sulfur dioxide abundance in the northern hemisphere also. It is not clear why there is more H_2SO_4 in the northern hemisphere. One way to increase the acid concentration of a droplet is to expose the particles to a low relative humidity environment. If the particles partially evaporate (but do not break down) and release some of the dissolved water to the environment, higher-concentration H_2SO_4 particles can result.

One possible mechanism for the water vapor dichotomy is virga. Quasi-periodic episodes of H_2SO_4 virga (rain that evaporates before reaching the ground) have been postulated to occur just below the Venusian lower cloud deck every few Earth months (Gao et al., 2014). If virga occurred in the northern hemisphere shortly before or during our 2010 observations, this may explain why 2010 has a water vapor dichotomy: H_2SO_4 falling in 2010 would enrich the northern hemisphere with water vapor as the H_2SO_4 breaks down into H_2O and SO_3. We might expect markedly less optically thick clouds in the regions of enhanced water vapor (if these are truly regions of cloud dissolution), but because there is a vertical shear in the Venusian winds at these altitudes, the lower altitude regions (with enhanced water) may become decoupled from the higher altitude cloud pattern. The Pioneer Venus probes measured winds of roughly 30-50 m/s between 30-40 km (Counselman et al., 1980), and lower latitude winds in the middle cloud deck have been measured at 60-70 m/s (Crisp et al., 1991b; Sánchez-Lavega et al., 2008).

In the lower atmosphere, SO_3 (a product of the thermal decomposition of H_2SO_4) can produce SO_2 (Krasnopolsky, 2007), so the SO_2 dichotomy we see in 2010 may also be linked to this postulated virga event. Also, on our 3 December maps, we point out that the two spots of enhanced SO_2 in the northern hemisphere towards the crescent are spatially coincident with regions of enhanced acid concentration (although not enhanced water vapor as well). Other areas of enhanced SO_2 do not show any obvious correlation to the acid maps, but a region of enhanced SO_2 near the equator on 2 December is coincident to a region of thick cloud. The SO_2 hemispherical dichotomy is variable and is particularly evident on 25 November, which shows a clear depletion in the southern hemisphere compared to the north. The hemispherical dichotomy in 2010 seems unrelated to cloud ghosting as it does not correlate to the cloud pattern.

There are problems with virga as the explanation for the northern 2010 hemispherical dichotomies we see. When a 75% H_2SO_4 droplet evaporates, it should produce a molecule of H_2O and 0.75 molecules of SO_2. In 2012, we see a dichotomy of 5-10 ppm of H_2O and 34 ppm of SO_2, If virga is part of the mechanism for the hemispherical dichotomies we see, there evidently must be an additional source enhancing SO_2 possibly relating to atmospheric circulation patterns as has been suggested for enhanced SO_2 in the upper atmosphere (Marcq et al., 2012).

Another problem with the virga explanation is the change in H_2O and SO_2 abundances that can be reasonably expected from cloud dissolution. Esposito et al. (1983) gives a column mass of 0.012 g/cm^2 for the cloud deck, which provides an upper bound for the number of cloud droplets that can be dissolved during virga events. Assuming 75% sulfuric acid droplets, this column mass corresponds to 1.1×10^{20} molecules/cm^2 of H_2O and 0.8×10^{20} molecules/cm^2 of SO_2. Compared to the atmospheric column at 30 km near where H_2O is measured (1.4×10^{26} molecules/cm^2) and at 40 km where SO_2 is measured (6×10^{25} molecules/cm^2), the maximum increase in the mole fraction at these levels is on the order of 1 ppm for both H_2O near 30 km and SO_2 at 40 km. This is much less than the observed variations. However, our results do suggest that higher opacity clouds are not unusual, so it is possible that a virga event from very thick clouds (3-4 times our nominal opacity such as the equatorial band on 27 November) could produce H_2O enhancement closer in agreement to our observations. Although we do not see a correspondence between thick clouds and the enhanced water hemispherical dichotomy, as discussed above, wind shear can decouple the higher altitude cloud pattern from lower atmospheric patterns. The amount of SO_2, however, still far exceeds what is reasonable from virga. We suggest that future studies of Venus' hemispherical dichotomies with finer temporal resolution and more extended temporal coverage than this study provides may help to clarify the timescales of the dichotomies and the mechanisms that produce them.

SO_2 is strongly correlated with the cloud maps in 2009, but these correlations are positive rather than negative as we might expect if optically thin clouds are regions of cloud dissolution. However, it is possible that the 2009 SO_2 maps are contaminated by residual cloud ghosting. SO_2 is measured near the long wavelength edge of the K-band window (near 2.5 μm), and cloud opacity has a pronounced wavelength-dependent impact on the spectrum here. The difficulties of removing cloud-ghosting patterns from our SO_2 maps are compounded by its relatively weak spectral signal. On the other hand, since Venusian cloud particles are comprised of H_2SO_4 droplets formed from photochemical reactions in-

Table 4.8: A summary of observed hemispherical dichotomies

2009 dominant in N	2009 dominant in S	2010 dominant in N	2010 dominant in S
CO	None	H_2SO_4 concentration	CO
H_2SO_4 concentration		Water	
SO_2? (probable cloud ghosting)		OCS	
		SO_2	

volving SO_2, it is possible the 2009 SO_2 maps illustrate a physical mechanism related to cloud droplet formation. Still, cloud ghosting is the most conservative explanation.

In addition to spatial variations in acid, H_2O, and SO_2 that may correlate to cloud processes, we see spatial variations in CO correlated to cloud patterns. Barstow et al. (2012) found a decrease in CO abundance in areas where the clouds have high opacity. This may be attributed to atmospheric upwelling in regions of thick clouds since CO is less abundant deeper in the atmosphere. We find a similar correlation for the band of high opacity clouds across the equator on 27 November 2010, which is closely coincident to a region of very low CO abundance. CO in this region reaches as low as 10 ppm, whereas the equatorial average is almost twice as much. However, 2 December similarly has thick equatorial clouds, but regions near the equator have elevated CO amounts compared to the poles.

4.5.3 An Overview of Hemispherical Dichotomies

The hemispherical dichotomies described above in Section 4.5.2 may be related to atmospheric circulation patterns, H_2SO_4 precipitation, and/or hemispherical differences in chemical reactions. Table 4.8 lists the observed hemispherical dichotomies. Here, we summarize the dichotomies and possible mechanisms for their formation.

In 2009, there is a hemispherical dichotomy with more CO and H_2SO_4 in the north. The small SO_2 dichotomy we see is likely a product of cloud ghosting. There is no apparent dichotomy in OCS or H_2O in 2009. The CO dichotomy in 2010 is the opposite of that in 2009 with more CO in the south. Anticorrelated to this are dichotomies in H_2O, OCS, H_2SO_4, and SO_2, all of which are more abundant in the north.

As discussed in Section 4.5.2, virga events are a possible cause of the water vapor and SO_2 dichotomies in 2010, although this mechanism is not consistent with typical clouds as discussed above.

The 2010 dichotomies of CO and OCS are the opposite of each other. These species are thought to be chemically connected in Venus' lower atmosphere, so their anticorrelated dichotomies may be related. If virga is actually occurring in Venus' atmosphere, the net result according to Krasnopolsky (2007) is

$$\mathrm{H_2SO_4 + 2\,OCS \longrightarrow H_2O + CO_2 + CO + SO_2 + S_2}$$

This would enhance H_2O and SO_2 in the north as expected (although the expected magnitude of this increase from virga is much smaller than we see as discussed in Section 4.5.2). However, this mechanism would also remove OCS in the northern hemisphere and increase CO, which is the opposite of the trend we see. Yung et al. (2009) argue that the Krasnopolsky (2007) models rely on reactions not validated by laboratory studies and suggest the scheme $\mathrm{2\,OCS \longrightarrow 2\,CO + S_2}$ for the destruction of OCS initiated by photolysis of S_n by long wavelength photons below the cloud deck. If this mechanism is more important than the Krasnopolsky scheme in the Venus atmosphere, then OCS should not be strongly affected by any enhancement of H_2SO_4 and may still anticorrelate with CO, but H_2O and SO_2 will still be enhanced as mentioned.

We favor the production of the excess northern OCS higher in the atmosphere (near the bottom of the cloud deck) rather than towards the surface. If the excess OCS were produced near the surface, it would need to be upwelled into the altitudes sensed by the 2.3 μm window in order to be detected. We also favor the production of the excess OCS higher in the atmosphere (near 37 km) rather than near the surface because a test varying the OCS gradient (ppm/km) and abundance simultaneously produces maps of the OCS distribution in which the hemispherical dichotomy is stronger near 37 km than near 30 km: the northern enhancement is 20% at 37 km and only 6% in our 30 km maps, further suggesting that the source of the OCS dichotomy is high in altitude. This was done by treating the OCS mixing ratio at 30 km and at 40 km as free parameters and assuming a linear slope in mixing ratio between these two altitudes (as we did in Section 4.4.3.f to estimate the OCS gradient).

The latitudinal distribution of CO in the lower atmosphere is thought to be strongly driven by atmospheric circulation patterns, so it seems likely that circulation patterns must be a component of the CO dichotomy (and likely also the OCS dichotomy since it is chemically linked to CO). Future work must be done to better understand the causes of the patterns we see.

Seasonal hemispherical dichotomies have been seen on other solar system bodies (e.g. Saturn as discussed by Sinclair et al. (2013)), although the root cause of the dichotomies on Venus are less clear as Venus' axial tilt is a mere 3° and seasonal effects should be minor. Nevertheless, changes in Venus' atmospheric circulation have been observed in other studies: SO_2 amounts in the upper atmosphere may periodically increase due to upwelling from the lower atmosphere (Marcq et al., 2012), upper-atmosphere SO_2 diurnal variations may be present (Sandor et al., 2010), cloud-top wind speeds have been observed by Venus Express to steadily increase between 2006 and 2012 (Khatuntsev et al., 2013), and periodic long-term oscillations of winds in the atmosphere have been reported based on tracking cloud motions (Kouyama et al., 2013). However, it is important to note that there is little or no direct evidence of dynamical changes below the cloud deck, because we have no direct measurements besides the profiles measured by entry probes.

4.5.4 Banding and North-South Motion in 2009

Our 2009 water maps display an unexpected latitudinal banding pattern (Figure 4.15). The enhancement of water vapor in the bands is 3-6 ppm. These bands are not present in the maps of other species (including the species measured adjacent to water vapor in the 2.3 μm spectral window), and there are no similar features in our maps of the cloud opacity or acid concentration. Since the pattern is unique to this species, it seems unlikely that the bands result from spectral contamination from another species. Like the hemispherical dichotomies, virga rainout over several ranges of latitudes is a possible cause of the banding, although the observed increase of 3-6 ppm in the bands implies that the clouds producing the potential virga must be denser than previous constraints for this mechanism to be viable. The H_2SO_4 would decompose to H_2O, and the Venusian zonal winds would produce quasi-zonal bands, shearing out the virga products.

The banding pattern appears to be shifting latitudinally from night-to-night: the prominent low-latitude band of enhanced water vapor abundance is centered near 10-20°S on 1 March and appears to have shifted to the equator by 3 March. This matches the position and drift rate seen in the CO low latitude minimum mentioned in Section 4.4.3.e. If we assume constant motion from 10-20°S to 0° from the first date to the last, this roughly corresponds to a northward motion of 6-12 m/s for the H_2O and CO minima. These values are significantly slower than the east-west wind velocities measured by the Pioneer Venus probes at 30-40 km in altitude of roughly 30-50 m/s (Counselman et al., 1980), but they are generally much higher than measured meridional wind speeds. Meridional wind flows have been measured in the middle and lower cloud region to be less than 5 m/s (Counselman et al., 1980; Sánchez-Lavega et al., 2008), and Carlson et al. (1991) measured the poleward high altitude meridional flow as 6.5 ± 4.5 m/s. Another, more direct, measurement of the middle cloud meridional winds was done by the VEGA balloons (Crisp et al., 1990), and even smaller meridional winds near the equator were measured (0.2 ± 1.3 to 2.5 ± 1.2 m/s). The much longer data sets described by (Crisp et al., 1991b) found no meridional motion, and placed an upper limit of 0.5 m/s. If the apparent motion we see is related to meridional flow, its velocity is much higher than most previous constraints.

We might expect the banding pattern to be present in the H- and J-band maps (1.74 and 1.18 μm, respectively), but the conclusion consistent with our J-H-K band water comparisons from both years is that water vapor variations in the 2.3 μm window do not persist lower into the atmosphere. This supports the idea that the variations originate at the cloud base and are dispersed zonally by the strong vertical shear long before they can reach altitudes detected in the H- and J-windows. We might also expect to see the same pattern in our SO_2 maps since SO_3 produced by H_2SO_4 should break down to SO_2, but if our interpretation of cloud ghosting contaminating our 2009 SO_2 maps is correct, the ghosting may wash out any banding pattern. Also, as discussed in Section 4.5.2, virga rainout should produce SO_2 variations much smaller than the limits of our SO_2 error bars.

4.5.5 CO-OCS Anticorrelation

Anticorrelation of the longitudinally-integrated latitudinal distributions of OCS and CO in the lower atmosphere has been previously reported (Marcq et al., 2005, 2006, 2008), and these anticorrelations are seen in some of our observations. The distributions of CO and OCS near 35 km are controlled by chemistry and transport processes mentioned in Section 4.5.3 in the context of anticorrelated CO-OCS hemispherical dichotomies.

In 2009, the equatorial region of enhanced OCS on 3 March appears to be anticorrelated with the region of CO depletion. Observations on 1 and 2 March show little spatial variability, though there may be a very slight equatorial enhancement on 1 March. In our 2009 observations, the only night with a prominent low-latitude enhancement of OCS (3 March) is also the night with the most equatorial CO. In 2010, most nights have a region of elevated OCS near the equator anticorrelated with depletion in CO. We also find more CO in the southern hemisphere than the northern one in our 2010 observations, and OCS has the opposite trend as discussed in Section 4.5.3.

4.5.6 Volcanism

With the arrival of Venus Express in 2006, searches for volcanism on the Venusian surface have been undertaken (e.g. Shalygin & Basilevsky, 2012), and some of these searches have been fruitful (see Chapter 1). Water vapor is expected to be a component of volcanic outgassing on Venus (Kumar et al., 1983; Grinspoon & Lewis, 1988). Therefore, if a volcanic eruption occurred during our observations, an injection of water vapor into the atmosphere would likely result. As discussed in Section 4.4.3.c, there are spatial variations in the water vapor maps of the K-band spectral region (near 2.3 μm), but these variations are unlikely to be due to volcanism because they are not matched by variation in the 1.18 μm window, which probes surface and near-surface water abundance and should therefore be most sensitive to surface-level injections.

Volcanoes should produce SO_2 and volcanic ash in addition to H_2O. All three would produce distinct spectral signatures. An ash cloud at levels above a few km in altitude would produce a dark feature resembling a mountain. However, the feature would move with the prevailing winds and not necessarily be taken out by the cloud screen. We do not see evidence for volcanism of this sort.

4.6 Concluding remarks

In this chapter, we presented the first simultaneous, spatially-resolved measurements and maps of H_2O, HCl, CO, OCS, CO_2, cloud opacity, and acid concentration in the Venus near-infrared spectral windows. These measurements show that the Venus lower atmosphere is complex and dynamic with changes occurring on short timescales. Venus scientists should rest assured that understanding the causes of the sometimes surprising variability and patterns seen here will require additional measurements and modeling efforts that should keep us busy for many years to come.

Observing Venus provides us a glimpse of the likely future of Earth: as the sun grows brighter, Earth will someday enter a runaway greenhouse state, losing its water to space, and may start to look more like Venus' twin than merely her sister. Venus and Earth may have started off more like twins early in their history, too. If Venus was able to support liquid water early in our solar system's history when the sun was fainter, it is just possible that a second origin of life occurred there that has since been lost to a hellish history of almost complete desiccation and catastrophic global resurfacing events. In the next chapter, I will discuss early Earth during the Archean geological period (3.8 - 2.5 billion years ago) when our planet's anoxic atmosphere may have occasionally hosted a global organic haze. Maybe – just maybe – early Venus was similar.

Chapter 5

THE PALE ORANGE DOT: THE SPECTRUM AND HABITABILITY OF HAZY ARCHEAN EARTH

Portions of this chapter were originally published in collaboration with S. D. Domagal-Goldman, V. S. Meadows, et al. in the journal *Astrobiology* (Arney et al., 2016, *Astrobiology*, ©2013 Mary Ann Liebert, Inc.), and are reproduced below with the permission of Mary Ann Liebert, Inc.

5.1 Introduction

As we discussed in Chapter 1, early in Earth's history, an anoxic atmosphere could have supported the formation of an organic haze (Pavlov et al., 2001b; Trainer et al., 2004, 2006; DeWitt et al., 2009; Hasenkopf et al., 2010; Zerkle et al., 2012; Kurzweil et al., 2013; Claire et al., 2014; Izon et al., 2015) that strongly interacted with visible and UV radiation, cooling the planet's climate (Pavlov et al., 2001a; Haqq-Misra et al., 2008; Domagal-Goldman et al., 2008; Wolf & Toon, 2010; Hasenkopf et al., 2011). This hydrocarbon haze, generated by methane (CH_4) photolysis, would have formed when the ratio of CH_4 to carbon dioxide (CO_2) in the atmosphere exceeded about 0.1 (Trainer et al., 2006).

Unlike the hazes that may exist around exoplanets with thick hydrogen-dominated atmospheres (Sing et al., 2011; Kreidberg et al., 2014; Knutson et al., 2014a), the Archean (3.8-2.5 billion years ago) haze was likely biologically-mediated via CH_4 produced from methanogenesis, one of the earliest metabolisms (Woese & Fox, 1977; Ueno et al., 2006). In addition, several abiotic processes including serpentinization (the hydration of ultramafic rocks, mainly olivine and pyroxenes) can form methane (Kelley et al., 2005; Guzmán-Marmolejo et al., 2013; Etiope & Sherwood Lollar, 2013), but the biotic flux of methane to the Archean atmosphere was likely much higher than the abiotic flux (Kharecha et al., 2005), as it is on Earth today. While the climatic effects of this haze have been studied (e.g. Pavlov et al. 2001a), impacts of haze on Archean Earth's habitability have not been previously investigated using tightly coupled climate-photochemical models. This coupling is critical to consider because of potential feedbacks between the impact of temperature on haze formation and the effects of haze on the atmosphere's temperature structure. Additionally, although we anticipate planetary diversity in the exoplanet population, existing spectral studies are largely focused on the observables of modern day Earth (e.g., Sagan et al., 1993; Woolf et al., 2002; Robinson et al., 2011, 2014a). Those spectral studies that consider Archean Earth and anoxic planets have not examined hazes (Meadows, 2006; Kaltenegger et al., 2007; Domagal-Goldman et al., 2011). As we will show, hydrocarbon haze has profound spectral impacts for both reflected light and transit transmission spectra.

5.1.1 Evidence for an Archean Haze

Geochemical data suggest 3-5 distinct intervals of organic haze during the later Archean (Zerkle et al., 2012; Izon et al., 2015), supporting theoretical studies on the causes and consequences of photochemical haze formation in the atmosphere (Pavlov et al., 2001b,a; Haqq-Misra et al., 2008; Domagal-Goldman et al., 2008; Kurzweil et al., 2013; Claire et al., 2014) as well as experimental data (Trainer et al., 2004, 2006; DeWitt et al., 2009; Hasenkopf et al., 2010, 2011) and theory on their potential radiative effects (Wolf & Toon, 2010). In addition, a recent study of micrometeorites suggests an oxygenated upper atmosphere at 2.7 billion years ago (Tomkins et al., 2016), and may suggest that a temperature inversion caused by an organic haze may have prevented an anoxic lower atmosphere and oxic upper atmosphere from mixing (however, this may be physically unrealistic as the temperature inversion in the current stratosphere does not prevent mixing on decadal timescales). The geochemical evidence for haze, described below, implies Neoarchean hazy intervals (Zerkle et al., 2012; Izon et al., 2015) lasting for less than 1 million years. The constraint on the duration of these intervals based on the lower limit of shale sedimentation rates. In addition, the modeling work of Domagal-Goldman et al. (2008) suggests a longer Meosarchean to Neoarchean hazy period between 3.2 and 2.7 Ga.

Here, we present an overview of the evidence for the Archean haze. The line of evidence most often invoked comes from analyses and modeling of sulfur isotope fractionation data from Earth's rock record. Several studies have proposed links between haze and the mass independent sulfur isotope fractionation signal (S-MIF) (Farquhar et al., 2000) preserved in the geologic record before the Great Oxygenation Event (GOE) at about 2.5 billion years ago (Ga) (Domagal-Goldman et al., 2008; Zerkle et al., 2012; Kurzweil et al., 2013; Claire et al., 2014; Izon et al., 2015). We present a brief review of this evidence here, beginning with an overview of sulfur mass-independent fractionation, on which much of the evidence for an Archean haze is based.

Sulfur has four stable isotopes: ^{32}S, ^{33}S, ^{34}S and ^{36}S. Isotope fractionations are reported in part per thousand (‰) using delta notation (δ) such that:

$$\delta^{x} S = \left[\frac{{}^{x}R_{sample}}{{}^{x}R_{standard}} - 1 \right] \times 10^{3} [‰] \tag{5.1}$$

Here, ^{x}R$_{sample}$ represents isotope ratios of the given minor to major isotope (for sulfur, ^{x}R means ^{x}S/^{32}S with x = 33, 34, 36) of sampled material. $^{x}R_{standard}$ represents isotope ratios of a standard reference material.

Reactions following classical equilibrium or kinetic behaviors produce isotope fractionation that depend only on the mass differences of the isotopes such that the δ^{33}S composition of a material is approximately half the δ^{34}S amount, and the δ^{36}S composition is roughly twice the δ^{34}S amount. For elements with more than two stable isotopes, mass dependent fractionation (MDF) quantifies this expected three-isotope relationship, and samples following MDF will have $\delta^{33}S \sim 0.515 \times \delta^{34}S$ and $\delta^{36}S \sim 1.89 \times \delta^{34}S$.

Mass-independent fractionation (MIF) occurs when samples deviate from this expected three isotope behavior and is quantified with "capital delta" notation where $\Delta^{33}S = \delta^{33}S - 0.515 \times \delta^{34}S$ and $\Delta^{36}S = \delta^{36}S - 1.89 \times \delta^{36}$S. MIF in naturally occurring samples is very unusual and is generally diagnostic of quantum chemistry such as can occur in certain atmospheric reactions. While the precise mechanism(s) that produce S-MIF are unknown, photolysis of sulfur gases in an anoxic atmosphere is the only known mechanism that produces large magnitude Δ^{33}S and Δ^{36}S seen in the rock record (Farquhar et al., 2001, 2007).

The S-MIF signal is variable throughout the Archean and it vanishes completely once

O_2 builds up to non-negligible levels in the atmosphere after the great oxygenation event (GOE) at 2.5 Ga. Its recurrence at both ends of the Archean Eon implies that, within 0.8 billion years of Earth's formation, a common mechanism for S-MIF production was already established in the atmosphere (Thomassot et al., 2015). After the GOE, O_2 and the ozone (O_3) derived from O_2 photochemical reactions block the UV photons necessary to photolyze sulfur gases and produce S-MIF. Also, S_8 can be the most important species to rain out S-MIF from a reducing atmosphere; because a more reducing atmosphere enhances the ability of S_8 to polymerize, S-MIF is more easily preserved under reducing conditions (Zahnle et al., 2006). After the GOE, all the sulfur in the atmosphere would have been oxidized into a single exit channel, eliminating any fractionation created in the atmosphere (Pavlov & Kasting, 2002). Thus, S-MIF is generally regarded as robust evidence for an anoxic Archean atmosphere.

$\Delta^{33}S$ typically correlates with enrichments in $\delta^{34}S$ and with depletions in $\delta^{36}S$, and variations in magnitude and sign of these isotopic signals in Earth's geologic record hint that strong constraints on Archean atmospheric chemistry will be possible when the precise S-MIF formation mechanisms are identified (Claire et al., 2014). $\Delta^{36}S/\Delta^{33}S$ in Archean sedimentary rocks is generally around -1, but stratigraphic variations in this slope have been observed in the geological record and interpreted as evidence of changes to the S-MIF production mechanism resulting from changes in atmospheric composition (Zerkle et al., 2012; Kurzweil et al., 2013; Izon et al., 2015), suggesting the influence of haze.

(Domagal-Goldman et al., 2008) and (Haqq-Misra et al., 2008) studied potential links between S-MIF, hazes, and Archean glaciation. At ~2.9 Ga, there is geological evidence suggesting a glaciation event (Young et al., 1998) may have occurred during the same period when the S-MIF $\Delta^{33}S$ signal dips to lower values. An upper atmosphere haze that decreased tropospheric SO_2 photolysis by blocking UV photons and cooled the planet could explain both the glaciation and the decrease in S-MIF. In this conceptual model, the end of the cold period typified by low $\Delta^{33}S$ may be due to a decrease in the atmospheric CH_4/CO_2 ratio, which would have cleared any haze present in the atmosphere. If true, this change in atmospheric composition and radiative scattering would have enabled UV photons to penetrate deeper into the atmosphere, interacting with sulfurous gases and affecting their isotopic signatures (Claire et al., 2014). Earth's record of sedimentary sulfides do show a significant change in their minor sulfate isotope behavior between 2.73 and 2.71 Ga (Kurzweil et al., 2013; Izon et al., 2015) that may in fact reflect this change, although predictive models of sulfur isotope fractionation are not yet able to reproduce these trends seen in the rock record (Claire et al., 2014).

Zerkle et al. (2012) discusses the discovery geochemical evidence consistent with the Archean haze hypothesis. The authors analyzed sediments aged 2.5-2.65 Ga collected from the Ghaap Group in South Africa and showed that variations of $\Delta^{36}S/\Delta^{33}S$ associated with changes in atmospheric chemistry were contemporaneous with highly negative excursions of $\delta^{13}C_{org}$ values. Negative values of $\delta^{13}C_{org}$ below -37 ‰are typically interpreted as evidence for methanogenesis (biological methane production) followed by subsequent incorporation into sediments by methanotrophy (methane consumption) which imparts a strongly negative $\delta^{13}C_{org}$ because organisms preferentially uptake the ^{12}C (Urey & Greiff, 1935; Schopf, 1983; Schidlowski, 2001; Eigenbrode & Freeman, 2006). The contemporaneous excursions of the sulfur and C_{org} isotopes suggests a close linkage between S-MIF signals and biogenic methane. The links between S-MIF signals and biogenic methane production have been recently expanded over multiple cores and locations, suggesting multiple changes in atmospheric chemistry during the Neoarchean (Izon et al., 2015). Changes observed in the slope of $\Delta^{36}S/\Delta^{33}S$ vary between -1.5 and -0.9 and are interpreted to reflect changes in the S-MIF source reactions driven by varying atmospheric haze thicknesses.

Kurzweil et al. (2013) note that an increase in magnitude of S-MIF signals after 2.73 Ga (Thomazo et al., 2009) occurred during a prolonged negative shift in $\delta^{13}C_{org}$, suggesting enhanced biological methane activity at this time. Similar to Zerkle et al. (2012), they discuss a change in the slope of $\Delta^{36}S/\Delta^{33}S$ from -1.5 to -0.9 at 2.71 Ga and interpret this to be caused by a decrease in the CH_4/CO_2 ratio at 2.71 Ga, possibly indicating an organic haze was present for some period of time prior to 2.71 Ga and cleared afterward. In this interpretation, haze-free and reducing atmospheric conditions dominated after 2.71 Ga, with haze reappearing in brief intervals of time as suggested by the Zerkle et al. (2012) and Izon et al. (2015) measurements.

Given the apparent occurrence of haze in the Archean according to these interpretations, we investigated the impact of this haze on the climate, spectral appearance and surface UV flux by simulating the hazy Archean environment with boundary conditions consistent with recent geochemical constraints. Unlike previous studies of the Archean climate under a haze, we use realistic fractal (rather than spherical) particles, which have different spectral properties and climatic effects. Our study also represents the first time temperature feedbacks have been investigated in relation to haze production in Archean Earth's atmosphere. Previous studies (Pavlov et al., 2001a; Haqq-Misra et al., 2008; Domagal-Goldman et al., 2008) involving climate modeling have included the haze's impact on temperature, but not corresponding temperature feedbacks on haze formation. Temperature feedbacks have significant impacts on the resultant hazes: as we discuss below, hazes produce stratospheric temperature inversions, and warmer atmospheres produce larger haze particles, so hazes generated by chemistry models without temperature feedbacks may not produce realistic results.

5.2 Model Inputs

We employ the `Atmos` model to generate self-consistent Archean atmospheres and hazes together with the `SMART` radiative transfer model to generate spectra of these worlds as discussed in Chapter 3.

In the photochemical model, we set a haze monomer density of 0.64 g/cm^3, which is consistent with the laboratory results of Trainer et al. (2006) for early Earth. This density is used in the model to calculate the masses of haze particles and is updated from the value of 1 g/cm^3 used by previous studies employing our photochemical model. Hörst & Tolbert (2013) measured a similar effective particle density, 0.65 g/cm^3, for a 0.1% CH_4 haze experiment using a UV lamp. 0.1% CH_4 is consistent with the atmospheres we simulate, although the Hörst & Tolbert (2013) hazes were Titan-analog simulants lacking the CO_2 present in the Trainer et al. experiments. We apply a Manabe/Wetherald relative humidity model for the troposphere (Manabe & Wetherald, 1967) with a surface relative humidity of 0.8 in both the climate and photochemistry models. This humidity parameterization is further described in Pavlov et al. (2000). Our Archean simulations use the solar constant at 2.7 Ga ($0.81 = S/S_0$, where S_0 is the modern solar constant and S is the solar constant at 2.7 Ga) modified by a wavelength-dependent solar evolution correction (Claire et al., 2012). We chose this time because it corresponds to the age of the constraints on CO_2 used by our study (Driese et al., 2011). We set the mixing ratio of O_2 at the surface to 1.0×10^{-8}, consistent with the Zerkle et al. (2012) study. These conditions reflect the time period after the evolution of oxygenic photosynthesis but prior to Earth's GOE in which substantial biogenic fluxes of both oxygen and methane would have vented into a predominantly reducing atmosphere (Claire et al., 2014). Unless otherwise specified, the surface albedo used by the climate model is 0.32. This includes the effect of clouds, which is standard in this 1D treatment (Kopparapu et al., 2013) and is the albedo that reproduces the average temperature of present day Earth (288 K) with modern atmospheric conditions. Of course, the true cloud distribution on Archean Earth is unknown, and clouds may have had important climatic effects on our early planet (Goldblatt & Zahnle, 2011). The solar zenith angles (SZA) used in the climate and photochemical models were chosen to best represent globally averaged behavior of the physics in each specific model, which Segura et al. (2003) finds as SZA = 45° in the photochemical model and SZA = 60° in the climate model. These zenith angles are both tuned to reproduce modern day Earth's average chemical profiles and climate, respectively, and SZA = 60° approximately simulates the global average heating.

For our `SMART` spectral simulations, our nominal spectra assume an ocean surface albedo (McLinden et al., 1997). In cases where an icy surface is used, we use an albedo from the USGS Digital Spectral Library (Clark et al., 2007). Our solar spectrum was modeled by Chance & Kurucz (2010), and was scaled by the solar evolution model (Claire et al., 2012) mentioned previously. The solar zenith angle is set at 60° for the reflection spectra, which approximates a planetary disk average near quadrature (planet half illuminated to the observer).

5.3 Results

In this section, we first describe the climate results from `Atmos`. Following this, we quantify the strength of a hazy UV shield for surface organisms, and we show and describe the spectral consequences of this haze in reflected light and transit transmission spectroscopy.

Recent paleosol measurements have constrained the CO_2 partial pressure (pCO_2) in the

Table 5.1: Atmosphere parameters for Cases A-D

	Case A	Case B	Case C	Case D
pCO_2 (bar)	0.01	0.018	0.01	0.0036
P_{surf} (bar)	1	1	0.5	0.5

Archean at 2.7 Ga to be between 0.0036-0.018 bars (10-50× the present atmospheric level (PAL)) (Driese et al., 2011). Estimates of Archean surface pressure (P_{surf}) are consistent with values as low as 0.5 bars (Som et al., 2012; Marty et al., 2013), although more recent estimates suggest even lower pressures (Som et al., 2016). We simulated four types of atmospheres that span these constraints to examine a range of conditions: $pCO_2 = 0.01$ and $P_{surf} = 1$ bar of total pressure (Case A), $pCO_2 = 0.018$ and $P_{surf} = 1$ bar (Case B), $pCO_2 = 0.01$ and $P_{surf} = 0.5$ bars (Case C), and lastly, $pCO_2 = 0.0036$ and $P_{surf} =$ 0.5 bars (Case D). These are summarized in Table 5.1. The haze thickness scales with the CH_4 abundance relative to CO_2, so we investigated a range of CH_4 levels for each of these atmospheres. In the sections below, we refer to these Case A-D planets. Figure 5.1 shows an example of the atmospheric profiles for several gases in atmospheres with two different CH_4/CO_2 ratios (0.1 and 0.2), plus the haze number density profiles scaled to fit on the same x-axis. The insignificant haze present in the $CH_4/CO_2 = 0.1$ atmosphere is spectrally indistinguishable from an atmosphere with no haze. The larger amounts of CH_4, C_2H_6, and H_2O at higher altitudes in the $CH_4/CO_2 = 0.2$ atmosphere illustrates how the haze can shield these gases from photolysis.

Our results presented here required about 60 `Atmos` model runs. In total, we ran about twice this number for model debugging and testing. Each coupled `Atmos` run can take between 3-15 hours depending on how many coupling iterations are required. Note that the runtime for the climate model scales nonlinearly with the number of radiatively active gases: a model run that takes less than 20 minutes without CH_4 or C_2H_6 will require well over an hour with both of these gases turned on. All of the results presented here, except as noted in Section 5.4, were generated with both CH_4 and C_2H_6.

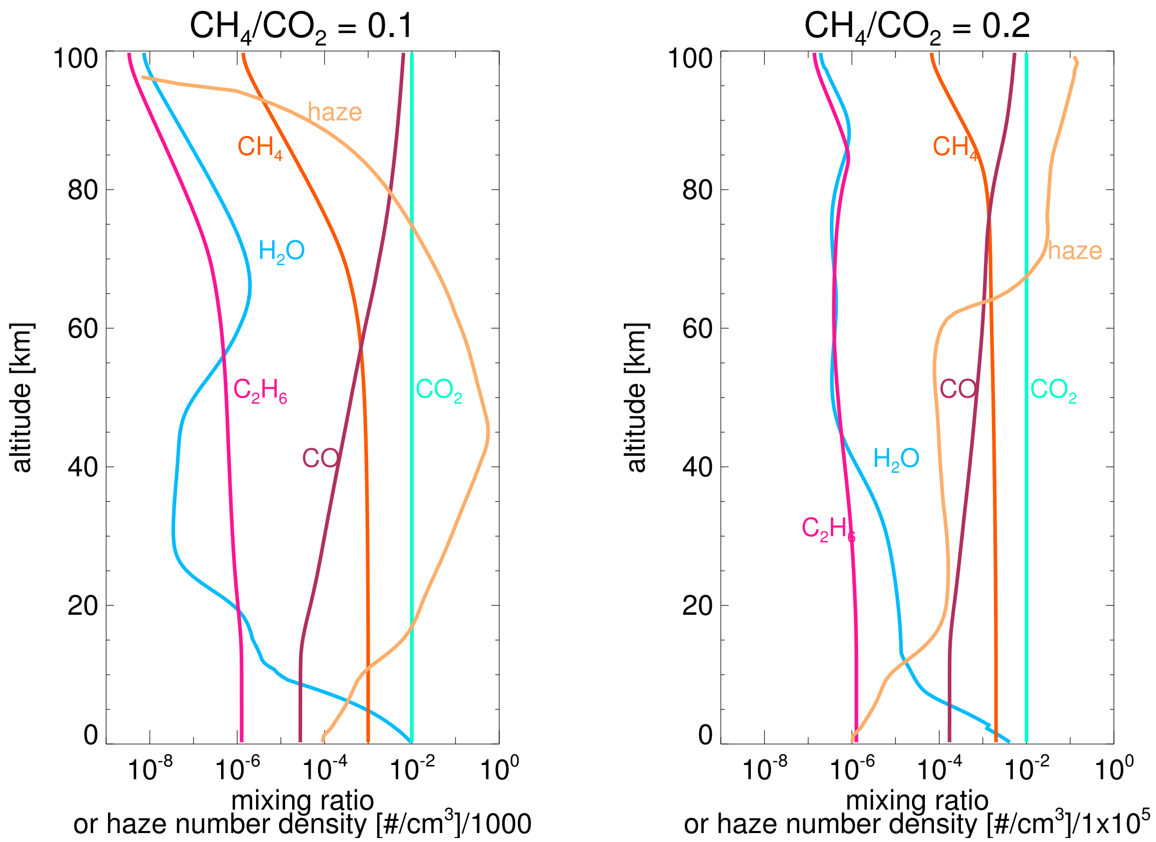

Figure 5.1: The gas profiles for H_2O, CH_4, CO, CO_2, and C_2H_6 for planets with $pCO_2 = 0.01$ bar for $CH_4/CO_2 = 0.1$ (on the left) and $CH_4/CO_2 = 0.2$ (on the right). Also shown are the profiles for the haze particle number density (in pale orange). The $CH_4/CO_2 = 0.1$ haze profile is divided by 1000 and the $CH_4/CO_2 = 0.2$ haze profile is divided by 1×10^5 in order to plot it on the same axis as the gases. The profiles in the right panel show larger amounts of CH_4, H_2O and C_2H_6 above 60 km in altitude, and illustrate how haze-induced shielding can prevent photolysis of these gases. The sharp decrease in haze particle number density between 60 and 70 km in the right panel shows where fractal coagulation occurs. The atmosphere above the fractal coagulation region is populated by spherical sub-monomer particles.

Note that in the context of the results presented here, a “thick” haze refers to the haze at a CH_4/CO_2 ratio ~ 0.2.

5.3.1 Hazy Climates

We find that hazy Archean climates were cold but most likely habitable (Figure 5.2). Previous 1D climate modeling efforts assumed that planets with globally averaged surface temperatures (T_{GAT}, which is equivalent to our 1D surface temperature, T_{surf}) below 273 K will experience runaway glaciation (e.g. Haqq-Misra et al., 2008; Domagal-Goldman et al., 2008). However, more recent 3D studies have shown that Archean Earth can maintain an open ocean fraction of $> 50\%$ for TGAT $\geq$ 260 K and an equatorial open ocean belt for $T_{GAT} \geq 248$ K (Wolf & Toon, 2013; Charnay et al., 2013). Furthermore, Abbot et al. (2011) argue that ocean open belts can remain climatologically stable, even if the ice latitude is reduced to 5-15°. Since a planet with any non-zero fraction of open ocean is habitable, we regard these updated globally-averaged temperatures – all of which are significantly below freezing – to be more realistic habitability thresholds than 273 K. We adopt $T_{GAT} \geq 248$ K as our habitability threshold here (Charnay et al., 2013).

Figure 5.2 shows that when haze reaches a threshold thickness, further increases in CH_4 result in rapid increases in haze thickness, and a corresponding steep falloff in surface temperature. However, at higher CH_4/CO_2 ratios, the haze thickness (and the surface temperature) stabilizes because UV self-shielding inhibits methane photolysis, shutting down haze formation. Thus, we find there is a maximum haze optical thickness – and a minimum temperature from haze-induced cooling – for each atmosphere. Interestingly, this negative feedback haze self-shielding appears to prevent catastrophic cooling. Note that even using the conventional habitability threshold of 273 K, Cases A-C have a hazy solution space where $T_{surf} > 273$ K, and Case B stabilizes at $T_{surf} = 274$ K with its thickest haze. Using the updated habitability threshold of $T_{surf} > 248$ K, all of our cases even with thick hazes are habitable (Charnay et al., 2013). Table 5.2 summarizes these results and includes a sensitivity test of the ice-albedo effect, described below.

Although the cold climates we have simulated are "habitable" in the sense that they have open ocean, a cold climate with extended ice caps ($T_{surf} < 273$ K) from a thick haze may be consistent with a reported glaciation event at 2.9 Ga (Young et al., 1998) as a previous study has suggested (Domagal-Goldman et al., 2008). Later purported hazy periods around

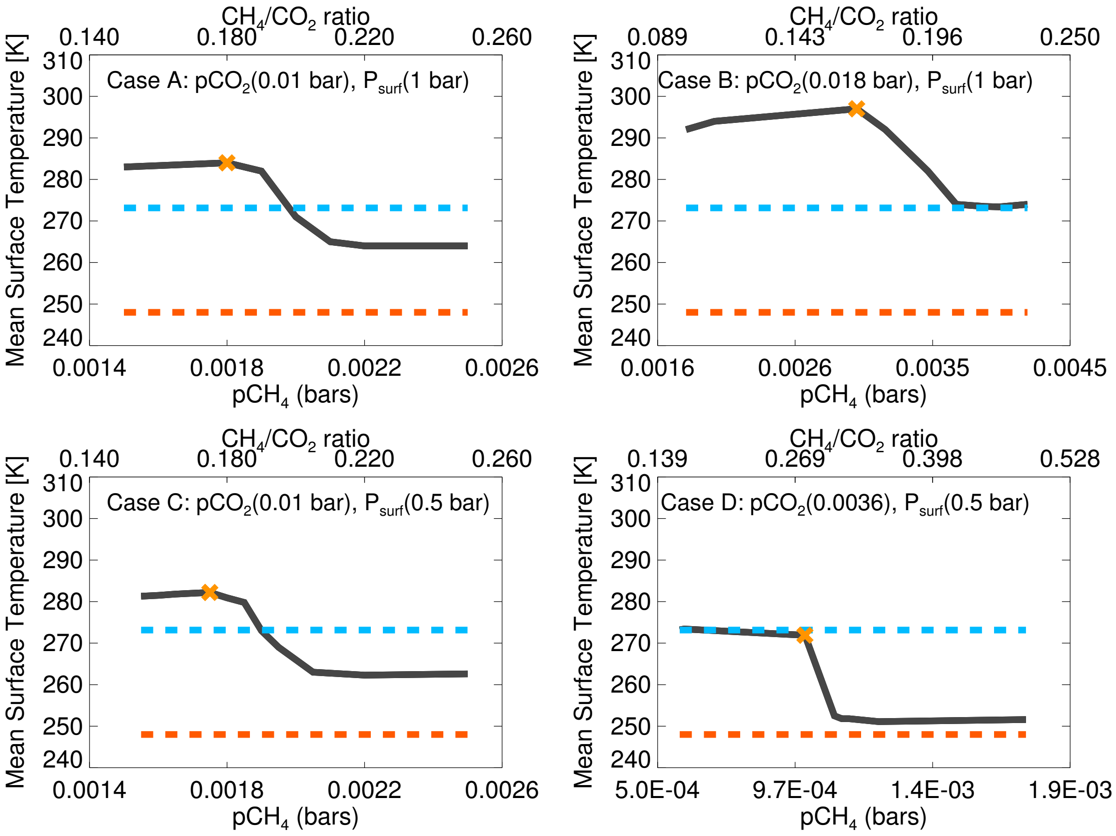

Figure 5.2: Mean surface temperatures as a function of CH_4 for Archean cases A-D. The dashed blue line shows the freezing point of water (273 K) and the dashed orange line marks our lower threshold of habitability (248 K) for an equatorial ocean belt (Charnay et al., 2013). The "X" in each panel indicates the initiation of haze-induced cooling.

2.7 Ga (Kurzweil et al., 2013; Izon et al., 2015) and between 2.65-2.5 Ga (Zerkle et al., 2012) are not associated with glaciations and may be consistent with the thinner-haze solution space of Cases A and C or even the thickest haze solution space of the warmer Case B.

5.3.1.a Ice-Albedo Feedback

To test how ice-albedo feedbacks can affect our retrieved temperatures, we tested the influence of these feedbacks on the minimum temperatures reached by our four Cases by parameterizing our model's 1D surface albedo (A) by the relation (based on the results of

Table 5.2: Temperature results for Cases A-D

	CH_4/CO_2 to initiate formation	Maximum T_{surf} without haze (K)	Stabilized T_{surf} with haze (K)	T_{surf} with ice-albedo feedback (K)
Case A	0.18	284	263	257
Case B	0.15	299	274	271
Case C	0.19	282	262	257
Case D	0.28	273	251	241

Charnay et al. (2013)) to include the albedo effect of clouds and ice as a function of the globally averaged temperature:

$$A(T_{GAT}) = 0.65 + (0.3 - 0.65) \times (\frac{T_{surf} - 240}{290 - 240})^{0.37} \tag{5.2}$$

As stated above, the surface albedo used by our nominal model is 0.32. The surface albedos for the Case A, B, C, and D minimum temperatures with this ice-albedo parameterization are 0.39, 0.35, 0.39, and 0.45. The climate model was run to convergence starting with the solution for the minimum stabilized temperature for each Case (i.e. when the haze becomes self-shielding and reaches maximal thickness) as a test of the sensitivity of our minimum temperatures to ice-albedo feedbacks. The temperatures of planets A, B, C, and D with ice albedo feedbacks are 257 K, 271 K, 257 K, and 241 K, a decrease of 3 to 10 K compared with simulations with the nominal albedo. The Bond albedos produced in these cases including haze are 0.26, 0.24, 0.26, and 0.29.

These ice-albedo temperatures may be under-estimates because once haze forms, deposition of dark hydrocarbons onto ice-covered areas will lower the albedo of the ice. This decreased ice albedo may then melt the ice, reverting parts of the surface back to ocean water. Because haze absorbs strongly at blue wavelengths, the radiation that reaches the surface under a haze would have a higher proportion of longer, redder wavelengths compared to shorter, bluer wavelengths. While ice is very reflective at visible wavelengths, it becomes more absorbing at wavelengths > 0.7 μm, changing the true ice-albedo parameterization. Because of this, planets orbiting stars emitting a high proportion of radiation at near-infrared wavelengths are harder to freeze (Shields et al., 2013). Additionally, stratospheric and mesospheric circulation patterns on Earth presently impact high-altitude aerosol distributions by transporting particles preferentially to the poles (Bardeen et al., 2008). In this case, the climatic impact of haze could be reduced with warmer surface temperatures at the equator. On the other hand, hazes can also act as cloud condensation nuclei, enhancing cloud formation (Hasenkopf et al., 2011). This might lead to cooling of the planet or even warming depending on cloud particle size and the altitude – and therefore temperature – of the cloud layer (Goldblatt & Zahnle, 2011). A complete treatment of the impact of ice-albedo feedback, haze deposition, haze circulation, and cloud feedbacks is left to future GCM studies better equipped to deal with these inherently 3D issues.

5.3.1.b Temperature Feedbacks on Haze Production

As the haze gets optically thicker, absorption of UV photons produces an atmospheric temperature inversion (Figure 5.3) similar to that produced by ozone in the modern atmosphere. We find there is a relationship between the size of the haze particles generated and the temperature of the atmosphere. To isolate the effect, we tested haze production by the photochemical model using two completely isothermal temperature profiles of 200 K and 250 K with all other parameters held constant (Figure 5.4). The largest particles produced by the 250 K atmosphere have a geometric radius of 0.8 μm compared to 0.65 μm radius particles for the 200 K atmosphere. In the photochemical model, when the coagulation timescale (τ_{coag}) is shorter than the timescale for removal in an atmospheric layer, the particles can grow. As temperature increases, τ_{coag} decreases since particles moving faster collide more frequently (Tolfo, 1977). In the hotter atmosphere, τ_{coag} is smaller than τ_{sed} through most of the atmospheric column.

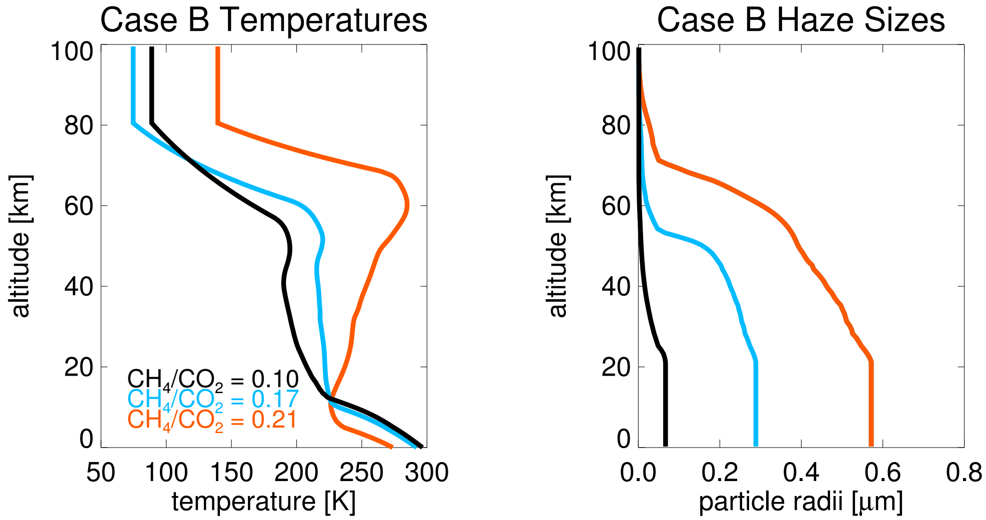

Figure 5.3: The left panel presents the temperature profiles of three CH_4/CO_2 ratios for the Case B planet. Note the strengthening temperature inversion as the CH_4 content of the atmosphere increases. The right panel shows the size of haze particles produced in these three atmospheres, showing the dependence of haze particle size on temperature. From least to most CH_4 (and thinnest to thickest haze), the particles reach a maximum radius of 0.067 μm, 0.28 μm, and 0.57 μm. Note that the temperature profiles become isothermal at the top of the climate model grid when transferred to the larger photochemical model grid.

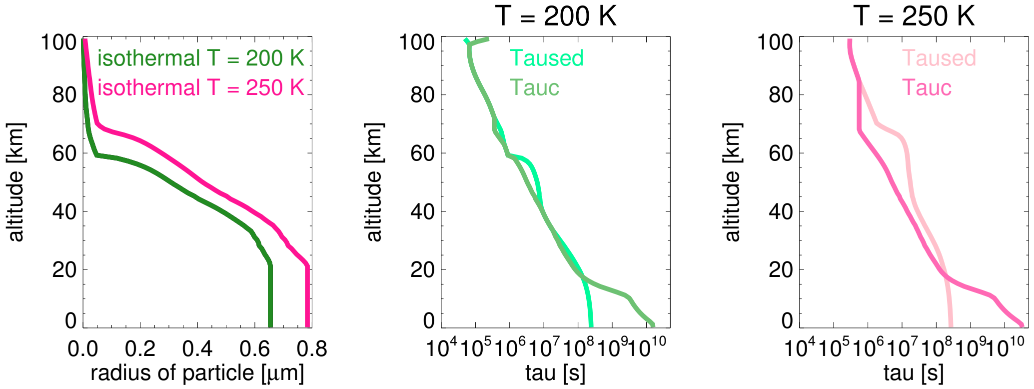

Figure 5.4: The haze particle sizes for two completely isothermal atmospheres together with the coagulation and sedimentation timescales for these atmospheres.

5.3.2 UV Shielding

The impact of these hazes on the biosphere goes beyond temperature reduction: their fractal nature makes them strong absorbers at short wavelengths and therefore a potential shield against damaging ultraviolet (UV) radiation for the anoxic Archean (Wolf & Toon, 2010), which would have received significantly more UV at the surface than the planet today (Rugheimer et al., 2015). DNA damage is most acute in the UVC ($\lambda < 0.28$ μm) wavelength range (Pierson et al., 1992; Dillon & Castenholz, 1999), but in the modern atmosphere, UVC is fully blocked by O_2 and ozone. For the haze-free Case B atmosphere ($CH_4/CO_2 = 0.1$), our models calculate the flux of UVC at the surface as about 0.93 W/m^2 for a solar zenith angle of 60° and 2.62 W/m^2 for SZA = 0°. Both of these values are sufficient for sterilization (Pierson et al., 1992). In contrast, the surface UVC flux under a haze for Case B (CH_4/CO_2 = 0.21) would have been about 0.03 W/m^2 for SZA = 60° and 0.22 W/m^2 for SZA = 0°. We compare these values to the tolerances of *Chloroflexus aurantiacus* (Pierson et al., 1992), a deep-branching, mat-forming anoxygenic phototroph with UV resistance that has been studied as an analog for Archean phototrophs. Our SZA = 60° flux, 0.03 W/m^2, is low enough to allow growth of *Chloroflexus aurantiacus* over the length of a day in the late Archean (about 18-19 hours for a day-night cycle; Denis et al. (2002)). Our SZA = 0° flux, 0.22 W/m^2, is naturally worse but does not cause immediate sterilization of *Chloroflexus aurantiacus*, allowing modest growth for roughly 10 hours. In a real atmosphere, the UV flux will change with solar zenith angle, but it will not exceed the SZA = 0° flux. At latitudes where the SZA is never 0°, UV survival prospects are better, although these higher latitudes may be icy for our cold planets. Under an Archean haze, it is possible that organisms similar to *Chloroflexus aurantiacus* with robust UV protection mechanisms could have lived at or near the planet's surface. We summarize the UV protection of several types of atmospheres, including ones with water clouds that can confer additional UV protection, in Table 5.3. This table only includes Case B, but the other cases produce similar results for UV shielding because they have similar optical thicknesses.

Possibly, an Archean haze aided the survival of life at or near the surface of our early planet. There is evidence that Archean stromatolitic communities lived in inter- and suprati-

Table 5.3: The UV fluxes at the planetary surface for several overlying atmospheres. All values quoted have units of W/m^2. The solar constant for geological times has been scaled according to Claire et al. (2012) at 2.5 Ga for the Proterozoic and 2.7 Ga for the Archean. All calculations have been performed assuming that the Sun is either directly overhead (Solar Zenith Angle = 0°) or at a Solar Zenith Angle of 60°. There are three Archean UV fluxes per UV Band and CH_4/CO_2 ratio: they refer to haze only (labeled “H”), haze plus cirrus cloud (labeled “H+C”), and haze plus stratocumulus cloud (labeled “H+S”). The Modern Earth and Proterozoic atmospheres are cloud- and haze-free. UVA spans $\lambda = 0.315$-$0.400\ \mu$m. UVB spans $\lambda = 0.280$-$0.315\ \mu$m. UVC is $\lambda < 0.280\ \mu$m.

	Modern Earth	Proterozoic 1% PAL O_2	Proterozoic 0.1% PAL O_2	Case B CH_4/CO_2 = 0.1			Case B CH_4/CO_2 = 0.17			Case B CH_4/CO_2 = 0.21		
SZA = 0°												
				H	H+C	H+S	H	H+C	H+S	H	H+C	H+S
UVA	70.5	59.1	59.3	55.5	50.84	38.1	48.8	44.3	33.2	22.8	20.2	15
UVB	2.49	6.18	10.6	10.2	9.32	7.26	8.11	7.38	5.76	2.19	1.96	1.52
UVC	∼0	0.00764	2.03	2.62	2.41	1.95	1.87	1.71	1.38	0.216	0.196	0.158
SZA = 60°												
UVA	28.9	24.4	24.5	23	18.42	13.2	17.7	14.4	10.4	4.93	4.14	3
UVB	0.446	1.77	3.9	3.82	3.29	2.51	2.51	2.18	1.67	0.337	0.29	0.22
UVC	∼0	7.29_10-4	0.565	0.932	0.841	0.673	0.512	0.471	0.376	0.0318	0.029	0.025

dal zones (Allwood et al., 2006; Noffke & Awramik, 2013) experiencing frequent, sometimes extended, exposure to the surface environment, and it has been suggested that microbial mats existed on land as early as 2.6-2.7 Ga (Watanabe et al., 2000). Interestingly, this interval overlaps with periods when haze has been proposed for the Archean atmosphere (Kurzweil et al., 2013; Zerkle et al., 2012; Izon et al., 2015). Life on land was also a conclusion of Stüeken et al. (2012) and was discussed in Lalonde & Konhauser (2015) in the context of microbial mats.

It has widely been assumed that Proterozoic Earth's surface received less UV than the Archean due to the rise of oxygen (O_2) and ozone (e.g. Rugheimer et al., 2015), but a recent study of chromium isotopes suggests that the Proterozoic O_2 mixing ratio was, at most, 0.1% PAL (Planavsky et al., 2014). We tested the strength of an ozone UV shield generated by our photochemical model under these low oxygen conditions against the strength of our hazy UV shield. For the Proterozoic atmospheres, we tested ozone generation at 0.1% and 1% PAL O_2 levels (Figure 5.5) with pCO_2 fixed at 0.01 bars and pCH_4 at 0.0003 bars. Total pressure is set to 1 bar at the surface. According to these assumptions, Proterozoic Earth with 0.1% PAL O_2 would have received 0.57 W/m^2 of UVC at the surface, so in this case, the Archean hazy UV shield was stronger. Note also that haze is a better shield against UVA ($\lambda = 0.315$ - 0.400 μm) and UVB ($\lambda = 0.280$ - 0.315 μm) than ozone or O_2.

5.3.3 Spectra

The strong interaction of haze with radiation means hazes can impact the exoplanet spectra that future space based telescopes will attempt to detect. In Figure 5.6, we show reflectance, thermal emission, and transit transmission spectra for our nominal Case B with an ocean surface; the other Cases produce similar spectra as discussed below. Our predicted spectra of hazy Archean Earth show diagnostic absorption features from H_2O, CO_2, CH_4, C_2H_6, CO, and from the haze itself. These features are labeled in Figure 5.6, and another way to show where these gases and the haze absorb is presented in Figures 5.7 and 5.8 for reflectance and transit transmission spectra, respectively. Figures 5.7 and 5.8 were produced by systematically removing each gas or the haze; in places where a given species absorbs, the original

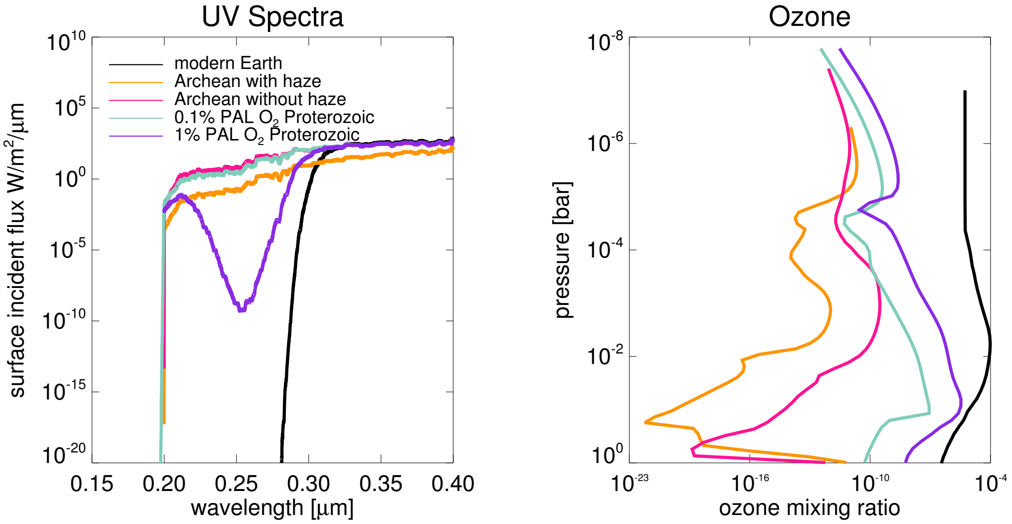

Figure 5.5: Shown are surface UV spectra (left) and ozone column abundances (right) for Archean, Proterozoic, and modern Earth atmospheres. A modest amount of O_2 in the Proterozoic (1% PAL) produces a stronger UV shield than the Archean haze, but the haze shown here cuts out more UVA (320-400 nm) and UVB (280-320 nm) radiation than ozone in all situations. The haze can produce a stronger UV shield compared to the low O_2 atmosphere (0.1% PAL) proposed recently by Planavsky et al. (2014) for our atmospheric assumptions.

spectrum differs from those with the absorbers removed. To consider the spectral effect of haze without contamination from other atmospheric aerosols, the spectra in this section do not include water clouds, even though cloud albedo is implicit in the parameterization of the `Atmos` model's surface albedo. This makes the albedos of the planets whose spectra are shown in this section darker than those in the `Atmos` parameterization. However, since clouds have a major impact on the planet's spectral appearance and albedo (e.g. Kitzmann et al., 2011a), we show spectra with water clouds included in Section 5.3.3.a. The best way to treat the climatic and spectral impact of both clouds and haze would be in a fully-coupled 3D climate-photochemical model that fully considers radiative and photochemical effects of cloud and haze particles, but this is outside the scope of this work. To our knowledge, such a 3D model does not yet exist, but its development would be useful for the comprehensive treatment of this problem.

In reflected light (Figure 5.6, panel a), the broad UV absorption feature reddens the color of the planet by masking the short-wavelength reflectivity due to Rayleigh scattering. See the bottom section of Figure 5.6 for the estimated color of the planet to the eye. The planet colors were calculated using the "Spectral Color Spreadsheet" from brucelindbloom.com with the same method used in Charnay et al. (2015) for GJ 1214b. A spectrum can be input to the calculator, which then outputs RGB values. While these colors should be understood as approximations, we tested the colors produced for the modern Earth sky and Titan as a check, and the results appeared reasonable. Colors and photometric bands have been considered as indicators of Earth-like worlds (Traub, 2003; Crow et al., 2011; Krissansen-Totton et al., 2016), but hazy Archean Earth suggests that not all Earth-like planets will be pale blue dots. Because methane-producing metabolisms evolved early and Earth's atmosphere was anoxic for about a billion years after the origin of life, pale orange dots may proliferate in the galaxy if other habitable worlds evolve on similar paths to Earth.

Several spectral features are apparent in Figure 5.6. The haze-mediated stratospheric thermal inversion is clearly seen in thermal emission near 8 μm and 16 μm (Figure 5.6, panel b). Similar to the Titan transmission spectrum derived from Cassini solar occultation measurements (Robinson et al., 2014b), our simulated hazy transit transmission spectra (Figure 5.6, panel c) are sloped in the visible and NIR. Gas absorption features in the visible and NIR are muted by the presence of a haze in transit transmission, but mid-IR absorption features are less affected because the haze is relatively transparent at longer wavelengths. In Earthlike clear-sky atmospheres, the minimum atmospheric altitude transit observations are able to probe will typically be limited by refraction (García Muñoz et al., 2012; Bétrémieux & Kaltenegger, 2014; Misra et al., 2014a,b), but in hazy atmospheres, haze controls the minimum effective tangent height, especially at shorter wavelengths where it dominates the transit transmission spectral slope. Absorption from the haze itself can be seen as the "bump" in the "thick" haze ($CH_4/CO_2 = 0.21$) transit transmission spectrum at 6 μm, a wavelength region accessible with the James Webb Space Telescope (Wright et al., 2004). There is also a very weak haze feature near 3 μm in transit transmission that can be most easily seen in Figure 5.8. These features can also be seen in the peaks of the haze imaginary refractive index (Figure 2.4).

Note the presence of a C_2H_6 absorption feature near 12 μm. This C_2H_6 forms from photochemistry involving CH_4, and its buildup in our spectra is not inconsistent with the results of Domagal-Goldman et al. (2011), which showed much greater C_2H_6 accumulation on planets orbiting low-mass stars compared to worlds orbiting the sun. However, the CH_4 levels in the Domagal-Goldman et al. (2011) solar simulations were an order of magnitude lower than the ones shown here. C_2H_6 is a greenhouse gas, and its ability to warm in a CH_4- and haze-rich atmosphere has been discussed previously (Haqq-Misra et al., 2008).

Figures 5.6-5.8 show spectra for our Case B planet, but Figures 5.9 and 5.10 show representative reflected light and transit transmission spectra for all of our Cases A-D in the visible and near-infrared. The reflectance spectra in Figure 5.6 and 5.7 assumed a pure ocean surface albedo to isolate the spectral consequence of atmospheric haze from other spectral changes, but the spectra shown in Figure 5.9 are constructed from a weighted average of ocean and ice surfaces according to the ice line latitudes reported in Wolf & Toon (2013) for Archean atmospheres with CO_2 and CH_4. The hazy planets in Figure 5.9 are more reflective than the spectra shown in Figure 5.6 due to this ice coverage. Figure 5.10 shows how thick hazes strongly mute the strength of gaseous absorption features in transit transmission at shorter wavelengths where these hazes are more optically thick.

5.3.3.a Water Clouds

The goal of the nominal haze spectra we have presented is to show the spectral impact of organic haze independent of any other atmospheric aerosols. However, it is interesting and important to also consider how water clouds affect our hazy spectra. To test the impact of clouds in addition to haze on the spectra of Earth-like planets, we added water clouds to the Case B atmospheres shown in Figure 5.6. Because these are 1D spectra, we incorporate clouds with a weighted average of cloudy and pure haze spectra where we assume 50% of the planet is covered by haze only, 25% is covered by cirrus clouds (at 10 km altitude) and haze, and 25% by strato cumulus clouds (at 1 km altitude) and haze (Robinson et al., 2011). The resulting spectra are presented in Figure 5.11. In contrast to hydrocarbon haze particles, which are more transparent in the near infrared compared to shorter wavelengths, water

Table 5.4: The relative brightness of spectra with and without water clouds.

$CH_4/CO_2 =$	0.4-1 μm With clouds/No clouds	1-2 μm With clouds/No clouds
0.1	2.34	4.8
0.17	2.12	4.24
0.21	1.56	2.24

vapor clouds have an approximately gray opacity from the visible into the near infrared. Thus, at longer wavelengths, cloudy worlds are brighter than their haze-only counterparts. Table 5.4 shows the total integrated brightness of the reflectance spectra for the worlds with clouds divided by their cloud-free counterparts between 0.4-1 μm and between 1-2 μm to quantify the spectral impact of clouds.

The disproportionate increase in brightness from clouds at longer wavelength compared to shorter wavelengths means that the peak of the reflectance spectrum also shifts towards longer wavelengths for the worlds with clouds: for $CH_4/CO_2 = 0.17$, the reflectance spectrum peak shifts from 0.31 μm to 0.38 μm, and for $CH_4/CO_2 = 0.21$, it shifts from 0.56 μm to 0.68 μm. Adding clouds also raises the spectral continuum level, making absorption features appear deeper. This enhanced reflectivity also potentially increases the detectability of water vapor in reflected light spectra, as more reflected flux from the planet reduces noise on the continuum, enhancing the detectability of absorption features that deviate from that continuum. A detailed discussion of the impact of water clouds on the spectra of Earthlike planets for different cloud altitudes and fractional cloud coverages can be found in Kitzmann et al. (2011b).

In transit transmission, water clouds have no spectral impact because they form in the atmosphere at a level below the maximum tangent height set by refraction. The tropopause on Earth is at roughly 10 km, and refraction prohibits transmission of path lengths below about 20 km even for our clear sky worlds. As water vapor is at very low abundance in the Earth's stratosphere (6 to 10 ppm), it would be difficult, in general, to see it in transmission observations that can only probe down to stratospheric altitudes. Abundant stratospheric water vapor would imply that the planet is in the midst of a moist or runaway greenhouse state, and thus is not conventionally habitable.

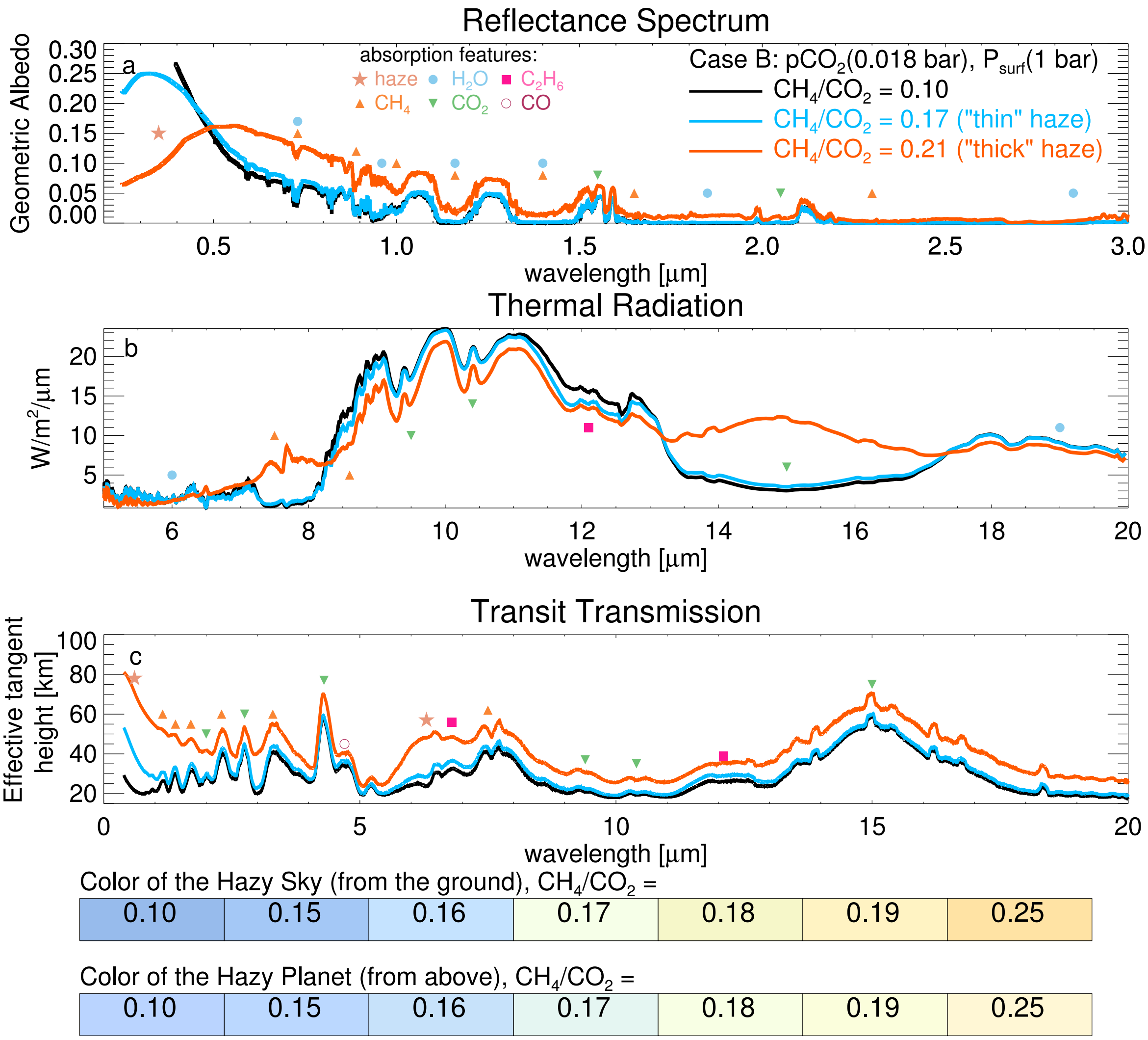

Figure 5.6: Shown here are spectra for Case B. Haze and gas absorption features are labeled with the symbols indicated. Panel a: At short wavelengths in direct imaging, haze absorption decreases the planet's brightness; scattering brightens the planet at longer wavelengths. Panel b: Thermal emission from the optically thick stratosphere of the thickest haze planet (CH_4/CO_2 = 0.21) fills in absorption bands near 8 μm and 16 μm. Panel c: The y-axis shows the effective transit height above the planet's surface that light is able to penetrate, and absorption features are inverted compared to panels a) and b) due to an increase in the effective planet radius during transit resulting from an increase in absorption at these wavelengths. The bottom section shows the approximate color of the hazy sky and planet. Sky colors are computed using the diffuse radiation spectrum at the ground. "Effective tangent height" refers to the minimum altitude above the planet's surface that light is able to penetrate on transit transmission paths.

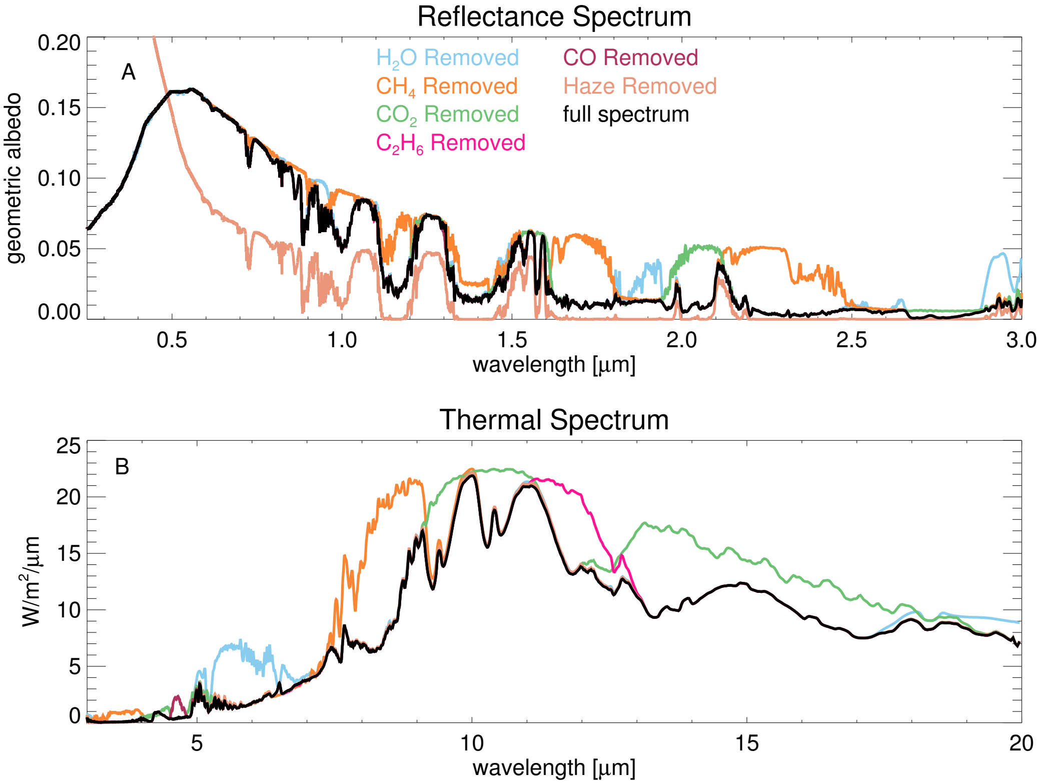

Figure 5.7: A reflectance spectrum for a hazy Case B planet in the visible and near-infrared (panel A), and mid-infrared (panel B) is presented with gases and the hydrocarbon haze removed to show where each spectral component interacts with radiation. The full spectrum is shown in black. Places where the black spectrum deviates from the colored spectra indicate where each gas or haze absorbs. For example, the green line shows a spectrum where CO_2 is omitted, and a strong CO_2 feature is present near 15 μm in panel B as shown by the deviation of the green spectrum from the black spectrum. At some wavelengths, gas and haze absorptions are complex to detangle because multiple species are absorbing: in these cases, the key on Figure 5.6 will indicate which gases are the dominant absorbers in a region.

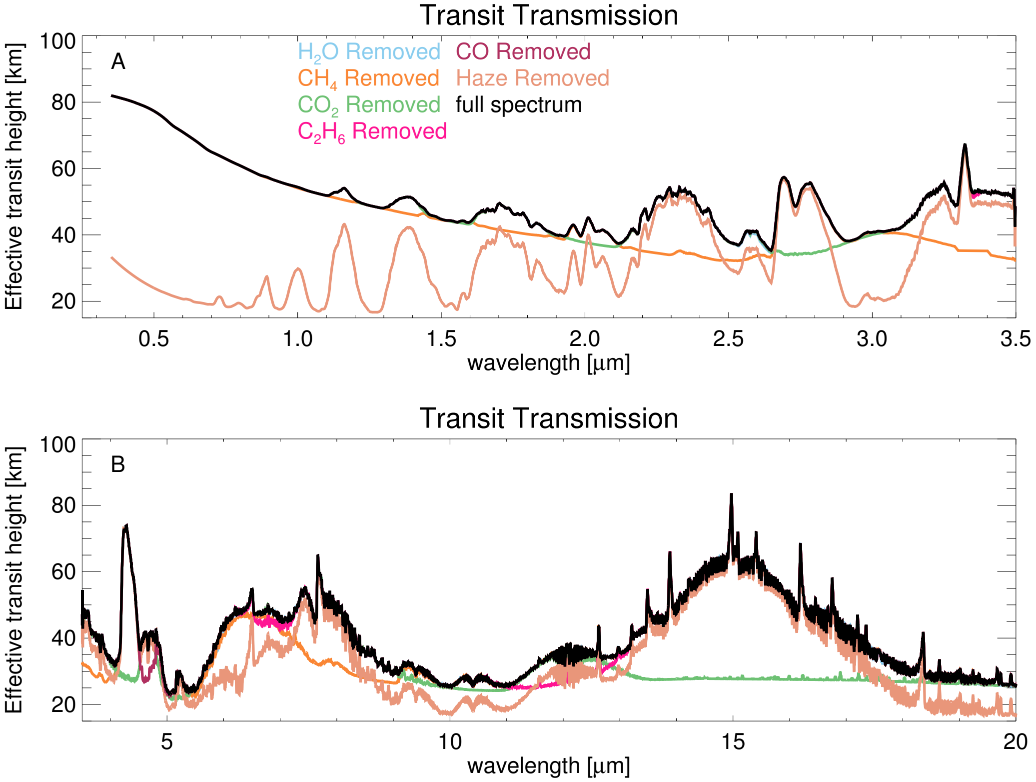

Figure 5.8: A transit transmission spectrum for a hazy Case B planet in the visible and near-infrared (panel A), and mid-infrared (panel B) is presented with gases and the hydrocarbon haze removed to show where each spectral component interacts with radiation. The full spectrum is shown in black. Places where the black spectrum deviates from the colored spectra indicate where each gas or haze absorbs. For example, the orange line in panel A indicates CH_4 absorption features near 1.15 μm, 1.4 μm, 1.7 μm, 2.3 μm, and 3.3 μm.

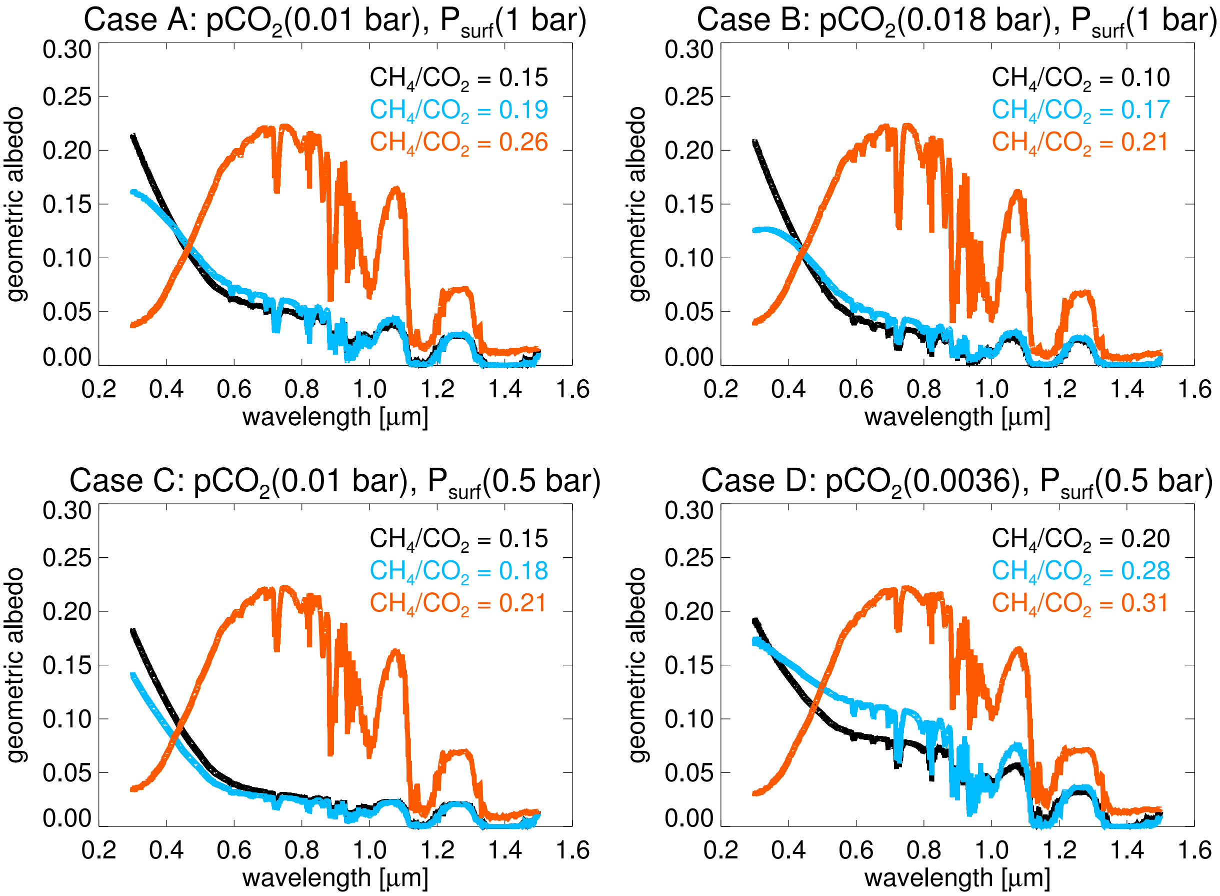

Figure 5.9: Example reflectance spectra, intended as analogs for exoplanets like Archean Earth, for all of the types of planets investigated in this study are presented here. Fractional ice coverage is included in these spectra using a weighted average of icy and liquid water surfaces as described in the text.

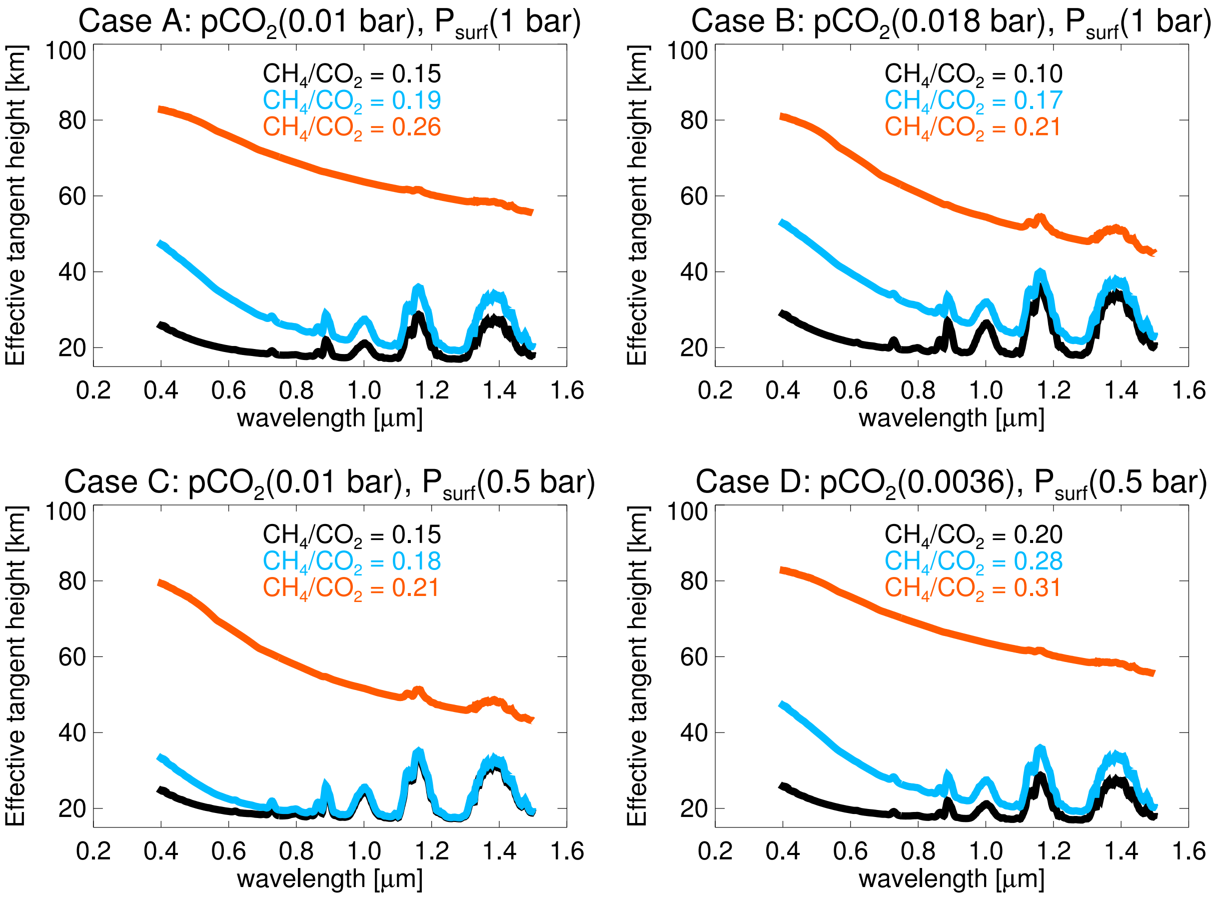

Figure 5.10: Transit transmission spectra in the visible and NIR for cases A-D are presented here. For thicker hazes, absorption features shortward of approximately 1 μm vanish. These relatively featureless spectra result because high altitude hazes are effective at obscuring the lower atmosphere with the long path lengths taken by light in transit spectroscopy measurements.

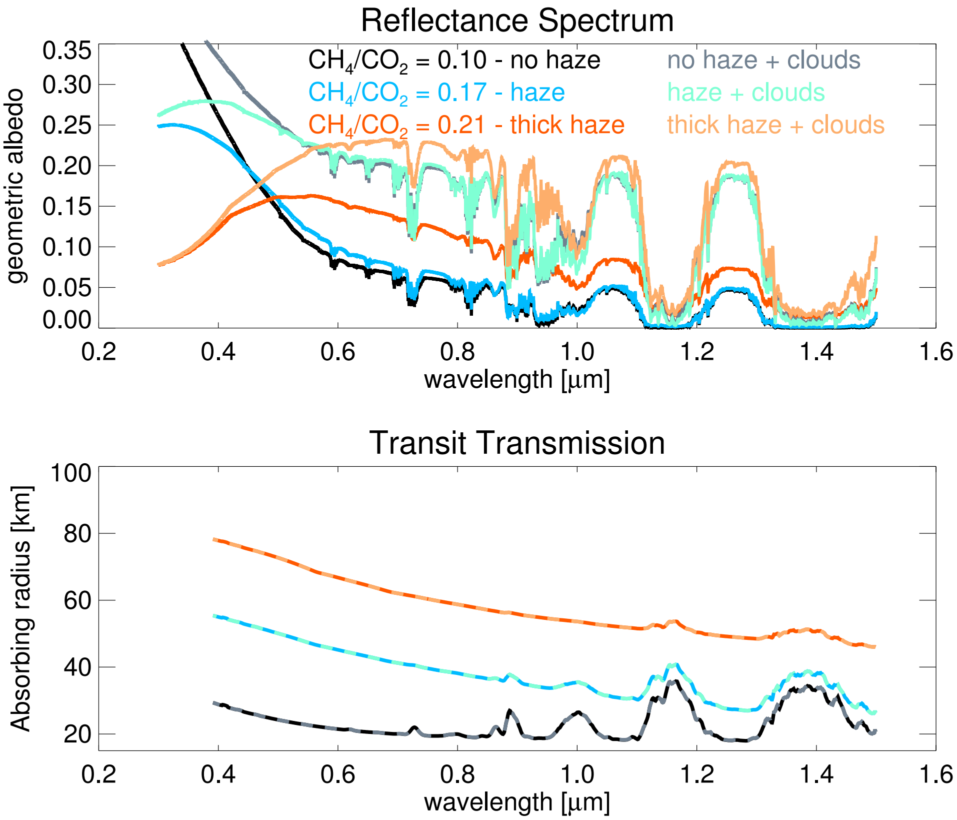

Figure 5.11: Here we show the impact of water clouds on our Case B spectra with no haze, a thin haze, and a thick haze. The spectra with cloud and haze are shown in the pale colored lines. The dashed lines over our transit transmission spectra indicate that the spectra with and without water clouds are the same.

5.4 Discussion

The hazes investigated here have a major spectral impact at short wavelengths due to their strong blue and UV absorption. It has been suggested that the Rayleigh scattering slope could be used to constrain atmospheric pressure on exoplanets (Benneke & Seager, 2012), but this would not be possible on planets with hydrocarbon hazes or other strong UV absorbers (Chapter 6) due to these strong short wavelength absorption effects. In reflected light, the haze's broadband UV absorption feature, observed together with methane bands, would strongly imply the existence of hydrocarbon haze in an atmosphere. In the infrared, the diagnostic haze absorption feature at 6 μm (and the weaker one at 3 μm) in transit transmission would allow chemical identification of hydrocarbon haze. Even absent the detection of these specific features in transit transmission, the presence of CH_4 bands together with the haze UV-visible-NIR spectral slope would strongly imply the presence of this haze.

5.4.1 Haze and biology

Our study shows how an Archean haze would have profoundly impacted our planet's environment, habitability, and spectrum. It is important to note that geochemical evidence suggests hazy conditions were not present throughout the entire Archean, and its periodic collapse may have put stress on the biosphere if organisms migrated to the surface or near-surface and adapted to lower UV levels created by the haze. On the other hand, if organisms remained protected by some other UV shield such as minerals, layers of overlying microbial mat, or water (Cockell, 1998), changes in UV radiation levels should not affect them as strongly, so the colder conditions created by the haze might have been the larger source of stress on organisms. These stressors might have driven evolutionary adaptations as life responded to its changing environment. Note that photosynthetic organisms would not likely have been photon limited by the lower light levels under the haze: the lower light limit for red algae is 6×10^{15} photons/m^2/s (Littler et al., 1986). Under our Case B $CH_4/CO_2 = 0.21$ haze, total PAR at the surface is 7.1×10^{20} photons/m^2/s, orders of magnitude above this extreme. Chapter 7 discusses connections between haze and photosynthetic organisms in more detail.

Laboratory experiments on organic haze formation have shown that haze-formation chemistry can involve the formation of important prebiotic molecules such as amino acids and nucleotide bases (Khare et al., 1986; McDonald et al., 1994; DeWitt et al., 2009; Hörst et al., 2012; Trainer, 2013) – see also our discussion of haze formation pathways in Section 5.4.4. Although the hazy periods we invoke here occurred hundreds of millions of years after the origin of life on Earth, there may be earlier hazy epochs not yet discovered in the geological record (see Kasting (2005) for a discussion of earlier atmospheric methane), and hazy Titan has been regarded as a type of prebiotic chemical laboratory (Khare et al., 1984b; Clarke & Ferris, 1997).

While we know that abiotic hydrocarbon hazes are possible (e.g. on extremely cold worlds like Titan with reducing atmospheres), on a planet like Archean Earth, the presence of hydrocarbon haze may require a higher level of methane production than is possible from abiotic sources alone. The maximum abiotic methane production rate from serpentinization, its primary nonbiological source, has been estimated as 6.8×10^8 and 1.3×10^9 molecules/cm^2/s for rocky planets of 1 and 5 Earth masses, respectively (Guzmán-Marmolejo et al., 2013), although there has been earlier speculation of higher abiotic production rates (Kasting, 2005; Shaw, 2008), especially if ancient seafloor spreading rates were faster or the amount of iron-rich ancient seafloor rock was greater. Based on their calculations, Guzmán-Marmolejo et al. (2013) suggest that an atmospheric CH_4 concentration greater than 10 ppmv is suggestive of life. At the range of pCO_2 allowed by Driese et al. (2011), we find that the CH_4 flux needed to initiate haze formation ranges between about $1 - 3 \times 10^{11}$ molecules/cm^2/s, broadly consistent with estimates for the biological Archean methane flux after the origin of oxygenic photosynthesis (Kharecha et al., 2005; Claire et al., 2014). The higher of the plausible rocky planet abiotic CH_4 fluxes from Guzmán-Marmolejo et al. (2013), 1.3×10^9 molecules/cm^2/s, will not form a haze in our model even at a pCO_2 level four orders of magnitude smaller than the lower limit allowed by Driese et al. (2011), and such a world would be completely frozen given the Archean solar constant. Remote identification of a hydrocarbon haze with a concurrent measurement of CO_2 around a planet that absorbs an Earth-like amount of radiation could therefore imply a surface methane flux consistent with biological production. The strength and width of the hydrocarbon haze absorption feature below about 0.5 μm implies it would be easier to detect than methane itself given sufficient instrumental sensitivity to this range, so the occurrence of haze in the habitable zone may be a way to flag interesting planets for careful follow-up study that would search for other indicators of life and quantify the concentration of CH_4 and other gases.

5.4.2 Comparison with other climate studies

To test the robustness of the mean surface temperatures calculated by our computationally efficient 1D climate model, we compared our temperature result for a haze-free Case A atmosphere with $pCO_2 = 0.01$ and $pCH_4 = 0.002$ (but no ethane) and a solar constant for 2.5 billion years ago to the Laboratoire de Météorologie Dynamique (LMD) General Circulation Model (GCM) run with the same inputs. We adopt the same average albedo produced by the LMD model in this simulation, setting A_{surf}=0.33 for our planet (as before, this albedo includes the effect of clouds). For an ocean-covered planet with no haze, the LMD model produces a mean surface temperature of 287 K (Charnay et al., 2013). This is comparable to, but 5 K warmer, than our global average 1D result of 282 K. The Charnay et al. results for the same atmospheric properties but with an equatorial supercontinent result in the same overall planetary albedo (0.33) but a lower mean temperature of 285 K, which is closer to our result. We achieve the closest match to the Charnay et al. results for a modern continental land mass arrangement: in the GCM, this yields an average albedo of 0.34 and a temperature of 283.7 K, close to our result of 281.1 K for this configuration.

We also tested our model results against the Community Atmosphere Model (CAM) GCM nominal Archean atmosphere reported in Wolf & Toon (2013). For this planet, the solar constant is 80% modern, $pCO_2 = 0.06$ bars, there is no CH_4, no haze, and the planet has an average albedo of 0.317. For this world, the CAM model produces a global average surface temperature of 287.9 K. Our model produces 285.3 K for this configuration, a difference of 2.6 K.

The GCMs we compare to can include a variety of effects our 1D model cannot, including atmospheric circulation, precipitation, cloud formation, and cloud scattering and absorption. Our comparison with these 3D models suggests the temperatures we present in this work are reasonable but may be under-estimates by about 3-5 K. One reason that our 1D results may be colder than the GCM results is that while we have incorporated identical planetary albedos (with clouds), we are still missing the longwave radiative forcing from clouds, which would have a warming effect.

Haqq-Misra et al. (2008) similarly studied the climate of Archean Earth with hydrocarbon hazes and high amounts of CO_2, CH_4, and C_2H_6 with an earlier incarnation of the 1D models we use here. The haze-free surface temperatures we generate are broadly consistent with the Haqq-Misra et al. (2008) non-hazy results with C_2H_6. Haqq-Misra et al. show that a planet with $pCO_2 = 0.01$ and $CH_4/CO_2 = 0.1$ has a surface temperature of about 282 K, which is close to our 283.4 K for a comparable atmosphere. Similar to our study, the Haqq-Misra et al. study found it was difficult to maintain surface temperatures above the freezing point of water with spherical haze particles. However, as we have argued, a mean surface temperature of the freezing point of water is not a useful threshold for global habitability (Shields et al., 2013; Charnay et al., 2013; Wolf & Toon, 2013; Kunze et al., 2014), so some of the Haqq-Misra et al. spherical haze results may actually be “habitable”. In general, we are able to achieve warmer hazy solutions in our study because, as previously discussed, fractal hydrocarbon hazes produce less extinction of visible wavelengths compared to equal mass spherical haze particles. For example, for a planet with 1 bar of pressure and 2% CO_2, the Haqq-Misra et al. spherical haze drops the planet’s temperature to below 260 K. The same planet with a fractal haze in our study remains above 273 K (without considering ice-albedo effects not examined in the Haqq-Misra et al. study) after haze self-shielding levels off the temperature. Our results suggest that fractal hazes do indeed produce less antigreenhouse cooling than spherical particles. However, since our non-hazy comparison atmosphere was about 1.4 K warmer than the comparable Haqq-Misra atmosphere, a small component of the warmer temperatures we see here may also result in part from updates to our climate model made by the Kopparapu et al. (2013) study.

5.4.3 Potential for NH_3 greenhouse gas shielding

The optical thickness of the haze impacts its ability to shield molecules from photodissociation. Once the UV opacity of the haze exceeds approximately unity, the surface flux of CH_4 necessary to maintain a given atmospheric methane mixing ratio drops due to haze-induced CH_4 shielding (Zerkle et al., 2012). At higher haze thicknesses, the opacity of the haze levels off because this self-shielding inhibits the methane photolysis needed to initiate haze formation. This “bistability” was first remarked on in Zerkle et al. (2012). Wolf & Toon (2010) commented on the possibility of a fractal hydrocarbon haze shielding ammonia (NH_3) from photolysis, allowing this greenhouse gas to build up in the Archean atmosphere. Following Sagan & Chyba (1997), Wolf and Toon calculated a NH_3 atmospheric lifetime of 7×10^7 years for a solar incident flux at a 45 degree angle assuming $\tau \sim 11$ at 200 nm. Following Wolf and Toon, we find our maximum haze thickness levels off at $\tau \sim 5$ at 200 nm, which results in a significantly shorter NH_3 lifetime of 1×10^4 years, although we did not include NH_3 in our photochemical scheme. Our future work will include NH_3 in the photochemical and climate model to study, in a self-consistent atmosphere, how much of this gas can exist in a hazy atmosphere and what its climatic effect could be.

5.4.4 Haze formation pathways

Following the mechanism proposed for the formation of Titan’s hydrocarbon haze (Allen et al., 1980; Yung et al., 1984), every model of hydrocarbon haze formation in early Earth’s atmosphere – including ours – has assumed that aerosol formation will occur through the formation of acetylene (C_2H_2) and its further polymerization to higher polyacetylene chains (Pavlov et al., 2001a,b; Domagal-Goldman et al., 2008; Haqq-Misra et al., 2008; Zerkle et al., 2012; Kurzweil et al., 2013; Claire et al., 2014). The two reaction pathways described in Section 3.1.1 provide an initial picture of the process, but haze formation is likely considerably more complex and is still not well understood. Unlike early Earth, we now have access to direct observations of the chemical processes ongoing in Titan’s atmosphere. In situ measurements by several instruments onboard Cassini have found direct evidence for long hydrocarbons and nitriles chains, benzene (C_6H_6) and toluene ($C_6H_5CH_3$), and indirect evidence for Polycyclic Aromatic Hydrocarbons (PAHs) and nitrogen-containing PAHs (PANHs), indicating that these compounds might play a role in the formation of Titan's hazes (Waite et al., 2007; López-Puertas et al., 2013).

Moreover, early Earth's atmosphere was likely not as reducing as Titan's. The chemical pathways for haze formation, including the C_2H_2 polymerization pathways, may therefore be inappropriate. Early Earth's atmosphere would have contained negligible O_2 but significant amounts of CO_2 (e.g., Kasting, 1993; Driese et al., 2011) whereas Titan's atmosphere is extremely reducing (de Kok et al., 2007). Even in Titan's highly reducing atmosphere, it was suggested that CO may contribute to oxygen incorporation in the organic aerosols (Hörst et al., 2012). This oxygen incorporation is expected to be much more important to aerosol chemistry in early Earth's far less reducing atmosphere. Using far ultraviolet (FUV) radiation (115-400 nm), organic aerosol production from a $CH_4/CO_2/N_2$ mixture was shown to exceed that from a pure CH_4/N_2 mixture (Trainer et al., 2006) and organic aerosol formation was experimentally observed to occur down to C/O ratios as low as 0.1 (Trainer et al., 2006; DeWitt et al., 2009). From the chemical analysis of primary condensed-phase products of photochemistry, it is clear that the composition of the aerosol analogs formed in early Earth-like atmospheres with $C/O < 1$ differs greatly from the aerosol analogs formed in Titan-like atmospheres where $C/O \gg 1$. Instead of limiting the formation of organic molecules as initially predicted, the O-atoms released from CO_2 photolysis are incorporated into the molecular structure of the organic aerosols. Mass spectrometry of aerosol analogs formed with $C/O = 0.1$ indicates the formation of carbonyl and carboxyl groups rather than aromatic cycles and long-aliphatic chains, and even suggests the formation of organic acids such as succinic acid ($C_4H_6O_4$) (DeWitt et al., 2009).

Finally, haze formation chemistry gets considerably more complex when one considers the coexistence not only of O-heteroatoms but also of N-heteroatoms in aerosol organics. Nitrogen incorporation was recently observed in the aerosols generated by far-UV photolysis of $CH_4/CO_2/N_2$ gas mixtures (Trainer, 2013) and in CH_4/N_2 mixtures (Sebree et al., 2015). These results bring to light a significant but still unknown mechanism regarding the activation of nitrogen and its inclusion in oxygenated organics, thus providing a new and quantifiable source for these two elements into the early Earth aerosols. Studies have shown the formation of HCN, CH_3CN and other nitrile gas species are formed using the same type of UV source in a CH_4/N_2 gas mixture, thus corroborating the indirect nitrogen photochemistry (Trainer et al., 2012; Yoon et al., 2014). These results suggest that N_2 chemical activation could be due to its reaction with the methylidyne (CH) radical formed from CH_4 photolysis, to form two radical intermediates, diazomethyl HCNN and its isomer HNCN, which might then react to form HCN and other products.

The formation of aerosols in early Earth's atmosphere is thus tightly intertwined with the formation of organic molecules containing more than a few C/H/N/O atoms. These compositional differences should change the properties of the aerosol material sufficiently to be able to distinguish a hazy early Earth from a modern-day Titan (Hasenkopf et al. 2010). For instance, organic molecules with oxygen-containing functional groups (alcohols, carbonyls) tend to have stronger absorbances at longer UV wavelengths as compared to similar hydrocarbon molecules (Workman 2000). The NIR absorption bands of the Archean aerosol analogs would also shift in response to the inclusion of the types of oxygen and nitrogen heteroatom functionalities that have been indicated in the compositional studies.

5.4.5 Optical constants

The implications of compositional differences of Archean hazes versus Titan hazes for the topics presented in this study and for prebiotic chemistry underscores the need for measurements of Archean Earth analog optical constants as well as a better understanding of the haze formation chemical pathways. Unfortunately, only one study, Hasenkopf et al. (2010), has measured an Archean Earth haze refractive index (as opposed to a Titan haze), and this was only done at a single wavelength (532 nm).

In our study, we have used the hydrocarbon refractive indices from (Khare et al., 1984a) to allow us to draw comparisons with previous works involving our suite of models (Domagal-Goldman et al., 2008; Pavlov et al., 2001a,b; Zerkle et al., 2012; Haqq-Misra et al., 2008; Kurzweil et al., 2013; Claire et al., 2014), as well as the Wolf & Toon (2010) study which all used the Khare optical constants. An additional advantage of the Khare refractive indices is that they span an extremely wide wavelength range, ranging from 0.02 μm to 920

μm, so only one set of optical constants is needed to cover all the wavelengths relevant to photochemistry, climate, and spectra.

However, more recent measurements of hydrocarbon refractive indices over more restricted wavelength ranges indicate disagreement with the Khare measurements (Imanaka et al., 2012; Mahjoub et al., 2012; Sciamma-O'Brien et al., 2012; Hasenkopf et al., 2010; Ramirez et al., 2002; Tran et al., 2003; Vuitton et al., 2009), although these measurements themselves show considerable variation amongst each other (Figure 5.12). Differences in the composition of Archean hazes compared to Titan's (and thus differences in their optical constants) are expected as discussed in section 5.4.4. Again, note the single measurement by Hasenkopf et al. (2010) for an Archean-analog haze; of all of the optical constants plotted in Figure 5.12, the Khare indices actually produce the closest (although still too low) match to the Hasenkopf Archean real refractive index (n) near 532 nm and produce a reasonable match to the Hasenkopf Archean imaginary refractive index (k), agreeing to within approximately 40% near 532 nm.

As an example and test of the impact different refractive indices have on our spectra, we examined the sensitivity of our nominal spectra to varied refractive indices measured by Mahjoub et al. (2012). The Mahjoub study tested the impact of methane concentration in the gas phase on the resultant hydrocarbon optical properties with gas mixtures containing 1%, 2%, 5% and 10% CH_4 in CH_4-N_2 mixtures. Note the 1% CH_4 Mahjoub imaginary refractive index agrees to within 5% of the Hasenkopf Archean measurement near 532 nm. Mahjoub et al. found that refractive indices have a strong dependency on the CH_4 concentration over 0.37-1 μm: results indicate that the imaginary index of refraction (k) decreases with increasing CH_4 concentration, and the real index of refraction (n) increases with CH_4 for the compositions tested. We generated the spectra shown in Figure 5.13 by producing new fractal input files using the Mahjoub optical constants. These files were then used to replace the Khare files in our `SMART` inputs for the nominal $CH_4/CO_2 = 0.21$ case B spectrum. In addition, we generated a spectrum to test the Hasenkopf Archean haze measurement by applying a scaling factor to the Khare optical constants to match the Hasenkopf n and k values at 532 nm. This spectrum is called "Khare-Hasenkopf" in the Figure 5.13 caption. Of course this does not account for differences expected in the spectral shape of Archean haze analogs across the UV-Visible-IR relative to the Titan haze analogs.

Besides affecting the top-of-atmosphere spectrum, these different optical constants alter how much radiation can reach the surface under a haze. We find that, for the Mahjoub 1%, 2%, 5%, and 10% CH_4 optical constants, 0.92, 1.11, 1.13, and 1.16 times the nominal (Khare) total integrated 0.37-1 μm flux reaches the surface of the planet. For the Khare-Hasenkopf spectrum, which shifts both the real and imaginary refractive indices to larger values, this drops to 0.89 times the nominal flux. The Mahjoub constants do not extend shortward of 0.37 μm, but we should anticipate variation at these shorter wavelengths as well.

The variation in surface-incident flux shows us that we should expect differences in the hazy Archean climates we calculate depending on the optical constants used. We tested how the Hasenkopf Archean measurement might impact the climate for a $pCO_2 = 0.01$ and $CH_4/CO_2 = 0.2$ atmosphere. The nominal Khare constants produce a surface temperature of 272 K for this atmosphere. The "Khare-Hasenkopf" optical constants yield a cooler temperature of 267 K, which is expected because these optical constants produce a haze with more efficient scattering and absorption. This difference in temperature is smaller than the difference of using spherical versus fractal particles: our comparison to the Haqq-Misra et al. (2008) study in Section 5.4.2 shows that particle shape can result in temperature differences > 10 K. A full treatment of the impact of varied optical constants using the coupled photochemical-climate model to generate new self-consistent atmospheres and climates is outside the scope of our present study.

Updated haze optical constants generated under Archean Earth-like laboratory conditions (rather than Titan-like conditions) to produce plausible Archean-analog haze compositions would be of immense value to future studies of organic hazes in Earthlike atmospheres, including exoplanets, and would allow updates of the results presented in this study. Due to the properties of fractal hazes, these particles are relatively transparent at wavelengths longer than approximately the visible range, so measurements of refractive indices at visible wavelengths in particular would allow us to improve our estimates of the climatic impacts of this haze. In addition, better constraints on Archean UV refractive indices would allow us to better quantify how good a UV shield these hazes actually are.

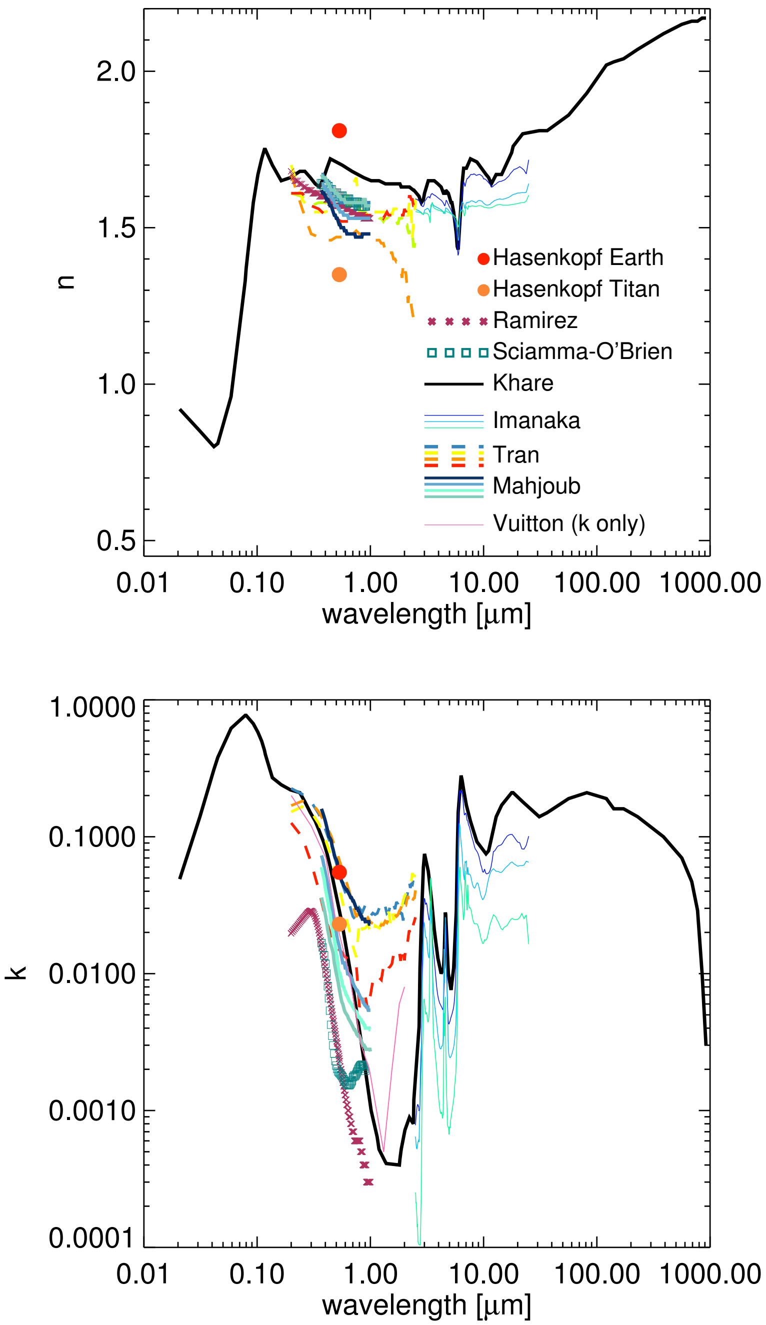

Figure 5.12: This shows the diversity of optical constants measured by several studies. The studies the figure key refers to are: Hasenkopf et al. (2010); Ramirez et al. (2002); Sciamma-O'Brien et al. (2012); Khare et al. (1984a); Imanaka et al. (2012); Tran et al. (2003); Mahjoub et al. (2012); Vuitton et al. (2009). Note in particular the single point measured under Archean Earth-like laboratory conditions by Hasenkopf et al. (2010).

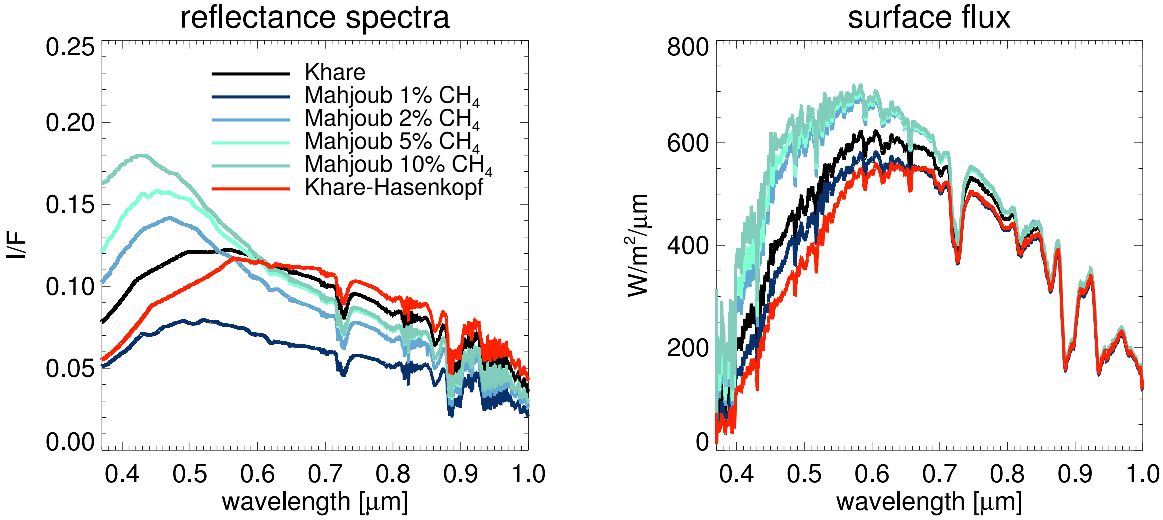

Figure 5.13: A comparison of reflectance spectra and surface flux spectra using Khare et al. (1984a) and Mahjoub et al. (2012) optical constants, plus a spectrum generated by shifting the Khare constants to match the Archean haze refractive indices measured by Hasenkopf et al. (2010) at 532 nm (called “Khare-Hasenkopf”).

5.5 Concluding remarks

In this chapter, we considered the habitability and spectrum of hazy early Earth. Despite the fainter young sun and geochemical constraints on CO_2, it is possible that habitable conditions existed on our planet even in the presence of a global haze deck. This haze would have produced strong spectral features that may be visible on distant exoplanets. In the next chapter, we will discuss the formation and detectability of organic haze on Archean-analog exoplanets orbiting several spectral types of stars. Because this haze is photochemically-produced, its production is a strong function of the UV spectral energy distribution of the host star. On stars where hazes are present on Archean analog worlds, detectability will vary depending on factors such as haze thickness, telescope instrumentation, and star-planet system distance.

Chapter 6

PALE ORANGE DOTS: THE IMPACT OF ORGANIC HAZE ON THE HABITABILITY AND DETECTABILITY OF EARTHLIKE EXOPLANETS

6.1 Introduction

As we discussed in Chapter 5, atmospheric hazes may frustrate attempts to characterize exoplanets with future telescopes. Therefore, it is important to understand which planets are more likely to form them. Hazes or clouds have been observed in the transit transmission spectra of several exoplanets (Bean et al., 2010; Kreidberg et al., 2014; Knutson et al., 2014a,b; Sing et al., 2011). However, the planets that have been characterized thus far are sub-Neptunes or larger and orbit close to their host stars with very warm upper atmospheres (typically $>$ 1000 K). From observations of planets in our own solar system we know that photochemical hazes occur frequently on rocky worlds whose atmospheres are as different as Venus (see Chapter 4), Titan, and even Pluto (Rannou & Durry, 2009). Since hazes are likely to be common, spanning a wide range of planet sizes from terrestrials to giants, it is important to understand the planetary conditions in which they are most likely to occur and the characteristics of the host star spectrum most likely to form them.

The best constrained example of a hazy terrestrial planet in the habitable zone of its parent star is provided by the ancient Earth. Hazy Archean Earth (Chapter 5) is interesting to consider as a distinctly different phase of our planet's evolution: it is a habitable (and inhabited) world whose spectrum bears little resemblance to our planet today (Figure 5.6). Because CH_4 can be produced by several abiotic processes (Etiope & Sherwood Lollar, 2013; Guzmán-Marmolejo et al., 2013; Kasting, 2005; Kelley et al., 2005), and CH_4-producing metabolisms (i.e., methanogenesis) are simple and evolved early on Earth (Kharecha et al., 2005; Ueno et al., 2006; Woese & Fox, 1977), Earthlike exoplanets with organic haze may be common. Chapter 5 examined the spectra and habitability of hazy Archean Earth. In this Chapter, we examine haze production on Archean-analog worlds orbiting F, G, K, and

M dwarf stars.

6.2 Methods and model inputs

For our study of haze formation around different types of stars, we use the same self-consistent types of photochemical-climate simulations we employed in Chapter 5. We present an analysis of organic haze production for Archean-analog planets orbiting several types of stars, and we show spectra of hazy words orbiting different stars to help guide future telescope observations of hazy habitable exoplanets. With the spectra we generate, we use instrument simulators with realistic noise sources for JWST and a future 10-meter class space telescope described in Chapter 3 to predict the detectability of spectral features from haze-rich atmospheres.

The stellar spectra we use in our models include the Archean Sun (2.7 Ga), the modern Sun, AD Leo (M3.5V), T3200, GJ 876 (M4V), ϵ Eridani (K2V) and σ Boötis (F2V). This stellar sample spans a range of stellar activity levels, UV fluxes, and UV spectral slopes.

As before, our modern solar spectrum was modeled by Chance & Kurucz (2010), and our "Archean" Sun uses a modified spectrum based on the wavelength-dependent solar evolution correction from Claire et al. (2012) for 2.7 Ga. This correction scales the absolute level of flux and accounts for the higher levels of solar activity, and therefore more UV radiation expected from a younger Sun.

To test the impact of the UV spectrum of M dwarfs on haze generation, we compare results from M dwarfs with different activity levels. M dwarfs can be highly active with frequent high-energy flares, although older M dwarfs may be more quiescent (West et al., 2008). For a perfectly quiet M dwarf, we use "T3200", a modeled quiescent M dwarf with no chromosphere and a temperature of 3200 K. Although this "star" is not physically realistic, is represents a useful lower bound for incident UV radiation on a planet. For a highly active flaring star, we use a time-averaged observed spectrum of AD Leo, an M dwarf with frequent flare events (Hawley & Pettersen, 1991; Hunt-Walker et al., 2012). Our AD Leo spectrum is discussed in Segura et al. (2005). We also test haze generation using a spectrum for GJ 876, a known M4V planet host (Von Braun et al., 2014). The spectrum of GJ 876 is described in Domagal-Goldman et al. (2014) based on the spectrum reported in France et al. (2012).

In addition to the M dwarfs, we use K2V (ϵ Eridani) and F2V (σ Boötis) spectra described in Segura et al. (2003). ϵ Eridani (3.2 pc) is a young star encircled by a dust ring (Greaves et al., 1998). ϵ Eridani is also chromospherically active (Noyes et al., 1984). σ Boötis is an F2V star 15.5 pc away.

For all stars except the modern Sun, we scale their total integrated fluxes to the solar constant for Earth at 2.7 Ga (0.8×1360 W/m^2) to compare with our Archean results. Unlike the Archean Sun, the other stars do not include a wavelength-dependent stellar evolution correction. Figure 6.1 shows a comparison of the stellar spectra in the UV, visible, and near infrared (NIR) together with the UV cross-sections of several important gases. These stellar spectra are available for download on the VPL Spectral Database[1].

The nominal results presented here are for $pCO_2 = 0.01$ bar, and $CH_4/CO_2 = 0.2$ (Figure 6.2). Note that the CH_4/CO_2 ratios we refer to apply to the planetary surface because CH_4 does not follow an isoprofile in the atmospheres we simulate. CO_2, on the other hand, is well-mixed. This CO_2 level is consistent with the paleosol measurements of Driese et al. (2011), and this CH_4/CO_2 ratio is sufficient to form organic haze on Archean Earth. Molecular oxygen (O_2) is set at a mixing ratio of $1{\times}10^{-8}$, corresponding to a time after the origin of oxygenic photosynthesis but prior to oxygen accumulation in the atmosphere. Haze particles are treated as fractals composed of 0.05 μm-sized spherical monomers, similar to the size of the monomers in Titan's hazes (Rannou et al., 1997; Tomasko et al., 2008) and the same size of the monomers used by Wolf & Toon (2010) in their study of fractal haze on Archean Earth. Haze scattering properties are derived using the optical constants of Khare et al. (1984a) through the fractal mean field approximation (Botet et al., 1997). A discussion of our choice of optical constants and caveats of this choice is in Section 5.4.5.

As before, we use the HITRAN 2012 linelists to generate our spectra (Rothman et al., 2013). The solar zenith angle is set at 60° for the direct imaging spectra, which approximates the average incoming solar flux at quadrature. As in `Atmos`, we use fractal particles with scattering, absorption, and extinction efficiencies generated with the mean field approximation (Botet et al., 1997) for our $/mathttSMART$ simulations, and we use the optical

---

[1] https://depts.washington.edu/naivpl/content/spectral-databases-and-tools

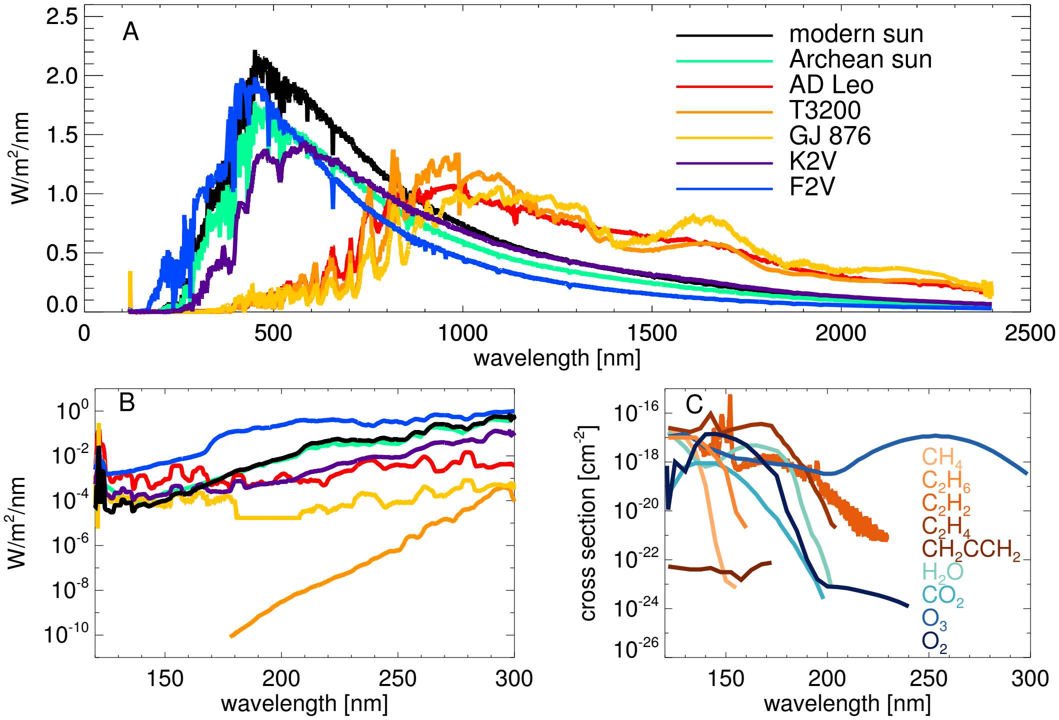

Figure 6.1: Panel (A) displays all of the stellar spectra investigated by this study. Panel (B) zooms into the UV region of the stellar spectra. In panel (C), UV cross sections of several interesting gases are shown with the same x-axis range as panel B.

constants from Khare et al. (1984a).

A surface pressure of 1 bar is assumed in all situations, although recent work has suggested lower pressures for the Archean (Som et al., 2016). Each planet was placed at an equivalent distance from its host star so that it receives approximately the same amount of incoming shortwave radiation as the Archean Earth, with the exception of the Archean-analog Earth orbiting the Modern Sun, which receives the modern Earth's level of insolation.

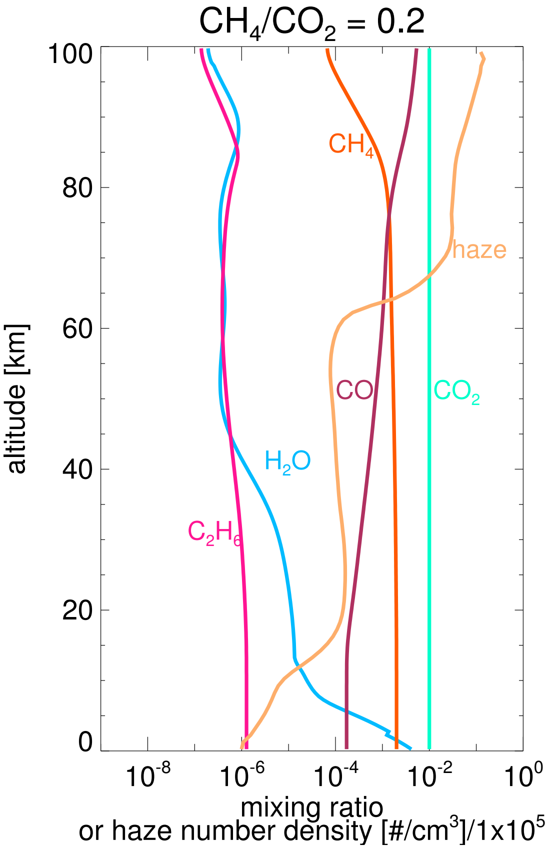

Figure 6.2: The gas profiles for the nominal atmosphere investigated by this study for $CH_4/CO_2 = 0.2$ and $pCO_2 = 0.01$ bar. This planets orbits the Archean sun (2.7 Ga) and corresponds to a “Case A” planet in the Chapter 5.

6.3 Results

In this section, we explore the factors affecting the formation of organic haze in Archean-analog planets orbiting stars of different spectral types, including the modern Sun. We then generate the spectra for the resultant planets. The strong UV and blue-wavelength absorption feature created by the haze may provide a UV shield for life on planetary surfaces, and we consider the strength of such a shield for each of the planets we simulate. Lastly, we consider the detectability of hazy spectral features using instrument simulators for JWST and a 10-m LUVOIR telescope.

6.3.1 Haze Formation and Surface Temperature Around Different Stellar Types

To explore the effect of the stellar UV spectrum on haze formation, we ran `Atmos` to obtain chemically and climatically self-consistent results for Archean-like atmospheres under the influence of different host star spectra. Most of these models were run with $CH_4/CO_2 = 0.2$. In the case of AD Leo and the K2V star, which did not form hazes with $CH_4/CO_2 = 0.2$, we ran additional atmospheres with higher CH_4/CO_2 ratios until a haze formed. These additional simulations have $CH_4/CO_2 = 0.9$ and 0.3, respectively. The F2V and T3200 stars did not form hazes at any CH_4/CO_2 ratios tested here (up to $CH_4/CO_2 = 2$).

The compositions of our planets' atmospheres are strongly influenced by their host star's spectrum despite equivalent gaseous surface boundary conditions, underscoring the importance of photochemistry in exoplanet atmospheres. Table 6.1 shows the diurnally averaged stellar UV fluxes incident on the planet for near-UV (NUV, 300-400 nm), mid-UV (MUV, 200-300 nm), and far-UV plus Lyman-alpha (FUV, 120-200 nm) for each star. Also shown in Table 6.1 are flux ratios of FUV/MUV and FUV/NUV. In general, two factors matter to haze formation: the absolute level of UV flux, and the ratio of FUV relative to MUV and NUV. In general, planets orbiting stars with higher absolute levels of UV flux incident on a planet, and higher ratios of FUV relative to MUV and NUV do not form hazes as readily – or do not form hazes at all – compared to stars with lower ratios of FUV to MUV and NUV. The exception to this higher FUV trend is T3200, whose very low UV flux drives very little photochemistry in general.

Table 6.2 presents a comparison of the total integrated column densities of key gases in the atmospheres of our simulated environments, including some of the hydrocarbons involved in haze formation and oxygen radicals involved in destroying hydrocarbons. The values presented in this table are divided by the nominal total integrated column density for Archean Earth (with $CH_4/CO_2 = 0.2$) at 2.7 Ga, and the diversity of gas abundances for each star clearly illustrate how photochemistry impacts these atmospheres. In this table, C_4H_2 and C_5H_2 are direct precursors to haze particles according to our simplified haze formation scheme as discussed above (Pavlov et al., 2001a). Ethane (C_2H_6) forms from photochemical reactions involving CH_4 and may be important for warming organic-rich

Table 6.1: The diurnally averaged UV fluxes from these stars at the top of the atmosphere for NUV (300-400 nm), MUV (200-300 nm), and FUV (122-200 nm) in W/m^2. The last two columns show FUV divided by MUV and FUV divided NUV for each star to show the contribution of the wavelengths that dissociate H_2O and CO_2.

Star	NUV (W/m^2)	MUV (W/m^2)	FUV (W/m^2)	FUV/MUV	FUV/NUV
Modern Sun	44.2	7.01	0.047	0.0067	0.0011
Archean Sun	31.2	4.79	0.041	0.0088	0.0013
AD Leo	0.42	0.17	0.063	0.37	0.15
GJ 876	0.51	0.0095	0.0020	0.21	0.0039
T3200	0.33	0.0020	∼0	∼0	∼0
K2V	15.2	1.27	0.014	0.011	0.0007
F2V	57.7	23.1	2.1	0.092	0.03

atmospheres (Haqq-Misra et al., 2008).

Stars that produce higher levels of FUV radiation compared to NUV and MUV tend to generate larger quantities of haze-destroying oxygen radicals because FUV can dissociate CO_2 and H_2O. An exception is GJ 876, which also has a higher proportion of FUV relative to NUV and MUV; however GJ 876 has a lower absolute level of UV flux at these wavelengths. A test scaling GJ 876's total amount of UV radiation to the total level of UV radiation produced by AD Leo diminishes GJ 876's haze production rate. Similarly, a test decreasing AD Leo's total UV flux to that of GJ 876 increases its haze production rate. Consequently both the slope of the incident radiation (ratio of FUV to NUV or MUV) and the overall intensity of that radiation appear to affect haze production. A well-characterized UV spectrum of the host star and good constraints on the planet's orbit will be important considerations for predicting incident UV radiation on a planet, the generation of hazes using photochemical models, and general constraints on photochemistry and climate of a planet.

In addition to the gas profiles, `Atmos` was also used to calculate the temperature profiles for the simulations shown in Table 6.2. The results of these climate calculations are provided

Table 6.2: This table contains ratios of the total integrated column densities of gases in the atmospheres of Archean-analog planets around different spectral types divided by the total integrated column densities of gases for Archean Earth orbiting the Sun. A value of 1 indicates a column density identical to our nominal Archean Earth atmosphere. These planets have $CH_4/CO_2 = 0.2$ except "AD Leo - haze" which has $CH_4/CO_2 = 0.9$ and "K2V - haze" which has $CH_4/CO_2 = 0.3$. Note C_4H_2 and C_5H_2 are direct precursors to hydrocarbon haze particles (Pavlov et al., 2001a).

Star	O	O_2	O_3	OH	NO	C_2H_6	C_4H_2	C_5H_2
Modern Sun	0.34	0.76	0.26	1.29	1.74	2.46	1.39	2.11
AD Leo - no haze	27.05	6.95	0.1	14.82	3.15	5	$1.86\text{x}10^{-5}$	$1.00\text{x}10^{-6}$
AD Leo - haze	12.69	2.15	0.022	3.24	4.21	19.2	0.069	0.024
GJ 876	0.076	0.68	0.33	1.1	10.6	1.74	1.25	5.21
T3200	0.001	0.95	0.44	0.0026	1.82	4.96	$1.27\text{x}10^{-13}$	$1.08\text{x}10^{-15}$
K2V - no haze	1.31	2.85	0.71	2.6	0.71	3.37	$3.84\text{x}10^{-4}$	$4.41\text{x}10^{-4}$
K2V - haze	0.5	2.66	0.31	0.99	1.65	2.33	1.28	5.94
F2V	78.64	265.5	169.4	34.11	0.19	1.74	$9.11\text{x}10^{-11}$	$1.02\text{x}10^{-12}$

Table 6.3: The surface temperatures of planets orbiting each spectral type for $CH_4/CO_2 = 0.2$ except "AD Leo - haze" which has $CH_4/CO_2 = 0.9$ and "K2V - haze" which has $CH_4/CO_2 = 0.3$. We also show the top-of-atmosphere planetary albedo, incoming shortwave radiation, outgoing shortwave radiation, and outgoing longwave radiation.

Star	Surface Temp	Planetary Albedo	Incoming shortwave (W/m^2)	Outgoing shortwave (W/m^2)	Outgoing longwave (W/m^2)
Modern Sun	299 K	0.216	342	74.6	267
Archean Sun	272 K	0.238	278	66.4	212
AD Leo - no haze	310 K	0.087	278	24.2	253
AD Leo - haze	317 K	0.067	278	18.7	259
GJ 876	301 K	0.137	278	38.3	240
T3200	305 K	0.093	278	26.3	252
K2V - no haze	297 K	0.202	278	56.4	221
K2V - haze	282 K	0.210	278	58.7	219
F2V	277 K	0.322	278	89.6	188

in Table 6.3. The diversity of surface temperatures in this table is due to the climatic effects of haze thickness, different greenhouse gas abundances, and the host star spectral energy distribution. These effects are discussed in detail in the sections below.

To illustrate these atmospheres' gas, haze, and temperature profiles, these quantities are shown for the $CH_4/CO_2 = 0.2$ planets in Figure 6.3. The profiles for the nominal Archean environment are shown with the green lines for comparison.

Below, we present an analysis of haze formation and its climatic consequence for each host star type compared to our nominal Archean results to explore the differing atmospheric compositions and temperatures of these worlds. Note that we do not extensively discuss Archean Earth orbiting the 2.7 Ga sun below because this type of planet has already been considered in detail in our previous work shown in Chapter 5.

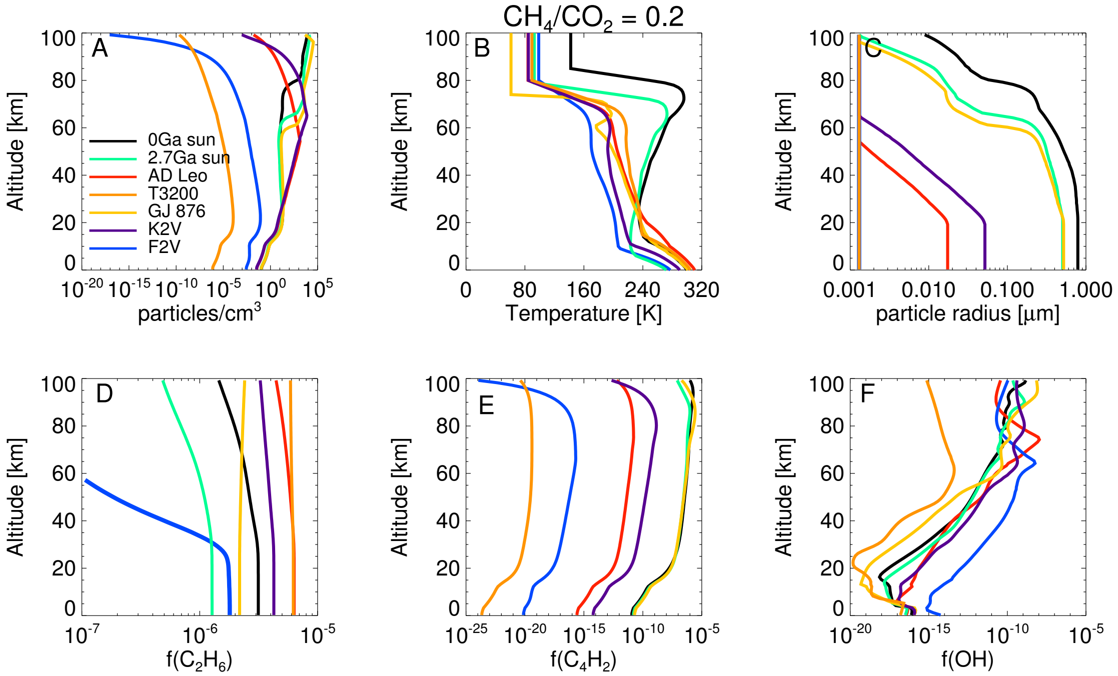

Figure 6.3: Displayed here are: A) the number density of haze particles, B) the temperatures of the $CH_4/CO_2 = 0.2$ atmospheres, C) radii of haze particles, D) the C_2H_6 mixing ratios, E) the mixing ratio of C_4H_2 particles, which is the primary vector that condenses directly out to form aerosols in our chemical scheme, and F) the mixing ratio of OH radicals, to illustrate the buildup of such oxygen species in the atmosphere of the F star and their scarcity in the atmosphere of the T3200 star.

6.3.2 Hazes with the Archean solar constant

We present a detailed discussion of haze formation for Archean Earth orbiting the sun at 2.7 billion years ago in Chapter 5. Haze formation for $pCO_2 = 0.01$ begins to noticeably impact the Earth's spectrum at $CH_4/CO_2 = 0.18$. The temperature of the planet's surface drops from ∼284 K when no haze is present to 272 K when a haze is in place at $CH_4/CO_2 = 0.2$. Although this surface temperature is below the freezing point of water, 3D climate studies have suggested planets with global average temperatures down to 250 K can still maintain stable open ocean waters near the equator (Charnay et al., 2013), so this cold temperature can still be considered "habitable" as the planet still supports liquid water at the surface.

6.3.2.a Hazes with the modern solar constant

We find that larger haze particles form around the planet orbiting the modern Sun compared to a planet orbiting a star with the Archean (2.7 Ga) solar constant. Our work in Chapter 5 found that haze particle size increases with the temperature of a planet's atmosphere, and the atmosphere of the planet around the modern Sun is warmer than the Archean due to the increased solar constant. At $CH_4/CO_2 = 0.2$, $T_{surf} = 299$ K at 0 Ga and $T_{surf} = 272$ K for 2.7 Ga. Particle coagulation proceeds more efficiently in a hotter atmosphere for the temperatures simulated here (Section 5.3.1.b). Accordingly, haze particles in the hotter 0 Ga atmosphere (Figure 6.3) reach a maximum radius of 0.79 μm, and the Archean particles only reach a maximum radius of 0.51 μm.

Haze formation is also more efficient in the modern planet's atmosphere because the present day solar spectrum is less active at UV wavelengths shorter than ∼150 nm (Figure 6.3) when compared to the early Sun. Therefore, it tends to generate smaller quantities of the types of oxygen species that destroy hydrocarbon haze precursors from H_2O and CO_2 photolysis (Table 6.2, and see Section 6.4.1 for a discussion of these processes).

6.3.2.b M dwarfs

T3200 has very low UV flux, and we find that it does not generate haze particles even for CH_4/CO_2 ratios exceeding unity. T3200 is unable to dissociate CH_4 or C_2H_6 to drive the haze-formation process, and the densities of haze-forming gases C_4H_2 and C_5H_2 in the T3200 planet's atmosphere are 13-15 orders of magnitude smaller than in the nominal Archean Earth atmosphere (Table 6.2). It may be unlikely that very quiet M dwarfs will host Earthlike planets with hydrocarbon hazes.

AD Leo outputs considerably more UV flux than T3200, but we find that it is also inefficient at generating hazes compared to the Archean and modern Sun. A scant haze of small particles (maximum particle radius = 0.017 μm) is present at $CH_4/CO_2 = 0.2$ and is spectrally indistinguishable from a world without haze (Section 6.3.3). The CH_4/CO_2

ratio must reach 0.9 before AD Leo's haze begins to alter the spectrum, but even then, the impact is small as discussed in Section 6.3.3.

AD Leo's inability to efficiently generate hydrocarbon haze is a result of the relatively large quantities of oxygen radicals generated in the atmosphere of its planet from its high FUV flux (Table 6.2). AD Leo is a highly active M dwarf and produces excess flux at $\lambda < 170$ nm compared to every other star considered except the F dwarf star. This spectral region is coincident to the peaks of the CO_2 and H_2O cross sections. Therefore, it is relatively efficient at photolyzing these gases to produce oxygen species such as O and OH that can destroy the higher order hydrocarbons necessary for haze formation (Section 6.4.1). For an Archean analog orbiting AD Leo, the "source" for the higher-order hydrocarbons goes up for these higher UV fluxes, but not as quickly as the "sink" for these species. Because of this, we find that even at the CH_4/CO_2 ratios exceeding unity that were tested, the haze around the AD Leo planet remains optically thin in the UV.

Our results for AD Leo and T3200 seem to indicate that Earthlike planets around M dwarfs are unlikely to have organic haze, but this is not the case for GJ 876. Table 6.2 shows how this star, like T3200, produces smaller amounts of hydrocarbon-destroying oxygen species due to its lower levels of UV radiation relative to every other star except T3200 (Table 6.1). However, unlike T3200, this star has sufficient UV flux <150 nm and is able to dissociate CH_4 to initiate the formation of haze. The low abundance of oxygen radicals it produces does not efficiently destroy higher order hydrocarbons. Haze particles for the GJ 876 planet reach radii of 0.52 μm at $CH_4/CO_2 = 0.2$, similar to the size of the particles around the Archean Sun. Haze begins to noticeably alter the spectrum for the GJ 876 planet at $CH_4/CO_2 = 0.12$, which is a lower ratio than for the equivalent planet orbiting the Archean Sun, for which the spectral impact of haze begins to become apparent at about $CH_4/CO_2 = 0.18$. In fact, GJ 876's planet exhibits the lowest CH_4/CO_2 ratio able to form a haze among the stars tested here. Hazy atmospheres around planets orbiting M dwarfs like GJ 876 may therefore occur at lower CH_4/CO_2 ratios than for other types of stars.

The Archean-analog planets around the M dwarfs are warmer than the one orbiting around the Archean Sun despite having equivalent levels of total incident radiation at the top of their atmospheres. For $CH_4/CO_2 = 0.2$, $T_{surf} = 310$ K for the AD Leo planet, T_{surf}

= 305K for the T3200 planet, and T_{surf} = 301 K for the GJ 876 planet. These relatively high temperatures are caused by three factors described below.

The first reason for the warm M dwarf planets, discussed in Kopparapu et al. (2013), is that M dwarfs produce the bulk of their radiation in the near-infrared where Rayleigh scattering is weak and gaseous absorbers, particularly water vapor, have broad absorption features. These factors act to reduce the planetary albedo relative to a planet with the same atmospheric composition, but orbiting a Sun-like star (Table 6.3). So, a planet around an M dwarf at the equivalent flux distance of a solar-type star will naturally produce warmer temperatures with an equivalent atmosphere.

The second reason for the warm M dwarf temperatures is that these atmospheres contain large amounts of greenhouse gases. Notice from Table 6.2 that at $CH_4/CO_2 = 0.2$, AD Leo and T3200 are able to build up about 5× as much C_2H_6 than the nominal Archean Earth, and C_2H_6 is a greenhouse gas. Accordingly, these two planets are warmer than the GJ 876 planet, which only has 1.74 × as much C_2H_6 as the nominal Archean planet. These findings are consistent with the results of Domagal-Goldman et al. (2011), which determined that AD Leo and T3100, a similar star to the T3200 star used here, build up larger amounts of C_2H_6 than a planet orbiting the Sun. It may seem counter-intuitive that C_2H_6 accumulates in the atmosphere of the T3200 planet given that photochemistry is not efficient in atmosphere of this star's planet. However, photolysis of NO_2 and subsequent oxidation of CH_4 can generate C_2H_6 in the atmosphere of the T3200 planet; we discuss this in Section 6.4.2.

The final reason for the warm temperatures of M dwarf planets with haze is due to the spectral properties of the haze itself. The bulk of the M dwarf radiation arrives between 700 and 2500 nm (Figure 6.1), but fractal particle extinction efficiency decreases by 1-2 orders of magnitude in the NIR compared to the visible, so the haze is relatively transparent at these wavelengths (Figure 6.1). Therefore, cooling from organic haze is far less relevant to planets orbiting M dwarfs than it is for other stellar types with bluer spectra. This is why the hazy AD Leo planet with $CH_4/CO_2 = 0.9$ is actually hotter (T_{surf} = 317 K) than the haze-free AD Leo planet (T_{surf} = 310 K); the hazy AD Leo planet has more methane and its haze does not effectively scatter the incident radiation back to space. Implications of these hazes' low NIR opacities are discussed in Section 6.4.3.

Although the hazy GJ 876 planet has a warmer surface temperature than the 0 Ga planet, the temperature feedbacks on particle size discussed in the context of the solar-type stars do not apply here because this star emits comparatively little UV for the haze to absorb and warm the upper atmosphere where particle coagulation proceeds. As can be seen in Figure 6.3, GJ 876 does not show a prominent stratospheric temperature inversion that the 0 Ga and 2.7 Ga solar-type planets have.

6.3.2.c K2V Dwarf

The K2V star has excess UV flux at wavelengths < 170 nm compared to the Archean Sun, as does AD Leo (Figure 6.1) – although with about one order of magnitude lower flux. The K2V star has a relatively high level of both FUV flux and FUV/MUV, and it is able to produce oxygen radicals and unable to form a thick haze at $CH_4/CO_2 = 0.2$. However, it is efficient at forming haze at slightly higher CH_4/CO_2 ratios. For $CH_4/CO_2 = 0.2$, the K2V planet generates a sparse haze of very small particles (radius < 0.05 μm) that produce a negligible spectral effect, while the Archean Earth haze particles are an order of magnitude larger. At $CH_4/CO_2 = 0.3$, the particles reach a radius of 0.51 μm, similar to the size of the particles for the planets orbiting the Archean Sun and GJ 876 planet.

For a planet with $CH_4/CO_2 = 0.2$, the K2V planet has an average surface temperature of 297 K, and at $CH_4/CO_2 = 0.3$, the average surface temperature drops by 15 K to 282 K due to the accumulation of haze and haze-induced cooling. This cooling is not as strong as for the hazy Archean planet orbiting the sun because the K dwarf spectrum is shifted slightly redward of the G dwarf spectrum where the haze is more transparent. Also, this hazy planet has more CH_4 than the corresponding hazy $CH_4/CO_2 = 0.2$ planet for the Archean sun so it is warmer.

6.3.2.d F2V Dwarf

We find that the F dwarf planet does not form a haze due to high incident UV flux. The F dwarf spectrum produces more UV flux than all the other stars we consider at all wavelengths except at Lyman α ($\lambda = 121.6$ nm). Its high UV flux efficiently photodissociates hydrocarbon species and generates extremely large quantities of oxygen radicals (Table 6.2) compared to the other stars (Section 6.4.1). This is consistent with the previously noted ability of F stars to generate amounts of oxygen large enough to significantly impact photochemistry (Domagal-Goldman et al., 2014). It is not possible to generate hazes in the F2V planet's atmosphere even with $CH_4/CO_2 > 1$. This is because hydrocarbons are too efficiently destroyed in this type of atmosphere, although significantly more reducing conditions without CO_2 (i.e. more Titan-like) that would produce fewer oxygen radicals were not tested here.

The climate of the haze-free F star planet is relatively cool compared to other spectral types: the $CH_4/CO_2 = 0.2$ planet has a mean surface temperature of 277 K despite its clear sky. This low temperature is due to the F star spectral energy distribution peaking near 400 nm, a wavelength at which Rayleigh scattering from the planet's atmosphere efficiently reflects much of the incident energy back to space, so that a larger fraction of the F star incident radiation avoids NIR absorption bands (Kopparapu et al., 2013). Therefore, at an equivalent flux distance, an F star planet would naturally be cooler than a planet orbiting a star with a redder spectrum.

6.3.3 Spectra

Reflectance, thermal emission, and transit transmission spectra for the Archean-analog planets are presented in Figure 6.4 for all stellar spectral types studied here. All of these planets have $CH_4/CO_2 = 0.2$ except the spectrum labeled "K2V - haze", which has $CH_4/CO_2 =$ 0.3 and "AD Leo - haze" which has $CH_4/CO_2 = 0.9$, the ratios required to form haze for these planets. At $CH_4/CO_2 = 0.2$, planets around AD Leo, T3200, the K2V star, and the F2V star do not have spectrally apparent hazes in their atmospheres, but the Archean Sun, modern Sun, and GJ 876 planets do. As noted before, T3200 and the F2V star do not generate hazes even at CH_4/CO_2 ratios greater than unity.

Haze absorbs strongly at blue and UV wavelengths, causing the reflectance spectra (top panel of Figure 6.4) of the hazy worlds to have lower albedos at these wavelengths. When the haze is thick enough to affect the spectrum, it creates a large absorption feature at these

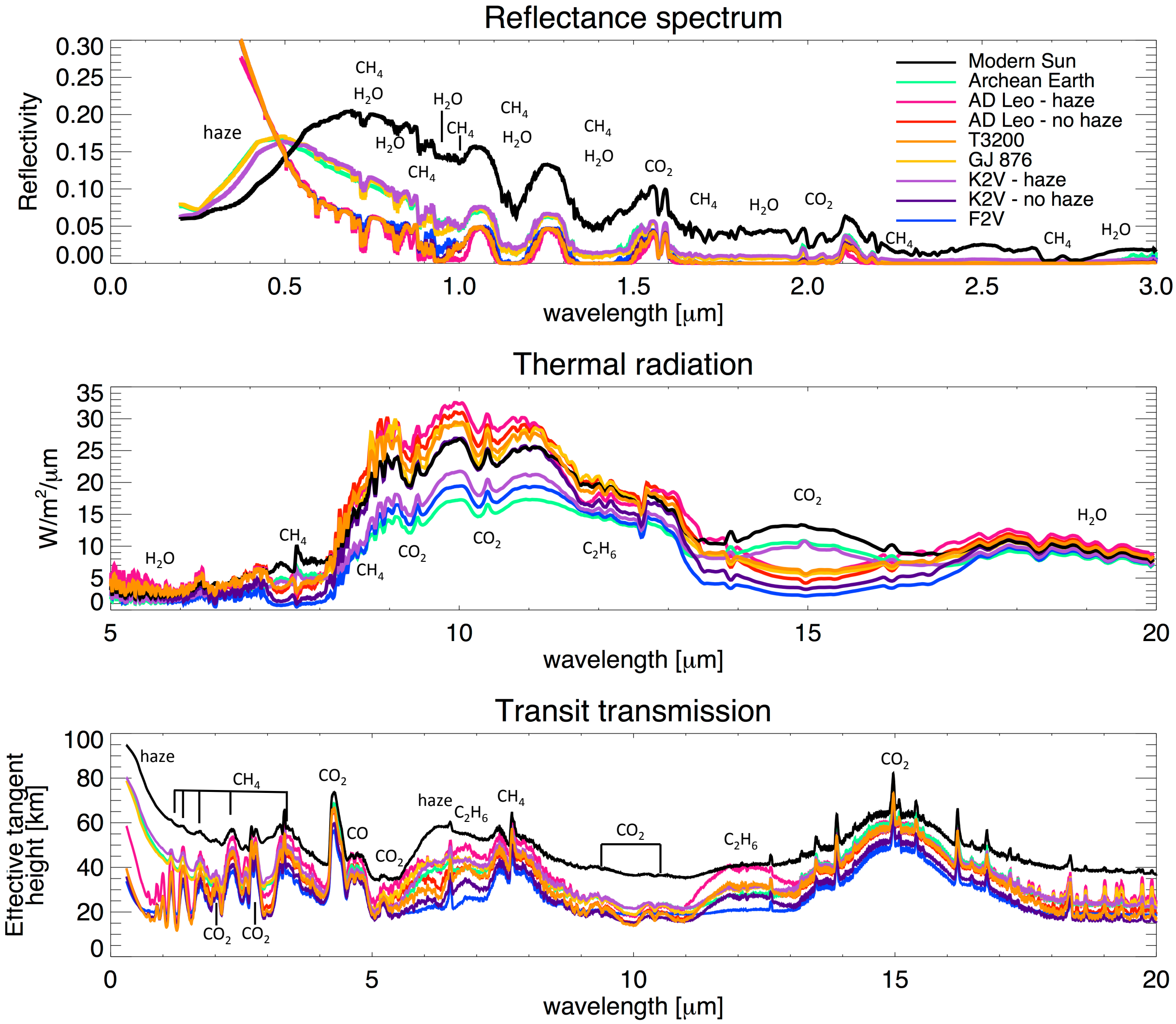

Figure 6.4: Reflectance spectra (top panel), thermal radiation (middle panel) and transit transmission spectra (bottom panel) for the Archean Earth-type planets around varied spectral types. The transit transmission spectra show the effective tangent height, which is the minimum altitude the atmosphere is transparent to as a function of wavelength for light traveling tangent to the planet surface. All spectra shown are for $CH_4/CO_2 = 0.2$ except spectrum labeled "K2V - haze", which has $CH_4/CO_2 = 0.3$, and the "AD Leo - haze" spectrum, which has $CH_4/CO_2 = 0.9$.

short wavelengths. Thus, rather than the Rayleigh scattering-induced increase in reflectivity at short wavelengths seen for the haze-free planets, hazy worlds produce their peak spectral brightness at visible wavelengths. The UV-blue haze absorption feature can be seen for the Archean and modern Sun, GJ 876, and hazy K2V planets, although the sparse haze around the $CH_4/CO_2 = 0.9$ AD Leo planet is thin enough to be almost spectrally indistinguishable from a clear sky world (Figure 6.4).

There are large spectral differences for the planet orbiting the modern sun compared to the stars emitting Archean-like levels of radiation. These differences are caused by the different temperature structure of these atmospheres, which caused differences in particle radii. As pointed out in Chapter 5, hotter atmospheres decrease coagulation timescales, which leads to larger particle sizes. The modern Sun planet has higher atmospheric temperatures (Figure 6.3), which causes the particles to have shorter coagulation times, and for them to grow larger in our simulations. The modern Sun's planet has the peak of its reflectance spectrum at $\lambda \sim 0.7$ μm, compared to $\lambda \sim 0.5$ μm for the Archean, GJ 876, and K2V planets, and this is due to the particle size: the maximum radius of the Archean, GJ 876, and K2V haze particles plotted here is $\sim$0.5 μm versus $\sim$0.79 μm for the modern Sun's planet. Absorption and scattering efficiencies, Q_{abs} and Q_{scat} (see Chapter 2), are both larger for bigger fractal particles, and Q_{scat} also trends towards flatter wavelength-dependence as particle size grows (Figure 2.6). Increased absorption (higher Q_{abs}) deepens the short wavelength absorption feature produced by a thick haze of larger particles. Meanwhile, the larger scattering efficiency (higher Q_{scat}) at longer wavelengths for larger particles increases the brightness of the planet at these wavelengths, pushing the peak of the reflectance spectrum redward. This demonstrates the need to simulate particles in coupled photochemical-climate models to capture the effects of atmospheric temperature on particle size and the resulting impacts on the planetary spectrum.

The impact of haze on the temperature structures of the atmospheres simulated here can also be seen in the thermal radiation spectra (middle panel of Figure 6.4). Hazes absorb UV photons and warm the stratosphere similar to ozone on modern-day Earth by absorbing UV photons. Evidence of warm stratospheres (thermal inversions) in the hazy atmospheres can be seen in the thermal emission spectra as CH_4 and CO_2 in emission rather than absorption near 8 and 15 μm for the Archean Sun, modern Sun, and hazy K2V spectra. The haze around the GJ 876 planet, however, does not produce a strong thermal inversion because its star emits less UV radiation (see also its temperature profile in Figure 6.3). On the other hand, all of the M dwarf planets have warmer surface temperatures for the reasons discussed in Section 6.3.2.b, and this is apparent from the larger amounts of surface thermal radiation emitted by these worlds in the atmospheric window between roughly 9 and 11 μm. Ethane, a strong greenhoues gas, can be seen near 12 μm in all spectra as a photochemical consequence of the large quantities of methane in these atmospheres compared to modern day Earth.

Hazes also strongly impact transit transmission spectra. Our transit spectra (bottom panel of Figure 6.4) include the effect of atmospheric refraction (Misra et al., 2014a,b), and this makes it impossible to the probe below 15-20 km in altitude for all model planets, including those with haze-free atmospheres. For atmospheres with haze, minimum altitude transit observations can probe is set by the altitude where the haze becomes optically thick. Note that because all of these transit spectra sense altitudes in the stratosphere, water vapor cannot be detected. Stratospheres on habitable planets are dry; a wet stratosphere would indicate a planet undergoing a runaway greenhouse. The transit spectra of the hazy worlds exhibit a scattering slope in the visible and NIR due to a combination of haze scattering and Rayleigh scattering. The thick haze shown around the modern Sun in particular produces a relatively featureless, sloped spectrum in which absorption features from gases are obscured at visible and NIR wavelengths shorter than $\sim$2 μm. At longer IR wavelengths where the haze is relatively transparent, its impact on the transit transmission spectra is diminished, and absorption features, particularly for CO_2 and CH_4, become apparent even for the modern Sun spectrum.

The transit spectra are sensitive to hazes that are barely detectable in reflected light due to the longer path length taken by light in transit observations. The haze around the AD Leo planet with $CH_4/CO_2 = 0.9$ is scarcely distinguishable from a planet without haze in reflected light. However, the AD Leo haze is more apparent in the transit transmission spectrum compared to the haze-free planets.

As first discussed Chapter 5, there is an absorption feature from the haze itself near 6 μm that may allow remote identification of hydrocarbon hazes on exoplanets. This feature produces the increase in effective tangent height in the hazy transit transmission spectra at this wavelength. Ethane and CH_4 absorption overlaps with the haze's 6 μm absorption feature, but the haze feature can be distinguished by higher opacity centered around 6.3 μm. We focus on this feature in Figure 6.5, which compares the AD Leo planet with a sparse haze to the Modern Sun planet with a thick haze. The AD Leo planet has more CH_4 and C_2H_6 than the modern Sun's planet. There is a peak in the haze extinction coefficient near 6.3 μm, which causes an increase in absorption for the modern Sun planet. The AD Leo planet's spectrum in this region is controlled by the behavior of the CH_4 and C_2H_6 absorption cross-sections because its haze is very thin.

In addition to the 6 μm feature, there is a much weaker haze absorption feature near 3 μm that is most easily seen as a small bump in the modern Sun spectrum. The weakness of the 3 μm haze feature makes it unlikely to be detectable. Both the 6 μm and 3 μm features can be seen as peaks in the haze Q_{abs} curve in Figure 2.4. These peaks appear to be general features of organic haze and are not specific to our use of the Khare et al. (1984a) optical constants (Chapter 5) for a comparison of haze optical constants in the literature).

6.3.4 UV irradiance at the surface of hazy worlds

Organic hazes are strong absorbers at UV wavelengths (Figure 6.4) and so could potentially act as a UV shield for planetary surfaces. Fractal organic hazes could have provided a UV shield for the Archean (Wolf & Toon, 2010; Arney et al., 2016), which had an anoxic atmosphere and lacked the UV shield provided by O_2 and O_3 for modern Earth. As discussed in Chapter 5, wavelengths of UVC radiation ($\lambda < 0.280$ μm) are especially damaging to DNA molecules (Dillon & Castenholz, 1999; Pierson et al., 1992). On modern Earth, UVC is completely blocked by O_2 and O_3, but on planets without significant atmospheric O_2 (such as Archean Earth) another shielding agent would assist the development of land-based life.

Table 6.4 summarizes the UV flux at the surface (W/m^2) for UVA ($\lambda = 0.315$ - 0.400 μm), UVB ($\lambda = 0.280$ - 0.315 μm), and UVC ($\lambda < 0.280$ μm) radiation for each of our planets except the one orbiting T3200, which does not produce a physically meaningful

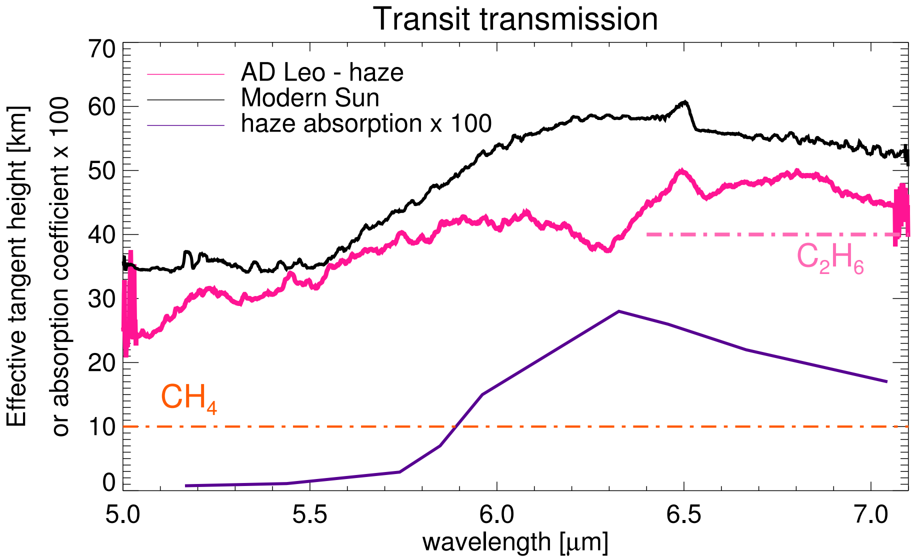

Figure 6.5: A zoom in on the region around 6 μm showing the transit transmission spectra of the modern Sun planet, which has the most optically thick haze of all the planets studied here, and the "AD Leo - haze" spectrum, which has a very thin haze but the largest amount of C_2H_6. The purple solid line shows the haze extinction coefficient (k, see Chapter 2) scaled by a factor of 100 to plot on the same y-axis, and the peak in this curve corresponds to the peak in the "modern Sun" spectrum. Dot-dashed lines show the wavelength ranges where CH_4 and C_2H_6 absorb. Absorption from haze occurs near 6.3 μm in the "modern Sun" spectrum, and absorption from C_2H_6 prominently occurs between 6.5 and 7 μm for the "AD Leo - haze" spectrum.

amount of UV radiation. For comparison, we also include the surface UV fluxes our model calculates for the actual modern day Earth atmosphere. Note that the "Archean Sun" results presented here are not the same as the results presented for UV shielding in Section 5.3.2. The haze for the "Archean Sun" here refers to simulations with $CH_4/CO_2 = 0.2$ for $pCO_2 = 0.01$, and this haze is slightly thinner than the one discussed in the context of UV shielding in Chapter 5, which referred to $CH_4/CO_2 = 0.21$ for $pCO_2 \sim 0.02$. The hazy "modern Sun" planet has less UVA and UVB at the surface compared to the actual modern day Earth, illustrating how the broadband UV absorption by organic haze cuts down UVA and UVB far better than gases in the actual modern day atmosphere. The haze-free UV fluxes we quote here are comparable to the fluxes for similar stars found by Rugheimer et al.

Table 6.4: The integrated UV fluxes (W/m^2) at the surface in UVA, UVB, and UVC for all of the spectra presented in our study except T3200, which is not meaningful to consider here. "Modern Day Earth" refers to the actual modern (haze-free) planet. All UV fluxes are presented for a solar zenith angle of 60°. As before, all of our planets have $CH_4/CO_2 = 0.2$ except the hazy K2V planet ($CH_4/CO_2 = 0.3$), the hazy AD Leo planet ($CH_4/CO_2 = 0.9$), and the modern day Earth which has the actual modern atmosphere. The stars here are assumed to be at a solar zenith angle of 60°.

Star	UVA	UVB	UVC
Modern Day Earth	29	0.45	~0
Modern Sun - no haze	29	5	1.26
Modern Sun - haze	0.72	0.012	0.00031
Archean Sun - no haze	23	3.8	0.93
Archean Sun - haze	8.3	0.76	0.11
AD Leo - no haze	0.41	0.041	0.043
AD Leo - haze	0.37	0.035	0.034
GJ 876 - no haze	0.53	0.0051	0.0031
GJ 876 - haze	0.18	0.00079	0.00018
K2V - no haze	13	2.1	0.29
K2V - haze	3.5	0.27	0.02
F2V - no haze	38	8.6	4.6

(2015) in a study of the UV surface environment of Earthlike planets orbiting various stellar types.

The surface UVC fluxes of the "Modern Sun - haze" planet and the "GJ 876 - haze" planet should be easily tolerated by *Chloroflexus aurantiacus*, the anoxygenic phototroph studied previously an analog for Archean photosynthetic life that was discussed in Section 5.3.2. *Chloroflexus aurantiacus* was shown in Pierson et al. (1992) to exhibit moderate growth under the UVC fluxes for every other star in Table 6.4 except the F2V star, the modern Sun with no haze, and the Archean Sun with no haze. Of course, life can also take refuge from UV radiation under other types of chemical or physical UV shields (e.g., within a liquid water column; see Chapter 7) so even these higher UV fluxes do not necessarily prohibit life (Cockell, 1998). Still, UV shielding is an important consideration for planetary habitability, so despite their cooling effects, UV-blocking hazes like the ones studied here may actually enhance planetary habitability.

Our analysis does not consider M dwarf flaring events, which can increase the UV irradiance by orders of magnitude (Segura et al., 2010). Since we have shown that stars with very high UV flux – particularly high FUV fluxes – do not form hazes as readily or at all compared to stars with lower FUV fluxes, frequent flaring events are expected to have a deleterious transient effect on a haze layer, although we have not examined the effects of time-dependent flares here.

6.3.5 Detectability of organic haze

Organic haze's strong absorption features provide an indirect way to sense atmospheres rich in CH_4 even if the CH_4 absorption features themselves are not distinguishable. Because attempts to characterize exoplanets have been frustrated by the presence of atmospheric aerosols (e.g., Kreidberg et al., 2014), haze is typically considered to obscure planetary characteristics. However, for the hazes presented here, gaseous absorption features can still be seen for $\lambda > 0.5$ μm in reflected light and for $\lambda > 1$ μm in transit transmission even in the hazy spectra.

As we discussed in Chapter 1, although they may obscure aspects of the planetary environment, organic hazes have the potential to unveil interesting ongoing planetary processes. The presence of CH_4 can be indicative of geological processes important to planetary habitability, and methane can also be produced by life. Haze production on the early Earth was likely driven by methane-producing metabolisms, which are simple and evolved early (Battistuzzi et al., 2004; Ueno et al., 2009) and likely were the dominant source of methane in the Archean (Kharecha et al., 2005). Therefore, the detection of organic haze on Earthlike planets can reveal interesting processes and help constrain key properties of the planetary environment.

Because methane can be produced by a variety of biological and non-biological means, there is no reason to expect organic-rich planets in the habitable zone to be rare. We should therefore be prepared for the detection of hazy habitable planets orbiting G, K, and M dwarfs. In this section, we discuss the detectability of organic haze around M dwarfs with JWST, and around G and K dwarfs with a future large 10-m direct imaging telescope.

6.3.5.a Simulated JWST observations

M dwarf planet hosts will be important targets for transit transmission observations by the James Webb Space Telescope (JWST) because the ratio of the planet's size relative to the star's size is largest for M dwarfs. Thus, their transit transmission signals are larger compared to equal-radius planets orbiting higher mass stars. Habitable zone planets also orbit closer to M dwarf stars, so their transits occur more frequently than for planets orbiting higher mass stars.

Figure 6.6 shows the results of these simulated observations over 65 hours of integration time (10 transits) per instrument for a planet orbiting GJ 876. The pink line shows the simulated spectrum, and the orange points with error bars denote the simulated JWST observations. The gray line shows the planet without haze, which is included for comparison. The error bars are calculated assuming photon limited noise, which is the same assumption made in Schwieterman et al. (2016).

We calculate the continuum level for the JWST observations by fitting a polynomial to continuum regions. To determine the detectability of spectral features, we determine the continuum level around absorption features, then subtract off that continuum. We calculate signal-to-noise (SNR) of absorption features in our simulations by binning across the features and comparing the signal to the noise level. The noise level is computed from the error on the binned absorption features and the error on the continuum estimate added in quadrature.

CH_4 and CO_2 can be detected across the NIRISS and NIRSpec bands. The CH_4 feature near 1.7 μm has SNR = 3.0, and CO_2 at 2 μm has SNR = 2.8. Detections of shorter wavelength features are $< 1\sigma$. However, the broader and stronger CH_4 feature near 2.3 μm is detectable at SNR = 6.4. For the NIRSpec absorption features, the opacity of the haze

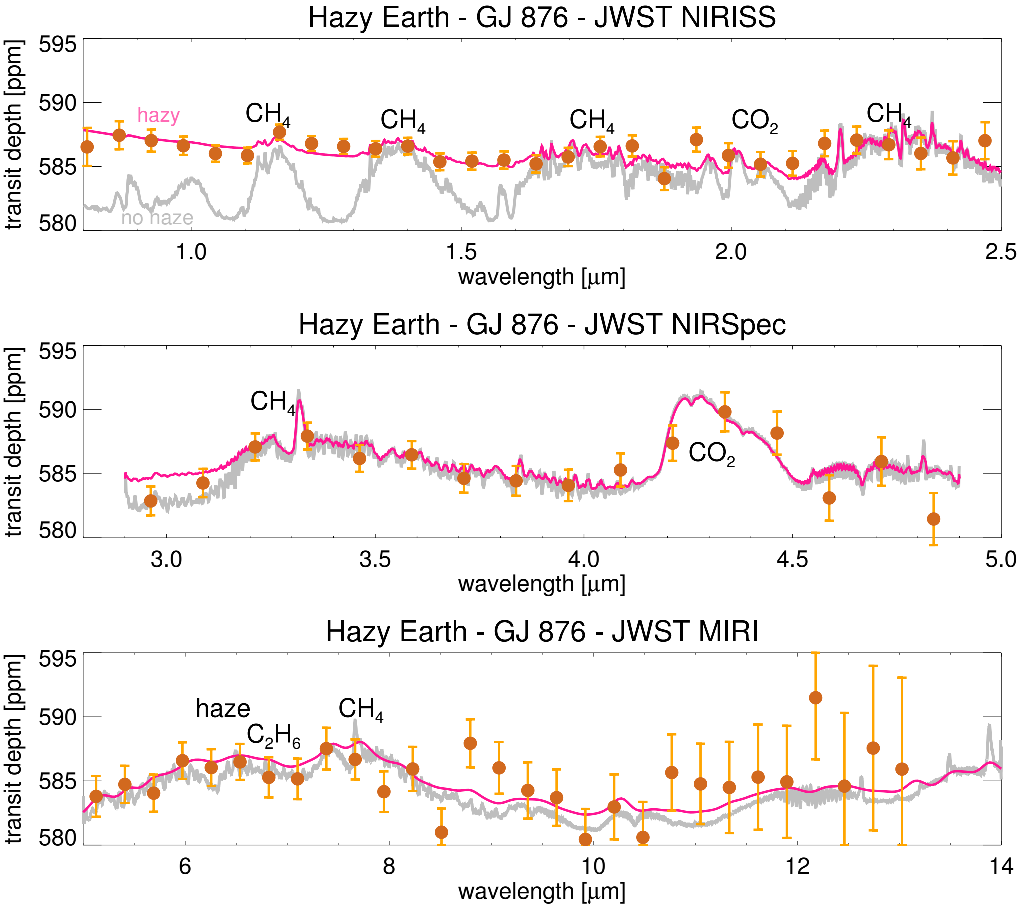

Figure 6.6: Shown are simulated spectra as seen by JWST for our hazy GJ 876 planet. The top panel simulates the NIRISS instrument, the middle panel simulates the NIRSpec instrument, and the bottom panel simulates the MIRI instrument. The pink spectrum shows the full spectrum prior to being fed into the simulator. The orange points with error bars are the spectrum as seen by JWST over 10 transits (65 hours of integration time). The gray spectrum shows a haze-free planet for comparison.

is negligible, and we measure SNR = 6.4 for the CH_4 feature near 3.3 μm and SNR = 5.9 for the CO_2 feature near 4.3 μm. In principle, therefore, it will be possible to measure CH_4 and CO_2 abundances and the CH_4/CO_2 ratio in transit transmission for the atmospheric altitudes probed by transit observations.

The haze is most transparent at the long wavelength end of the of the NIRISS bandpass and in NIRSpec. The abundances of CH_4 and CO_2 inferred from these longer wavelengths will be larger than the gas abundances inferred from the absorption features at shorter NIRISS wavelengths that are truncated by the haze. Based on the size of the error bars in the continuum regions around absorption bands, the absorption features in the hazy spectrum < 2.5 μm are about 2-10σ shallower than they would be in a spectrum without haze. The inconsistency between the retrieved gas abundances at longer wavelengths compared to abundances retrieved at shorter wavelengths would suggest the presence of a haze whose opacity increases towards shorter wavelengths.

Detection of spectral features in MIRI is in principle more challenging than NIRISS and NIRSpec because of the decline of the stellar blackbody at these longer wavelengths. However, if we define the MIRI continuum from between the first point in the MIRI bandpass and the points between 8-10 μm, we can measure SNR $= 5.1$ for the set of absorption features between 6-8 μm, which includes the haze absorption feature. Higher signal-to-noise would be needed to distinguish the haze from other absorbers in this region, but the presence of haze can be inferred separately from the NIRISS and NIRSpec observations of the CH_4/CO_2 ratio, the hazy spectral slope, and the depths of the NIRISS absorption features compared to the expected haze-free level.

The instrument models above do not include any contributions from systematic noise. Systematic noise sources come, in large part, from instrumentation and detectors, will not be fully characterized until after launch, and will tend to decrease in time as instrument and detector models are improved and new observing techniques are developed. The simulated observations presented here indicate that achieving a combined noise (random plus systematic) at the level of several ppm will be essential for characterizing hazy exo-Earths. Such precision may be possible if the systematic noise sources are characterized to a level well below the random noise. However, if the JWST systematic noise represents a floor at the $>$ 10 ppm level, as proposed by Greene et al. (2016), then characterizing the hazy exo-Earths presented here becomes extremely difficult, and the error bars on our simulated JWST measurements will become much larger. However, note that these simulations adopt multiple transits, and any error source (systematic or random) that is independent between transits will average down as the square root of the number of transits. However, because systematic noise can impart a spectrally-dependent signal in addition to a temporally-dependent one, this may never average down. One must also consider other systematic errors in the retrieval process such as missing or incorrectly specified absorbers.

6.3.5.b Simulated direct imaging observations

Unlike for JWST transit observations, M dwarf planets hosts are generally poor targets for direct imaging surveys because, except for the closest M dwarfs, it will probably not be possible to angularly separate their habitable planets from the host stars. The inner working angle (IWA), which defines the smallest angular separation between a planet and its host star at which the planet can be detected, scales with $\sim$Nλ/D where D is the telescope diameter and N is a small-valued constant of order 10^0. F dwarf habitable planets, which will naturally orbit farther from their stars than planets orbiting cooler hosts (Kopparapu et al., 2013), are most likely to be observable outside the IWA for the star types we simulate here, but we have shown that Archean-like worlds orbiting F dwarfs are less likely to have organic hazes. G and K dwarf planets, on the other hand, may have organic haze, and such stars will be important targets for future direct imaging missions (Stark et al., 2014).

We tested what a hazy Archean Earth analog orbiting the modern Sun, the Archean Sun, and the K2V dwarf would look like to a future 10-m LUVIOR-type space telescope (Bolcar et al., 2015; Dalcanton et al., 2015; Postman et al., 2010) using the coronagraph instrument noise model described in Robinson et al. (2016). The star-planet systems are assumed to be located at a distance of 10 parsecs (pc). The results of these simulations are presented in Figure 6.7. A spectrum with the haze removed (gray line) is presented alongside the hazy spectra (pink line) for comparison in all three cases. The “observed” spectra are simulated assuming 200 hours (roughly 1 week) of integration time per coronagraphic bandpass (which may not span the entire wavelength region of interest) for a planet at quadrature. If the planets were at a distance of 3 pc instead of 10 pc, the integration time needed to achieve the same signal-to-noise decreases by about an order of magnitude; we use 10 pc here to be conservative and to be able to consider the challenges of detecting distant planets. The spectral resolution (R = λ/ $\Delta\lambda$) is 70, and the telescope wavelength range is 0.4 - 3 μm.

We chose an outer working angle of $20\lambda/D$, and an inner working angle of $3\lambda/D$. For a 10 m mirror, the inner working angle limits the longest wavelengths that can be observed in all three cases: the planets orbiting the G2V star cut off near 1.5 μm, and the planet orbiting the K2V star cuts off near 1 μm. Visible and NIR wavelength ranges are observed by separate detectors as described in Robinson et al. (2016). It is assumed that the telescope system will be cooled to a sufficiently low temperature to minimize detector thermal noise ($T < 80$ K) that would otherwise contribute to spectral noise in the NIR. Thermal noise should not contribute appreciably to wavelengths < 1.6 μm, so our assumption of a cold telescope should not strongly impact the results shown here.

To test the detectability of spectral features, we followed a similar procedure to our JWST analysis. We fit a polynomial to the continuum regions near features of interest, then removed the continuum using the procedure described above. We then binned across the absorption features to determine their SNR compared to the continuum level.

We find that, for all three stars, the haze absorption feature at UV-blue wavelengths is easily detected against the expected extrapolated continuum level. The modern Sun haze absorption feature has an extremely robust detection of SNR = 70, the Archean Sun haze has SNR = 12, and the K2V haze has SNR = 27. Our extrapolated continuum only extends the polynomial fit to longer wavelengths and does not include the expected Rayleigh scattering, so these detections are likely under-estimates compared to a model that includes Rayleigh scattering. An absorption feature from overlapping CH_4 and H_2O can be seen near 0.72 μm for all three planets. It can be detected at SNR = 3.1 for the modern Sun, SNR = 2.6 for the Archean Sun, and SNR = 3.3 for the K star.

Features can be seen in the modern and Archean Sun spectra near 1.15 and 1.4 μm that are caused by overlapping H_2O and CH_4 absorption bands. The 1.15 and 1.4 μm features are detected at SNR = 16 and SNR = 11 for the modern Sun, and at SNR = 11 and SNR = 9 for the Archean Sun, respectively. At 10 pc, these features are cut off by the K star inner working angle and cannot be observed.

Note that because of the $\sim$1 μm IWA cutoff for a K star planet at 10 pc, the haze absorption band is the strongest feature that can be seen, providing indirect evidence of methane. Because sources of methane on an Earthlike planet are likely to involve water

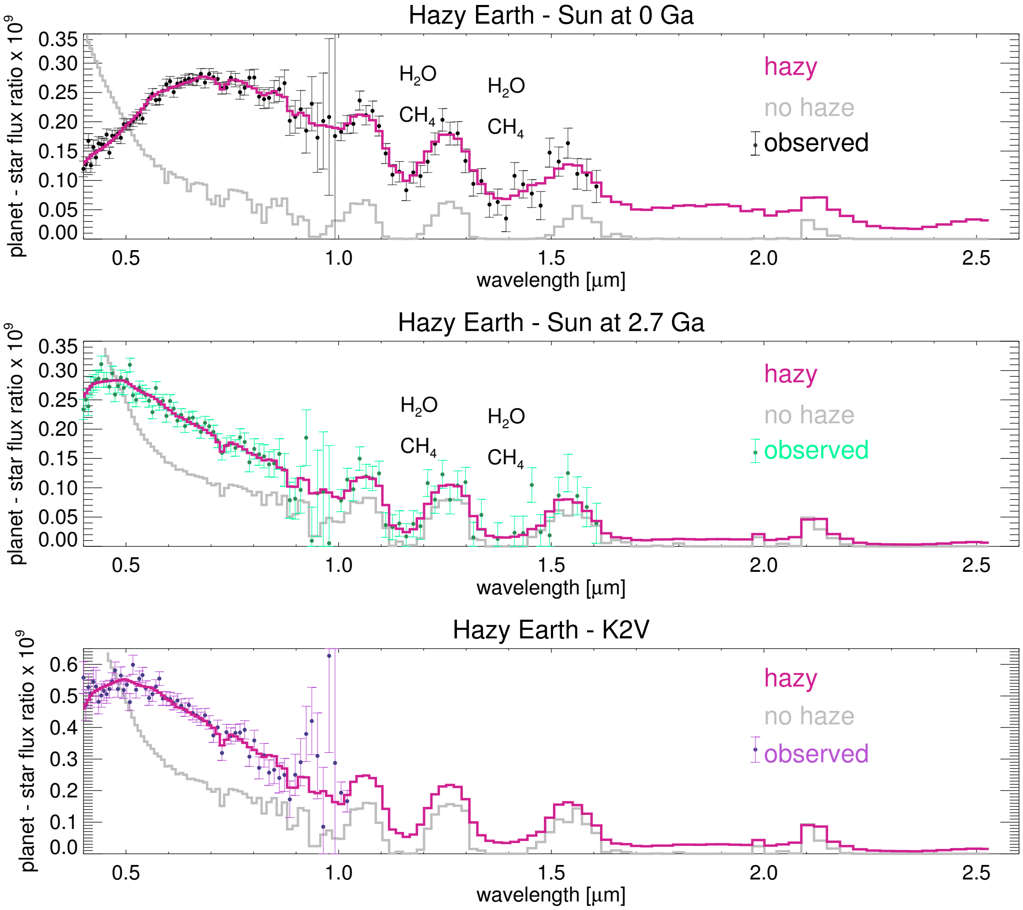

Figure 6.7: These are simulated spectra as seen by a 10-m LUVIOR-type telescope over 200 hours of integration time in each spectral band for planets at 10 pc. The colored lines show the hazy spectra without noise added, and the gray spectra are the corresponding haze-free planets for comparison. Points with error bars simulate the hazy spectrum seen by the telescope with realistic noise sources.

(either through biological production or serpentinization, the dominant abiotic methane source on Earth, and one which requires water), the indirect detection of methane on a terrestrial planet could also be argued to suggest the presence of water, particularly in an atmosphere with CO_2 that necessitates a vigorous CH_4 flux to produce haze. Unfortunately, CO_2 cannot be detected in reflected light for any planets shown here. Although there is a CO_2 feature near 1.5 μm, it is not detectable at the spectral resolution and noise level we simulate. Detecting CO_2 should be a priority because it can constrain the redox state of the atmosphere and can help determine whether a planet is in fact a terrestrial one in the absence of other data suggesting mass or planetary radius.

The large error bars around 1 μm are caused by falloff in both CCD and InGaAs detector quantum efficiencies, making it difficult to detect spectral features here. In the NIR, considering the frequent overlap between CH_4 and H_2O bands, to detect water even for the G star spectra, good sensitivity to clean, methane-free water bands near 0.82 μm and especially the stronger band near 0.94 μm (Figure 6.4) is crucial. Therefore, improved detectors in this spectral range ought to be a priority. Thinned HgCdTe detectors may work for this purpose. Because water cannot be cleanly detected in these spectra with the assumed detector technology, retrievals of gas abundances would exhibit degeneracies in the retrieved amounts of H_2O and CH_4.

6.4 Discussion

We have found that organic haze should be detectable with future space-based telescopes on nearby Archean-analog exoplanets. However, haze does not form around all of the stars we tested. Here, we discuss the reasons for different rates of haze formation and the differing impacts of haze on their planets' climates around different stars. We also compare the haze's UV-blue absorption feature to other UV-blue absorbers.

6.4.1 Destruction of organic haze by oxygen species

Our results suggest that G dwarfs, K dwarfs, and some M dwarfs are more likely to generate hydrocarbon hazes in Earthlike atmospheres compared to F dwarfs, very quiet M dwarfs, and highly flaring stars such as AD Leo. To generate hazes, stars need sufficient UV flux to drive the relevant photochemistry through reactions such as $CH_4 + h\nu(\lambda < 150\,\mathrm{nm}) \longrightarrow CH_3 + H$, but too much FUV flux generates oxygen radicals through reactions such as $CO_2 + h\nu(\lambda < 200\,\mathrm{nm}) \longrightarrow CO + O$ and $CO_2(\lambda < 200\,\mathrm{nm}) + h\nu \longrightarrow CO + O^1D$ that halt the haze formation process.

The generation of O from CO_2 photolysis (and photolysis of other O-bearing species such as NO_2) leads to the creation of oxidized species (including O itself) that can react with organics on the reaction pathway to haze formation. This includes O_2 and O_3, which can form via the Chapman mechanism, which is important to the formation of Earth's ozone layer:

$$O_2 + h\nu(\lambda < 240\,\mathrm{nm}) \longrightarrow O + O \tag{R1}$$

$$O + O_2 + M \longrightarrow O_3 + M \tag{R2}$$

$$O_3 + h\nu(\lambda < 340\,\mathrm{nm}) \longrightarrow O_2 + O \tag{R3}$$

$$O + O_3 \longrightarrow O_2 + O_2 \tag{R4}$$

Reactive hydroxyl radicals (OH) can be created by processes such as

$$O(^1D) + H_2O \longrightarrow 2\,OH \tag{R5}$$

$$H_2O + h\nu(\lambda < 200\,\mathrm{nm}) \longrightarrow H + OH \tag{R6}$$

Table 6.5 shows a comparison of the principle photolysis reactions involving CO_2, H_2O, and NO_2 in each atmosphere that produce hydrocarbon-consuming oxygen species. An asterisk marks the fastest reaction in each atmosphere. CO_2 photolysis is the most efficient source of O and O^1D in every atmosphere except for T3200, whose oxygen is sourced from NO_2 photolysis as discussed in Section 6.4.2. The reaction rates scale with the amount of UV flux able to dissociate a given species. For instance, compare the reaction rates in Table 6.5 with the UV fluxes and cross sections in Figure 6.1: stars with elevated fluxes at the wavelengths overlapping the UV cross sections of these O-producing species produce higher amounts of oxygen species through photolysis. In general, the more oxygen an atmosphere produces from photolysis of species like H_2O, CO_2, and NO_2, the thinner the hazes. Thus, to predict whether a star is likely to have a planet with organic haze in the habitable zone, we will require measurements of the shape of its UV spectrum, especially for wavelengths < 200 nm to understand the efficiency of H_2O and CO_2 photolysis, and around 400 nm for NO_2 photolysis.

Table 6.5: Column integrated rates (reactions/sec) for photolysis of H_2O, CO_2, and NO_2 in the atmospheres of the $CH_4/CO_2 = 0.2$ planets around each star.

Star	Oxygen-producing photolysis reactions	Rates
Modern Sun	$*CO_2 + h\nu \longrightarrow CO + O$	$3.12x10^{11}$
	$CO_2 + h\nu \longrightarrow CO + O^1D$	$2.02x10^{11}$
	$H_2O + h\nu \longrightarrow H + OH$	$7.024x10^{10}$
	$NO_2 + h\nu \longrightarrow NO + O$	$1.52x10^{11}$
Archean Sun	$*CO_2 + h\nu \longrightarrow CO + O$	$3.87x10^{11}$
	$CO_2 + h\nu \longrightarrow CO + O^1D$	$3.38x10^{11}$
	$H_2O + h\nu \longrightarrow H + OH$	$5.65x10^{10}$
	$NO_2 + h\nu \longrightarrow NO + O$	$1.40x10^{11}$
AD Leo	$*CO_2 + h\nu \longrightarrow CO + O$	$2.19x10^{12}$
	$CO_2 + h\nu \longrightarrow CO + O^1D$	$2.51x10^{11}$
	$H_2O + h\nu \longrightarrow H + OH$	$5.78x10^{11}$
	$NO_2 + h\nu \longrightarrow NO + O$	$6.84x10^{10}$
GJ 876	$CO_2 + h\nu \longrightarrow CO + O$	$4.17x10^{9}$
	$*CO_2 + h\nu \longrightarrow CO + O^1D$	$1.18x10^{11}$
	$H_2O + h\nu \longrightarrow H + OH$	$3.76x10^{10}$
	$NO_2 + h\nu \longrightarrow NO + O$	$4.37x10^{10}$
T3200	$CO_2 + h\nu \longrightarrow CO + O$	$3.28x10^{5}$
	$CO_2 + h\nu \longrightarrow CO + O^1D$	2820
	$H_2O + h\nu \longrightarrow H + OH$	$3.38x10^{5}$
	$*NO_2 + h\nu \longrightarrow NO + O$	$5.41x10^{10}$
K2V	$*CO_2 + h\nu \longrightarrow CO + O$	$3.69x10^{11}$
	$CO_2 + h\nu \longrightarrow CO + O^1D$	$3.42x10^{11}$
	$H_2O + h\nu \longrightarrow H + OH$	$9.21x10^{10}$
	$NO_2 + h\nu \longrightarrow NO + O$	$1.2x10^{11}$
F2V	$*CO_2 + h\nu \longrightarrow CO + O$	$1.05x10^{14}$
	$CO_2 + h\nu \longrightarrow CO + O^1D$	$7.774x10^{12}$
	$H_2O + h\nu \longrightarrow H + OH$	$8.22x10^{12}$
	$NO_2 + h\nu \longrightarrow NO + O$	$1.31x10^{11}$

Although the F2V planet produces a significant amount of oxygen radicals compared to our other stars, the absolute level of oxygen in its atmosphere is not large enough to be detectable. The column densities of O_2 and O_3 in the F2V atmosphere are 9.0×10^{18} molecules/cm^2 and 2.61×10^{14} molecules/cm^2, respectively. The column density of methane is 4.27×10^{22} molecules/cm^2. As discussed in Domagal-Goldman et al. (2014), it is difficult to accumulate abiotic oxygen at detectable levels in atmospheres rich in organics because reactions with reduced gases are major oxygen sinks. Domagal-Goldman et al. (2014) show that at lower CH_4 column densities than the ones we simulate here (e.g. $\sim 10^{16}$ molecules/cm^2), O_2 and O_3 can reach column densities of $10^{18} - 10^{21}$ molecules/cm^2 and $10^{16} - 10^{18}$ molecules/cm^2, respectively, and O_3 can produce significant spectral signatures. Another study, Harman et al. (2015), showed that O_2 can reach detectable levels in organic-poor atmospheres around GJ 876, which is different from the behavior we see. However, for atmospheres similar to those studied here with 1% CO_2 and 0.2% CH_4, the model used in the Harman et al. (2015) study produces O_3 and O_2 column depths 500× and 100× higher on a planet orbiting an F2V star compared to GJ 876 (C. Harman, personal communication). This is broadly similar to the trend we observe.

Figure 6.8 shows the hydrocarbon chemical reaction network with the fastest reactant rates that lead to haze production or haze sinks for each star. "HCAER" in this figure stands for the hydrocarbon species that most efficiently condenses out as haze particles, C_4H_2. Species outlined by hexagons represent major sinks of haze-forming gases, and essentially a truncation of the haze-forming reaction network.

At the start of the haze forming process, the methyl radical (CH_3) must form so it can participate in reactions that create carbon chains of two or more carbon atoms. Although oxygen radicals can frustrate haze formation later on in the reaction network, they are initially helpful in forming CH_3. For every star but AD Leo, the most efficient vectors towards forming CH_3 are

$$CH_4 + O \longrightarrow CH_3 + OH \tag{R7}$$

$$CH_4 + OH \longrightarrow CH_3 + H_2O \tag{R8}$$

AD Leo, meanwhile, most efficiently forms CH_3 from CH_4 photolysis due to its high Lyman-α output overlapping with the peak of the CH_4 UV cross section, but this is only a factor of 1.15 times faster than CH_4 + OH.

Once CH_3 forms, an exit from the haze-formation network occurs if it reacts with O to form formaldehyde, CH_2O, which ultimately ends up as CO_2:

$$\mathrm{CH_3 + O \longrightarrow CH_2O + H} \tag{R9}$$

We can re-write equations R7 and R9 as the following net reaction (because the O and OH will react to form H_2O):

$$\mathrm{CH_4 + 2\,O \longrightarrow CH_2O + H + OH \longrightarrow CH_2O + H_2O} \tag{R10}$$

If we let k_{R7} and k_{R9} be the rate coefficients of R7 and R9, the reaction rates R_{R7} and R_{R9} can be written as

$$R_{R7} = k_{R7} \times f\mathrm{CH_4} \times fO \tag{6.1}$$

$$R_{R9} = k_{R9} \times f\mathrm{CH_3} \times fO \tag{6.2}$$

Here, $f\mathrm{CH_4}$, $f\mathrm{CH_3}$, and $f\mathrm{O_2}$ are the mixing ratios of CH_4, CH_3, and O_2, respectively. But, the rate of reaction 6.2 depends on the rate of reaction 6.1 because it requires CH_3 generated by reaction 6.1. So, we can rewrite the net reaction rate as:

$$R_{net} = k_{R7} \times k_{R9} \times f\mathrm{O_2}^2 \tag{6.3}$$

What this means is that R_{R7} proceeds as a linear function of fO, but the net reaction that leads to haze truncation is dependent on fO^2. At low O concentrations, an increase in

O should increase CH_3 faster than it increases CH_2O. But at high O concentrations, CH_2O formation will become important.

Oxidation of CH_3 competes with the formation of ethane (C_2H_6) via reaction of CH_3 with another CH_3 or more commonly with CH_3CO (produced from CH_3 + CO).

A number of reactions can then occur with C_2H_6 that are relevant to haze formation. Ethane can react with oxygen radicals to form C_2H_5. Then, C_2H_5 can either react with H or O_2 to re-form CH_3, or it can react with CH_3 to advance towards C_2H_4. Alternatively, C_2H_6 can be photolyzed to form C_2H_4 directly (and, less efficiently, C_2H_2). However, the most efficient source of C_2H_4 for every planet (except the T3200 and F2V planets) is $CH + CH_4 \longrightarrow C_2H_4 + H$. The CH in this reaction is ultimately sourced from methane photolysis, so this reaction path is not efficient for planets around stars that cannot photolyze methane (T3200) or planets around stars whose methane photolysis products favor reactions that produce CH_2O or CO (the F2V planet).

Once C_2H_4 forms, it can exit the haze-formation path if it reacts with O to form HCO, or it can continue on the haze-formation path if it is photolyzed to form C_2H_2. Then, C_2H_2 can react to produce C_2H.

At this point, the reaction network has produced the gases needed to form C_4H_2, which condenses out as haze particles via $C_2H_2 + C_2H \longrightarrow C_4H_2 + H$. Alternatively, C_2H_2 can react with CH to form C_3H_2, which begins a second chain of polymerizations that can lead to C_5H_4, which also condenses out as haze particles. However, this is less efficient than the process forming C_4H_2 and is not shown in Figure 6.8.

Table 6.6 shows the ratios of the total integrated reaction rates that remove hydrocarbons from the haze formation chain (via reaction with oxygen radicals) versus the reactions that step toward haze particle formation at key stages of the haze-formation process. There is a clear difference between the planets that form haze and those that do not. The haze-poor planets generally favor reactions with oxygen radicals over reactions that lead to haze formation. The T3200 planet has little oxygen in its atmosphere (6.2), but oxygen reactions out-compete haze-forming reactions in its atmosphere because it is unable to photolyze hydrocarbons.

Table 6.6: In this table, "Ratio X" (where X is either CH, C_2H_4, C_2H_2 or C_2H) represents the haze network truncation ratio, which is the ratio of the total integrated reaction rates of X with oxygen species (thus frustrating the haze-formation process) to the total integrated reaction rates of X that step towards haze formation. A horizontal line separates the stars that form haze at $CH_4/CO_2 = 0.2$ (above the line) from the ones that do not (below the line). Ratios exceeding unity mean that reactions with oxygen species are more efficient than reactions towards haze particle formation. Reactions with oxygen species are not always less efficient than reactions leading towards haze formation even in the hazy atmospheres (e.g., for C_2H_4 and C_2H_2), but they are markedly faster in the haze-free atmospheres compared to the hazy ones. An exception is reactions involving CH for T3200, but the CH itself is formed 8-9 orders of magnitude slower in the T3200 planet's atmosphere compared to the others because T3200 cannot photolyze methane.

Star	Ratio CH	Ratio C_2H_4	Ratio C_2H_2	Ratio C_2H
GJ 876	0.12	1.88	1.7	0.07
Modern sun	0.15	3.22	2.48	0.13
Archean	0.29	4.92	2.8	0.45
K star	1.45	86	10	60
AD Leo	1.78	121	42	703
F star	16.2	60	7.5	1.51×10^6
T3200	0.09	5.70×10^6	2.3×10^5	249

6.4.2 Ethane formation for the T3200 planet

Like the other stars, the most efficient reaction that forms C_2H_6 in the T3200 planet's atmosphere is:

$$\mathrm{CH_3CO + CH_3 \longrightarrow C_2H_6 + CO} \tag{R11}$$

Again, similar to most of the other stars, the CH_3 here is most efficiently sourced from oxidation of methane:

$$\mathrm{CH_4 + O \longrightarrow CH_3 + OH} \tag{R12}$$

$$\mathrm{CH_4 + OH \longrightarrow CH_3 + H_2O} \tag{R13}$$

This CH_3 can react with CO to produce the CH_3CO needed in the dominant ethane-producing reaction, R11. Interestingly, the dominant production mechanism of the oxygen radicals in R12 and R13 for the low-FUV T3200 planet can be ultimately traced to NO_2 photolysis, which produces NO and O:

$$\mathrm{NO_2 + h\nu \longrightarrow NO + O} \tag{R14}$$

NO_2 can be photolyzed around this star, despite the inefficient photolysis of other species, because this gas has a broad UV cross section peaking at 400 nm where T3200 produces flux from its blackbody radiation.

The C_2H_6 produced through this scheme is inefficiently destroyed in the atmosphere of the T3200 planet because it cannot be photolyzed. Thus, ethane can accumulate and provide a source of greenhouse warming for the T3200 planet.

6.4.3 Haze-induced cooling of planetary surfaces

Since haze can cool a planetary climate, there may be a “hazy habitable zone” (HHZ) inner edge closer to the star than the traditional habitable zone boundaries (Kasting, 1993; Kopparapu et al., 2013) for planets with organic-rich atmospheres. However, the results presented here indicate that the inner edge of the HHZ will not be relevant to certain types of stars such as F and M dwarfs. As we have seen, F2V planets with atmospheres containing CO_2 and H_2O do not generate this haze even at high CH_4/CO_2 ratios due to the buildup of haze-destroying oxygen-containing species. Some M dwarf planets are able to generate haze for the types of atmospheres considered here, but its cooling effects would be small because the M dwarf spectral output is in a wavelength range where these hazes are relatively transparent.

The outer edge of the habitable zone (OHZ) may also be affected by organic hazes. The OHZ is traditionally defined as the distance where CO_2 warming is maximized. In principle, the warming potential for organic-rich planets at the outer edge of the habitable zone would be limited by the formation of haze. This process could define the “maximum greenhouse effect” for organic-rich worlds orbiting G and K stars. However, all of this is subject to the caveat that habitable planets near the OHZ may not be able to generate organic hazes in the first place. If the maximum CO_2 greenhouse limit allows for several bars of CO_2, implausibly large CH_4 fluxes may be required to achieve a high enough CH_4/CO_2 ratio to create a haze in such atmospheres.

6.4.4 A comparison to other hazes and UV-absorbers

The haze’s broadband UV and blue wavelength absorption feature is prominent and distinctive in reflected light, but to ensure accurate interpretation of this feature, it is important to explore similar UV absorbers that might mimic this feature in a planet’s spectrum. We compare this haze’s spectral signature with other short wavelength absorbers in Figure 6.9, which plots hazy Archean Earth alongside modern Earth with clouds, Venus, Mars, modern Earth with a Mars-like surface, and Earth with a ZnS haze. We also show hazy Archean Earth with water clouds constructed using a weighted average of 50% haze-only, 25% haze and cirrus cloud, and 25% haze and strato cumulus cloud (Robinson et al., 2011, and see also our discussion of water clouds in hazy Archean spectra in Section 5.3.3.a). The ZnS spectrum is not intended to be physically realistic and is provided simply to show the absorptive effects of ZnS particles, which have strong UV absorption similar to organic haze.

In the modern Earth atmosphere, the ozone Chappuis band is a broad feature centered near 0.5-0.7 μm, but its absorption does not continue farther into the UV the way haze does, so the Rayleigh scattering slope becomes prominent for $\lambda < 0.5$ μm, broadly distinguishing this spectrum from a hazy one. In addition, hydrocarbon hazes should not be present in atmospheres with spectrally apparent ozone.

Mars is red because iron oxide absorbs strongly at blue wavelengths. A spectrum of the Earth with the wavelength-dependent surface albedo of Mars shows what Earth could look like with a surface rich in iron oxide. On an Earthlike planet with a 1 bar atmosphere, the blue-absorbing iron oxide feature is unlikely to be mistaken for hydrocarbon haze due to increased reflectivity for $\lambda < 0.5$ μm due to Rayleigh scattering. However, on Mars itself, Rayleigh scattering is non-apparent, so the strong iron oxide absorption feature could mimic haze. Mars's iron oxide feature from the surface and airborne dust could be distinguished from haze by the absence of CH_4 features in the spectrum. Absorption from airborne iron-rich dust is dependent on the Fe^{2+}/Fe^{3+} ratio, dust particle size, and any possible ice coatings (and note that Earthlike planet atmospheres can contain large quantities of dust – e.g. in the 1930s during the dust bowl).

Earth with a thick haze of ZnS particles is the closest mimic we found to our cloud free spectrum of Archean Earth with a hydrocarbon haze. However, ZnS is not a realistic aerosol candidate for Earthlike atmospheres because it condenses at temperatures close to 1000 K (Morley et al., 2012). Charnay et al. (2015) and Morley et al. (2015) show what a ZnS haze would look like in a more realistic atmosphere for GJ 1214b. Therefore, constraints on surface temperature or semi-major axis could eliminate this as a potential source of UV absorption.

Venus's broad UV absorption caused by its unknown UV absorber (Markiewicz et al., 2014) and SO_2 can also mimic the UV absorption of organic haze. However, the Venus spectrum lacks CH_4 features and strong water features that would indicate habitability. Venus' oxidizing atmosphere is very different from Archean Earth. In Venus' upper atmosphere, > 70 km, photochemical reactions involving SO_2 and H_2O produce a H_2SO_4 haze (Yung & DeMore, 1982). See Chapters 1, 2, and 4 for additional discussion of Venus' cloud and haze. On the other hand, sulfur allotropes such as S_8 exhibit a range of UV features (not shown here), and some of these sulfur compounds may have played a role in creating the sulfur MIF signal in the Archean (see Chapter 5).

Organic haze's blue and UV wavelength absorption feature together with observations of methane bands would strongly imply the existence of haze in an atmosphere. The UV absorbers we compared to here can be distinguished from organic haze through the appearance the Rayleigh scattering slope, the lack of CH_4 features, or (in the case of ZnS) cannot exist for an Earthlike atmosphere at all. In the modern Earth atmosphere, the ozone Chappuis band is a broad feature centered near 0.5-0.7 μm, but its absorption does not continue farther into the UV the way haze does, so the Rayleigh scattering slope becomes prominent for $\lambda < 0.5$ μm, distinguishing this spectrum from a hazy one. In addition, hydrocarbon hazes are unlikely to be present in atmospheres with spectrally apparent ozone.

Mars is red because iron oxide absorbs strongly at blue wavelengths. A spectrum of the Earth with the wavelength-dependent surface albedo of Mars shows what Earth could look like with a surface rich in iron oxide. On an Earthlike planet with a 1 bar atmosphere, the blue-absorbing iron oxide feature is unlikely to be mistaken for hydrocarbon haze due to increased reflectivity for $\lambda < 0.5$ μm due to Rayleigh scattering. It is also important to note that at low spectral resolution, iron oxide could also be mistaken for ozone absorption. However, on Mars itself, Rayleigh scattering is non-apparent, so the strong iron oxide absorption feature could mimic haze. Mars's iron oxide feature could be distinguished from haze by the absence of CH_4 features in the spectrum.

Earth with a thick haze of ZnS particles is the closest mimic we found to our cloud-free spectrum of Archean Earth with a hydrocarbon haze. However, ZnS is not a realistic aerosol candidate for Earthlike atmospheres because it condenses at temperatures close to 1000 K (Morley et al., 2012). Charnay et al. (2015) and Morley et al. (2015) show what a ZnS haze would look like in a more realistic atmosphere for GJ 1214b. Therefore, constraints on surface temperature or semi-major axis could eliminate this as a potential source of UV absorption.

Venus's broad UV absorption caused by its unknown UV absorber (Markiewicz et al., 2014) and SO_2 can also mimic the UV absorption of organic haze. However, the Venus spectrum lacks CH_4 features and strong water features that would indicate habitability. Venus' oxidizing atmosphere is very different from Archean Earth.

Organic haze's blue and UV wavelength absorption feature together with observations of methane bands would strongly imply the existence of haze in an atmosphere. The UV absorbers we compared to here can be distinguished from organic haze through the appearance the Rayleigh scattering slope, the lack of CH_4 features, or (in the case of ZnS) are highly unlikely for an Earthlike atmosphere.

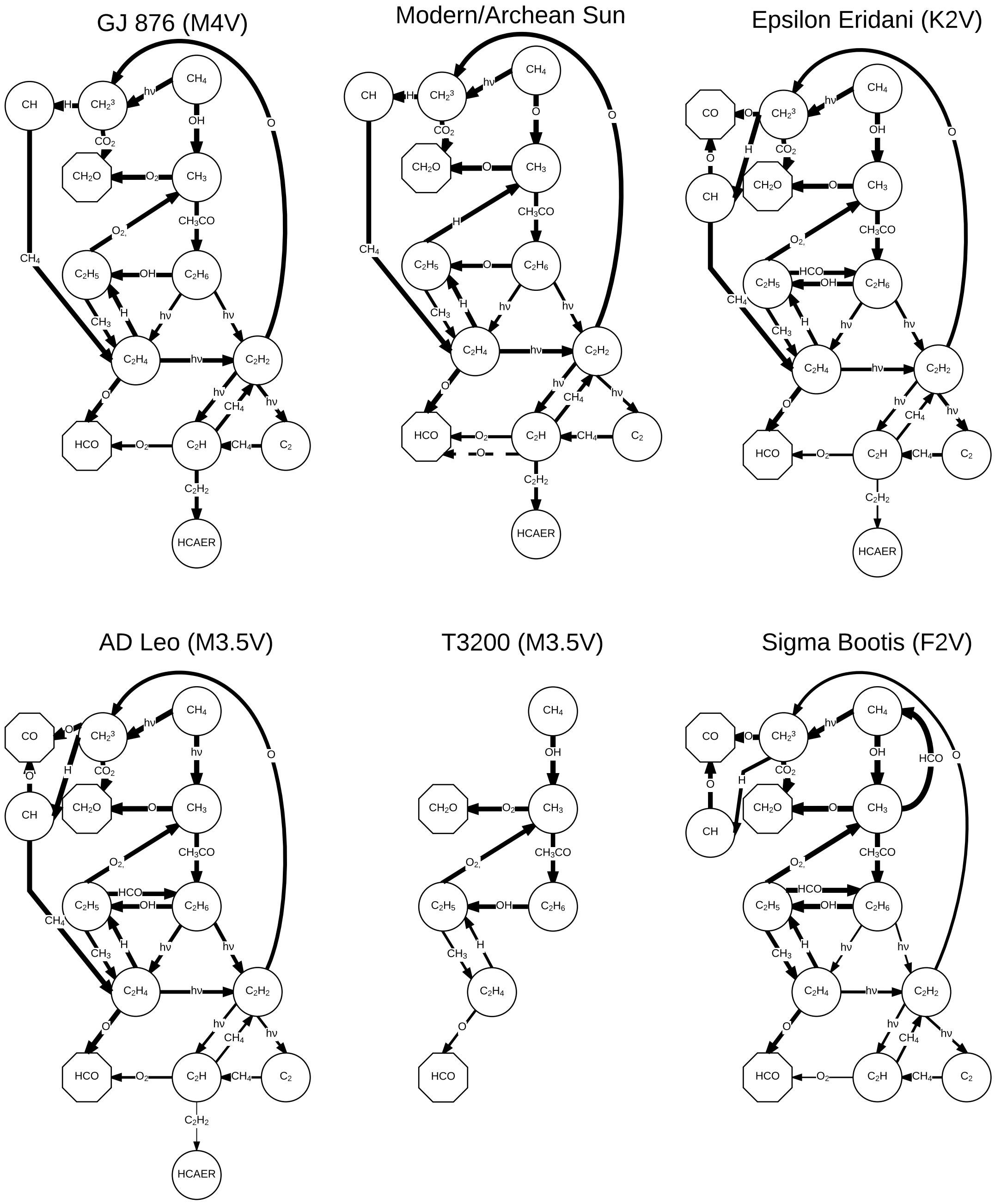

GJ 876 (M4V)

Modern/Archean Sun

Epsilon Eridani (K2V)

AD Leo (M3.5V)

T3200 (M3.5V)

Sigma Bootis (F2V)

Figure 6.8: The fastest reaction network towards haze formation (HCAER) and the fastest hydrocarbon sinks for each planet. The Archean and modern sun reaction networks are the same except for the reaction forming HCO from C_2H: the dominant reaction involves O_2 for the modern sun (solid arrow) and O for the Archean sun (dashed arrow). T3200 has a very simple reaction network that terminates before haze is formed because it cannot photolyze hydrocarbons. The F2V star, on the other hand, has a complex network in which hydrocarbons efficiently react with oxygen species, and haze is not formed. Thicker arrows indicate faster reaction rates.

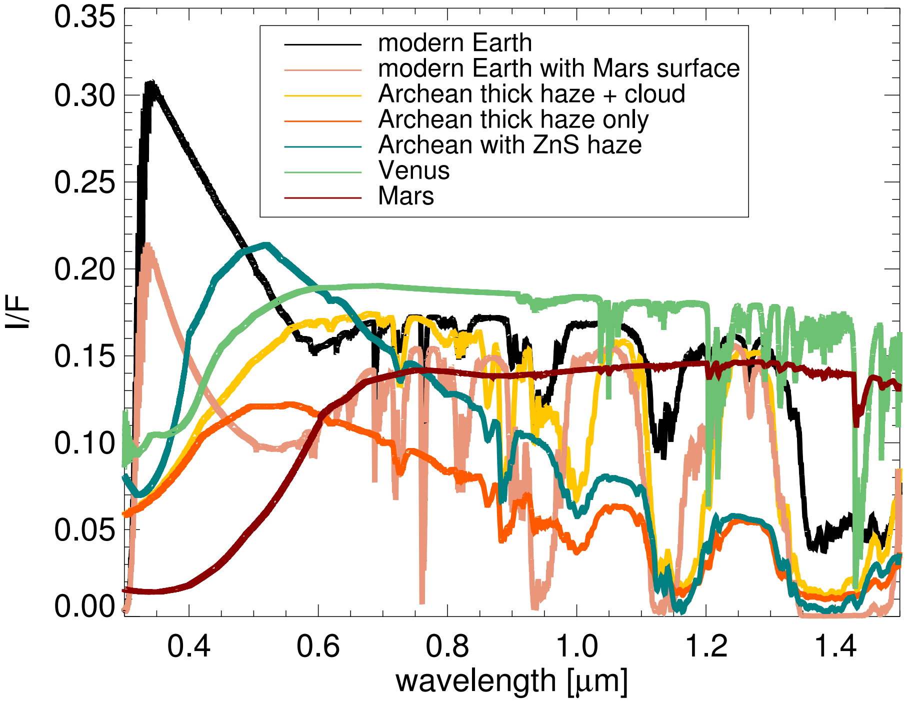

Figure 6.9: This shows a comparison of several types of spectra with broad short wavelength absorption features to compare haze's short wavelength absorption feature to similar features produced by different types of absorbers. These spectra have been scaled in the y-dimension to plot together on the same axis.

6.5 Concluding remarks

We have seen that organic haze occurs on Archean-analog planets orbiting different types of stars. Haze on Earthlike planets orbiting nearby M dwarfs should be detectable with JWST, and future space missions such as LUVOIR will allow us to detect hazes on planets around hotter G and K stars. Not all stars can form organic haze, however. Stars with very low UV fluxes may be unable drive hydrocarbon photochemistry; stars with very high FUV fluxes, meanwhile, can generate large amounts of abiotic oxygen radicals that destroy hydrocarbons. The climate impacts of haze on planetary environments vary with stellar type as well. In particular, hazes on planets orbiting M dwarfs have minimal impact on the climate because the hazes simulated here are relatively transparent at wavelengths where their stars are most luminous.

These hazes can also provide UV shields for their planets. In the next chapter, we will expand on our discussion of haze as a UV shield for the Archean under a water column because, despite suggestions of Archean surface-dwelling life (Watanabe et al., 2000), most life from this time period was likely aquatic. We will also expand on our discussion of haze as a biosignature, especially in the context of planets with biogenic sulfur gases. It is important and interesting to consider organic haze as a biosignature because, as we saw in this chapter, these hazes produce strong, detectable spectral signatures.

Chapter 7

EXPLORATION OF ORGANIC HAZE AS A SIGN OF BIOLOGICAL ACTIVITY AND POSSIBLE IMPACTS OF HAZE ON ARCHEAN PHOTOTROPHS

7.1 Introduction

The organic haze examined in Chapters 5 and 6 was intimately intertwined with the Archean biosphere. Previously, we discussed how this haze in the Archean was likely generated largely by biologically-produced methane, so life was probably a major driver of its formation. However, the links between a biogenic haze and the biosphere extend deeper than this: the haze would, in turn, have impacted Archean life. We examined two of these impacts in Chapters 5 and 6. There, we showed how organic haze could have cooled the surface temperature of our early planet and putative Earthlike hazy exoplanets, but the despite this cooling, these hazy worlds could have remained habitable even with the fainter young sun. We also showed that haze could have provided a UV shield of sufficient opacity to allow the survival of radiation-tolerant organisms at the planet's surface. Haze can even be a better shield for UVA and UVB radiation than ozone (see Chapters 5 and 6).

In this chapter, we present a deeper exploration of some of the connections between the Archean haze and biology, including haze's effect on the light reaching the surface environment. Haze would have altered both the quantity and quality of light reaching the surface of our planet: under a global haze, the total number of photons reaching the surface is diminished, and blue wavelengths are strongly absorbed. This may have impacted the productivity of Archean photosynthetic organisms and the wavelengths of light preferred for photosynthetic pigments. The peak of the photon distribution at Earth's surface today corresponds closely to the peak wavelength of chlorophyll absorption (Kiang et al., 2007b,a), and it has been suggested that over Earth's geological history, the evolution of organic pigments would have been affected by the wavelength-dependent transparency of Earth's atmosphere and the evolving solar spectrum (Michaelian & Simeonov, 2015). Previous theoretical work on the impact of stellar spectra on photosynthetic pigments suggests that wavelengths of pigment maximum absorbances should shift according to the spectrum of the host star (Kiang et al., 2007b). For instance, evolutionary pressures from F stars might be expected to lead to blue-absorbing pigments, and red-orange absorption should be preferred for photosynthesizers living under K stars. A blue-absorbing haze in the Archean atmosphere may therefore have driven evolution towards redshifted pigments compared to those used by modern day organisms.

We have discussed how haze blocks UV radiation, and other UV shields could protect Archean phototrophs in addition to a haze. Different types of chemical and physical UV shields have been proposed for protecting Archean photosynthetic life such as water, sediments, overlying layers of microbial mats, and minerals dissolved in the water column (Olson & Pierson, 1986; Cockell, 1998; Garcia-Pichel & Bebout, 1996; Garcia-Pichel, 1998). If these shields were present in addition to a hazy atmosphere, the colors and intensity of radiation reaching organisms would be further altered by the each layer of UV screen.

Aqueous Fe(II) may have been an important UV shielding compound for Archean organisms. There have been hints of life on the Earth's surface during the Archean (Watanabe et al., 2000), but most organisms were probably restricted to aquatic environments. The Archean oceans likely contained large amounts of dissolved Fe(II) (Garcia-Pichel, 1998). The evidence for this iron comes from banded iron formations (Figure 7.1), which indicate the Archean oceans had several ppm of dissolved reduced Fe (Konhauser et al., 2007; Holland, 1973). Iron absorbs UV radiation efficiently, making it a potentially effective Archean UV screening compound in the water column (Olson & Pierson, 1986). Garcia-Pichel (1998) considered the impact of Fe(II) on UV transmittance in an ocean and found that it could have been substantial. Therefore, a UV shield provided by both haze and dissolved Fe(II) in water could have provided a formidable screen against UV damage. We explore this topic in Section 7.3.1.

In addition to interacting with life through its UV shielding abilities, haze in the Archean was likely driven by biological methane production (see Chapters 5 and 6 for the previous discussion of hazes in the context of spectral biosignatures). Of course, abiotic processes can also produce methane, so while an organic haze in an atmosphere rich in CO_2 would be tantalizing and suggestive, it would not on its own be conclusive of the presence of life.

As we will show, biogenic organic sulfur gases (S_{org}) can contribute to the atmospheric budget of hydrocarbon species needed to form haze. Atmospheres with S_{org} can form hazes at lower CH_4/CO_2 ratios than would be expected if haze formation was driven by methane production alone. Similarly, Domagal-Goldman et al. (2011) showed that S_{org} photochemistry can lead to the buildup of ethane in excess of methane-only photochemistry, especially in the atmospheres of planets orbiting M dwarfs. The Domagal-Goldman study, however, excluded atmospheres that might form hazes, but the hydrocarbons contributed by S_{org} gases should be incorporated into the haze formation process when a haze is able to form. This is because S_{org} gases participate in photochemistry that generates CH_3 radicals that can be incorporated into haze formation. These methyl radicals can be generated by reactions such as:

$$\mathrm{CH_3SH} + \mathrm{O} \longrightarrow \mathrm{CH_3} + \mathrm{HSO} \tag{R15}$$

$$\mathrm{CH_3SH} + \mathrm{h}\nu \longrightarrow \mathrm{CH_3} + \mathrm{HS} \tag{R16}$$

Therefore, detection of a haze at an unexpectedly low CH_4/CO_2 radio could lend support to biological mediation of haze formation by implying biological organic sulfur gas production if the haze can be spectrally distinguished from other UV absorbers (Chapter 6).

Figure 7.1: Walls of 2.45 Ga banded iron formations (BIFs) line Dales Gorge in Karijini National Park, Western Australia. Photograph by G. Arney.

7.2 Methods

We used the same types of self-consistent `Atmos` (see Chapter 3) simulations described in Chapters 5 and 6 to generate haze around Archean-analog planets in this chapter. To test the strengths of hazy UV-shields, we generated spectra of the incident sunlight at the surfaces of these atmospheres with the `SMART` model (see Chapter 3) through the procedure described previously.

The haze production considered in Section 7.3.2 in the absence of S_{org} is simulated using our Archean chemical species templates (Appendix Tables 1 and 2). Our template with S_{org} gases included is based on the reaction list discussed in Domagal-Goldman et al. (2011). However, we removed the NH_3-related gases and reactions from the templates shown in Domagal-Goldman et al. (2011) because we have not yet incorporated NH_3 into our climate model, and it is a potentially significant greenhouse gas. Inclusion of NH_3 remains an important area of future work because it may play a role in warming our early planet under the fainter young sun, especially under a haze that could protect it from UV-photolysis (Pavlov et al., 2001a; Wolf & Toon, 2010, and Section 5.4.3).

Following Domagal-Goldman et al. (2011), the Sorg gases included in our model are carbon disulfide (CS_2), carbonyl sulfide (OCS), methanethiol (also called methyl mercaptan, CH_3SH) dimethyl sulfide (CH_3SCH_3, also abbreviated as DMS), and dimethyl disulfide ($CH_3S_2CH_3$, also abbreviated as DMDS).

We used Beer's Law (Chapter 2) to simulate UV irradiance under a water column with and without dissolved Fe(II). Given the absorption coefficient of light in a water column, β_a (1/cm), we can calculate the absorption through water of a given thickness with:

$$I = I_0 \times e^{-\beta_a \times z} \tag{7.1}$$

Here, I_0 is the intensity of radiation incident at the top of the water column, z is the depth into the water, and I is the intensity of radiation at that depth. We used the wavelength-dependent water absorption coefficient reported in Segelstein (1981). For water with dissolved Fe(II), we constructed a UV absorption coefficient (1/cm) for water with 5 ppm dissolved Fe(II) (in the form of $FeSO_4$) based on the transmittance spectrum reported in

Garcia-Pichel (1998) for 1 m of seawater and the absorbance spectrum of $FeSO_4$ reported in Olson & Pierson (1986). $FeSO_4$ is assumed to have no absorption at wavelengths longer than 400 nm; transmittance in the $FeSO_4$ solutions reported in Garcia-Pichel (1998) and Olson & Pierson (1986) approach 1 at 400 nm, and we could not find sources in the literature with measurements of $FeSO_4$ transmittance or optical constants at visible wavelengths.

All spectra presented in this chapter assume a solar zenith angle of 60° to approximate the diurnal average. For stellar spectra, we use the GJ 876 spectrum reported in France et al. (2012) that was used in Chapter 6, and our solar spectrum was modeled by Chance & Kurucz (2010) as in Chapters 5 and 6.

7.3 Results

In this section, we consider two different ways hazes and biospheres can interact. First, we examine the spectrum of light and strength of the UVC shield at the surface under a haze and varying depths of water with and without dissolved Fe(II). Following this, we expand on our earlier analysis of haze as a biosignature by considering haze formation in atmospheres containing S_{org} gases.

7.3.1 Archean UV Shields

We previously discussed the ability of an organic haze in the Archean to act as a pre-oxygen and pre-ozone UV shield in Earth's atmosphere (Arney et al., 2016, and Chapter 5). Here, we examine the shielding capabilities of this haze under different depths of water with and without 5 ppm dissolved Fe(II) under the sun at 2.7 Ga. These planets assume 1 bar of atmospheric pressure and $pCO_2 = 0.018$ bar. Our "no haze" planet has $CH_4/CO_2 = 0.1$, our "thin haze" planet assumes $CH_4/CO_2 = 0.17$, and our "thick haze" planet assumes $CH_4/CO_2 = 0.21$, which are the same "Case B" planets we considered in the context of UV shielding in Chapter 5. Table 7.1 presents the UV fluxes in these simulations with no Fe(II), and Table 7.2 presents the same results with 5 ppm dissolved Fe(II). We define photosynthetically-active radiation (PAR) as wavelengths between 0.4 and 1 μm.

The fluxes shown in Tables 7.1 and 7.2 illustrate how a thick haze alone can cut down the total incident UV ($\lambda < 0.40$ μm) flux at the surface by a factor of about 5 and the UVC

Table 7.1: Photosynthetically-active radiation (PAR), UVC flux ($\lambda < 0.280\ \mu$m), and total UV ($\lambda < 0.4\ \mu$m) flux under five different water depths for the atmosphere types specified in the table.

Planet	Depth underwater	PAR (photons/m^2/s/μm)	UVC flux (W/m^2)	Total UV flux (W/m^2)
"No Haze"	0 cm	9.9×10^{20}	0.93	27.8
Archean	1 cm	9.4×10^{20}	0.93	27.7
	10 cm	8.0×10^{20}	0.9	27.5
	50 cm	5.9×10^{20}	0.77	26.3
	100 cm	4.9×10^{20}	0.64	25
"Thin haze"	0 cm	8.5×10^{20}	0.51	20.7
Archean	1 cm	8.3×10^{20}	0.51	20.7
	10 cm	7.19×10^{20}	0.49	20.5
	50 cm	5.4×10^{20}	0.43	19.7
	100 cm	4.5×10^{20}	0.36	18.7
"Thick haze"	0 cm	7.1×10^{20}	0.032	5.3
Archean	1 cm	6.8×10^{20}	0.032	5.3
	10 cm	5.6×10^{20}	0.031	5.3
	50 cm	4.0×10^{20}	0.029	5.1
	100 cm	3.2×10^{20}	0.024	4.9
Modern Earth	0 cm	1.1×10^{21}	~0	29.2
	1 cm	1.1×10^{21}	~0	29.2
	10 cm	9.2×10^{21}	~0	29
	50 cm	6.9×10^{20}	~0	28.1
	100 cm	5.8×10^{20}	~0	26.9
Modern Earth	0 cm	1.2×10^{21}	1.1	36.1
without ozone	1 cm	1.1×10^{21}	1.1	36
	10 cm	9.5×10^{20}	1	35.7
	50 cm	7.1×10^{20}	0.9	34.3
	100 cm	6.0×10^{20}	0.76	32.6

Table 7.2: Photosynthetically-active radiation (PAR), UVC flux ($\lambda < 0.280$ μm), and total UV ($\lambda < 0.4$ μm) flux under five different water depths with 5 ppm dissolved Fe (II) for the atmosphere types specified in the table.

Planet	Depth underwater+Fe(II)	PAR (photons/m^2/s/μm)	UVC flux (W/m^2)	Total UV flux (W/m^2)
"No Haze"	0 cm	9.9×10^{20}	0.93	27.8
Archean	1 cm	9.4×10^{20}	0.89	27.5
	10 cm	8.0×10^{20}	0.63	25.7
	50 cm	5.9×10^{20}	0.17	20.1
	100 cm	4.9×10^{20}	0.042	16.1
"Thin haze"	0 cm	8.5×10^{20}	0.51	20.6
Archean	1 cm	8.3×10^{20}	0.49	20.5
	10 cm	7.19×10^{20}	0.35	18.3
	50 cm	5.4×10^{20}	0.099	15.4
	100 cm	4.5×10^{20}	0.025	12.4
"Thick haze"	0 cm	7.1×10^{20}	0.032	5.3
Archean	1 cm	6.8×10^{20}	0.031	5.2
	10 cm	5.6×10^{20}	0.023	5.1
	50 cm	4.0×10^{20}	0.0076	4.3
	100 cm	3.2×10^{20}	0.0019	3.6
Modern Earth	0 cm	1.1×10^{21}	∼0	29.2
	1 cm	1.1×10^{21}	∼0	29.1
	10 cm	9.2×10^{21}	∼0	28
	50 cm	6.9×10^{20}	∼0	23.5
	100 cm	5.8×10^{20}	∼0	20
Modern Earth	0 cm	1.2×10^{21}	1.1	36.1
without ozone	1 cm	1.1×10^{21}	1	35.7
	10 cm	9.5×10^{20}	0.78	33.4
	50 cm	7.1×10^{20}	0.23	26.2
	100 cm	6.0×10^{20}	0.058	20.9

($\lambda < 0.280$ μm) flux by a factor of 30. As we mentioned in Chapter 5, UVC wavelengths are particularly detrimental to life because they can directly damage DNA. Including Fe(II) in the water column provides an even better UV shield than water alone, especially for UVC: at a depth of 100 cm, the Archean UVC flux under a haze and water with dissolved Fe(II) is 12 times lower than it would be under the same depth of water with no Fe(II), and almost 340 times lower than it would be under that depth of water without haze and without Fe(II).

Note that although these UVC fluxes are substantially lower than those unshielded organisms would be subject to in the Archean, ozone and oxygen in the modern atmosphere provide a far better UVC shield than haze and iron. The UVC flux at the surface of modern Earth is 27 orders of magnitude smaller than the UVC flux at the surface of Archean Earth without a haze. UVC is not a problem that modern life has to contend with in any meaningful way, so even moderately shielded Archean life near the surface would have to be radiation-tolerant.

We have discussed how *Chloroflexus aurantiacus* has been studied as a type of UV-resistant Archean-analog phototroph (Pierson et al., 1992). Figure 3 in Pierson et al. (1992) appears to show a breakpoint in the survivability of this organism over about 10 hours of UVC irradiation at 0.025 W/m^2. While *Chloroflexus aurantiacus* can exhibit moderate growth over the length of an Archean day at higher UVC fluxes than this, below 0.025 W/m^2, its survivability prospects appear to dramatically increase. UVC fluxes below this apparent 0.025 W/m^2 threshold should be possible under about 10 cm of water with 5 ppm dissolved Fe(II) and a thick haze, 100 cm of water with Fe(II) and a thin haze, and 100 cm of water with no dissolved iron and a thick haze.

Recall from Chapter 5 that phototrophs can survive at light levels as low as 6×10^{15} photons/m^2/s (Littler et al., 1986). This is about five orders of magnitude smaller than the smallest PAR fluxes shown in Tables 7.1 and 7.2, so we do not anticipate difficultly for organisms to photosynthesize at the light levels considered here.

Figure 7.2 shows the incident solar flux under the five water depths considered in Tables 7.1 and 7.2 for the Archean with no haze, the Archean with a thick haze, and modern Earth. The peaks of the Archean photon spectra under 0 cm, 1 cm, 10 cm, 50 cm, and 100 cm of water without a haze occur at 0.61, 0.61, 0.58, 0.53, and 0.53 μm, but with a haze they occur at longer wavelengths: 0.75, 0.68, 0.68, 0.58, and 0.57 μm. We discuss some possible implications of the redder photon photon distribution under an Archean haze Section 7.4. The reason why the peak of the photon distribution shifts to bluer wavelengths at deeper depths of water is because water itself is an effective absorber of long wavelength photons – this is why the ambiant light looks blue in the deep ocean.

By comparison with the hazy and non-hazy Archean, the peak photon flux for the modern Earth under these same depths occurs at 0.68, 0.67, 0.52, 0.52, and 0.49 μm. Due to absorption from the ozone Chappuis band centered near 0.6 μm that the Archean spectra do not have, the modern Earth peak flux occurs slightly redward compared to the haze-free Archean spectrum at the surface and shallow depths of water. Under deeper water, the peak of the modern photon distribution shifts blueward of the haze-free Archean distribution because overlapping absorption from water and the Chappuis band both act to remove radiation longward of $\sim$0.5 μm.

7.3.2 Organic haze as a spectral biosignature in the presence of S_{org}

As we have shown, organic haze could have benefited life by blocking UV radiation. This UV shield in the Archean was probably a result of life itself: geochemical evidence suggests the putative hydrocarbon haze in the Neoarchean was biologically mediated via CH_4 produced by methanogenesis (Zerkle et al., 2012). Biogenic hazes may also occur on exoplanets, and while the presence of a haze on an exoplanet with a high level of CO_2 would be tantalizing, implying a high production rate of methane, abiotic processes like serpentinization can also produce CH_4, and abiotic hydrocarbon hazes exist on worlds such as Titan. Therefore, methods to help distinguish abiotic and biotic hazes are needed for establishing the biogenecity of a haze on an Earthlike planet. There may be no single “smoking gun” that would indicate a haze is biological, but here, we discuss how biological sulfur gases could affect haze formation and lend support to biological mediation of a haze layer.

First, we will consider haze formation in the absence of biogenic sulfur gases. Figure 7.3 shows the optical thickness of an organic haze in the atmosphere an Earthlike planet with

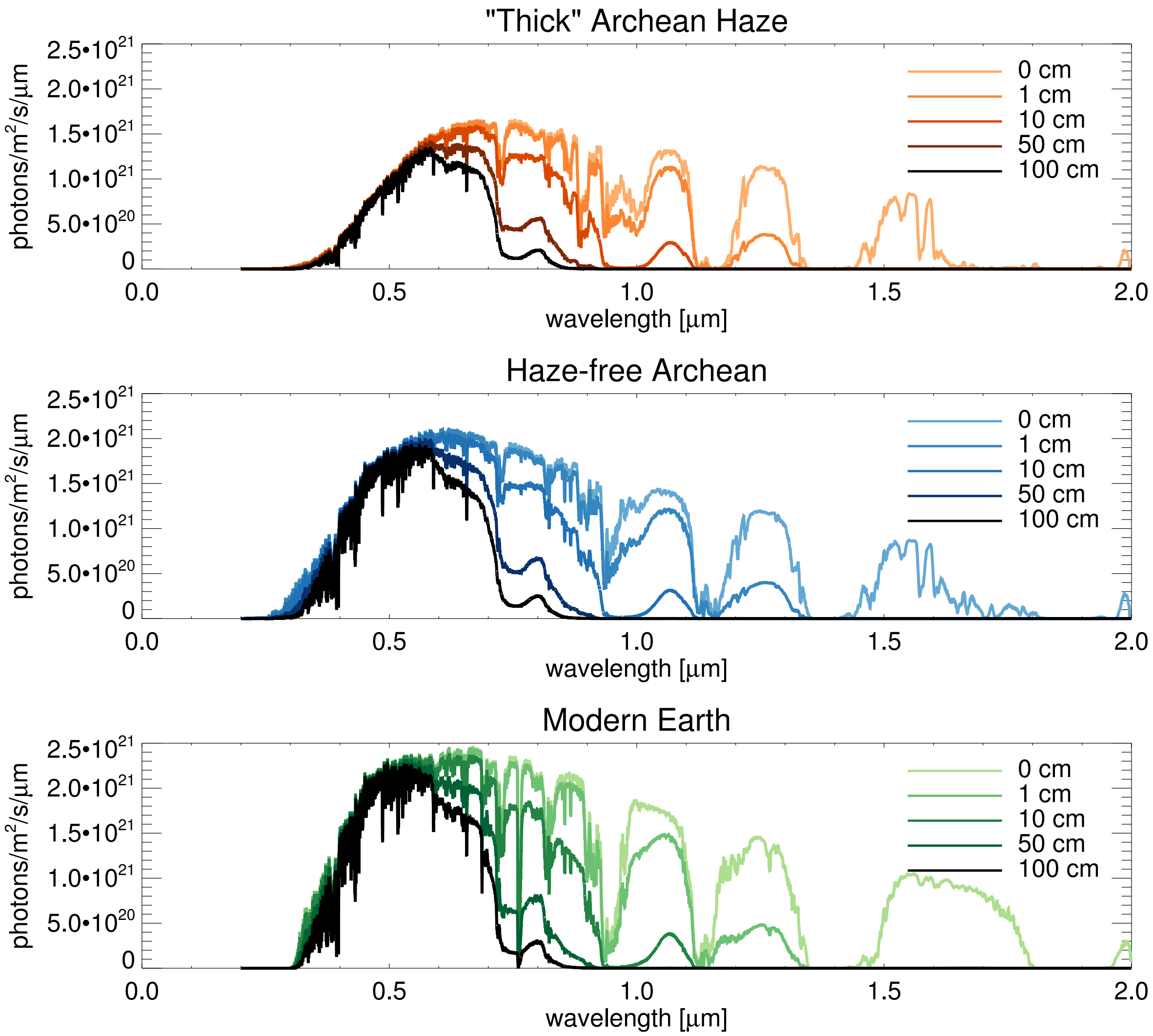

Figure 7.2: Photon fluxes under five depths of water with 5 ppm dissolved Fe(II) for a "Thick" Archean Haze ($CH_4/CO_2 = 0.21$), a haze-free Archean atmosphere ($CH_4/CO_2 = 0.1$), and the modern Earth with no clouds.

1 bar of total pressure and no S_{org}. Optical depth of unity at 190 nm (chosen to represent hazes that begin to significantly impact photochemistry) is marked with the solid black line overlying the colored contours. The CO_2 atmospheric fractions (fCO_2) range from 1×10^{-5} to 1×10^{-1}; our lower limit on CO_2 abundance was chosen to roughly represent the limit for C4 photosynthesis (Kestler et al., 1975; Tolbert et al., 1995), which is determined by

the ability of plant stomata to maintain a diffusive gradient of CO_2 concentration from the atmosphere into the cellular structure. CH_4 surface fluxes were chosen to range between 6.8×10^8 - 1×10^{12} molecules/cm^2/s. The lower limit on methane production is taken from the Guzmán-Marmolejo et al. (2013) theoretical study of serpentinization-driven methane. The upper limit on methane is roughly an order of magnitude larger than biological production on modern Earth – the modern biotic CH_4 flux is about 1×10^{11} molecules/cm^2/s, and fluxes between 1/3 - 2.5 times this value have been considered plausible for the Archean (Kharecha et al., 2005). These estimated biotic fluxes are broadly consistent with the methane fluxes needed to form a haze at Archean-like pCO_2 values (i.e. at $fCO_2 \sim 1 \times 10^{-3}$ - 1×10^{-2}, Driese et al. 2011). Thus, as we have argued in Chapter 5, haze formation in atmospheres with Archean-like levels of CO_2 indicates methane production consistent with known and theoretical biogenic methane production rates on modern and Archean Earth.

We will now consider haze production in the presence of S_{org}. Figure 7.3 showed the CH_4 flux needed to form a haze as a function of different CO_2 levels to show how haze formation at Archean-like CO_2 levels can suggest biological methane production rates. When we observe terrestrial exoplanets, the CH_4 mixing ratio – not the CH_4 flux – will be the actual spectral observable (although the latter could be inferred through photochemical modeling). In accordance with the actual spectral observables, Figures 7.4 and 7.5 show the 190 nm haze optical thickness with S_{org} as a function of the CH_4/CO_2 ratio (which can be measured by retrieving the mixing ratios of both of these species) and fCO_2 for planets orbiting the sun at 2.7 Ga and orbiting the M dwarf GJ 876. Both planets receive the same total level of incident stellar radiation. In both figures, the top panel corresponds to the optical depth contours for 1x the modern S_{org} fluxes as defined in Domagal-Goldman et al. (2011), and the bottom panel corresponds to 30x the modern S_{org} fluxes. In both panels, the solid red line denotes where the haze's 190 nm optical depth equals unity for 1x S_{org}, and the solid black line denotes where the haze optical depth is unity for 30x S_{org}.

Interestingly, Figures 7.4 and 7.5 show that as fCO_2 decreases, the CH_4/CO_2 ratio needed for haze formation increases – this is because the total carbon budget of the atmosphere decreases as CO_2 is removed. In other words, "thick" hazes do not form at low CH_4/CO_2 ratios when the absolute level of CO_2 is low because this means that the absolute amount

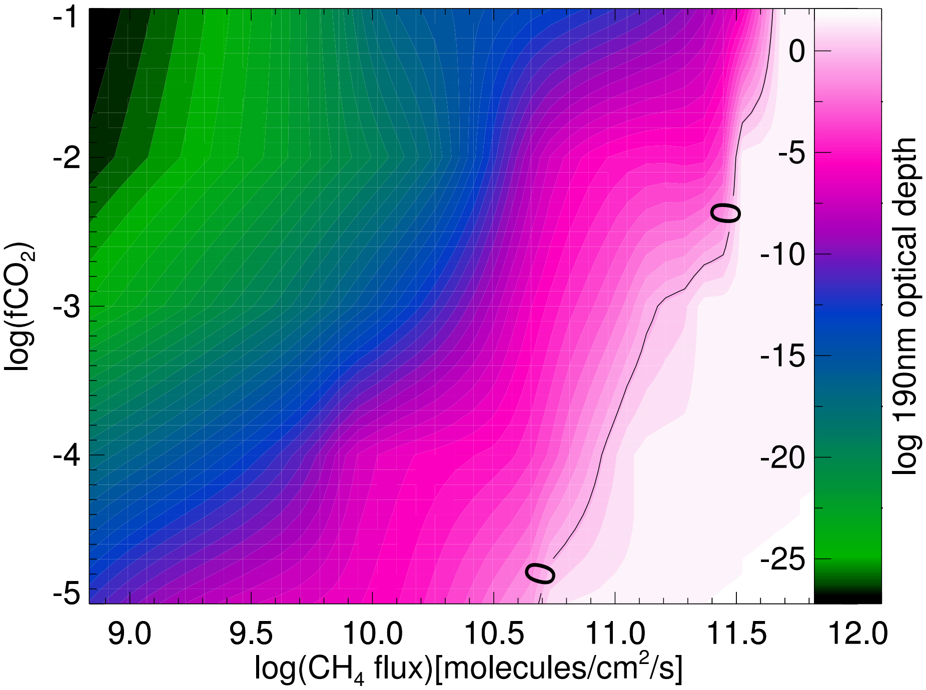

Figure 7.3: The colored contours show the log optical depth of the Archean haze at 190 nm as a function of $log(f\mathrm{CO}_2)$ and $log(\mathrm{CH}_4$ flux$)$. Optical depth of unity is marked by the solid black line. Note how at higher CO_2 levels, higher methane fluxes are needed to produce a haze.

of CH_4 that haze forms out of is also very small. Significantly, when fluxes of S_{org} increase, the CH_4/CO_2 ratio necessary to form a haze decreases at all CO_2 levels.

For a planet orbiting a solar-type star, at $fCO_2 = 10^{-2}$, the CH_4/CO_2 ratio needed to form a haze with $\tau = 1$ at 190 nm is about 0.2 for $1 \times S_{org}$ and about 0.16 for $30 \times S_{org}$. This difference may not be large for the planet around the sun, but around GJ 876, S_{org} has a larger impact on haze formation. For the GJ 876 planet, at $fCO_2 = 10^{-2}$, the haze becomes optically thick at slightly less than $CH_4/CO_2 = 0.2$ for $1 \times S_{org}$, but for $30 \times S_{org}$, the haze becomes optically thick at $CH_4/CO_2 \sim 0.02$, an order of magnitude lower. This effect is more pronounced around the M dwarf planet because hazes form more efficiently in atmospheres with low production of abiotic oxygen radicals as we saw in Chapter 6. The

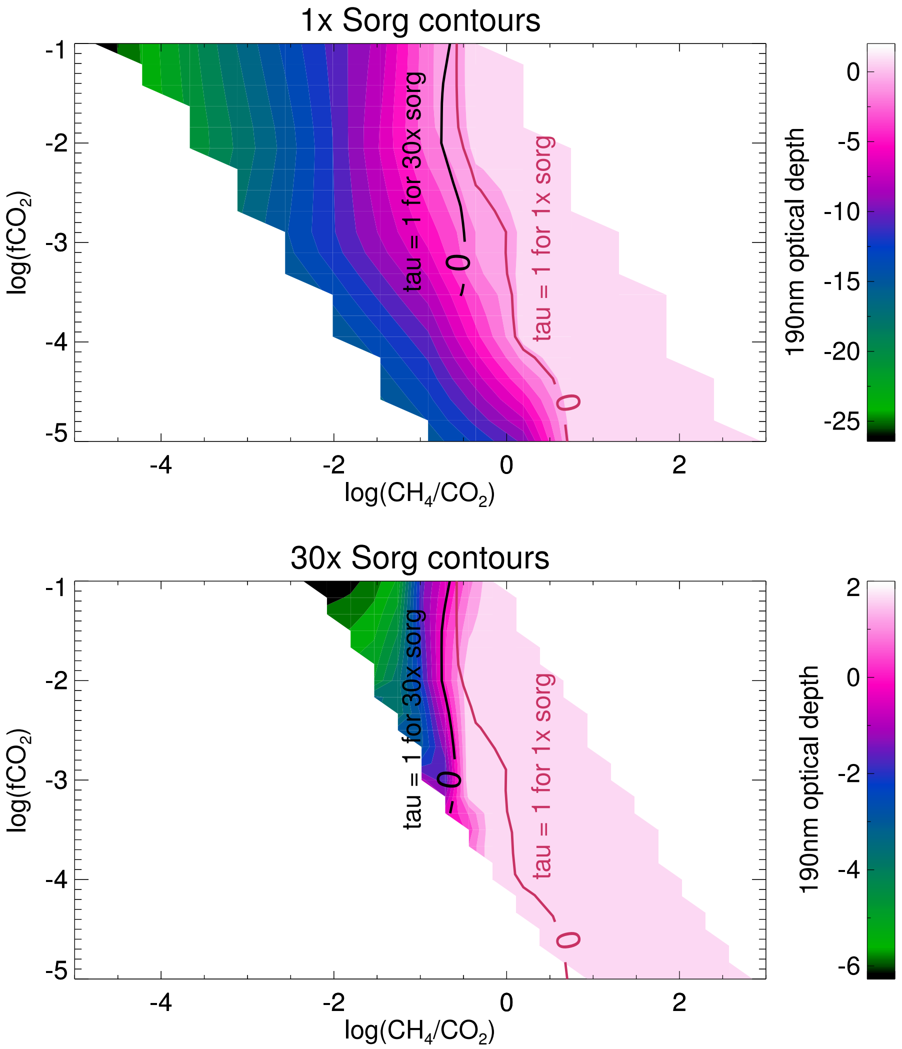

Figure 7.4: The log of the 190 nm optical depth of organic haze for planets around the sun at 1 x S$_{org}$ and 30 x S$_{org}$ as a function of $log(f\mathrm{CO}_2)$ and $log(\mathrm{CH}_4$ flux). The red line in both panels shows where optical depth is unity for 1 x S$_{org}$ and the black line in both panels shows where optical depth is unity for 30 x S$_{org}$.

difference between the CH$_4$/CO$_2$ ratios needed for haze formation with 1× S$_{org}$ versus 30× S$_{org}$ increases as fCO$_2$ decreases.

For the 30×S$_{org}$ atmospheres, for the range of CH$_4$ fluxes tested here, hazes formed at the lowest CH$_4$ flux levels (and, therefore, the lowest CH$_4$/CO$_2$ ratios simulated in the model) in

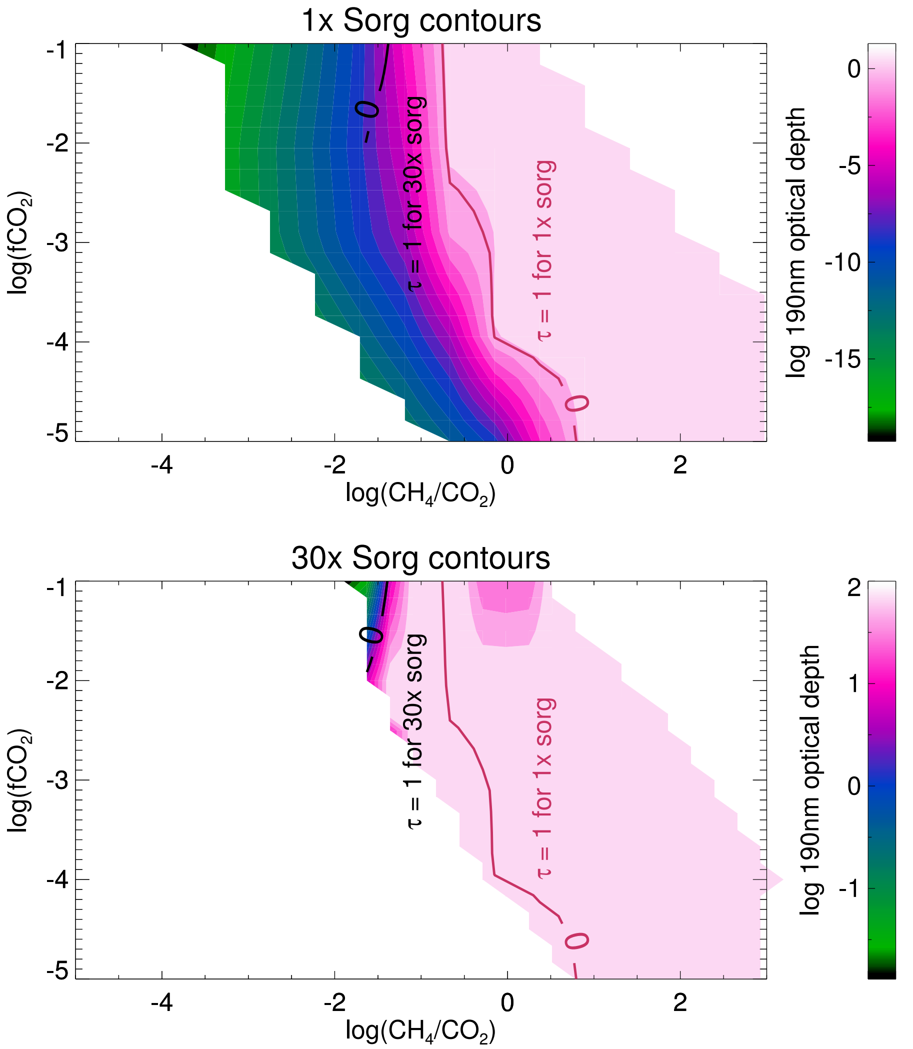

Figure 7.5: The log of the 190 nm optical depth of organic haze for planets around the GJ 876 at 1 x S$_{org}$ and 30 x S$_{org}$ as a function of $log(f\text{CO}_2)$ and $log(\text{CH}_4$ flux). The red line in both panels shows where optical depth is unity for 1 x S$_{org}$ and the black line in both panels shows where optical depth is unity for 30 x S$_{org}$.

all atmospheres with fCO$_2$ $< 10^{-3}$ around the solar-type star and for all atmospheres with fCO$_2$ $< 10^{-2}$ around GJ 876. This is because the S$_{org}$ gases provide enough hydrocarbons to control haze-formation in low-methane atmospheres. The S$_{org}$ gases also control the atmospheric CH$_4$ budget at low methane amounts – the lowest CH$_4$/CO$_2$ ratios simulated for 30 × S_{org} are higher than the lowest CH_4/CO_2 ratios for 1 × S_{org}. The largest sources of CH_4 in the 30 × S_{org} atmospheres are $CH_3 + HCO \longrightarrow CH_4 + CO$ and $CH_3 + H \longrightarrow CH_4$. These reactions are one to two orders of magnitude faster in the 30 × S_{org} atmosphere than the largest atmospheric sources of CH_4 in the 1 × S_{org} atmosphere, $CH_4 + H \longrightarrow CH_4$ and $CH_3 + HCO \longrightarrow CH_4 + CO$.

Figure 7.5 shows a decrease in haze opacity for the GJ 876 planet at $CH_4/CO_2 \sim$ -0.5 to 0.5 for $log(fCO_2 > -2)$. The model runs in this region of parameter space did not converge, so this effect is probably not real.

7.4 Discussion

Organic hazes and biospheres interact in multiple ways. We have showed how haze could have affected Archean life through its UV shielding abilities, especially in conjunction with an ocean containing UV-absorbing Fe (II). We have also demonstrated how organic haze on an Archean-like planet could imply CH_4-fluxes consistent with known biological production rates. Even stronger evidence for a biologically-driven haze could come from haze formation occurring at at lower CH_4/CO_2 ratios than would be predicted if methane was the only contributor to the hydrocarbon budget of the atmosphere. This can occur when S_{org} gases are present, and a decrease in the CH_4/CO_2 level needed for haze formation caused by S_{org} is even more pronounced around GJ 876 compared to a solar-type star.

7.4.1 Possible impacts of haze on photosynthetic pigments

Kiang et al. (2007a,b) noted that the wavelength of the peak photon flux incident on a planet's surface environment is the primary environmental pressure driving the evolution of photosynthetic pigment absorption. Photon flux, rather than energy flux, is the important quantity to consider for pigment absorption because photosynthesis depends on photon counts rather than total energy (Kiang et al., 2007b). On the modern Earth, the maximum photon flux occurs near 680 nm, and this is closely coincident to chlorophyll a's absorption peak. Based on this, Kiang et al. (2007b) hypothesizes that the dominant photosynthetic pigments on the surfaces of exoplanets orbiting different colored stars will have different peak absorptivities corresponding to their stars' unique peak photon fluxes under different stars and atmospheres. Photosynthetic organisms on Earth whose pigment absorption spectra peak at different wavelengths than chlorophyll have adapted to the light in their own environmental niches. For example, photosynthetic bacteria living under layers of overlying algae and sediments have absorption peaks in the NIR, and this may be because these longer wavelengths penetrate deepest into these layers in shallow water environments (Fenchel & Straarup, 1971).

In this Chapter, we showed that the wavelengths of light reaching the surface change under a hazy sky. The peak of the surface photon flux distribution occurs at 610 nm in the Archean atmosphere without a haze, and it occurs at 750 nm when a "thick" haze corresponding to $CH_4/CO_2 = 0.21$ is in place. We can hypothesize that this could lead to evolutionary pressures pushing organisms towards using redder-absorbing pigments under a hazy Archean sky. However, as we discussed previously, water also absorbs red light. Coincidentally, the peak of the photon flux under a haze and 10 cm of water – which should be sufficient for shielding an organism like *Chloroflexus aurantiacus* if 5 ppm Fe (II) is dissolved in it – occurs at almost the same wavelength as the modern photon flux peak because of red wavelength absorption by water. So, at depth, organisms may be minimally influenced by the redder sunlight reaching the surface under a haze.

On the other hand, as we discussed in Chapter 5, we know that stromatolites – photosynthetic microbial mat communities that still exist on Earth today in environments shielded from predators (Figure 7.6) – lived in intra- and supratidal zones in the Archean (Allwood et al., 2006; Noffke & Awramik, 2013). Under these conditions, stromatolites would have experienced direct contact with the surface environment at low tide.

To protect life at the planet's surface, other UV shields than the ones considered here may have existed to shield organisms from UV radiation. For example, scytonemin, an extracellular sheath pigment in modern cyanobacteria, strongly absorbs UVC radiation and has been found to confer protection against these short UV wavelengths (Dillon & Castenholz, 1999). Scytonemin can be seen in Figure 7.6 as the brown-colored pigment on these modern stromatolite communities. UVC wavelengths do not reach the ground in the modern oxygenated atmosphere, which suggests that scytonemin's UVC protectant abilities evolved prior to 2.5 when the rise of atmospheric oxygen occurred (Holland, 2006).

Archean stromatolite communities, protected by a haze and a pigment like the ancestor to modern scytonemin, may have directly experienced light at the surface under a haze. Thus, evolutionary pressures favoring absorption of the peak photon flux at the surface under a haze may have caused their pigment absorption peaks to shift to around 750 nm where the hazy peak photon flux occurs.

Figure 7.6: Living stromatolites in Hamelin Pool at Shark Bay in Western Australia. The stromatolites can be seen here as the dark and tan-colored pillow-shaped and flat objects in the water. The dark upper layer on the stromatolites has been identified as scytonemin, a UV absorbing pigment (Tewari & Seckbach, 2011). Due to predation by grazing organisms, stromatolites can survive in very few environments on modern Earth. They thrive in Hamelin Pool because the water's hypersalinity and high alkalinity inhibits the survival of their predators. Shark Bay is a special and precious environment that has been identified as a UNESCO World Heritage Site. Photograph by G. Arney.

Figure 7.7 shows the absorption spectra of several modern organisms provided by N. Parenteau. The organisms plotted are the following. *Rosiflexus castenholzii* is a green non-sulfur filamentous anoxygenic phototroph that uses bacteriochlorophyll a (Bchl a). *Thermochromatium tepidum* is a purple sulfur bacteria using Bchl a. *Rhodobacter capsulatus* is a purple non-sulfur bacteria using Bchl a. *Prosthecochloris aestuarii* is a green sulfur bacteria, and this spectrum contains absorption from Bchl a, Bchl c, and chlorophyll a (Chl a). *Chloroflexus aurantiacus*, discussed above, is a green non-sulfur filamentous anoxygenic phototroph using Bchl a and Bchl c. *Heliobacterium modesticaldum* is a heliobacterium using Bchl g. *Acaryochloris marina* is a type of cyanobacteria using Chl d, and its absorption spectrum is scaled up by a factor of 2 in the figure to more clearly show its spectral shape. From these spectra, it is apparent that a range of absorption peaks are possible for organisms. For example, the absorption peak for Chl d, which is used by oxygenic photosynthesis, occurs in the NIR at 720 nm (Larkum & Kuhl, 2005). This absorption peak can be seen in the spectrum of *Acaryochloris marina* in Figure 7.7. Kiang et al. (2007b) suggests that this particular type of cyanobacteria adapted to use longer wavelengths filtered through overlying layers of other organisms. This may imply that for some organisms such as those not directly living at the surface, the local environment may be a stronger evolutionary driver than incident sunlight.

The visible wavelength absorption peak for *Chloroflexus aurantiacus* occurs at 740 nm from absorption by Bchl c, and it is closely coincident to the peak photon flux at the surface under an Archean haze. Evolutionary pressures under a haze in the Archean may have driven photosynthetic organisms to absorb light similar to the way the modern *Chloroflexus aurantiacus* does.

7.4.2 CO_2 observations needed to suggest a haze as biogenic

A haze at a lower than expected CH_4/CO_2 ratio could imply the influence of biogenic sulfur gases. This is similar to the suggestion of ethane as a spectral biosignature in Domagal-Goldman et al. (2011), which showed that ethane concentrations reach higher levels in atmospheres with higher S_{org} fluxes even if the S_{org} gases themselves are not directly detectable.

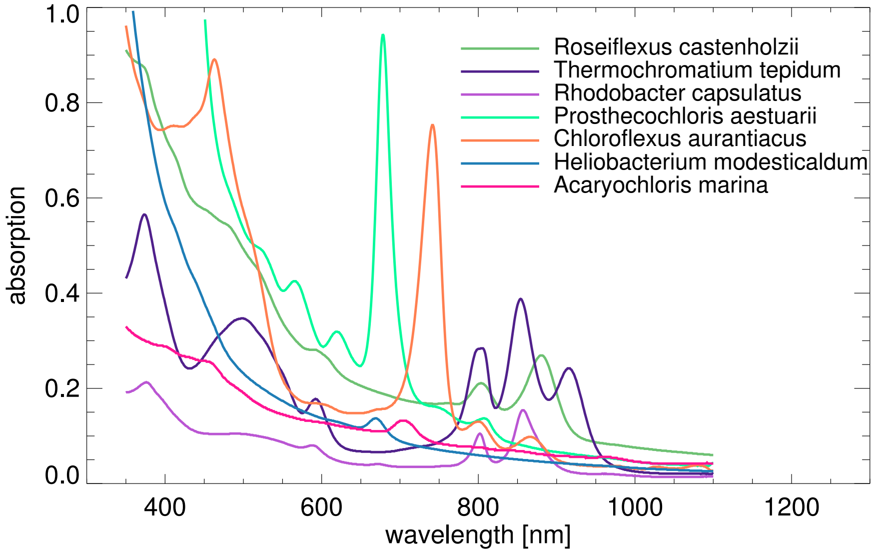

Figure 7.7: The absorption spectra for seven types of photosynthetic organisms. The peak near 670 nm is due to chlorophyll a.

This effect is more pronounced around M dwarf stars like GJ 876 because the lower overall UV flux around this star leads to smaller sinks of hydrocarbon gases (Domagal-Goldman et al., 2011, and Chapter 6). These hazy worlds around M dwarfs may be observable in transit with the James Webb Space Telescope (Chapter 6), and JWST observations of Archean-analog worlds may provide access to measurements of the atmospheric inventories of CH_4 and CO_2 needed to argue for mediation of haze production by biogenic sulfur gases.

In all situations – including planets without S_{org} gases – it will be important to know the redox state and temperature of an atmosphere to argue for the plausibility of a biogenic haze. Titan shows us that abiotic hazes can form in highly reducing cold atmospheres with long residence lifetimes for methane. Therefore, in cold reducing atmospheres such as Titan's, hazes can form at low CH_4 production rates easily explained by nonbiological processes (Figure 7.3).

Transit observations with JWST should provide access to NIR wavelengths with CO_2 bands that can be used to constrain the atmospheric CO_2 budget. The strongest CO_2

feature occurs near 4.3 μm in the JWST simulations we presented in Section 6.3.5.a. It is unlikely that a feature at this long a wavelength would be detectable with a near-future direct imaging mission due to inner working angle constraints, but other much weaker CO_2 bands near 1.5, 1.4, 1.57, 1.61, and 2 μm could be accessible with a mission like LUVOIR.

In direct imaging, two factors may limit our ability to sense CO_2 at 1.5 μm and 2 μm. First, as we saw from Section 6.3.5.b, the inner working angle can limit the longest wavelengths we can measure, and this cutoff may occur shortward of the CO_2 bands for more distant planets. Second, thermal radiation can become a significant noise source at wavelengths longer than about 1.6 μm if a telescope is not cryogenically cooled. Finally, the 1.4, 1.57, and 1.61 μm CO_2 bands are very weak. Figure 7.8 shows the integration times needed to achieve a signal-to-noise ratio (SNR) of 10 as a function of wavelength for two 10-m telescopes with 20% throughput chosen to represent a coronagraphic instrument. These simulations were performed with the Robinson et al. (2016) coronagraph noise model used for our simulations in Chapter 6. The teal line shows the performance of a telescope with T = 274 K, while the blue line shows the performance of a telescope with T = 180 K. The thermal background becomes apparent at wavelengths > 1.6 μm. Because of this thermal background, the integration time needed to detect CO_2 near 2 μm with the same SNR for a telescope at T = 274 K takes two orders of magnitude longer than it would for a telescope cooled to T = 180 K. For telescopes that are not cooled, the 2 μm CO_2 band may be inaccessible even if it is not cut off by the inner working angle.

Carbon dioxide is an important gas. Measuring it can help constrain the efficiency of a planet's greenhouse, the atmospheric redox state, and can even support the interpretation of a planet as a rocky (rather than gaseous) body. Therefore, mission architectures that maximize our probability of detecting CO_2 on an exoplanet should be seriously studied for mission concepts like LUVOIR and HabEx.

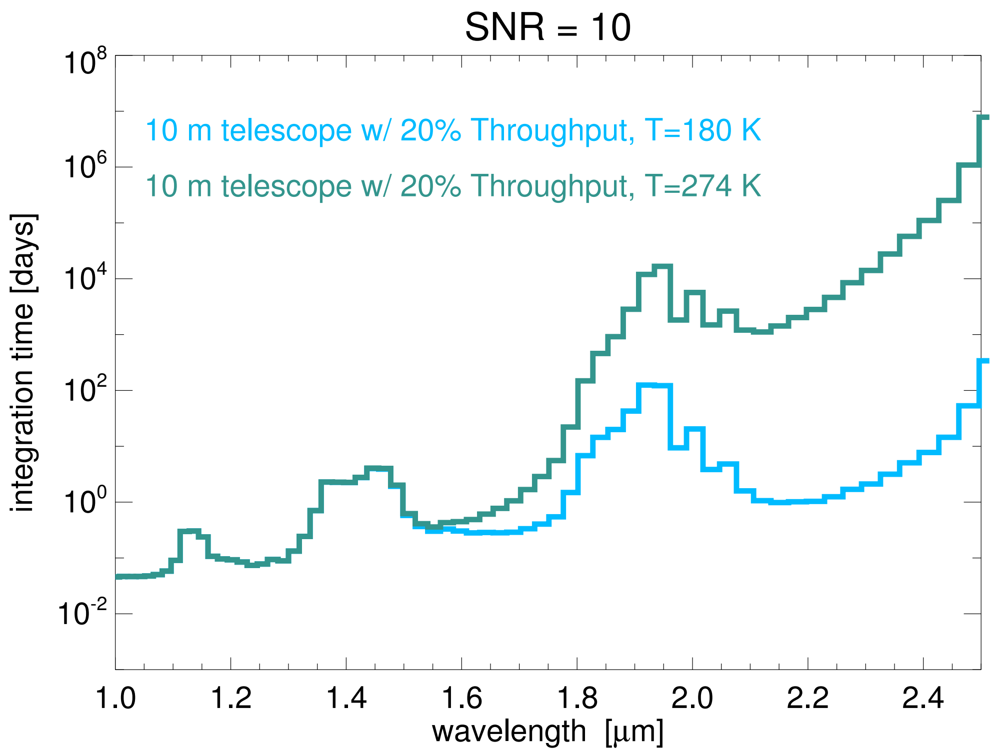

Figure 7.8: The wavelength-dependent telescope integration time needed to achieve a signal-to-noise ratio (SNR) of 10 for modern Earth at 10 parsecs. Shown are two 10 m telescopes with 20% throughput with T = 180 K and T = 274 K. Thermal noise becomes significant for wavelengths > 1.6 μm. Spectral resolution = 70.

7.5 Directions for future work

In future work with N. Parentaeu, we will expand our study of the links between haze and biology and will experimentally test how photosynthetic organisms grow and respond to light levels under a haze. N. Parenteau has a LED setup at NASA Ames Research Center that can simulate different spectral energy distributions by altering the strengths of individual LEDs. Also available is a germicidal lamp that can produce UVC radiation. With this setup, will be able to test the actual survivability and productivity of oxygenic and anoxygenic photosynthetic organisms under the light levels we predict under the Archean haze. While we expect that the protection offered by the haze will aid organisms like *Chloroflexus* *aurantiacus*, their actual survivability rate has yet to be quantified in the context of a hazy atmosphere. The productivity rate for microbes employing oxygenic photosynthesis can be quantified by measuring oxygen production. For anoxygnenic phototrophs, productivity should be quantifiable by measuring their consumption of the electron donor (N. Parenteau, personal communication).

These experiments can also take into account the Archean diurnal cycle, which was 18-19 hours long (Denis et al., 2002). `SMART` can provide spectra as a function of solar zenith angle that we can use to vary the luminosity the individual LEDs over the course of a simulated "day." Spending time in darkness during the simulated "night" may give organisms time to repair damage caused by high UV light levels during the "day." Day-night cycles were not included in the previous UVC-irradiance experiments on *Chloroflexus aurantiacus* by Pierson et al. (1992) This exciting area of future work may offer new insights on the evolution of photosynthetic life in the Archean.

7.6 Concluding remarks

This chapter explored the efficacy of a UV shield from an Archean haze under different depths of water with and without dissolved Fe(II) – which is also an efficient UV absorber. Haze may have allowed UV-tolerant organisms to live in the upper part of the water column or even the surface without experiencing UV damage. We also explored how this haze may be a type of a biosignature in the presence of biogenic sulfur gases. These gases can contribute to the hydrocarbon budget of the atmosphere and can result in haze formation at a lower CH_4/CO_2 ratio than we would expect from methane photochemistry alone, suggesting biological mediation. When future telescopes attempt to detect these hazes (Chapter 6), determining their potential biogenecity will be a difficult yet important task.

7.7 Note of acknowledgement

Parts of this chapter were inspired by a field trip to Western Australia organized by the Australian Centre for Astrobiology (ACA) and the University of New South Wales. I am grateful to the NASA Astrobiology Institute for awarding me a scholarship that allowed me to participate in this amazing adventure. I also thank the VPL for enabling richly interdisciplinary work like the concepts presented in this chapter. This chapter builds off of previous heavily interdisciplinary VPL work by Kiang et al. (2007b), Kiang et al. (2007a), and Domagal-Goldman et al. (2011), and I am grateful to be part of a team of researchers spanning a wide range of scientific disciplines.

Chapter 8

CONCLUSIONS

Aerosols are crucial components of planetary atmospheres, impacting planetary climate, spectra, UV shielding, photochemistry, and habitability. Hazes and clouds globally enshroud Venus, the planet next door, and a global organic haze may have existed on Earth during the Archean. It is important to understand how to characterize enshrouded worlds such as these because hazes and clouds are likely to be common on exoplanets. In this thesis, I explored these topics in detail (Figure 8.1).

Chapter 4 presented the first simultaneous maps of water vapor, CO, HCl, OCS, SO_2, cloud opacity, and sulfuric acid concentration in the Venusian lower atmosphere. We saw evidence of correlations between the cloud deck and several gases, suggesting active processes in the Venus lower atmosphere. While the night side disk average measurements remained constant from year to year, there was considerable spatial variability across the disk for many species on timescales as short as 24 hours. This suggests active processes with conservation between species. The most variable regions were seen just below the Venus cloud deck. Banding patterns seen in our 2009 water vapor maps might result from virga of H_2SO_4 droplets, which break down into H_2O and SO_3 in the lower atmosphere and are sheared out by zonal winds. There was also evidence of variable hemispherical dichotomies: in the 2009 Venus maps, there was more CO and H_2SO_4 in the northern hemisphere, while in 2010, there was more H_2SO_4, water vapor, OCS, and SO_2 in the north, but CO was more abundant in the south. My work on Venus showed that the Venus lower atmosphere is just as dynamic and complex as the higher layers. An improved understanding of the processes that occur in Venus' atmosphere will help us to better understand Earth's "sister planet" and potentially will aid our understanding of exo-Venus planets in other solar systems.

Closer to home, Chapter 5 showed that a hazy Archean Earth consistent with geochemical constraints on CO_2 concentration could have had habitable surface temperatures.

Figure 8.1: A word cloud of topics discussed in this dissertation.

Although the fractal hazes simulated here cool the planet by up to ~20-25 K, these fractal particles produce significantly less cooling than a haze of equivalent mass spherical particles. The climatic effects of this haze could have been part of feedbacks between biological CH_4 production, atmospheric chemistry, surface UV radiation, and photosynthetic processes.

Haze can cut down the surface-incident UVC radiation on Archean Earth from ∼0.9 W/m^2 to ∼0.03 W/m^2 for a solar zenith angle of 60° and may have allowed survival of otherwise unshielded life at the surface of our early planet. On Archean Earth, haze may even have affected the evolution of photosynthetic pigments by dramatically altering the colors of radiation able to reach the planet's surface, as discussed in Chapter 7.

By examining Archean-analog Earths orbiting other types of stars, Chapter 6 showed that the ability of a planet to form organic hazes varies strongly with host star spectral type. For the atmospheres considered, stars with very high FUV fluxes (e.g., F stars) are unlikely to form organic haze due to the buildup of oxygen species that destroy hydrocarbons. At the other extreme, stars with very low UV fluxes (e.g., inactive M dwarfs) were unable to form organic haze in the simulations shown in Chapter 6 due to the inability to drive the photochemical reactions needed in haze formation. For planets with haze, antigreenhouse cooling is relevant to G and K dwarf planets, but because M dwarfs emit the bulk of their radiation at wavelengths where these hazes are relatively transparent, haze-induced cooling for M dwarf planets is unimportant.

The presence of similar hydrocarbon haze on an exoplanet could be observed, as demonstrated by strong features present in synthetic spectra of these worlds. Hydrocarbon haze may also be a more detectable indication of high CH_4 abundances in terrestrial planetary atmospheres than the CH_4 itself. Organic haze produces a broad, deep absorption feature at UV-blue wavelengths that should be detectable with direct imaging telescopes like LUVOIR in the future. In transit transmission, a spectral slope caused by the haze is detectable at visible and NIR wavelengths from our JWST simulations. There is an organic haze absorption feature near 6 μm, and this feature may be detectable with JWST's MIRI instrument.

For habitable exoplanets similar to Archean Earth, hydrocarbon haze may be strongly biologically mediated, and it might serve as a novel non-gaseous biosignature with a prominent spectral signature. As discussed in Chapter 7, this may be especially true in the presence of biological sulfur gases that allow hazes to form at lower CH_4/CO_2 ratios than we would predict from methane photochemistry alone. Even a non-biological haze would be interesting to detect in an Earth-like atmosphere because this would imply geological activity producing methane. Therefore, although haze is often considered to be a feature that conceals certain atmospheric features and surface processes, haze itself can indicate a geologically active planet – and therefore a potentially habitable one – and possibly even reveal the presence of life.

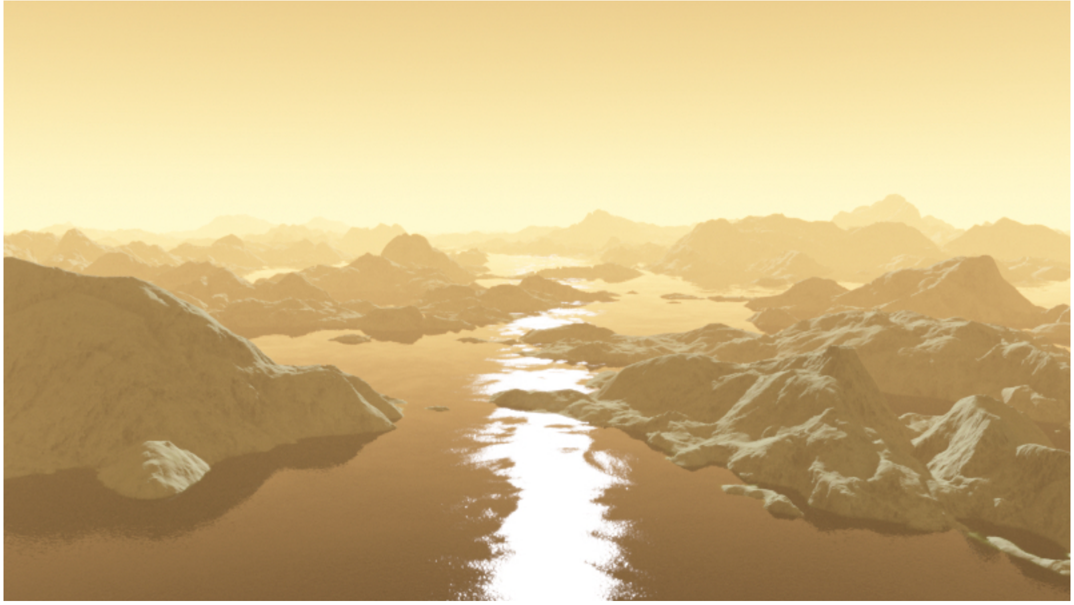

Figure 8.2: Hazy Archean Earth? Or a possible version of early Venus protected from overheating by an organic haze?

Discovering habitable exoplanets dissimilar to modern Earth will increase the diversity of known habitable environments. Leveraging our understanding of Earth's history provides us with a variety of analogs with which we can expand our expectations for "Earth-like" planets beyond our Solar System; future observations of such worlds can provide us with a window into the evolution of terrestrial worlds like our home. Venus, meanwhile, provides an example of a radically different type of world that is highly interesting and may represent a common class of planets orbiting other stars. By "pulling back the veil" on these worlds, we have revealed how complex, dynamic, and fascinating enshrouded planet atmospheres can be.

Appendix Table 1: List of reactions with rate constants and sources for the Archean photochemical code. For photolysis reactions at the bottom of the table, the "Reaction Rate Constant" refers to the reaction rate at the top of the atmosphere during a "standard" simulation for $pCO_2 = 0.02$, $pCH_4 = 0.0035$, 1 bar total pressure (a moderately hazy Case B atmosphere). Refer to Sander et al. (2006) for more information about reaction rate calculations.

Rxn. #	Reaction	Reaction Rate Constant	Reference
1.	$OCS + CH \rightarrow CO + HCS$	$1.99\cdot10^{-10} \times e^{-190/T}$	(Zabarnick *et al.*, 1989)
2.	$OCS + H \rightarrow CO + HS$	$9.07\cdot10^{-12} \times e^{-1940/T}$	(Lee *et al.*, 1977)
3.	$OCS + O \rightarrow S + CO_2$	$8.3\cdot10^{-11} \times e^{-5530/T}$	(Singleton and Cvetanovic 1988)
4.	$OCS + O \rightarrow SO + CO$	$2.1\cdot10^{-11} \times e^{-2200/T}$	(Toon *et al.*, 1987)
5.	$OCS + OH \rightarrow CO_2 + HS$	$1.1\cdot10^{-13} \times e^{-1200/T}$	(Atkinson *et al.*, 2004)
6.	$OCS + S \rightarrow CO + S_2$	$1.5\cdot10^{-10} \times e^{-1830/T}$	(Schofield 1973)
7.	$OCS + S + M \rightarrow OCS_2 + M$	$8.3\cdot10^{-33} \times$ den	(Basco and Pearson 1967)
8.	$OCS_2 + CO \rightarrow OCS + OCS$	$3.0\cdot10^{-12}$	(Zahnle *et al.*, 2006)
9.	$OCS_2 + S \rightarrow OCS + S_2$	$2.0\cdot10^{-11}$	(Zahnle *et al.*, 2006)
10.	$CH + CS_2 \rightarrow HCS + CS$	$3.49\cdot10^{-10} \times e^{-40/T}$	(Zabarnick *et al.*, 1989)
11.	$CS + HS \rightarrow CS_2 + H$	$1.5\cdot10^{-13} \times (1 + 0.6 \times \text{den})$	Assumed same as k(CO + OH)
12.	$CS + O \rightarrow CO + S$	$2.7\cdot10^{-10} \times e^{-760/T}$	(Atkinson *et al.*, 2004)
13.	$CS + O_2 \rightarrow CO + SO$	$5\cdot10^{-20}$	(Wine *et al.*, 1981)
14.	$CS + O_2 \rightarrow OCS + O$	$4\cdot10^{-19}$	(Wine *et al.*, 1981)
15.	$CS + O_3 \rightarrow CO + SO_2$	$3\cdot10^{-12}$	(Wine *et al.*, 1981)
16.	$CS + O_3 \rightarrow OCS + O_2$	$3\cdot10^{-12}$	(Wine *et al.*, 1981)
17.	$CS + O_3 \rightarrow SO + CO_2$	$3\cdot10^{-12}$	(Wine *et al.*, 1981)
18.	$CS_2 + O \rightarrow CO + S_2$	$5.81\cdot10^{-14}$	(Singleton and Cvetanovic 1988)
19.	$CS_2 + O \rightarrow OCS + S$	$3\cdot10^{-12\times}\, e^{-650/T}$	(Toon *et al.*, 1987)
20.	$CS_2 + O \rightarrow SO + CS$	$3.2\cdot10^{-11} \times e^{-650/T}$	(Toon *et al.*, 1987)
21.	$CS_2 + OH \rightarrow OCS + HS$	$2\cdot10^{-15}$	(Atkinson *et al.*, 2004)
22.	$CS_2 + S \rightarrow CS + S_2$	$1.9\cdot10^{-14} \times e^{-580/T} \times (T/300)^{3.97}$	(Woiki and Roth 1995)
23.	$CS_2 + SO \rightarrow OCS + S_2$	$2.4\cdot10^{-13} \times e^{-2370/T}$	Assumed same as k(SO* + O_2)
24.	$CS_2^* + CS_2 \rightarrow CS + CS + S_2$	$1\cdot10^{-12}$	Assumed same as k(CS_2^* + CS_2)
25.	$CS_2^* + M \rightarrow CS_2 + M$	$2.5\cdot10^{-11}$	(Wine *et al.*, 1981)
26.	$CS_2^* + O_2 \rightarrow CS + SO_2$	$1\cdot10^{-12}$	(Wine *et al.*, 1981)
27.	$C + HS \rightarrow CS + H$	$4\cdot10^{-11}$	Assumed same as k(C + OH)
28.	$C + S_2 \rightarrow CS + S$	$3.3\cdot10^{-11}$	Assumed same as k(C + O_2)
29.	$C_2 + S \rightarrow C + CS$	$5\cdot10^{-11}$	Assumed same as k(C_2 + O)
30.	$C_2 + S_2 \rightarrow CS + CS$	$1.5\cdot10^{-11} \times e^{-550/T}$	Assumed same as k(C_2 + O_2)
31.	$CH + S \rightarrow CS + H$	$9.5\cdot10^{-11}$	Assumed same as k(CH + CS_2)

32.	$CH + S_2 \rightarrow CS + HS$	$5.9\cdot10^{-11}$	Assumed same as k($CH + O_2$)
33.	$CH_2^1 + S_2 \rightarrow HCS + HS$	$3\cdot10^{-11}$	Assumed same as k($CH_2^1 + O_2$)
34.	$CH_3 + HCS \rightarrow CH_4 + CS$	$5.0\cdot10^{-11}$	Assumed same as k($CH_3 + HCO$)
35.	$H + CS + M \rightarrow HCS + M$	$2.0\cdot10^{-33} \times e^{-850/T} \times \mathrm{den}$	Assumed same as k(H + CO)
36.	$H + HCS \rightarrow H_2 + CS$	$1.2\cdot10^{-10}$	Assumed same as k(H + HCO)
37.	$HS + CO \rightarrow OCS + H$	$4.2\cdot10^{-14} \times e^{-7650/T}$	(Kurbanov and Mamedov 1995)
38.	$HS + HCS \rightarrow H_2S + CS$	$2.0\cdot10^{-11}$	Assumed same as k(HS + HCO)
39.	$OCS + CH \rightarrow CO + HCS$	$1.99\cdot10^{-10} \times e^{-190/T}$	(Zabarnick *et al.,* 1989)
40.	$S + CO + M \rightarrow OCS + M$	$6.5\cdot10^{-33} \times e^{-2180/T} \times \mathrm{den}$	Assumed same as k(CO + O)
41.	$S + HCS \rightarrow H + CS_2$	$5.0\cdot10^{-11}$	Assumed same as k(O + HCO → H + CO_2)
42.	$S + HCS \rightarrow HS + CS$	$5.0\cdot10^{-11}$	Assumed same as k(O + HCO → HS + CO)
43.	$2CH_2^3 \rightarrow C_2H_2 + H_2$	$5.3\cdot10^{-11}$	(Braun *et al.,* 1970)
44.	$C + H_2 + M \rightarrow CH_2^3 + M$	$k_0 = 8.75\cdot10^{-31} \times e^{524/T}$ $k_\infty = 8.3\cdot10^{-11}$	(Zahnle 1986)
45.	$C + O_2 \rightarrow CO + O$	$3.3\cdot10^{-11}$	(Donovan and Husain 1970)
46.	$C + OH \rightarrow CO + H$	$4\cdot10^{-11}$	(Giguere and Huebner 1978)
47.	$C_2 + CH_4 \rightarrow C_2H + CH_3$	$5.05\cdot10^{-11} \times e^{-297/T}$	(Pitts *et al.,* 1982)
48.	$C_2 + H_2 \rightarrow C_2H + H$	$1.77\cdot10^{-10} \times e^{-1469/T}$	(Pitts *et al.,* 1982)
49.	$C_2 + O \rightarrow C + CO$	$5\cdot10^{-11}$	(Prasad and Huntress 1980)
50.	$C_2 + O_2 \rightarrow CO + CO$	$1.5\cdot10^{-11} \times e^{-550/T}$	(Baughcum and Oldenborg 1984)
51.	$C_2H + C_2H_2 \rightarrow HCAER + H$	$1.5\cdot10^{-10}$	(Stephens *et al.,* 1987)
52.	$C_2H + C_2H_6 \rightarrow C_2H_2 + C_2H_5$	$3.6\cdot10^{-11}$	(Lander *et al.,* 1990)
53.	$C_2H + C_3H_8 \rightarrow C_2H_2 + C_3H_7$	$1.4\cdot10^{-11}$	(Okabe 1983)
54.	$C_2H + CH_2CCH_2 \rightarrow HCAER2 + H$	$1.5\cdot10^{-10}$	(Pavlov *et al.,* 2001b)
55.	$C_2H + CH_4 \rightarrow C_2H_2 + CH_3$	$6.94\cdot10^{-12} \times e^{-250/T}$	(Allen *et al.,* 1992; Lander *et al.,* 1990)
56.	$C_2H + H + M \rightarrow C_2H_2 + M$	$k_0 = 2.64\cdot10^{-26} \times e^{-721/T} \times (T/300)^{-3.1}$ $k_\infty = 3.0\cdot10^{-10}$	(Tsang and Hampson 1986)
57.	$C_2H + H_2 \rightarrow C_2H_2 + H$	$5.58\cdot10^{-11} \times e^{-1443/T}$	(Allen *et al.,* 1992; Stephens *et al.,* 1987)
58.	$C_2H + O \rightarrow CO + CH$	$1\cdot10^{-10} \times e^{-250/T}$	(Zahnle 1986)
59.	$C_2H + O_2 \rightarrow CO + HCO$	$2\cdot10^{-11}$	(Brown and Laufer 1981)
60.	$C_2H_2 + H + M \rightarrow C_2H_3 + M$	$k_0 = 2.6\cdot10^{-31}$ $k_\infty = 8.3\cdot10^{-11} \times e^{-1374/T}$	(Romani *et al.,* 1993)
61.	$C_2H_2 + O \rightarrow CH_2^3 + CO$	$2.9\cdot10^{-11} \times e^{-1600/T}$	(Zahnle 1986)
62.	$C_2H_2 + OH + M \rightarrow C_2H_2OH + M$	$k_0 = 5.5\cdot10^{-30}$ + $k_\infty = 8.3\cdot10^{-13} \times (T/300)^{-2}$	(Sander *et al.,* 2006)
63.	$C_2H_2 + OH + M \rightarrow CH_2CO + H + M$	$k_0 = 5.8\cdot10^{-31} \times e^{1258/T}$ $k_\infty = 1.4\cdot10^{-12} \times e^{388/T}$	(Perry and Williamson 1982)
64.	$C_2H_2 + OH \rightarrow CO + CH_3$	$2.\cdot10^{-12} \times e^{-250/T}$	(Hampson and Garvin 1977)
65.	$C_2H_2OH + H \rightarrow H_2 +$	$3.3\cdot10^{-11} \times e^{-2000/T}$	(Miller *et al.,* 1982)

	CH_2CO		
66.	$C_2H_2OH + H \rightarrow H_2O + C_2H_2$	$5\cdot10^{-11}$	(Miller *et al.,* 1982)
67.	$C_2H_2OH + O \rightarrow OH + CH_2CO$	$3.3\cdot10^{-11} \times e^{-2000/T}$	(Miller *et al.,* 1982)
68.	$C_2H_2OH + OH \rightarrow H_2O + CH_2CO$	$1.7\cdot10^{-11} \times e^{-1000/T}$	(Miller *et al.,* 1982)
69.	$C_2H_3 + C_2H_3 \rightarrow C_2H_4 + C_2H_2$	$2.4\cdot10^{-11}$	(Fahr *et al.,* 1991)
70.	$C_2H_3 + C_2H_5 \rightarrow C_2H_4 + C_2H_4$	$3\cdot10^{-12}$	(Laufer *et al.,* 1983)
71.	$C_2H_3 + C_2H_5 + M \rightarrow CH_3 + C_3H_5 + M$	$k_0 = 1.9\cdot10^{-27}$ $k_\infty = 2.5\cdot10^{-11}$	(Romani *et al.,* 1993)
72.	$C_2H_3 + C_2H_6 \rightarrow C_2H_4 + C_2H_5$	$3.\cdot10^{-13} \times e^{-5170/T}$	(Kasting *et al.,* 1983)
73.	$C_2H_3 + CH_3 \rightarrow C_2H_2 + CH_4$	$3.4\cdot10^{-11}$	(Fahr *et al.,* 1991)
74.	$C_2H_3 + CH_3 + M \rightarrow C_3H_6 + M$	$k_0 = 1.3\cdot10^{-22}$ $k_\infty = 1.2\cdot10^{-10}$	(Raymond *et al.,* 2006)
75.	$C_2H_3 + CH_4 \rightarrow C_2H_4 + CH_3$	$2.4\cdot10^{-24} \times e^{-2754/T} \times T^{4.02}$	(Tsang and Hampson 1986)
76.	$C_2H_3 + H \rightarrow C_2H_2 + H_2$	$3.3\cdot10^{-11}$	(Warnatz 1984)
77.	$C_2H_3 + H_2 \rightarrow C_2H_4 + H$	$2.6\cdot10^{-13} \times e^{-2646/T}$	(Allen *et al.,* 1992)
78.	$C_2H_3 + O \rightarrow CH_2CO + H$	$5.5\cdot10^{-11}$	(Hoyermann *et al.,* 1981)
79.	$C_2H_3 + OH \rightarrow C_2H_2 + H_2O$	$8.3\cdot10^{-12}$	(Benson and Haugen 1967)
80.	$C_2H_4 + H + M \rightarrow C_2H_5 + M$	$k_0 = 2.15\cdot10^{-29} \times e^{-349/T}$ $k_\infty = 4.95\cdot10^{-11}\times e^{-1051/T}$	(Lightfoot and Pilling 1987)
81.	$C_2H_4 + O \rightarrow HCO + CH_3$	$5.5\cdot10^{-12} \times e^{-565/T}$	(Hampson and Garvin 1977)
82.	$C_2H_4 + OH + M \rightarrow C_2H_4OH + M$	$k_0 = 1.0\cdot10^{-28} \times (T/300)^{4.5}$ $k_\infty = 8.8\cdot10^{-12} \times (T/300)^{0.85}$	(Sander *et al.,* 2006)
83.	$C_2H_4 + OH \rightarrow H_2CO + CH_3$	$2.2\cdot10^{-12} \times e^{385/T}$	(Hampson and Garvin 1977)
84.	$C_2H_4OH + H \rightarrow H_2 + CH_3CHO$	$3.3\cdot10^{-11} \times e^{-2000/T}$	(Zahnle and Kasting 1986)
85.	$C_2H_4OH + H \rightarrow H_2O + C_2H_4$	$5\cdot10^{-11}$	(Miller *et al.,* 1982)
86.	$C_2H_4OH + O \rightarrow OH + CH_3CHO$	$3.3\cdot10^{-11} \times e^{-2000/T}$	(Zahnle and Kasting 1986)
87.	$C_2H_4OH + OH \rightarrow H_2O + CH_3CHO$	$1.7\cdot10^{-11} \times e^{-1000/T}$	(Zahnle and Kasting 1986)
88.	$C_2H_5 + C_2H_3 \rightarrow C_2H_6 + C_2H_2$	$6\cdot10^{-12}$	(Laufer *et al.,* 1983)
89.	$C_2H_5 + C_2H_5 \rightarrow C_2H_6 + C_2H_4$	$2.3\cdot10^{-12}$	(Tsang and Hampson 1986)
90.	$C_2H_5 + CH_3 \rightarrow C_2H_4 + CH_4$	$1.88\cdot10^{-12} \times (T/300)^{-0.5}$	(Romani *et al.,* 1993)
91.	$C_2H_5 + CH_3 + M \rightarrow C_3H_8 + M$	$k_0 = 3.9\cdot10^{-10} \times (T/300)^{2.5}$ $k_\infty = 1.4\cdot10^{-8}\times (T/300)^{0.5}$	(Romani *et al.,* 1993)
92.	$C_2H_5 + H \rightarrow C_2H_4 + H_2$	$3\cdot10^{-12}$	(Tsang and Hampson 1986)
93.	$C_2H_5 + H + M \rightarrow C_2H_6 + M$	$k_0 = 5.5\cdot10^{-23} \times e^{-1040/T}$ $k_\infty = 1.5\cdot10^{-10}$	(Gladstone *et al.,* 1996)
94.	$C_2H_5 + H \rightarrow CH_3 + CH_3$	$6.00\cdot10^{-11}$	(Baluch, 1992)
95.	$C_2H_5 + HCO \rightarrow C_2H_6 + CO$	$1\cdot10^{-10}$	(Pavlov *et al.,* 2001b)
96.	$C_2H_5 + HNO \rightarrow C_2H_6 + NO$	$3\cdot10^{-14}$	(Pavlov *et al.,* 2001b)
97.	$C_2H_5 + O \rightarrow CH_3 + HCO + H$	$3.0\cdot10^{-11}$	(Tsang and Hampson 1986)
98.	$C_2H_5 + O \rightarrow CH_3CHO + H$	$1.33\cdot10^{-10}$	(Tsang and Hampson 1986)

99.	$C_2H_5 + O \rightarrow H_2CO + CH_3$	$2.67\cdot10^{-11}$	(Tsang and Hampson, 1986)
100	$C_2H_5 + O_2 + M\rightarrow CH_3 + HCO + OH + M$	$k_0 = 1.5\cdot10^{-28} \times (T/300)^{3.0}$ $k_\infty = 1.9\cdot10^{-11}$	(Sander *et al.,* 2006)
101	$C_2H_5 + OH \rightarrow CH_3CHO + H_2$	$1\cdot10^{-10}$	(Pavlov *et al.,* 2001b)
102	$C_2H_5 + OH \rightarrow C_2H_4 + H_2O$	$4.0\cdot10^{-11}$	(Pavlov *et al.,* 2001b)
103	$C_2H_6 + O \rightarrow C_2H_5 + OH$	$8.62\cdot10^{-12} \times e^{-2920/T} \times (T/300)^{1.5}$	(Baulch *et al.,* 1994)
104	$C_2H_6 + O^1D \rightarrow C_2H_5 + OH$	$6.29\cdot10^{-10}$	(Matsumi *et al.,* 1993)
105	$C_2H_6 + OH \rightarrow C_2H_5 + H_2O$	$8.7\cdot10^{-12} \times e^{-1070/T}$	(Sander *et al.,* 2006)
106	$C_3H_2 + H + M \rightarrow C_3H_3 + M$	$k_0 = 1.7\cdot10^{-26}$ $k_\infty = 1.5\cdot10^{-10}$	(Yung *et al.,* 1984)
107	$C_3H_3 + H + M \rightarrow CH_2CCH_2 + M$	$k_0 = 1.7\cdot10^{-26}$ $k_\infty = 1.5\cdot10^{-10}$	(Yung *et al.,* 1984)
108	$C_3H_3 + H + M \rightarrow CH_3C_2H + M$	$k_0 = 1.7\cdot10^{-26}$ $k_\infty = 1.5\cdot10^{-10}$	(Yung *et al.,* 1984)
109	$C_3H_5 + CH_3 \rightarrow CH_2CCH_2 + CH_4$	$4.5\cdot10^{-12}$	(Yung *et al.,* 1984)
110	$C_3H_5 + CH_3 \rightarrow CH_3C_2H + CH_4$	$4.5\cdot10^{-12}$	(Yung *et al.,* 1984)
111	$C_3H_5 + H + M \rightarrow C_3H_6 + M$	$k_0 = 1.0\cdot10^{-28}$ $k_\infty = 1.0\cdot10^{-11}$	(Yung *et al.,* 1984)
112	$C_3H_5 + H \rightarrow CH_2CCH_2 + H_2$	$1.5\cdot10^{-11}$	(Yung *et al.,* 1984)
113	$C_3H_5 + H \rightarrow CH_3C_2H + H_2$	$1.5\cdot10^{-11}$	(Yung *et al.,* 1984)
114	$C_3H_5 + H \rightarrow CH_4 + C_2H_2$	$1.5\cdot10^{-11}$	(Yung *et al.,* 1984)
115	$C_3H_6 + H + M \rightarrow C_3H_7 + M$	$k_0 = 2.15\cdot10^{-29} \times e^{-349/T}$ $k_\infty = 4.95\cdot10^{-11}\times e^{-1051/T}$	(Pavlov *et al.,* 2001b) assumed same as $k(C_2H_4 + H)$
116	$C_3H_6 + O \rightarrow CH_3 + CH_3CO$	$4.1\cdot10^{-12} \times e^{-38/T}$	(Hampson and Garvin 1977)
117	$C_3H_6 + O \rightarrow CH_3 + CH_3 + CO$	$4.1\cdot10^{-12}\ e^{-38/T}$	Hampson and Garvin (1977)
118	$C_3H_6 + OH \rightarrow CH_3CHO + CH_3$	$4.1\cdot10^{-12} \times e^{540/T}$	(Hampson and Garvin 1977)
119	$C_3H_7 + CH_3 \rightarrow C_3H_6 + CH_4$	$2.5\cdot10^{-12} \times e^{-200/T}$	(Yung *et al.,* 1984)
120	$C_3H_7 + H \rightarrow CH_3 + C_2H_5$	$7.95\cdot10^{-11} \times e^{-127/T}$	(Pavlov *et al.,* 2001b)
121	$C_3H_7 + O \rightarrow C_2H_5CHO + H$	$1.1\cdot10^{-10}$	(Pavlov *et al.,* 2001b)
122	$C_3H_7 + OH \rightarrow C_2H_5CHO + H_2$	$1.1\cdot10^{-10}$	(Pavlov *et al.,* 2001b)
123	$C_3H_8 + O + M \rightarrow C_3H_7 + OH + M$	$k_0 = 1.6\cdot10^{-11} \times e^{-2900/T}$ $k_\infty = 2.2\cdot10^{-11}\times e^{-2200/T}$	(Hampson and Garvin 1977)
124	$C_3H_8 + O^1D \rightarrow C_3H_7 + OH$	$1.4\cdot10^{-10}$	(Pavlov *et al.,* 2001b)
125	$C_3H_8 + OH \rightarrow C_3H_7 + H_2O$	$1.1\cdot10^{-11} \times e^{-700/T}$	(DeMore *et al.,* 1992)
126	$CH + C_2H_2 + M\rightarrow C_3H_2 + H + M$	$k_0 = 2.15\cdot10^{-29} \times e^{-349/T}$ $k_\infty = 4.95\cdot10^{-11}\times e^{-1051/T}$	(Romani *et al.,* 1993)
127	$CH + C_2H_4 + M \rightarrow CH_2CCH_2 + H + M$	$k_0 = 1.75\cdot10^{-10} \times e^{61/T}$ $k_\infty = 5.3\cdot10^{-10}$	(Romani *et al.,* 1993)
128	$CH + C_2H_4 + M \rightarrow CH_3C_2H + H + M$	$k_0 = 1.75\cdot10^{-10} \times e^{61/T}$ $k_\infty = 5.3\cdot10^{-10}$	(Romani *et al.,* 1993)
129	$CH + CH_4 + M \rightarrow C_2H_4 + H + M$	$k_0 = 2.5\cdot10^{-11} \times e^{200/T}$ $k_\infty = 1.7\cdot10^{-10}$	(Romani *et al.,* 1993)
130	$CH + CO_2 \rightarrow HCO + CO$	$5.9\cdot10^{-12} \times e^{-350/T}$	(Berman *et al.,* 1982)
131	$CH + H \rightarrow C + H_2$	$1.4\cdot10^{-11}$	(Becker *et al.,* 1989)

132	$CH + H_2 \rightarrow CH_2^3 + H$	$2.38\cdot10^{-10} \times e^{-1760/T}$	(Zabarnick *et al.,* 1986)
133	$CH + H_2 + M \rightarrow CH_3 + M$	$k_0 = 8.75\cdot10^{-31} \times e^{524/T}$ $k_\infty = 8.3\cdot10^{-11}$	(Romani *et al.,* 1993)
134	$CH + O \rightarrow CO + H$	$9.5\cdot10^{-11}$	(Messing *et al.,* 1981)
135	$CH + O_2 \rightarrow CO + OH$	$5.9\cdot10^{-11}$	(Butler *et al.,* 1981)
136	$CH_2^1 + CH_4 \rightarrow CH_3 + CH_3$	$7.14\cdot10^{-12} \times e^{-5050/T}$	(Böhland *et al.,* 1985)
137	$CH_2^1 + CO_2 \rightarrow H_2CO + CO$	$1\cdot10^{-12}$	(Zahnle 1986)
138	$CH_2^1 + H_2 \rightarrow CH_2^3 + H_2$	$1.26\cdot10^{-11}$	(Romani *et al.,* 1993)
139	$CH_2^1 + H_2 \rightarrow CH_3 + H$	$5\cdot10^{-15}$	(Tsang and Hampson 1986)
140	$CH_2^1 + M \rightarrow CH_2^3 + M$	$8.8\cdot10^{-12}$	(Ashfold *et al.,* 1981)
141	$CH_2^1 + O_2 \rightarrow HCO + OH$	$3\cdot10^{-11}$	(Ashfold *et al.,* 1981)
142	$CH_2^3 + C_2H_2 + M \rightarrow CH_2CCH_2 + M$	$k_0 = 3.8\cdot10^{-25}$ $k_\infty = 3.7\cdot10^{-12}$	(Laufer 1981; Laufer *et al.,* 1983)
143	$CH_2^3 + C_2H_2 + M \rightarrow CH_3C_2H + M$	$k_0 = 3.8\cdot10^{-25}$ $k_\infty = 2.2\cdot10^{-12}$	(Laufer 1981; Laufer *et al.,* 1983)
144	$CH_2^3 + C_2H_3 \rightarrow CH_3 + C_2H_2$	$3\cdot10^{-11}$	(Tsang and Hampson 1986)
145	$CH_2^3 + C_2H_5 \rightarrow CH_3 + C_2H_4$	$3\cdot10^{-11}$	(Tsang and Hampson 1986)
146	$CH_2^3 + CH_3 \rightarrow C_2H_4 + H$	$7\cdot10^{-11}$	(Tsang and Hampson 1986)
147	$CH_2^3 + CO + M \rightarrow CH_2CO + M$	$k_0 = 1.0\cdot10^{-28}$ $k_\infty = 1.0\cdot10^{-15}$	(Yung *et al.,* 1984)
148	$CH_2^3 + CO_2 \rightarrow H_2CO + CO$	$1.0\cdot10^{-14}$	(Laufer 1981)
149	$CH_2^3 + H \rightarrow CH + H_2$	$4.7\cdot10^{-10} \times e^{-370/T}$	(Zabarnick *et al.,* 1986)
150	$CH_2^3 + H + M \rightarrow CH_3 + M$	$k_0 = 3.1\cdot10^{-30} \times e^{457/T}$ $k_\infty = 1.5\cdot10^{-10}$	(Gladstone *et al.,* 1996)
151	$CH_2^3 + O \rightarrow CH + OH$	$8\cdot10^{-12}$	(Huebner and Giguere 1980)
152	$CH_2^3 + O \rightarrow CO + HH$	$8.3\cdot10^{-11}$	(Homann and Wellmann 1983)
153	$CH_2^3 + O \rightarrow HCO + H$	$1\cdot10^{-11}$	(Huebner and Giguere 1980)
154	$CH_2^3 + O_2 \rightarrow HCO + OH$	$4.1\cdot10^{-11} \times e^{-750/T}$	(Baulch *et al.,* 1994)
155	$CH_2^3 + S_2 \rightarrow HCS + HS$	$4.1\cdot10^{-11}\ e^{-750/T}$	Assumed same as $k(CH_2^3 + O_2)$
156	$CH_2CCH_2 + H \rightarrow C_3H_5$	$k_0 = 8.9\cdot10^{-29} \times e^{-1225/T} \times (T/300)^{-2.0}$ $k_\infty = 1.4\cdot10^{-11} \times e^{-1000/T}$	(Yung *et al.,* 1984)
157	$CH_2CCH_2 + H \rightarrow CH_3 + C_2H_2$	$k_0 = 8.9\cdot10^{-29} \times e^{-1225/T} \times (T/300)^{-2.0}$ $k_\infty = 9.7\cdot10^{-13} \times e^{-1550/T}$	(Yung *et al.,* 1984)
158	$CH_2CCH_2 + H \rightarrow CH_3C_2H + H$	$1\cdot10^{-11} \times e^{-1000/T}$	(Yung *et al.,* 1984)
159	$CH_2CO + H \rightarrow CH_3 + CO$	$1.9\cdot10^{-11} \times e^{-1725/T}$	(Michael *et al.,* 1979)
160	$CH_2CO + O \rightarrow H_2CO + CO$	$3.3\cdot10^{-11}$	(Lee 1980; Miller *et al.,* 1982)
161	$CH_3 + C_2H_3 \rightarrow C_3H_5 + H$	$2.4\cdot10^{-13}$	(Romani *et al.,* 1993)
162	$CH_3 + CH_3 + M \rightarrow C_2H_6 + M$	$k_0 = 4.0\cdot10^{-24} \times e^{-1390/T} \times (T/300)^{-7.0}$ $k_\infty = 1.79\cdot10^{-10} \times e^{-329/T}$	(Wagner and Wardlaw 1988)
163	$CH_3 + CO + M \rightarrow CH_3CO + M$	$1.4\cdot10^{-32} \times e^{-3000/T} \times$ den	(Watkins and Word 1974)
164	$CH_3 + H + M \rightarrow CH_4 + M$	$k_0 = 1.0\cdot10^{-28} \times (T/298)^{-1.80}$ $k_\infty = 2.0\cdot10^{-10} \times (T/298)^{-0.40}$	(Baulch *et al.,* 1994; Tsang and Hampson 1986)
165	$CH_3 + H_2CO \rightarrow CH_4 + HCO$	$1.60\cdot10^{-16} \times e^{899/T} \times$	(Baulch *et al.,* 1994)

		$(T/298)^{6.10}$	
166	$CH_3 + HCO \rightarrow CH_4 + CO$	$5.0\cdot10^{-11}$	(Tsang and Hampson 1986)
167	$CH_3 + HNO \rightarrow CH_4 + NO$	$3.3\cdot10^{-12} \times e^{-1000/T}$	(Choi and Lin 2005)
168	$CH_3 + O \rightarrow H_2CO + H$	$1.1\cdot10^{-10}$	(Sander *et al.,* 2006)
169	$CH_3 + O_2 \rightarrow H_2CO + OH$	$k_0 = 4.5\cdot10^{-31} \times (T/300)^{-3.0}$ $k_\infty = 1.8\cdot10^{-12} \times (T/300)^{-1.7}$	(Sander *et al.,* 2006)
170	$CH_3 + O_3 \rightarrow H_2CO + HO_2$	$5.4\cdot10^{-12} \times e^{-220/T}$	(Sander *et al.,* 2006)
171	$CH_3 + O_3 \rightarrow CH_3O + O_2$	$5.4\cdot10^{-12}\ e^{-220/T}$	(Sander *et al.,* 2006)
172	$CH_2^3 + C_2H^3 \rightarrow CH_3 + C_2H_2$	$3\cdot10^{-11}$	Tsang and Hampson (1986)
173	$CH_3 + OH \rightarrow CH_3O + H$	$9.3\cdot10^{-11} \times e^{-1606/T} \times (T/298)$	(Jasper *et al.,* 2007)
174	$CH_3 + OH \rightarrow CO + H_2 + H_2$	$6.7\cdot10^{-12}$	
175	$CH_3C_2H + H + M \rightarrow C_3H_5 + M$	$k_0 = 8.88\cdot10^{-29} \times e^{-1225/T} \times (T/300)^{-2}$ $k_\infty = 9.7\cdot10^{-12} \times e^{-1550/T}$	(Yung *et al.,* 1984)
176	$CH_3C_2H + H \rightarrow CH_3 + C_2H_2$	$k_0 = 8.88\cdot10^{-29} \times e^{-1225/T} \times (T/300)^{-2}$ $k_\infty = 9.7\cdot10^{-12} \times e^{-1550/T}$	(Whytock *et al.,* 1976)
177	$CH_3CHO + CH_3 \rightarrow CH_3CO + CH_4$	$2.8\cdot10^{-11} \times e^{-1540/T}$	(Zahnle 1986)
178	$CH_3CHO + H \rightarrow CH_3CO + H_2$	$2.8\cdot10^{-11} \times e^{-1540/T}$	(Zahnle 1986)
179	$CH_3CHO + O \rightarrow CH_3CO + OH$	$5.8\cdot10^{-13}$	(Washida 1981)
180	$CH_3CHO + OH \rightarrow CH_3CO + H_2O$	$1.6\cdot10^{-11}$	(Niki *et al.,* 1978)
181	$CH_3CO + CH_3 \rightarrow C_2H_6 + CO$	$5.4\cdot10^{-11}$	(Adachi *et al.,* 1981)
182	$CH_3CO + CH_3 \rightarrow CH_4 + CH_2CO$	$8.6\cdot10^{-11}$	(Adachi *et al.,* 1981)
183	$CH_3CO + H \rightarrow CH_4 + CO$	$1\cdot10^{-10}$	(Zahnle 1986)
184	$CH_3CO + O \rightarrow H_2CO + HCO$	$5\cdot10^{-11}$	(Zahnle 1986)
185	$CH_3O + CO \rightarrow CH_3 + CO_2$	$2.6\cdot10^{-11} \times e^{-5940/T}$	(Wen *et al.,* 1989)
186	$CH_3O_2 + H \rightarrow CH_4 + O_2$	$1.4\cdot10^{-11}$	(Tsang and Hampson 1986)
187	$CH_3O_2 + H \rightarrow H_2O + H_2CO$	$1\cdot10^{-11}$	(Zahnle *et al.,* 2006)
188	$CH_3O + NO \rightarrow HNO + H_2CO$	$2.3\cdot10^{-12} \times (300/T)^{0.7}$	IUPAC datasheet
189	$NO_2 + CH_3O \rightarrow H_2CO + HNO_2$	$9.6\cdot10^{-12}\ e^{-1150/T}$	IUPAC datasheet
190	$CH_3O_2 + O \rightarrow H_2CO + HO_2$	$1\cdot10^{-11}$	(Vaghjiani and Ravishankara 1990)
191	$CH_3O_2 + NO \rightarrow CH_3O + NO_2$	$2.8\cdot10^{-12}\ e^{-300/T}$	(Sander *et al.,* 2006)
192	$CH_4 + HS \rightarrow CH_3 + H_2S$	$2.99\cdot10^{-31}$	(Kerr and Trotman-Dickenson 1957)
193	$CH_4 + O \rightarrow CH_3 + OH$	$8.75\cdot10^{-12} \times e^{-4330/T} \times (T/298)^{1.5}$	(Tsang and Hampson 1986)
194	$CH_4 + O^1D \rightarrow CH_3 + OH$	$1.125\cdot10^{-10}$	(Sander *et al.,* 2006)
195	$CH_4 + O^1D \rightarrow H_2CO + H_2$	$7.5\cdot10^{-12}$	(Sander *et al.,* 2006)
196	$CH_4 + O^1D \rightarrow CH_3O + H$	$3.0\cdot10^{-11}$	(Sander *et al.,* 2006)
197	$CH_4 + OH \rightarrow CH_3 + H_2O$	$2.45\cdot10^{-12} \times e^{-1775/T}$	(Sander *et al.,* 2006)

198	$CO + O + M \rightarrow CO_2 + M$	$2.2\cdot10^{-33} \times e^{-1780/T} \times den$	(Tsang and Hampson 1986)
199	$CO + OH \rightarrow CO_2 + H$	$1.5\cdot10^{-13} \times (1 + 0.6 \times den)$	(Sander *et al.,* 2006)
200	$CO + O^1D \rightarrow CO + O$	$7.0\cdot10^{-11}$	(Sander *et al.,* 2006)
201	$H + CO + M \rightarrow HCO + M$	$1.4\cdot10^{-34} \times e^{-100/T} \times den$	(Baulch *et al.,* 1994)
202	$H + H + M \rightarrow H_2 + M$	$8.85\cdot10^{-33} \times (T/298)^{-0.6} \times den$	(Baulch *et al.,* 1994)
203	$H + HCO \rightarrow H_2 + CO$	$1.8\cdot10^{-10}$	(Baulch *et al.,* 1992)
204	$H + HNO \rightarrow H_2 + NO$	$3.01\cdot10^{-11} \times e^{500/T}$	(Tsang and Herron 1991)
205	$H + HO_2 \rightarrow H_2 + O_2$	$7.2\cdot10^{-12}$	(Sander *et al.,* 2006)
206	$H + HO_2 \rightarrow H_2O + O$	$1.60\cdot10^{-12}$	(Sander *et al.,* 2006)
207	$H + HO_2 \rightarrow OH + OH$	$7.12\cdot10^{-11}$	(Sander *et al.,* 2006)
208	$H + NO + M \rightarrow HNO + M$	$2.1\cdot10^{-32} \times (T/298)^{1.00} \times den$	(Hampson and Garvin 1977)
209	$H + O_2 + M \rightarrow HO_2 + M$	$5.7\cdot10^{-32} \times 7.5\cdot10^{-11} \times (T/298)^{1.6}$	(Sander *et al.,* 2006)
210	$H + O_3 \rightarrow OH + O_2$	$1.4\cdot10^{-10} \times e^{-470/T}$	(Sander *et al.,* 2006)
211	$H + OH + M \rightarrow H_2O + M$	$6.8\cdot10^{-31} \times (T/300)^{-2} \times den$	(McEwan and Phillips 1975)
212	$H + SO + M \rightarrow HSO + M$	$k_0 = 5.7\cdot10^{-32} \times (T/298)^{1.6}$ $k_\infty = 7.5\cdot10^{-11}$	(Kasting 1990)
213	$H_2 + O \rightarrow OH + H$	$1.34\cdot10^{-15} \times e^{-1460/T} \times (T/298)^{6.52}$	(Robie *et al.,* 1990)
214	$H_2 + O^1D \rightarrow OH + H$	$1.1\cdot10^{-10}$	(Sander *et al.,* 2006)
215	$H_2 + OH \rightarrow H_2O + H$	$5.5\cdot10^{-12} \times e^{-2000/T}$	(Sander *et al.,* 2006)
216	$H_2CO + H \rightarrow H_2 + HCO$	$2.14^{-12} \times e^{-1090/T} \times (T/298)^{1.62}$	(Baulch *et al.,* 1994)
217	$H_2CO + O \rightarrow HCO + OH$	$3.4\cdot10^{-11} \times e^{-1600/T}$	(Sander *et al.,* 2006)
218	$H_2CO + OH \rightarrow H_2O + HCO$	$5.5\cdot10^{-12} \times e^{125/T}$	(Sander *et al.,* 2006)
219	$H_2O + O^1D \rightarrow OH + OH$	$2.2\cdot10^{-10}$	(Sander *et al.,* 2006)
220	$H_2O_2 + O \rightarrow OH + HO_2$	$1.4\cdot10^{-12} \times e^{-2000/T}$	(Sander *et al.,* 2006)
221	$H_2O_2 + OH \rightarrow HO_2 + H_2O$	$2.9\cdot10^{-12} \times e^{-160/T}$	(Sander *et al.,* 2006)
222	$H_2S + H \rightarrow H_2 + HS$	$3.66\cdot10^{-12} \times e^{-455/T} \times (T/298)^{1.94}$	(Peng *et al.,* 1999)
223	$H_2S + O \rightarrow OH + HS$	$9.2\cdot10^{-12} \times e^{-1800/T}$	(Sander *et al.,* 2006)
224	$H_2S + OH \rightarrow H_2O + HS$	$6.0\cdot10^{-12} \times e^{-70/T}$	(Sander *et al.,* 2006)
225	$HCO + H_2CO \rightarrow CH_3O + CO$	$3.8\cdot10^{-17}$	(Wen *et al.,* 1989)
226	$HCO + HCO \rightarrow H_2CO + CO$	$4.5\cdot10^{-11}$	(Tsang and Hampson 1986)
227	$HCO + NO \rightarrow HNO + CO$	$1.3\cdot10^{-11}$	(Tsang and Hampson 1986)
228	$HCO + O_2 \rightarrow HO_2 + CO$	$5.2\cdot10^{-12}$	(Sander *et al.,* 2006)
229	$HNO_2 + OH \rightarrow H_2O + NO_2$	$1.8\cdot10^{-11} \times e^{-390/T}$	(Sander *et al.,* 2006)
230	$HNO_3 + OH \rightarrow H_2O + NO_2 + O$	$7.2\cdot10^{-15} \times e^{-785/T} + (1.9\cdot10^{-33} \times e^{725/T} \times den)/(1 + 4.6\cdot10^{-16} \times e^{-715/T} \times den)$	(Sander *et al.,* 2006)
231	$HO_2 + HO_2 \rightarrow H_2O_2 + O_2$	$k_0 = 2.3\cdot10^{-13} \times e^{590/T}$ $k_\infty = 1.7\cdot10^{-33} \times e^{1000/T}$	(Sander *et al.,* 2006)
232	$HO_2 + O \rightarrow OH + O_2$	$3.0\cdot10^{-11} \times e^{200/T}$	(Sander *et al.,* 2006)
233	$HO_2 + O_3 \rightarrow OH + O_2 + O_2$	$1.0\cdot10^{-14} \times e^{-490/T}$	(Sander *et al.,* 2006)
234	$HO_2 + NO_2 \rightarrow HNO_2 + O_2$	$5.0\cdot10^{-16}$	(Sander *et al.,* 2006)

235	$HS + H \rightarrow H_2 + S$	$2.0\cdot10^{-11}$	(Schofield 1973)
236	$HS + HCO \rightarrow H_2S + CO$	$2.0\cdot10^{-11}$	(Kasting 1990)
237	$HS + HO_2 \rightarrow H_2S + O_2$	$1.0\cdot10^{-11}$	(Stachnik and Molina 1987)
238	$HS + HS \rightarrow H_2S + S$	2.0^{-11}	(Schofield 1973)
239	$HS + NO_2 \rightarrow HSO + NO$	$2.9\cdot10^{-11} \times e^{240/T}$	(Sander *et al.,* 2006)
240	$HS + O \rightarrow H + SO$	$7.0\cdot10^{-11}$	(Sander *et al.,* 2006)
241	$HS + O_3 \rightarrow HSO + O_2$	$9.0\cdot10^{-12} \times e^{-280/T}$	(Sander *et al.,* 2006)
242	$HS + S \rightarrow H + S_2$	$1.0\cdot10^{-11}$	(Kasting 1990)
243	$HSO + H \rightarrow H_2 + SO$	$1.0\cdot10^{-11}$	(Kasting 1990)
244	$HSO + H \rightarrow HS + OH$	$2.0\cdot10^{-11}$	(Kasting 1990)
245	$HSO + HS \rightarrow H_2S + SO$	$3.0\cdot10^{-12}$	(Kasting 1990)
246	$HSO + O \rightarrow OH + SO$	$3.0\cdot10^{-11}$	(Kasting 1990)
247	$HSO + OH \rightarrow H_2O + SO$	$3.0\cdot10^{-11}$	(Kasting 1990)
248	$HSO + S \rightarrow HS + SO$	$1.0\cdot10^{-11}$	(Kasting 1990)
249	$HSO_3 + O_2 \rightarrow HO_2 + SO_3$	$1.3\cdot10^{-12} \times e^{-330/T}$	(Sander *et al.,* 2006)
250	$N + NO \rightarrow N_2 + O$	$2.1\cdot10^{-11} \times e^{-100/T}$	(Sander *et al.,* 2006)
251	$N + O_2 \rightarrow NO + O$	$1.5\cdot10^{-12} \times e^{-3600/T}$	(Sander *et al.,* 2006)
252	$N + OH \rightarrow NO + H$	$3.8\cdot10^{-11} \times e^{85/T}$	(Atkinson *et al.,* 1989)
253	$N + HO_2 \rightarrow NO + OH$	$2.2\cdot10^{-11}$	(Brune et al. 1983)
254	$NO + HO_2 \rightarrow NO_2 + OH$	$3.5\cdot10^{-12} \times e^{250/T}$	(Sander *et al.,* 2006)
255	$NO + O + M \rightarrow NO_2 + M$	$9\cdot10^{-31} 3.\cdot10^{-11} \times (T/298)^{1.5}$	(Sander *et al.,* 2006)
256	$NO + O_3 \rightarrow NO_2 + O_2$	$2.0\cdot10^{-12} \times e^{-1500/T}$	(Sander *et al.,* 2006)
257	$NO + OH + M \rightarrow HNO_2 + M$	$k_0 = 7\cdot10^{-31} \times (T/298)^{2.6}$ $k_\infty = 3.6\cdot10^{-11} \times (T/298)^{0.1}$	(Sander *et al.,* 2006)
258	$NO_2 + H \rightarrow NO + OH$	$4.\cdot10^{-10} \times e^{-340/T}$	(Sander *et al.,* 2006)
259	$NO_2 + O \rightarrow NO + O_2$	$5.6\cdot10^{-12} \times e^{180/T}$	(Sander *et al.,* 2006)
260	$NO_2 + OH + M \rightarrow HNO_3 + M$	$k_0 = 2.0\cdot10^{-30} \times (T/298)^{3.0}$ $k_\infty = 2.5\cdot10^{-11}$	(Sander *et al.,* 2006)
261	$O + HCO \rightarrow H + CO_2$	$5.0\cdot10^{-11}$	(Tsang and Hampson 1986)
262	$O + HCO \rightarrow OH + CO$	$1.0\cdot10^{-10}$	(Hampson and Garvin 1977)
263	$O + HNO \rightarrow OH + NO$	$3.8\cdot10^{-11}$	(Tsang and Hampson 1986)
264	$O + O + M \rightarrow O_2 + M$	$9.46\cdot10^{-34} \times e^{480/T} \times \text{den}$	(Campbell and Gray 1973)
265	$O + O_2 + M \rightarrow O_3 + M$	$6\cdot10^{-34} \times 3\cdot10^{-11} \times (T/298)^{2.40}$	(Sander *et al.,* 2006)
266	$O + O_3 \rightarrow O_2 + O_2$	$8.0\cdot10^{-12} \times e^{-2060/T}$	(Sander *et al.,* 2006)
267	$O^1D + M \rightarrow O + M$	$1.8\cdot10^{-11} \times e^{110/T}$	(Sander *et al.,* 2006)
268	$O^1D + O_2 \rightarrow O + O_2$	$3.2\cdot10^{-11} \times e^{70/T}$	(Sander *et al.,* 2006)
269	$OH + HCO \rightarrow H_2O + CO$	$1.0\cdot10^{-10}$	(Baulch *et al.,* 1992)
270	$OH + HNO \rightarrow H_2O + NO$	$5\cdot10^{-11}$	(Sun *et al.,* 2001)
271	$OH + HO_2 \rightarrow H_2O + O_2$	$4.8\cdot10^{-11} \times e^{250/T}$	(Sander *et al.,* 2006)
272	$OH + O \rightarrow H + O_2$	$2.2\cdot10^{-11} \times e^{120/T}$	(Sander *et al.,* 2006)
273	$OH + O_3 \rightarrow HO_2 + O_2$	$1.6\cdot10^{-12} \times e^{-940/T}$	(Sander *et al.,* 2006)
274	$OH + OH \rightarrow H_2O + O$	$4.2\cdot10^{-12} \times e^{-240/T}$	(Sander *et al.,* 2006)
275	$OH + OH \rightarrow H_2O_2$	$6.9\cdot10^{-31} \times 2.6\cdot10^{-11} \times (T/298)^{1.00}$	(Sander *et al.,* 2006)

276	$S + HCO \rightarrow HS + CO$	$1.0\cdot10^{-11}$	(Kasting 1990)
277	$S + HO_2 \rightarrow HS + O_2$	$5.0\cdot10^{-12}$	(Kasting 1990)
278	$S + HO_2 \rightarrow SO + OH$	$5.0\cdot10^{-12}$	(Kasting 1990)
279	$S + O_2 \rightarrow SO + O$	$2.3\cdot10^{-12}$	(Sander *et al.,* 2006)
280	$S + O_3 \rightarrow SO + O_2$	$1.2\cdot10^{-11}$	(Sander *et al.,* 2006)
281	$S + OH \rightarrow SO + H$	$6.6\cdot10^{-11}$	(Sander *et al.,* 2006)
282	$S + S + M \rightarrow S_2 + M$	$1.98\cdot10^{-33} \times e^{-206/T} \times \text{den}$	(Du *et al.,* 2008)
283	$S + S_2 + M \rightarrow S_3 + M$	$2.8\cdot10^{-32} \times \text{den}$	(Kasting 1990)
284	$S + S_3 + M \rightarrow S_4 + M$	$2.8\cdot10^{-31} \times \text{den}$	(Kasting 1990)
285	$S_2 + O \rightarrow S + SO$	$1.1\cdot10^{-11}$	(Hills *et al.,* 1987)
286	$S_2 + S_2 + M \rightarrow S_4 + M$	$2.8\cdot10^{-31} \times \text{den}$	(Baulch *et al.,* 1976)
287	$S_4 + S_4 + M \rightarrow S_8AER + M$	$2.8\cdot10^{-31} \times \text{den}$	(Kasting 1990)
288	$SO + HCO \rightarrow HSO + CO$	$5.6\cdot10^{-12} \times (T/298)^{-0.4}$	(Kasting 1990)
289	$SO + NO_2 \rightarrow SO_2 + NO$	$1.4\cdot10^{-11}$	(Sander *et al.,* 2006)
290	$SO + O + M \rightarrow SO_2 + M$	$5.1\cdot10^{-31} \times \text{den}$	(Sander *et al.,* 2006)
291	$SO + O_2 \rightarrow O + SO_2$	$2.6\cdot10^{-13} \times e^{-2400/T}$	(Sander *et al.,* 2006)
292	$SO + O_3 \rightarrow SO_2 + O_2$	$4.5\cdot10^{-12} \times e^{-1170/T}$	(Atkinson *et al.,* 2004)
293	$SO + OH \rightarrow SO_2 + H$	$8.6\cdot10^{-11}$	(Sander *et al.,* 2006)
294	$SO + SO \rightarrow SO_2 + S$	$3.5\cdot10^{-15}$	(Martinez and Herron 1983)
295	$SO_2 + HO_2 \rightarrow SO_3 + OH$	$8.63\cdot10^{-16}$	(Lloyd 1974)
296	$SO_2 + O + M \rightarrow SO_3 + M$	$k_0 = 1.3\cdot10^{-33} \times (T/298)^{-3.6}$ $k_\infty = 1.5\cdot10^{-11}$	(Sander *et al.,* 2006)
297	$SO_2 + OH + M \rightarrow HSO_3 + M$	$k_0 = 3\cdot10^{-31} \times (T/298)^{3.3}$ $k_\infty = 1.5\cdot10^{-12}$	(Sander *et al.,* 2006)
298	$SO_2^1 + O_2 \rightarrow SO_3 + O$	$1.0\cdot10^{-16}$	(Turco *et al.,* 1982)
299	$SO_2^1 + SO_2 \rightarrow SO_3 + SO$	$4.0\cdot10^{-12}$	(Turco *et al.,* 1982)
300	$SO_2^3 + SO_2 \rightarrow SO_3 + SO$	$7.0\cdot10^{-14}$	(Turco *et al.,* 1982)
301	$SO_3 + H_2O \rightarrow H_2SO_4$	$1.2\cdot10^{-15}$	(Sander *et al.,* 2006)
302	$SO_3 + SO \rightarrow SO_2 + SO_2$	$2.0\cdot10^{-15}$	(Chung *et al.,* 1975)
303	$SO_2^1 + h\nu \rightarrow SO_2 + h\nu$	$0.0\cdot10^{0}$	(Turco *et al.,* 1982)
304	$SO_2^1 + h\nu \rightarrow SO_2^3 + h\nu$	$0.0\cdot10^{0}$	(Turco *et al.,* 1982)
305	$SO_2^3 + h\nu \rightarrow SO_2 + h\nu$	$0.0\cdot10^{0}$	(Turco *et al.,* 1982)
306	$O_2 + h\nu \rightarrow O + O^1D$	$2.38\cdot10^{-06}$	
307	$O_2 + h\nu \rightarrow O + O$	$4.77\cdot10^{-08}$	
308	$H_2O + h\nu \rightarrow H + OH$	$8.25\cdot10^{-06}$	
309	$O_3 + h\nu \rightarrow O_2 + O^1D$	$2.47\cdot10^{-03}$	
310	$O_3 + h\nu \rightarrow O_2 + O$	$7.37\cdot10^{-04}$	
311	$H_2O_2 + h\nu \rightarrow OH + OH$	$3.65\cdot10^{-05}$	
312	$CO_2 + h\nu \rightarrow CO + O$	$1.00\cdot10^{-09}$	
313	$H_2CO + h\nu \rightarrow H_2 + CO$	$2.51\cdot10^{-05}$	
314	$H_2CO + h\nu \rightarrow HCO + H$	$2.86\cdot10^{-05}$	
315	$CO_2 + h\nu \rightarrow CO + O^1D$	$2.90\cdot10^{-07}$	
316	$HO_2 + h\nu \rightarrow OH + O$	$2.17\cdot10^{-04}$	
317	$CH_4 + h\nu \rightarrow CH_2^1 + H_2$	$2.08\cdot10^{-06}$	

318	$C_2H_6 + h\nu \rightarrow CH_4 + CH_2^1$	$1.34\cdot10^{-06}$
319	$HNO_2 + h\nu \rightarrow NO + OH$	$1.58\cdot10^{-09}$
320	$HNO_3 + h\nu \rightarrow NO_2 + OH$	$7.40\cdot10^{-05}$
321	$HNO + h\nu \rightarrow NO + N$	$7.0\cdot10^{-04}$
322	$HCO + h\nu \rightarrow H + CO$	$1.0\cdot10^{-02}$
323	$NO + h\nu \rightarrow N + O$	$1.92\cdot10^{-06}$
324	$NO_2 + h\nu \rightarrow NO + O$	$3.23\cdot10^{-03}$
325	$CH_3 + h\nu \rightarrow CH_2^1 + H$	$1.64\cdot10^{-01}$
326	$SO + h\nu \rightarrow S + O$	$1.65\cdot10^{-04}$
327	$SO_2 + h\nu \rightarrow SO + O$	$7.27\cdot10^{-05}$
328	$H_2S + h\nu \rightarrow HS + H$	$1.02\cdot10^{-04}$
329	$SO_2 + h\nu \rightarrow SO_2^1$	$7.14\cdot10^{-04}$
330	$SO_2 + h\nu \rightarrow SO_2^3$	$4.94\cdot10^{-07}$
331	$S_2 + h\nu \rightarrow S + S$	$4.56\cdot10^{-04}$
332	$SO_3 + h\nu \rightarrow SO_2 + O$	$1.57\cdot10^{-05}$
333	$SO_2^1 + h\nu \rightarrow SO_2^3 + h\nu$	$0.00\cdot10^{0}$
334	$SO_2^1 + h\nu \rightarrow SO_2 + h\nu$	$0.00\cdot10^{0}$
335	$SO_2^3 + h\nu \rightarrow SO_2 + h\nu$	$0.00\cdot10^{0}$
336	$HSO + h\nu \rightarrow HS + O$	$2.17\cdot10^{-04}$
337	$S_4 + h\nu \rightarrow S_2 + S_2$	$4.56\cdot10^{-04}$
338	$S_3 + h\nu \rightarrow S_2 + S$	$4.45\cdot10^{-04}$
339	$C_2H_2 + h\nu \rightarrow C_2H + H$	$1.02\cdot10^{-06}$
340	$C_2H_2 + h\nu \rightarrow C_2 + H_2$	$4.65\cdot10^{-07}$
341	$C_2H_4 + h\nu \rightarrow C_2H_2 + H_2$	$1.60\cdot10^{-05}$
342	$C_3H_8 + h\nu \rightarrow C_3H_6 + H_2$	$0.00\cdot10^{-00}$
343	$C_3H_8 + h\nu \rightarrow C_2H_6 + CH_2^1$	$1.43\cdot10^{-06}$
344	$C_3H_8 + h\nu \rightarrow C_2H_4 + CH_4$	$6.98\cdot10^{-06}$
345	$C_3H_8 + h\nu \rightarrow C_2H_5 + CH_3$	$3.69\cdot10^{-06}$
346	$C_2H_6 + h\nu \rightarrow C_2H_2 + H_2 + H_2$	$1.46\cdot10^{-06}$
347	$C_2H_6 + h\nu \rightarrow C_2H_4 + H + H$	$1.67\cdot10^{-06}$
348	$C_2H_6 + h\nu \rightarrow C_2H_4 + H_2$	$9.15\cdot10^{-07}$
349	$C_2H_6 + h\nu \rightarrow CH_3 + CH_3$	$4.31\cdot10^{-07}$
350	$C_2H_4 + h\nu \rightarrow C_2H_2 + H + H$	$1.67\cdot10^{-05}$
351	$C_3H_6 + h\nu \rightarrow C_2H_2 + CH_3 + H$	$1.07\cdot10^{-05}$
352	$CH_4 + h\nu \rightarrow CH_2^3 + H + H$	$3.94\cdot10^{-06}$
353	$CH_4 + h\nu \rightarrow CH_3 + H$	$1.93\cdot10^{-06}$
354	$CH + h\nu \rightarrow C + H$	$3.27\cdot10^{-05}$
355	$CH_2CO + h\nu \rightarrow CH_2^3 + CO$	$1.53\cdot10^{-04}$
356	$CH_3CHO + h\nu \rightarrow CH_3 + HCO$	$3.25\cdot10^{-05}$
357	$CH_3CHO + h\nu \rightarrow CH_4 + CO$	$3.25\cdot10^{-05}$
358	$C_2H_5CHO + h\nu \rightarrow C_2H_5 + HCO$	$7.77\cdot10^{-05}$

359	$C_3H_3 + h\nu \rightarrow C_3H_2 + H$	$7.16 \cdot 10^{-04}$
360	$CH_3C_2H + h\nu \rightarrow C_3H_3 + H$	$1.75 \cdot 10^{-05}$
361	$CH_3C_2H + h\nu \rightarrow C_3H_2 + H_2$	$6.57 \cdot 10^{-06}$
362	$CH_3C_2H + h\nu \rightarrow CH_3 + C_2H$	$8.75 \cdot 10^{-07}$
363	$CH_2CCH_2 + h\nu \rightarrow C_3H_3 + H$	$1.91 \cdot 10^{-11}$
364	$CH_2CCH_2 + h\nu \rightarrow C_3H_2 + H_2$	$7.16 \cdot 10^{-12}$
365	$CH_2CCH_2 + h\nu \rightarrow C_2H_2 + CH_2^3$	$2.87 \cdot 10^{-12}$
366	$C_3H_6 + h\nu \rightarrow CH_2CCH_2 + H_2$	$1.80 \cdot 10^{-05}$
367	$C_3H_6 + h\nu \rightarrow C_2H_4 + CH_2^3$	$6.30 \cdot 10^{-07}$
368	$C_3H_6 + h\nu \rightarrow C_2H + CH_4 + H$	$1.58 \cdot 10^{-06}$
369	$OCS + h\nu \rightarrow CO + S$	$8.71 \cdot 10^{-06}$
370	$CS_2 + h\nu \rightarrow CS + S$	$9.33 \cdot 10^{-04}$
371	$CS_2 + h\nu \rightarrow CS_2^*$	$9.71 \cdot 10^{-05}$

Appendix Table 2. Atmospheric species in the Archean photochemical code with lower boundary condition type and values. Lower boundary conditions are given in cm/s for deposition velocity (V_{dep}), a dimensionless mixing ratio by volume for fixed concentration (f_o), and molecules/cm2/s for flux (flux). Species names ending in "AER" are types of aerosols.

Species	Lower Boundary Type	V_{dep}/f_0/flux
	Long-Lived Species	
O	constant deposition velocity	1
O_2	constant mixing ratio	$1 \cdot 10^{-08}$
H_2O	constant deposition velocity	0
H	constant deposition velocity	1
OH	constant deposition velocity	1
HO_2	constant deposition velocity	1
H_2O_2	constant deposition velocity	$2 \cdot 10^{-01}$
H_2	constant deposition velocity*	$2.4 \cdot 10^{-04}$
CO	constant deposition velocity	$1.2 \cdot 10^{-04}$
HCO	constant deposition velocity	1
H_2CO	constant deposition velocity	$2 \cdot 10^{-01}$
CH_4	constant mixing ratio	variable†
CH_3	constant deposition velocity	1
C_2H_6	constant deposition velocity	0
NO	constant deposition velocity	$3 \cdot 10^{-04}$
NO_2	constant deposition velocity	$3 \cdot 10^{-03}$
HNO	constant deposition velocity	1
O_3	constant deposition velocity	$7 \cdot 10^{-02}$
HNO_3	constant deposition velocity	$2 \cdot 10^{-01}$
N	constant deposition velocity	0
H_2S	constant deposition velocity*	$2 \cdot 10^{-02}$
HS	constant deposition velocity	0
S	constant deposition velocity	0
SO	constant deposition velocity	0
SO_2	constant deposition velocity*	1
SO_3	constant deposition velocity	0
H_2SO_4	constant deposition velocity	1
HSO	constant deposition velocity	1
S_2	constant deposition velocity	0
C_2	constant deposition velocity	0
CH	constant deposition velocity	0
C_2H	constant deposition velocity	0
CH_2^3	constant deposition velocity	0
C_2H_5	constant deposition velocity	0
C_2H_2	constant deposition velocity	0
C_2H_4	constant deposition velocity	0
C_3H_8	constant deposition velocity	0
C_3H_7	constant deposition velocity	0
C_3H_5	constant deposition velocity	0
C_2H_3	constant deposition velocity	0
C_3H_6	constant deposition velocity	0

C_3H_2	constant deposition velocity	0
C_3H_3	constant deposition velocity	0
CH_2CCH_2	constant deposition velocity	0
CH_2CO	constant deposition velocity	0
CH_3CO	constant deposition velocity	0
CH_3CHO	constant deposition velocity	0
CH_3O	constant deposition velocity	0
CH_3O_2	constant deposition velocity	0
C_2H_4OH	constant deposition velocity	0
C_2H_2OH	constant deposition velocity	0
C_2H_5CHO	constant deposition velocity	0
CH_3C_2H	constant deposition velocity	0
CS_2	constant deposition velocity	0
HCS	constant deposition velocity	0
OCS	constant deposition velocity	0
CS	constant deposition velocity	0
SO_4AER	constant deposition velocity	$1\cdot10^{-02}$
S_8AER	constant deposition velocity	$1\cdot10^{-02}$
HCAER	constant deposition velocity	$1\cdot10^{-02}$
HCAER2	constant deposition velocity	$1\cdot10^{-02}$
	Short-Lived Species	
HNO_2	constant deposition velocity	0
O^1D	constant deposition velocity	0
CH_2^1	constant deposition velocity	0
C	constant deposition velocity	0
SO_2^1	constant deposition velocity	0
SO_2^3	constant deposition velocity	0
HSO_3	constant deposition velocity	0
OCS_2	constant deposition velocity	0
CS_2*	constant deposition velocity	0
S_3	constant deposition velocity	0
S_4	constant deposition velocity	0
	Inert Species	
CO_2	constant mixing ratio	variable[†]
N_2	constant mixing ratio	remainder[‡]

* - In addition to a constant deposition velocity, we also use a volcanic flux for these gases. Specifically, we used volcanic fluxes of $3.5\cdot10^9$ molecules/cm^2/s of H_2, $1\cdot10^{10}$ molecules/cm^2/s of SO_2, and $3.5\cdot10^8$ molecules/cm^2/s of H_2S.

† - See text for information on these mixing ratios.

‡ - N_2 fills the remainder of the atmosphere

BIBLIOGRAPHY

Abbot, D. S., Voigt, A., & Koll, D. 2011, Journal of Geophysical Research, 116, doi:10.1029/2011JD015927

Allen, D., & Crawford, J. 1984, Nature, 307, 222

Allen, D. A. 1987, Icarus, 69, 221

Allen, M., Pinto, J. P., & Yung, Y. L. 1980, The Astrophysical Journal, 242, L125

Allwood, A. C., Walter, M. R., Kamber, B. S., Marshall, C. P., & Burch, I. W. 2006, Nature, 441, 714

Arney, G., Meadows, V., Crisp, D., et al. 2014, Journal of Geophysical Research: Planets, 119, 1860

Arney, G. N., Domagal-Goldman, S. D., Meadows, V. S., et al. 2016, Astrobiology

Atreya, S. K., Adams, E. Y., Niemann, H. B., et al. 2006, Planetary and Space Science, 54, 1177

Avduevsky, V., Marov, M. Y., & Rozhdestvensky, M. 1968, Journal of the Atmospheric Sciences, 25, 537

Bailey, J. 2009, Icarus, 201, 444

Barber, R. J., Tennyson, J., Harris, G. J., & Tolchenov, R. N. 2006, Monthly Notices of the Royal Astronomical Society, 368, 1087

Bardeen, C. G., Toon, O. B., Jensen, E. J., Marsh, D. R., & Harvey, V. L. 2008, Journal of Geophysical Research Atmospheres, 113, 1

Barstow, J., Tsang, C., Wilson, C., et al. 2012, Icarus, 217, 542

Battistuzzi, F. U., Feijao, A., & Hedges, S. B. 2004, BMC evolutionary biology, 4, 44

Bean, J., Kempton, E., & Homeier, D. 2010, Nature, 468, 669

Beichman, C., Benneke, B., Knutson, H., et al. 2014, Astronomical Society of the Pacific, 126, 1134

Bell, J. F., Crisp, D., Lucey, P. G., et al. 1991, Science (New York, N.Y.), 252, 1293

Benneke, B., & Seager, S. 2012, The Astrophysical Journal, 753, 100

Bétrémieux, Y., & Kaltenegger, L. 2014, The Astrophysical Journal, 791, 7

Bézard, B., Bergh, C. D., Crisp, D., & Maillard, J. 1990, Nature, 345, 508

Bézard, B., de Bergh, C., Fegley, B., et al. 1993, Geophysical Research Letters, 20, 1587

Bézard, B., Fedorova, A., Bertaux, J.-L., Rodin, A., & Korablev, O. 2011, Icarus, 216, 173

Bézard, B., Tsang, C., Carlson, R., et al. 2009, Journal of Geophysical Research, 114, 1

Bolcar, M. R., Balasubramanian, K., Clampin, M., et al. 2015, Proceedings of SPIE, 9602, 1

Botet, R., Rannou, P., & Cabane, M. 1997, Applied Optics, 36, 8791

Brasil, A., Farias, T., & Carvalho, M. 1999, Journal of Aerosol Science, 30, 1379

Brodbeck, C., Van-Thanah, N., Bouanich, J.-P., et al. 1991, Journal of Geophysical Research, 96, 17497

Brown, M. E., Bouchez, A. H., & Griffith, C. a. 2002, Nature, 420, 795

Bullock, M., & Grinspoon, D. 2001, Icarus, 150, 19

Byrne, B., & Goldblatt, C. 2015, Climate of the Past, 11, 559

Carlson, R., Baines, K., Encrenaz, T., et al. 1991, Science, 253, 1541

Catling, D. C., Claire, M. W., Zahnle, K. J., et al. 2010, Journal of Geophysical Research: Planets, 115, doi:10.1029/2009JE003425

Chamberlain, S., Bailey, J., Crisp, D., & Meadows, V. 2013, Icarus, 222, 364

Chance, K., & Kurucz, R. 2010, Journal of Quantitative Spectroscopy and Radiative Transfer, 111, 1289

Charnay, B., Forget, F., Wordsworth, R., et al. 2013, Journal of Geophysical Research: Atmospheres, 118, 10,414

Charnay, B., Meadows, V., Misra, A., Leconte, J., & Arney, G. 2015, The Astrophysical Journal Letters, 813, L1

Claire, M. W., Kasting, J. F., Domagal-Goldman, S. D., et al. 2014, Geochimica et Cosmochimica Acta, 141, 365

Claire, M. W., Sheets, J., Cohen, M., et al. 2012, The Astrophysical Journal, 757, doi:10.1088/0004-637X/757/1/95

Clark, R. N., Swayze, G. A., Wise, R., et al. 2007, USGS digital spectral library splib06a: U.S. Geologial Survey, Digital Data Series 231, http://speclab.cr.usgs.gov/spectral.lib06

Clarke, D. W., & Ferris, J. P. 1997, in Planetary and Interstellar Processes Relevant to the Origins of Life, ed. D. C. B. Whittett (Springer Netherlands), 225–248

Cockell, C. S. 1998, Journal of Theoretical Biology, 193, 717

Collard, A. D., Taylor, F. W., Calcutt, S. B., et al. 1993, Planet. Space Sci., 41, 487

Cotton, D. V., Bailey, J., Crisp, D., & Meadows, V. 2012, Icarus, 217, 570

Counselman, C., Gourevitch, S., King, R., Loriot, G., & Ginsberg, E. 1980, Journal of Geophysical Research, 85, 8026

Crisp, D. 1986, Icarus, 514, 484

—. 1997, Geophysical Research Letters, 24, 571

Crisp, D., Allen, D., Grinspoon, D., & Pollack, J. 1991a, Science, 253, 1263

Crisp, D., a.P. Ingersoll, Hildebrand, C., & Preston, R. 1990, Advances in Space Research, 10, 109

Crisp, D., Sinton, W. M., Hodapp, K. W., et al. 1989, Science (New York, N.Y.), 246, 506

Crisp, D., McMuldroch, S., Stephens, S., et al. 1991b, Science, 253, 1538

Crow, C. A., McFadden, L. A., Robinson, T., et al. 2011, The Astrophysical Journal, 729, 130

Cushing, M., Vacca, W., & Rayner, J. 2004, Publications of the Astronomical Society of the Pacific, 116, 362

Dalcanton, J., Seager, S., Aigrain, S., et al. 2015, Association of Universities for For Research in Astronomy, arXiv:arXiv:1011.1669v3

de Bergh, C., Bezard, B., Crisp, D., et al. 1995, Advances in Space Research, 15, 79

de Kok, R., Irwin, P. G. J., Teanby, N. A., et al. 2007, Icarus, 186, 354

Deming, D., Seager, S., Winn, J., et al. 2009, Publications of the Astronomical Society of the Pacific, 121, 952

Denis, C., Schreider, A. A., Varga, P., & Závoti, J. 2002, Journal of Geodynamics, 34, 667

Des Marais, D. J., Harwit, M. O., Jucks, K. W., et al. 2002, Astrobiology, 2, 153

DeWitt, H. L., Trainer, M. G., Pavlov, A. A., et al. 2009, Astrobiology, 9, 447

Dickel, J. R. 1966, Icarus, 5, 305

Dillon, J. G., & Castenholz, R. W. 1999, Journal of Phycology, 35, 673

Domagal-Goldman, S. D., Kasting, J. F., Johnston, D. T., & Farquhar, J. 2008, Earth and Planetary Science Letters, 269, 29

Domagal-Goldman, S. D., Meadows, V. S., Claire, M. W., & Kasting, J. F. 2011, Astrobiology, 11, 419

Domagal-Goldman, S. D., Segura, A., Claire, M. W., Robinson, T. D., & Meadows, V. S. 2014, The Astrophysical Journal, 792, 90

Donahue, T., & Hodges, R. 1992, Journal of Geophysical Research, 97, 6083

Doyon, R., Hutchings, J. B., Beaulieu, M., et al. 2012, Proceedings of SPIE, 8442, 84422R

Dressing, C. D., & Charbonneau, D. 2015, The Astrophysical Journal, 807, 1

Driese, S. G., Jirsa, M. A., Ren, M., et al. 2011, Precambrian Research, 189, 1

Drossart, P., Piccioni, G., Adriani, a., et al. 2007, Planetary and Space Science, 55, 1653

Eigenbrode, J. L., & Freeman, K. H. 2006, Proceedings of the National Academy of Sciences, 103, 15759

Emmanuel, S., & Ague, J. J. 2007, Geophysical Research Letters, 34, 1

Esposito, L., Bertaux, J.-L., Krasnopolsky, V., Moroz, V., & Zasova, L. 1997, in Venus II, ed. S. Bougher, D. Hunten, & R. Phillips (Tucson: Univ. of Arizona Press), 415–458

Esposito, L., Knollenberg, R., Marov, M., Toon, O., & Turco, R. 1983, in Venus, univ. of a edn., ed. D. Hunten, L. Colin, T. Donahue, & V. Moroz (Tucson: The University of Arizona Press), 484–564

Esposito, L. W. 1980, Journal of Geophysical Research: Space Physics, 85, 8151

Etiope, G., & Sherwood Lollar, B. 2013, Reviews of Geophysics, 51, 276

Farquhar, J., Huiming, B., & Thiemens, M. 2000, Science, 289, 756

Farquhar, J., Peters, M., Johnston, D. T., et al. 2007, Nature, 449, 706

Farquhar, J., Savarino, J., Airieau, S., & Thiemens, M. H. 2001, Journal of Geophysical Research, 106, 32829

Fegley, B., & Prinn, R. 1989, Nature, 337, 55

Fenchel, T., & Straarup, B. J. 1971, Oikos, 22, 172

Ferruit, P., Bagnasco, G., Barho, R., et al. 2012, Proceedings of SPIE, 8442, 84422O

Fraine, J., Deming, D., Benneke, B., et al. 2014, Nature, 513, 556

France, K., Linsky, J. L., Tian, F., Froning, C. S., & Roberge, A. 2012, The Astrophysical Journal, 750, L32

Gao, P., Zhang, X., Crisp, D., Bardeen, C., & Yung, Y. 2014, Icarus, 1

García Muñoz, A., Zapatero Osorio, M. R., Barrena, R., et al. 2012, The Astrophysical Journal, 755, 103

Garcia-Pichel, F. 1998, Origins of Life and Evolution of the Biosphere, 28, 321

Garcia-Pichel, F., & Bebout, B. M. 1996, Marine Ecology Progress Series, 131, 257

Goldblatt, C., Robinson, T. D., Zahnle, K. J., & Crisp, D. 2013, Nature Geoscience, 6, 661

Goldblatt, C., & Watson, A. 2012, Philosophical Transactions of the Royal Society, 370, 4197

Goldblatt, C., & Zahnle, K. J. 2011, Climate of the Past, 7, 203

Greaves, J., Holland, W., Moriarty-Schieven, G., et al. 1998, The Astrophysical Journal, 506, 133

Greene, T. P., Line, M. R., Montero, C., et al. 2016, The Astrophysical Journal, 817, 17

Grenfell, J. L., Stracke, B., von Paris, P., et al. 2007, Planetary and Space Science, 55, 661

Grinspoon, D., & Lewis, J. 1988, Icarus, 74, 21

Grinspoon, D., Pollack, J., Sitton, B., et al. 1993, Planetary and Space Science, 41, 515

Guzmán-Marmolejo, A., Segura, A., & Escobar-Briones, E. 2013, Astrobiology, 13, 550

Hallquist, M., Wenger, J. C., Baltensperger, U., et al. 2009, Atmospheric Chemistry and Physics, 9, 5155

Hamano, K., Abe, Y., & Genda, H. 2013, Nature, 2

Haqq-Misra, J. D., Domagal-Goldman, S. D., Kasting, P. J., & Kasting, J. F. 2008, Astrobiology, 8, 1127

Harman, C. E., Kasting, J. F., & Wolf, E. T. 2013, Origins of Life and Evolution of Biospheres, 43, 77

Harman, C. E., Schwieterman, E. W., Schottelkotte, J. C., & Kasting, J. F. 2015, The Astrophysical Journal, 812, 137

Hasenkopf, C. A., Beaver, M. R., Trainer, M. G., et al. 2010, Icarus, 207, 903

Hasenkopf, C. A., Freedman, M. A., Beaver, M. R., Toon, O. B., & Tolbert, M. A. 2011, Astrobiology, 11, 135

Hashimoto, G., & Sugita, S. 2003, Journal of Geophysical Research, 108, 1

Hashimoto, G. L., & Imamura, T. 2001, Icarus, 154, 239

Haus, R., & Arnold, G. 2010, Planetary and Space Science, 58, 1578

Hawley, S., & Pettersen, B. 1991, The Astrophysical Journal, 378, 725

Henyey, L. C., & Greenstein, J. L. 1941, The Astrophysical Journal, 93, 70

Hicks, R. K., Day, D. A., Jimenez, J. L., & Tolbert, M. A. 2015, Analytical Chemistry, 87, 2741

Holland, H. D. 1973, Economic Geology, 68, 1169

—. 2006, Philosophical transactions of the Royal Society of London. Series B, Biological sciences, 361, 903

Hörst, S. M., & Tolbert, M. A. 2013, The Astrophysical Journal, 770, L10

Hörst, S. M., Yelle, R. V., Buch, A., et al. 2012, Astrobiology, 12, 809

Hu, R., Seager, S., & Bains, W. 2013, The Astrophysical Journal, 769, 6

Hunt-Walker, N., Hilton, E., Kowalski, A., Hawley, S., & Matthews, J. 2012, Publications of the . . . , 124, 545

Hunten, M. 1974, Icarus, 22, 111

Imanaka, H., Cruikshank, D. P., Khare, B. N., & McKay, C. P. 2012, Icarus, 218, 247

Ingersoll, A. 1969, Journal of the Atmospheric Sciences, 26, 1191

Iwagami, N., Ohtsuki, S., Tokuda, K., et al. 2008, Planetary and Space Science, 56, 1424

Izon, G., Zerkle, A. L., Zhelezinskaia, I., et al. 2015, Earth and Planetary Science Letters, 431, 264

Kaltenegger, L., Traub, W. A., & Jucks, K. W. 2007, The Astrophysical Journal, 658, 598

Kane, S. R., Kopparapu, R. K., & Domagal-Goldman, S. D. 2014, The Astrophysical Journal, 794, L5

Kasting, J. 1988, Icarus, 74, 472

Kasting, J., & Ackerman, T. 1986, Science, 234, 1383

Kasting, J., & Catling, D. 2003, Annu. Rev. Astron. Astrophys., 41, 429

Kasting, J., Pollack, J., & Ackerman, T. 1984, Icarus, 57, 335

Kasting, J., Zahnle, K., Pinto, J., & Young, A. 1989, Origins of Life and Evolution of the Biosphere, 19, 95

Kasting, J. F. 1993, Science, 259, 920

—. 2005, Precambrian Research, 137, 119

Kasting, J. F., & Donahue, T. M. 1980, Journal of Geophysical Research, 85, 3255

Kasting, J. F., Liu, S. C., & Donahue, T. M. 1979, Journal of Geophysical Research, 84, 3097

Kasting, J. F., Whitmire, D. P., & Reynolds, R. T. 1993, Icarus, 101, 108

Kasting, J. F., Zahnle, K. J., & Walker, J. C. G. 1983, Developements in Precambrian Geology, 13

Kelley, D. S., Karson, J. A., Fru, G. L., et al. 2005, Science, 307, 1428

Kerrich, R., & Polat, A. 2006, Tectonophysics, 415, 141

Kestler, D., Mayne, B., Ray, T., et al. 1975, Biochemical and Biophysical Research Communications, 66, 1439

Khare, B. N., Sagan, C., Arakawa, E. T., et al. 1984a, Icarus, 60, 127

Khare, B. N., Sagan, C., Ogino, H., et al. 1986, Icarus, 68, 176

Khare, B. N., Sagan, C., Thompson, W. R., et al. 1984b, Advances in Space Research, 4, 59

Kharecha, P., Kasting, J., & Siefert, J. 2005, Geobiology, 3, 53

Khatuntsev, I., Patsaeva, M., Titov, D., et al. 2013, Icarus, 226, 140

Kiang, N. Y., Siefert, J., Govindjee, & Blankenship, R. E. 2007a, Astrobiology, 7, 222

Kiang, N. Y., Segura, A., Tinetti, G., et al. 2007b, Astrobiology, 7, 252

Kitzmann, D., Patzer, A. B. C., von Paris, P., Godolt, M., & Rauer, H. 2011a, Astronomy & Astrophysics, 531, 1

—. 2011b, Astronomy & Astrophysics, 531, A62

Kitzmann, D., Patzer, A. B. C., von Paris, P., et al. 2010, Astronomy & Astrophysics, 511, 1

Knollenberg, R., & Hunten, D. 1980, Journal of Geophysical Research, 85, 8039

Knutson, H., Benneke, B., Deming, D., & Homeier, D. 2014a, Nature, 505, 66

Knutson, H., Dragomir, D., Kreidberg, L., et al. 2014b, The Astrophysical Journal, 794, 155

Konhauser, K. O., Amskold, L., Lalonde, S. V., et al. 2007, Earth and Planetary Science Letters, 258, 87

Kopparapu, R. K., Ramirez, R., Kasting, J. F., et al. 2013, The Astrophysical Journal, 765, 131

Kouyama, T., Imamura, T., Nakamura, M., Takehiko, S., & Futaana, Y. 2013, Journal of Geophysical Research: Planets, 118, 37

Köylü, Ü. Ö., Faeth, G. M., Farias, T. L., & Carvalho, M. G. 1995, Combustion and Flame, 100, 621

Krasnopolsky, V. 1986, Photochemistry in the Atmospheres of Mars and Venus, ed. U. Zahn (Berlin: Springer-Verlag)

—. 2007, Icarus, 191, 25

—. 2010a, Icarus, 208, 539

—. 2010b, Icarus, 209, 314

—. 2012, Icarus, 218, 230

Kreidberg, L., Bean, J. L., Désert, J.-M., et al. 2014, Nature, 505, 69

Krissansen-Totton, J., Schwieterman, E. W., Charnay, B., et al. 2016, The Astrophysical Journal, 817, 31

Kuiper, G. 1944, The Astrophysical Journal, 100, 378

Kumar, S., Hunten, D., & Pollack, J. 1983, Icarus, 55, 369

Kunze, M., Godolt, M., Langematz, U., et al. 2014, Planetary and Space Science, 98, 77

Kurzweil, F., Claire, M., Thomazo, C., et al. 2013, Earth and Planetary Science Letters, 366, 17

Lalonde, S. V., & Konhauser, K. O. 2015, Proceedings of the National Academy of Sciences, 112, 995

Larkum, A. W., & Kuhl, M. 2005, Trends in Plant Science, 10, 355

Larson, E. J., Toon, O. B., West, R. A., & Friedson, A. J. 2015, Icarus, 254, 122

Littler, M. M., Littler, D. S., Blair, S. M., & Norris, J. N. 1986, Deep-water plant communities from an uncharted seamount off San Salvador Island, Bahamas: distribution, abundance, and primary productivity, doi:10.1016/0198-0149(86)90003-8

López-Puertas, M., Dinelli, B. M., Adriani, A., et al. 2013, The Astrophysical Journal, 770, 132

Mahjoub, A., Carrasco, N., Dahoo, P.-R., et al. 2012, Icarus, 221, 670

Manabe, S., & Wetherald, R. T. 1967, Thermal Equilibrium of the Atmosphere with a Given Distribution of Relative Humidity, doi:10.1175/1520-0469(1967)024¡0241:TEOTAW¿2.0.CO;2

Marcq, E., Bertaux, J.-L., Montmessin, F., & Belyaev, D. 2012, Nature Geoscience, 6, 1

Marcq, E., Bézard, B., Drossart, P., et al. 2008, Journal of Geophysical Research, 113, E00B07

Marcq, E., Bézard, B., Encrenaz, T., & Birlan, M. 2005, Icarus, 179, 375

Marcq, E., Encrenaz, T., Bézard, B., & Birlan, M. 2006, Planetary and Space Science, 54, 1360

Markiewicz, W. J., Petrova, E., Shalygina, O., et al. 2014, Icarus, 234, 200

Marty, B., Zimmermann, L., Pujol, M., Burgess, R., & Philippot, P. 2013, Science, 342, 101

Mayer, C. H., McCullough, T. P., & Sloanaker, R. M. 1958, Astroph. J., 127, 1

McDonald, G. D., Thompson, W. R., Heinrich, M., Khare, B. N., & Sagan, C. 1994, Icarus, 108, 137

McElroy, M., Prather, M., & Rodriguez, J. 1982, Science, 215, 1614

McKay, C. P., Pollack, J. B., & Courtin, R. 1991, Science (New York, N.Y.), 253, 1118

McLinden, C. A., McConnell, J. C., Griffoen, E., McElroy, C. T., & Pfister, L. 1997, Journal of Geophysical Research, 102, 18801

Meadows, V., & Crisp, D. 1996, Journal of Geophysical Research:, 101, 4595

Meadows, V. S. 2006, Proceedings of the International Astronomical Union, 1, 25

Michaelian, K., & Simeonov, A. 2015, Biogeosciences, 12, 4913

Misra, A., Krissansen-Totton, J., Koehler, M. C., & Sholes, S. 2015, Astrobiology, 15, 462

Misra, A., Meadows, V., Claire, M., & Crisp, D. 2014a, Astrobiology, 14, 67

Misra, A., Meadows, V., & Crisp, D. 2014b, The Astrophysical Journal, 792, 61

Moore, J. 1971, Phd thesis, Columbia University

Morley, C. V., Fortney, J. J., Marley, M. S., et al. 2012, The Astrophysical Journal, 756, 172

—. 2015, The Astrophysical Journal, 815, 110

Morton, T. D., & Swift, J. 2014, The Astrophysical Journal, 791, 10

Moskalenko, N. 1979, Izv. Acad. Sci. USSR Atmos. and Oceanic Phys, 15, 912

Niemann, H. B., Atreya, S. K., Bauer, S. J., et al. 2005, Nature, 438, 779

Noffke, N., & Awramik, S. M. 2013, GSA Today, 23, 4

Noyes, R., Baliunas, S., Belserene, E., et al. 1984, The Astrophysical Journal, 285, L23

Olson, J. M., & Pierson, B. K. 1986, Photosynthesis Research, 9, 251

Ono, S., Eigenbrode, J. L., Pavlov, A. A., et al. 2003, Earth and Planetary Science Letters, 213, 15

Palmer, K. F., & Williams, D. 1975, Applied optics, 14, 208

Pavlov, A., Brown, L., & Kasting, J. 2001a, Journal of Geophysical Research, 106, 23267

Pavlov, A., Kasting, F., Brown, L. L., Rages, K. A., & Freedman, R. 2000, Journal of Geophysical Research, 105, 11981

Pavlov, A., & Kasting, J. 2002, Astrobiology, 2, 27

Pavlov, A., Kasting, J., Eigenbrode, J., & Freeman, K. 2001b, Geology, 29, 1003

Petty, G. 2006, A First Course in Atmospheric Radiation (Madison, Wisconsin: Sundog Publishing)

Pierson, B., Mitchell, H., & Ruff-Roberts, A. 1992, Origins of Life and Evolution of the Biosphere, 23, 243

Planavsky, N. J., Reinhard, C. T., Wang, X., et al. 2014, Science, 346, 635

Pollack, J., Strecker, D., Witteborn, F., Erickson, E., & Baldwin, B. 1978, Icarus, 34, 28

Pollack, J., Dalton, J., Grinspoon, D., et al. 1993, Icarus, 103, 1

Postman, M., Traub, W., Krist, J., et al. 2010, ASP Conference Series, 430, 6

Ramirez, R. M., Kopparapu, R., Zugger, M. E., et al. 2013, Nature Geoscience, 7, 59

Ramirez, S., Coll, P., da Silva, A., et al. 2002, Icarus, 156, 515

Rannou, P., Cabane, M., Botet, R., & Chassèfiere, E. 1997, Journal of Geophysical Research, 102, 10997

Rannou, P., & Durry, G. 2009, Journal of Geophysical Research: Planets, 114, E11013

Robinson, T. D., Ennico, K., Meadows, V. S., et al. 2014a, The Astrophysical Journal, 787, 171

Robinson, T. D., Maltagliati, L., Marley, M. S., & Fortney, J. J. 2014b, Proceedings of the National Academy of Sciences of the United States of America, 111, 9042

Robinson, T. D., Stapelfeldt, K. R., & Marley, M. S. 2016, Publications of the Astronomical Society of the Pacific, 128, 39

Robinson, T. D., Meadows, V. S., Crisp, D., et al. 2011, Astrobiology, 11, 393

Rothman, L., Gordon, I., Barber, R., et al. 2010, Journal of Quantitative Spectroscopy and Radiative Transfer, 111, 2139

Rothman, L., Gordon, I. E., Babikov, Y., et al. 2013, Journal of Quantitative Spectroscopy and Radiative Transfer, 130, 4

Rugheimer, S., Kaltenegger, L., Zsom, A., Segura, A., & Sasselov, D. 2013, Astrobiology, 13, 251

Rugheimer, S., Segura, A., Kaltenegger, L., & Sasselov, D. 2015, The Astrophysical Journal, 806, 137

Sagan, C., & Chyba, C. 1997, Science, 276, 1217

Sagan, C., Thompson, W., Carlson, R., Gurnett, D., & Hord, C. 1993, Nature, 365, 715

Sánchez-Lavega, A., Hueso, R., Piccioni, G., et al. 2008, Geophysical Research Letters, 35, L13204

Sandor, B. J., Todd Clancy, R., Moriarty-Schieven, G., & Mills, F. P. 2010, Icarus, 208, 49

Satoh, T., Imamura, T., Hashimoto, G. L., et al. 2009, Journal of Geophysical Research, 114, E00B37

Schidlowski, M. 2001, Precambrian Research, 106, 117

Schopf, J. W., ed. 1983, Earth's earliest biosphere: Its origin and evolution (Princeton, NJ, USA: Princeton University Press)

Schwieterman, E. W., Meadows, V. S., Domagal-Goldman, S. D., et al. 2016, The Astrophysical Journal Letters, 819, L13

Sciamma-O'Brien, E., Dahoo, P.-R., Hadamcik, E., et al. 2012, Icarus, 218, 353

Seager, S., Dalcanton, J. J., Postman, M., Tumlinson, J., & Mather, J. C. 2015, 21

Sebree, J. A., Stern, J. C., Mandt, K. E., Domagal-Goldman, S. D., & Trainer, M. G. 2015, Icarus, 2, 1

Segelstein, D. J. 1981, PhD thesis, UMKC

Segura, A., Kasting, J. F., Meadows, V., et al. 2005, Astrobiology, 5, 706

Segura, A., Krelove, K., Kasting, J. F., et al. 2003, Astrobiology, 3, 689

Segura, A., Meadows, V., Kasting, J., Crisp, D., & Cohen, M. 2007, Astronomy & Astrophysics, 472, 665

Segura, A., Walkowicz, L. M., Meadows, V., Kasting, J., & Hawley, S. 2010, Astrobiology, 10, 751

Seiff, A., Schofield, J., Kliore, A, J., et al. 1985, Adv. Space Res., 5, 3

Selsis, F. 2000, in Proceedings of the Conference 'Darwin and Astronomy - The Infrared Space Interferometer', 133–140

Shalygin, E., & Basilevsky, A. 2012, Planetary and Space . . . , 73, 294

Shalygin, E. V., Markiewicz, W. J., Basilevsky, A. T., et al. 2015, Geophysical Research Letters, 42, 4762

Shaw, G. H. 2008, Chemie der Erde - Geochemistry, 68, 235

Sheldon, K. F. 2000, Smoke, Dust, and Haze: Fundamentals of Aerosol Dynamics (Oxford Univ. Press, New York)

Shields, A. L., Meadows, V. S., Bitz, C. M., et al. 2013, Astrobiology, 13, 715

Sill, G., & Carm, O. 1972, Comm. Lunar Planet Lab., 9, 191

Sinclair, J. a., Irwin, P. G. J., Fletcher, L. N., et al. 2013, Icarus, 225, 257

Sing, D. K., Pont, F., Aigrain, S., et al. 2011, Monthly Notices of the Royal Astronomical Society, 416, 1443

Smrekar, S. E., Stofan, E. R., Mueller, N., et al. 2010, Science (New York, N.Y.), 328, 605

Snels, M., Stefani, S., Piccioni, G., & Bézard, B. 2014, Journal of Quantitative Spectroscopy and Radiative Transfer, 133, 464

Som, S. M., Buick, R., Hagadorn, J. W., et al. 2016, Nature Geoscience, 9, 1

Som, S. M., Catling, D. C., Harnmeijer, J. P., Polivka, P. M., & Buick, R. 2012, Nature, 484, 359

Spergel, D., Gehrels, N., Baltay, C., et al. 2015, Wide-Field Infrared Survey Telecope - Astrophysics Focused Telescope Assets WFIRST-AFTA, Tech. rep., SDT and WFIRST Study Office, arXiv:1305.5422

Stapelfeldt, K. R., Dekens, F. G., Brenner, M. P., et al. 2015, Proceedings of SPIE, 9605, 96050T

Stark, C. C., Roberge, A., Mandell, A., & Robinson, T. D. 2014, The Astrophysical Journal, 795, 122

Stüeken, E., Catling, D., & Buick, R. 2012, Nature Geoscience, doi:10.1038/NGEO1585

Taylor, F., Crisp, D., & Bézard, B. 1997, in Venus II, ed. S. Bougher, D. Hunten, & R. Phillips (Tuscon: The University of Arizona Press), 325–351

Tewari, V., & Seckbach, J. 2011, Stromatolites: interaction of microbes with sediments, Vol. 18 (Springer Science & Business Media)

Thomassot, E., O'Neil, J., Francis, D., Cartigny, P., & Wing, B. A. 2015, Proceedings of the National Academy of Sciences of the United States of America, 112, 707

Thomazo, C., Ader, M., Farquhar, J., & Philippot, P. 2009, Earth and Planetary Science Letters, 279, 65

Tian, F., Claire, M. W., Haqq-Misra, J. D., et al. 2010, Earth and Planetary Science Letters, 295, 412

Tobie, G., Lunine, J. I., & Sotin, C. 2006, Nature, 440, 61

Tolbert, N., Benker, C., & Beck, E. 1995, Proceedings of the National Academy of Sciences, 92, 11230

Tolfo, F. 1977, Journal of Aerosol Science, 8, 9

Tomasko, M., Doose, L., Engel, S., et al. 2008, Planetary and Space Science, 56, 669

Tomasko, M., Doose, L., & Smith, P. 1985, Advances in Space Research, 5, 71

Tomkins, A. G., Bowlt, L., Genge, M., et al. 2016, Nature, 533, 235

Tonkov, M., Filippov, N., Bertsev, V., et al. 1996, Applied Optics, 35, 4863

Toon, O., Ragent, B., Colburn, D., Blamont, J., & Cot, C. 1984, Icarus, 57, 143

Toon, O. B., Kasting, J. F., Turco, R. P., & Liu, M. S. 1987, Journal of Geophysical Research, 92, 943

Toon, O. B., Mckay, C. P., Ackerman, T. P., & Santhanam, K. 1989, Journal of Geophysical Research, 94, 16287

Trainer, M. G. 2013, Current Organic Chemistry, 17, 1710

Trainer, M. G., Jimenez, J. L., Yung, Y. L., Toon, O. B., & Tolbert, M. A. 2012, Astrobiology, 12, 315

Trainer, M. G., Pavlov, A. a., DeWitt, H. L., et al. 2006, Proceedings of the National Academy of Sciences of the United States of America, 103, 18035

Trainer, M. G., Pavlov, A. a., Curtis, D. B., et al. 2004, Astrobiology, 4, 409

Tran, B. N., Joseph, J. C., Ferris, J. P., Persans, P. D., & Chera, J. J. 2003, Icarus, 165, 379

Traub, W. A. 2003, in Proceedings of the Conference on Towards Other Earths: DARWIN/TPF and the Search for Extrasolar Terrestrial Planets No. April 22-25, Heidelberg, Germany, 231–239

Tsang, C., Irwin, P., Taylor, F., & Wilson, C. 2008a, Journal of Quantitative Spectroscopy and Radiative Transfer and Radiative Transfer, 109, 1118

Tsang, C., Taylor, F., Wilson, C., et al. 2009, Icarus, 201, 432

Tsang, C., Irwin, P., Wilson, C., et al. 2008b, Journal of Geophysical Research, 113, E00B08

Tsang, C. C. C., Wilson, C. F., Barstow, J. K., et al. 2010, Geophysical Research Letters, 37, L02202

Ueno, Y., Johnson, M. S., Danielache, S. O., et al. 2009, Proceedings of the National Academy of Sciences of the United States of America, 106, 14784

Ueno, Y., Yamada, K., Yoshida, N., Maruyama, S., & Isozaki, Y. 2006, Nature, 440, 516

Urey, H. C., & Greiff, L. J. 1935, Journal of the American Chemical Society, 57, 321

Vacca, W., Cushing, M., & Rayner, J. 2003, Publications of the Astronomical Society of the Pacific, 115, 389

—. 2004, Publications of the Astronomical Society of the Pacific, 116, 352

Vance, S., Harnmeijer, J., Kimura, J., et al. 2007, Astrobiology, 7, doi:10.1089/ast.2007.0075

Ver Eecke, H. C., Butterfield, D. A., Huber, J. A., et al. 2012, Proceedings of the National Academy of Sciences, 109, 13674

Veverka, J. 1973, Icarus, 18, 657

Von Braun, K., Boyajian, T. S., van Belle, G. T., et al. 2014, Monthly Notices of the Royal Astronomical Society, 438, 2413

Vuitton, V., Tran, B. N., Persans, P. D., & Ferris, J. P. 2009, Icarus, 203, 663

Waite, J. H., Young, D. T., Cravens, T. E., et al. 2007, Science (New York, N.Y.), 316, 870

Walker, J. C., Hays, P., & Kasting, J. 1981, Journal of Geophysical Research: Oceans, 86, 9776

Watanabe, Y., Martini, J. E. J., & Ohmoto, H. 2000, Nature, 408, 574

West, A. A., Hawley, S. L., Bochanski, J. J., et al. 2008, The Astronomical Journal, 135, 785

Wilson, J. C., Henderson, C. P., Herter, T. L., et al. 2004, Proceedings of SPIE, 5492, 1295

Wiscombe, W. J. 1980, Appl. Opt., 19, 1505

Woese, C. R., & Fox, G. E. 1977, Proceedings of the National Academy of Sciences of the United States of America, 74, 5088

Wolf, E., & Toon, O. B. 2014, Geophysical Research Letters, 41, 167

Wolf, E. T., & Toon, O. B. 2010, Science (New York, N.Y.), 328, 1266

—. 2013, Astrobiology, 13, 656

Woolf, N., Smith, P., Traub, W., & Jucks, K. 2002, The Astrophysical Journal, 574, 430

Wright, G. S., Rieke, G. H., Colina, L., et al. 2004, Proceedings of SPIE, 5487, 653

Yamamoto, M., & Takahashi, M. 2004, Geophysical Research Letters, 31, n/a, l09701

Yoon, Y. H., Hörst, S. M., Hicks, R. K., et al. 2014, Icarus, 233, 233

Young, A. 1975, Journal of Atmospheric Sciences, 32, 1125

Young, G., von Brunn, V., Gold, D., & Minter, W. 1998, The Journal of Geology, 106, 523

Yung, Y., & DeMore, W. 1982, Icarus, 51, 199

Yung, Y. L., Allen, M., & Pinto, J. P. 1984, The Astrophysical Journal Supplement Series, 55, 465

Yung, Y. L., Yang, D., Lee, C., et al. 2009, 0, 1

Zahnle, K., Claire, M., & Catling, D. 2006, Geobiology, 4, 271

Zerkle, A. L., Claire, M. W., Domagal-Goldman, S. D., Farquhar, J., & Poulton, S. W. 2012, Nature Geoscience, 5, 359

Zhang, X., Liang, M., Mills, F., Belyaev, D., & Yung, Y. 2012, Icarus, 217, 714

VITA

Dr. Giada Nicole Arney

Education

- Ph.D. in Astronomy and Astrobiology, University of Washington (UW) (2016)
- M.Sc. in Astronomy, UW (2012)
- B.A. Astrophysics, with distinction, University of Colorado at Boulder (CU) (2009)
- Linguistics Minor

Fellowships

- NASA Postdoctoral Program Fellowship (2016)
- NSF Integrative Graduate Education and Research Traineeship (2010-2011)

Honors and Awards

- Postdoctral Associate on winning Habitable Worlds Proposal (2016)
- Co-I on winning NAI Director's Discretionary Fund Proposal (2016)
- Student travel award to attend Earth Life Science Institute International Symposium in Tokyo, Japan (January 2016)

- Scholarship attendee of Australian Centre for Astrobiology “Grand Tour” (summer 2015)
- Co-lead on UW Student Technology Fee winning proposal “Revitalizing the UW Planetarium” (Jan. 2015)
- NASA Astrobiology Institute Early Career Collaboration Award (2014)
- Seattle Astronomical Society Outreach Award (2013)
- Phi Beta Kappa (2008)
- University of Colorado Wesley Scholarship (2007)

Teaching

- Mentor for UW Undergraduate student Guadalupe Tovar (2013-2016)
- Guest Lecturer, ESS 495 “NASA Space Grant Seminar: Rocks-n-Stars”, undergraduate lecture entitled “Seeing Through the Clouds of Venus” (2013)
- Pre Major in Astronomy Program mentor (2012)
- Teaching Assistant, ASTR 101 “Astronomy” (Spring 2011, Winter 2012)
- Teaching Assistant, ASTR 150 “The Planets” (Fall 2011)

Service

- Lead for VEXAG Early Career Scholars focus group (Aug. 2016 - present)
- Member of LUVOIR exoplanets science working group (June 2016 - present)
- Executive secretary at LUVOIR STDT meeting (May 2016)

- Co-chair of session “Extrasolar Planets: Terrestrial and Neptunian Planets” (DPS Conference, Fall 2015)
- Deputy lead for VEXAG Early Career Scholars Focus Group (2015 - 2016)
- UW Astrobiology Program steering group student representative (Fall 2014 - present)
- Planetarium coordinator for the University of Washington (Fall 2013 - Fall 2015)
- Organizer for Astrobiology Graduate Science Conference (AbGradCon) (2011)
- Executive secretary on a NASA grant review program
- External reviewer on NESSF graduate fellowships
- External reviewer on ROSES proposals
- Reviewer for papers published in *The Astrophysical Journal* and *Geology*

Public Outreach

- Planetarium shows at UW (Fall 2010 - present)
- “Astronomy on Tap” presentation entitled “Hot Planets” on Venus and Earth climate change: Seattle, WA (June 2016)
- Panelist at Sammamish High School STEM Fair: Bellevue, WA (May 2016)
- Speaker for Lakewood High School astrobiology class visiting UW (May 2016, March 2015)
- “Space in Your Face” hazy Archean presentation: Bainbridge Island, WA (November 2015)

- Participated in FameLab: Chicago, IL (June 2015)
- “Space in Your Face” Venus presentation: Denver, CO (December 2014)
- AAS Astronomy Ambassadors Program: Tucson, AZ (Fall 2014)
- UW Astronomy Open House coordinator (Spring 2013)
- “Local expert” for *Cosmos* viewing at UW (Fall 2013)
- Fiske Planetarium: Boulder, CO (2005-2009)

Press

- http://www.washington.edu/news/2015/11/12/pale-orange-dot-early-earths-haze-may-give-clue-to-habitability-elsewhere-in-space/
- http://motherboard.vice.com/read/we-should-look-for-orange-exoplanets-because-thats-what-earth-used-to-look-like
- http://www.iflscience.com/space/earth-used-look-orange
- http://www.rdmag.com/articles/2015/11/ancient-earth-relevant-search-alien-life
- http://news.discovery.com/space/alien-life-exoplanets/could-pale-orange-worlds-lead-us-to-alien-life-151113.htm
- http://gizmodo.com/hazy-orange-planets-may-be-good-places-to-live-1741820253
- http://www.astronomy.com/news/2015/11/astronomers-look-to-titan-for-clouds-haze-and-et
- http://stellaraperture.com/2015/11/13/dps-2015-days-3-and-4-venusian-aircraft-pale-orange-dots-and-magma-oceans/

- http://www.dailymail.co.uk/sciencetech/article-3316249/An-orange-GLOW-guide-alien-life-Researchers-finds-mists-key-finding-habitable-planets.html

Refereed Publications

- **Arney, G.**, S. D. Domagal-Goldman, V. S. Meadows, E. T. Wolf, E. Schwieterman, B. Charnay, M. W. Claire, E. Hébrard, M. Trainer The Pale Orange Dot: The Spectrum and Habitability of Hazy Archean Earth. In review at Astrobiology.

- Schwieterman, E.W., Meadows, V.S., Domagal-Goldman, S.D., Deming, D., **Arney, G.N.**, Luger, R., Harman, C.E., Misra, A. Barnes, R. (2016) Identifying Planetary Biosignature Impostors: Spectral Features of CO and O4 Resulting from Abiotic O2/O3 Production. The Astrophysical Journal Letters 819:L13.

- Krissansen-Totton, J., E. Schwieterman, B. Charnay, **G. Arney**, T. Robinson, V. S. Meadows, D. Catling (2016). Is the Pale Blue Dot unique? Optimized photometric bands for identifying Earth-like exoplanets. The Astrophysical Journal.

- Charnay, B., V. S. Meadows, A. Misra, J. Leconte, **G. Arney** (2015). 3D modeling of GJ1214b's atmosphere: formation of inhomogeneous high clouds and observational implications. The Astrophysical Journal Letters, 813: L1 (7pp)

- **Arney, G.**, V. S. Meadows, D. Crisp, S. J. Schmidt, T. Robinson (2014). Spatially Resolved Measurements of H2O, HCl, CO, OCS, SO2, Cloud Opacity, and Acid Concentration in the Venus Near-Infrared Spectral Windows. Journal of Geophysical Research: Planets, 119: 1860-1891.

- **Arney, G.**, "How do we define habitable zones?" In S. Domagal-Goldman and K. Wright (Eds.), Astrobiology Primer 2.0, In review at Astrobiology.

- **Arney, G.**, V. S. Meadows, S. D. Domagal-Goldman, D. Deming, T. Robinson, G. Tovarg, E. T. Wolf, E. Schwieterman (in preparation). "Pale Orange Dots: The Impact of Organic Haze on the Habitability and Detectability of Earthlike Planets Orbiting Other Stars."

- Roberge, A., A. Lincowski, M. Rizzo, C. Stark, **G. Arney**, T. Robinson, M. Kuchner, E. Nesvoid, V. S. Meadows, A. Wilkins, M. McElwain, M. Turnbull. Finding the Needle in the Haystack: A High-Fidelity Model of the Solar System for Simulating Exoplanet Observations. In preparation.

- J. Krissansen-Totton, **G. Arney**, D. C. Catling. A model of ocean pH and atmospheric pCO_2 over Earth history. In preparation.

Conference Publications (Oral)

- Arney et al. (2016) Pale Orange Dots: Earthlike Worlds with Organic Hazes. The Astrophysics of Planetary Habitability Conference, Vienna, Austria. February 2016. Oral presentation.

- Arney et al (2015) Under an Orange Sky: The Many Implications of Organic Haze for Earthlike Planets. DPS, National Harbor, MD. November 2015. Oral presentation.

- Arney et al. (2015) Under an Orange Sky: The Many Implications of an Archean Haze. Comparative Climates of Terrestrial Planets II. Mountain View, CA. September 2015. Oral presentation.

- Arney et al. (2015) The Pale Orange Dot: Spectra and Climates of Hazy Archean Earthlike Worlds. AbSciCon, Chicago, IL, June 2015. Oral Presentation.

- Arney et al. (2015) The Pale Orange Dot: The Climactic and Spectral Effects of Haze in Archaen Earth's Atmosphere. Emerging Researchers in Exoplanet Science Symposium, State College, PA, May 2015. Oral Presentation.

- Arney, et al. (2015) Hazy Archean Earth as an Analog for Hazy Earthlike Exoplanets. 225th AAS Meeting, Seattle, WA, January 2015. Oral presentation.

- Arney, et al. (2013) Spatially-Resolved Measurements of H2O, HCl, CO, OCS, SO2 and cloud opacity in the Venus Near-Infrared Windows. DPS, Denver, CO, October 2013. Oral presentation.

- Arney, et al. (2013) Pale Yellow Dots. AbGradCon, Montreal, Québec, June 2013. Oral Presentation.

Conference Publications (Poster)

- Arney et al. (2016) Pulling Back the Veil: The Habitability and Characterization of Hazy Worlds. Earth Life Science Institute International Symposium, Tokyo, Japan. January 2016. Poster Presentation.

- Arney, et al. (2014) The Pale Orange Dot: Spectral Effects of a Hazy Early Earth. AGU Fall Meeting, San Francisco, CA, December 2014. Poster presentation.

- Arney, et al. (2014) Pale Orange Dots: Hazy Archean Earth as an Analog for Hazy Earthlike Exoplanets. DPS, Tucson, AZ, November 2014. Poster presentation.

- Arney, et al. (2014) The Pale Orange Dot: Spectral Effects of a Hazy Early Earth. Exoplanets, Biosignatures, and Instruments Conference, Tucson, AZ, March 2014. Poster presentation.

- Arney, et al. (2012) Characterizing the Surface Conditions of Hazy Exoplanets. AbGradCon, Pasadena, CA, August 2012. Poster presentation.

- Arney, et al. (2012) Characterizing the Surface Environment of Exo-Venus Analogs. AbSciCon, Atlanta, GA, March 2012. Poster presentation.

- Arney et al. (2011) Remote sensing of surface characteristics of cloud-enshrouded planets. AbGradCon, Bozeman, MT, June 2011. Poster presentation.

Invited Talks

- Arney et al. (2015) The Pale Orange Dot: The Spectrum and Climate of Hazy Archean Earth. Solar System Exploration Fall Seminar Series. Goddard Space Flight Center, Greenbelt, MD. November 2015. Invited talk.

- Arney et al. (2015) Ground Based Measurements of Trace Gases Below the Cloud Deck. 13th Meeting of the Venus Exploration Analysis Group Meeting. Washington, D.C. October 2015. Invited talk.

Other

- Colorado state first place winner at high school level for 2002 PTA “Reflections” program in Literature category (2002)

- First Year Writing Award from CU Program for Writing and Rhetoric (2005)

- Worked on a conservation project in New Zealand through International Student Volunteers (June 2006)

- Co-founder and co-president of the University of Colorado Astrobiology Club (2007)

- Studied abroad in Ireland at University College Cork (2008)